Design and Analysis of Electric Powertrains for Offshore Drilling Applications

Witold Paweł Pawlus

Design and Analysis of Electric Powertrains for Offshore Drilling Applications

A dissertation submitted to the University of Agder for the degree of Doctor of Philosophy, Specialization in Mechatronics

University of Agder
Faculty of Engineering and Science
2016

. . . to Basia.

Acknowledgments

I would like to thank Martin Choux, Michael R. Hansen, and Geir Hovland for contributions to the research results presented in this thesis. I acknowledge the support from the Norwegian Research Council and the company MHWirth AS that allowed me to pursue my Ph.D. degree.

I appreciate the group of people at MHWirth AS with whom I had the occasion to work over the past three years. Søren Øydna's ideas influenced some of the initial research directions and Kristin Wallevik's experience played an important role in starting the project. Tor Inge Waag's dedication and eagerness to help, as well as the excellent and timely feedback on several manuscripts I received from Kristin Wallem Timenes, saved me probably from a few more rounds of peer reviews of my articles. Bjarne Sandrib and Pål Skogerbø are recognized for always finding time for me despite their busy schedules.

The most rewarding and inspiring time in my Ph.D. project was the three months I spent at the Automatic Control Laboratory at ETH Zürich. My sincere gratitude goes to Manfred Morari for giving me the opportunity to carry out a part of my research in one of the most reputable control institutes worldwide. It has been an honor and privilege working with you.

My thanks go to Damian Frick for patiently teaching me the fundamentals of optimization and for his support during my stay at IfA. I want to thank the other people who one way or another influenced my research perspective: Giampaolo Torrisi, Robin Vujanic, and Alexander Domahidi. Although we did not collaborate full-time, I benefited from our meetings probably more than you are aware. Also, friendly attitude of Alice Vyskocil remains a memory that brings a smile to my face. Last but not least, I will never forget the enjoyable discussions we had with Stanisław Pietrzko. I am thankful to him for openly sharing his opinions, reflections, and lessons.

My stay at the Automatic Control Laboratory was made possible thanks to involvement of Geir Hovland for which I am particularly indebted to him. I am also grateful for his practical advices and hands-on help on many occasions. Michael R. Hansen deserves warm thanks for always being available to lend a helpful hand and for just being supportive. If it were not for Huynh Van Khang, I would have probably missed some of the greatest joys of being a Ph.D. student. Thank you for being a great example of a researcher truly dedicated to science, for your exceptional attitude towards co-workers, and for not being afraid to take the responsibility.

My gratitude also goes to the people who supported me in the experimental work. Trond Ove Nygård is acknowledged for providing useful information and documents regarding the gantry crane machine. I would like to thank Luis Pimentel, Tor Martin Heggland, and Rune Risholt for sharing their expertise about the vertical pipe racker. Steve Schading, Roy Werner Folgerø, and Carl Thomas Duus are co-responsible for creating probably the most good looking VFD test bench out there. The professional support from Rune Eilertsen and Ivar Dyrendahl from ABB removed many obstacles from my way and made my learning curve steeper.

Among all these people I met during my journey, my special thanks and personal gratitude go to Surya Teja Kandukuri with whom I had the pleasure of sharing the office over the last two years. It is difficult to find the proper words to express how grateful I am for your

honesty, support, and distractions (yes, especially for distractions). I cannot imagine how much I would have missed if you had not decided to come here and we had never met. I thank you and Sowmya for the great time we had together and I wish you all the best for your future. The discussions over a cup of coffee we had with Jagath Sri Lal Senanayaka lead to many interesting scientific discoveries and – probably even more interesting – non-scientific contemplations. Thank you, gentlemen, for being my most excellent office mates.

But most importantly, I would like to thank my family. I am grateful to my parents for teaching me that after all, what really matters is to be rather than to have, and to my brother for always believing in me. Finally, my deepest gratitude goes to my wife Basia for simply everything – without her, all of that would have not been possible and would make no sense whatsoever.

<div align="right">

Witold Pawlus
Grimstad, Summer 2016

</div>

Contents

Abstract

The global energy market is challenged with an ever increasing need for resources to meet the growing demands for electric power, transportation fuels, etc. Although we witness the expansion of the renewable energy industry, it is still the fossil fuels, with oil and gas dominating the scene of global energy supply sector, that provide majority of worldwide power generation. However, many of the easily accessible hydrocarbon reserves are depleted which requires from the producers of drilling equipment to focus on cost-effective operations and technology to compete in a challenging market.

Particularly high level of activity is observed in both industry and academia in the field of electrical actuation systems of drilling machines, as control methods of alternating current (AC) motor drives have become an industrially mature technology over the past few decades. In addition, state-of-the-art AC motors manufacturing processes allow to conform to the strict requirements for safe operation of electrical equipment in explosive atmospheres. These two main reasons made electric actuation systems a tough competitor to hydraulic powertrains used traditionally by the industry. However, optimal design of induction motor drives and systematic analysis of factors associated with operation in harsh offshore conditions are still considered as a major challenge.

In this thesis, effective methods for design and analysis of induction motor drives are proposed, including aspects of optimization and simulation-based engineering. The first part of the thesis is devoted to studying methods for modeling, control, and identification of induction machines operating in offshore drilling equipment with the focus to improve their reliability, extend lifetime, and avoid faults and damage, whereas the second part introduces more general approaches to the optimal selection of components of electric drivetrains and to the improvement of the existing dimensioning guidelines.

A multidisciplinary approach to design of actuation systems is explored in this thesis by studying the areas of motion control, condition monitoring, and thermal modeling of electric powertrains with an aspiration to reach the level of design sophistication which goes beyond what is currently considered an industrial standard. We present a technique to reproduce operation of a full-scale offshore drilling machine on a scaled-down experimental setup to estimate the mechanical load that the designed powertrain must overcome to meet the specification requirements. The same laboratory setup is used to verify the accuracy of the estimation and control method of an induction motor drive based on the extended Kalman filter (EKF) to confirm that the sensorless control techniques can reduce the number of data acquisition devices in offshore machines, and thus decrease their failure rate without negatively affecting their functionality. To address the challenge of condition monitoring of induction motor drives, we propose a technique to assess the expected lifetime of electric drivetrain components when subjected to the desired duty cycles by comparing the effects of a few popular motion control signals on the cumulative damage and vibrations. As a result, the information about the influence of a given control strategy on drivetrain lifecycle is made available early in the design stage which can significantly affect the choice of the optimal powertrain components.

The results show that some of the techniques that have a well-proven track record in other industries can be successfully applied to solve challenges associated with operation of offshore drilling machines. One of the most essential contributions of this thesis, optimal selection of drivetrain components, is based on formulating the drivetrain dimensioning problem as a mixed integer optimization program. The components of powertrain that satisfy the design constraints and are as cost-effective as possible are found to be the global optimum, contrary to the functionality offered by some commercially available drivetrain sizing software products. Another important drawback of the dimensioning procedures recommended by the motor drives manufacturers is the inability to assess if the permissible temperature limits given in the standards do not become violated when the actuation system experiences overloads different than these tabulated in the catalogs. Hence, the second most significant contribution is to propose a method to monitor thermal performance of induction motor drives that is based exclusively on publicly available catalog data and allows for evaluating whether the standard thermal performance limits are violated or not under arbitrary load conditions and at any ambient temperature. Both these solutions can effectively enrich the industrially accepted dimensioning procedures to satisfy the level of conservatism that is demanded by the offshore drilling business but, at the same time, provide improved efficiency and flexibility of the product design process and guarantee optimality (quantitatively, not qualitatively, measurable) of the final solution. An attractive direction for additional development is to further integrate knowledge from different fields relevant to electric powertrains to enable design of tailored solutions without compromising on their cost and performance.

1 Introduction

1.1 Motivation

It is expected that the global net electricity generation will increase by 93 %, from 20.2 trillion kWh in 2010 to 39.1 trillion kWh in 2040, according to [86]. 42 % of this energy is nowadays used in industry. Specifically, electric motors use 67 % of this share, which corresponds to approx. 30 % of global electricity consumption [49]. The number of industrial electric motors installed worldwide amounts to 300 million and this figure increases by 10 % each year [352]. Over the past decades, direct current (DC) commutator machines have gradually been replaced by alternating current (AC) motors: induction motors (IMs) and permanent magnet brushless motors (PMBMs) [121]. PMBMs can be further classified into two principal groups: sinusoidally excited motors, called permanent magnet synchronous machines (PMSMs); and trapezoidally excited motors, called brushless DC motors (BDCMs). Currently, IMs are by far the most popular in industry, as almost 50 % of all the electricity generated is converted back to mechanical energy using these machines [149]. The history of induction motor dates back to 1885 and 1886 when Galileo Ferraris and Nicola Tesla made their inventions. These milestones were possible thanks to discovery of electromagnetic induction law by Michael Faraday around 1831 and formulation of laws of electricity by James Clerk Maxwell around 1860. Actually, electrical engineering is among the most popular and oldest engineering disciplines [210]. More than 200 years of modern applied research (dated back to the invention of an early electric battery by Alessandro Volta in 1800) and around 140 years of formal education in this field (e.g first official curricula in the U.S. started in the 1880's [334]) created a thorough foundation for further innovation and development.

Despite the fact that usage of IMs in industry have steadily increased since the end of 19th century, until the 1980's a DC machine was a natural choice in applications where speed or torque control was required [149]. Complex governing equations of induction machine became tractable with computer simulation in the 1970's, which increased understanding of stator currents regulation to achieve torque control. Development of pulse-width modulation (PWM) inverters enabled fast current control in AC machines but it turned into an industrially mature technology only after power electronics components became cheap and fast enough to handle such control strategies as field-oriented control (FOC) [46] or direct torque control (DTC) ([97] and [328]). Since then, variable-frequency drives (VFDs) began to be more popular and accessible, mainly thanks to higher efficiency, feasible speed/torque control, and improved cost-effectiveness. Electric motors and drives have been put into use in an increasing number of applications over the past few decades, such as e.g. locomotives [114], automotive [288], robotic assembly [264]/manufacturing [365], aerospace [48], ship propulsion [185], or energy [57]. The overall trend to electrify more and more industrial processes and areas is attributed to improved control features, reduced energy consumption, higher reliability over time as well as minimal routine and preventive maintenance of VFDs [349].

Petroleum drilling industry recognized the importance of electric motors as early as in the 1940's – see for instance [293]. Initially, diesel engines and locomotive traction type DC motors were applied on onshore drilling rigs, however, discoveries of oil and gas offshore necessitated development of more compact and reliable powertrains. The first oilfield in North Sea, "Ekofisk", has been found in 1969 by Phillips Petroleum Company and oil production started two years later [147]. At that time, however, because of the problems associated with control of AC machines, still either DC motors or mechanical transmissions were applied on offshore oil platforms [323]. These were not favorable due to risk of spark generation or too large footprint. A solution that offered a significant improvement was to utilize a fluid coupling (i.e. a hydraulic drivetrain) which is by far more flexible and provides for effective speed control. Hydraulic actuation systems turned out to be particularly well suited for offshore drilling applications due to higher power densities than those available from electric motors, fail-safe circuits which prevent dropping the load in case of power loss, convenient translational motion control, or effective heat dissipation [166]. These features made fluid power transmissions dominant in the offshore drilling industry for a few decades [335]. It was not until the 1990's when the advent of modern power electronics and novel control methods of AC machines made producers of offshore drilling equipment start to investigate feasibility of electric actuation systems [351]. Although the drawbacks (e.g. nonlinearities of valves, difficulties with control systems' tuning, deterioration of hydraulic components, or risk of leakage) of hydraulic powertrains are well-known, it was only recently that electrically actuated equipment has become more common in offshore drilling applications. This is dictated by the fact that as the search for oil and gas gradually moves into more hostile and harsh environments (Arctic, subsea), drivetrain solutions that are efficient, easy to maintain, and environmentally friendly are favorable. However, the petroleum industry is one of the most conservative industries when it comes to adoption of new technology [317]. This is of course understandable and dictated by high financial, environmental, social, and political consequences of serious failures of drilling equipment. It is common that solutions which have a long track record are preferable ("We-have-always-done-it-that-way" attitude) and potential innovations require extensive testing before they become an industrially accepted standard. Therefore, there still exists a gap in knowledge base and expertise within the offshore drilling industry regarding feasibility of electrical actuation systems. The objective of this Ph.D. thesis is to reduce it.

1.2 Actuation Systems

The ongoing process of integration of products or processes and electronics has been observed (especially for mechanical systems) since the 1980's [45]. The old-fashioned electro-mechanical systems, considered to be sum of separate parts and subsystems, have been gradually replaced by integrated electronic-mechanical systems with sensors, actuators, and digital microelectronics. These synergistic combinations of components from various domains are called mechatronic systems. The following elements are considered to be their main building blocks [95]: mechanical structure, actuators, sensors, controllers, signal conditioning devices, computer hardware and software, interface devices, and power sources, as illustrated in Fig. 1.1. This Ph.D. thesis focuses on the actuation part of the system. Actuator is a functional element which connects the information processing part of the control system with the controlled process [166]. Actuators typically control the flow of energy, mass, or volume; and their functional components are classified into two main groups:

1. Energy controllers – the energy of the power supply is controlled via the input variable to generate actuator's output (classic examples are transistors and valves).
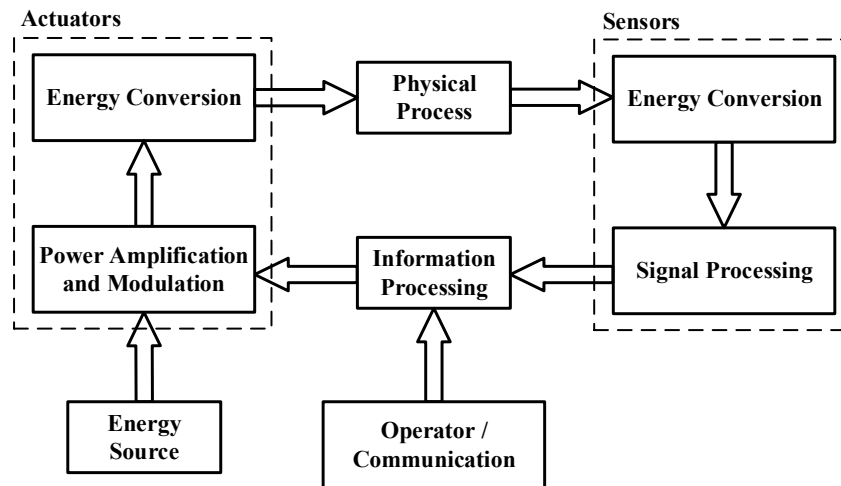
Figure 1.1: Mechatronic system [45].

2. Energy converters – input and output are energies: they might be of the same type (e.g. gears or transformers) or different (e.g. electric motors or hydraulic cylinders).

Actuators are therefore normally composed of at least one energy controller (to control flow of matter or energy) and one energy converter. To enable control of an actuator, it is required to intensify the low-power electrical command signal, hence, the energy controller is often referred to as the power amplifier. According to [45], there are three main types of power utilized by actuation systems:

1. Electric power.

2. Hydraulic power.

3. Pneumatic power.

Motors (linear and rotating), solenoids, and electromagnets are typically used with the option no.1 above. The remaining two options take advantage of cylinders (linear motors) and rotary motors, which motion is regulated by flow of compressible (e.g. compressed air) or incompressible (e.g. hydraulic liquid) fluids. As discussed in Section 1.1, electric and hydraulic actuation systems are the most popular in offshore drilling industry nowadays. Therefore, we review their characteristic features and components in more detail.

Hydraulic Actuation System

Fig. 1.2 illustrates a typical hydraulic actuation system. The energy conversion part of the actuator is in this case a double-acting cylinder. The energy controller (also called an interface) is a 4/2 distributor valve which regulates the flow of hydraulic fluid by receiving order signals from the control system. Controller's outputs are generated according to the operator's commands (e.g. to achieve a certain motion pattern of the cylinder) and feedback signals provided by the sensors (depicted here by the limit switches). The complete actuation system is therefore composed of an actuator (including interface and transformer – e.g. a gearbox), sensors, and controller [45]. Electric power (typically, an induction motor operated at full rated load) is used to drive a hydraulic pump which provides fluid flow to the actuation system. The displacement of the pump might also be controlled to regulate the speed of the actuator. This solution is referred to as a hydrostatic transmission [166].
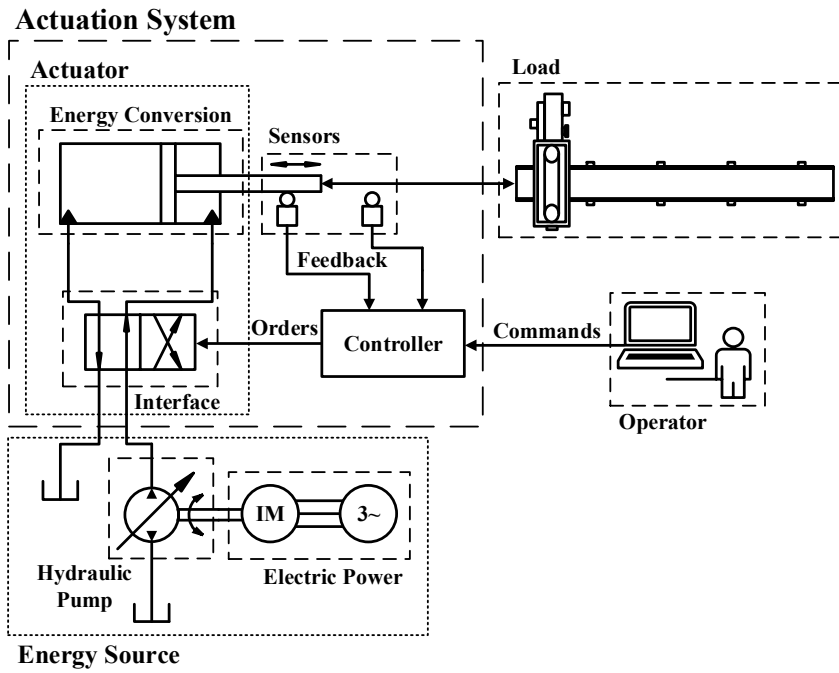
Figure 1.2: Typical hydraulic actuation system [45].

Electrical Actuation System

An example of an electrically actuated system is shown in Fig. 1.3. Since induction motor
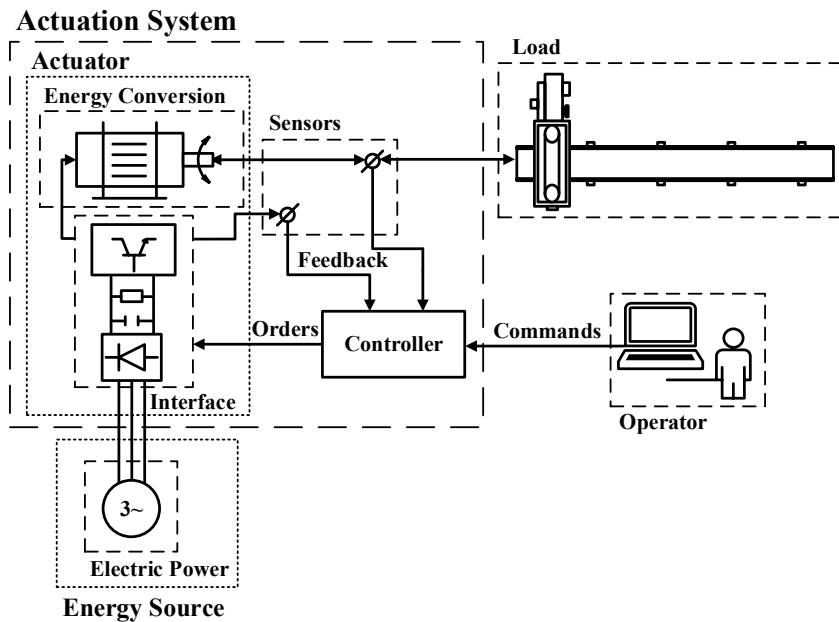
Figure 1.3: Typical electrical actuation system [73].

is among the most popular electric machines used in industry, it is illustrated as the energy conversion part of the considered electric powertrain. The AC motor is supplied with electric power by the connection of two energy converters, a rectifier and an inverter [111]. The AC power from the grid is converted to DC power on the rectifier. Control of the voltage in DC link is not always implemented but it allows e.g. to regenerate power to the grid. The inverter transforms the DC voltage into the AC voltage with a frequency and amplitude specified by

the controller, which enables variable speed operation of the motor. Current and voltage sensors are normally utilized in torque control applications, whereas encoders (or sophisticated speed/position estimation algorithms) make it possible to control motor's speed/position.

Remark 1.1. *In this thesis, the term "actuation system" is used interchangeably with "drive-train" and "powertrain". Also, if not specified otherwise, an "electric(al) actuation system" is by default composed of an induction motor, a VFD (including control software and necessary sensors), and a gearbox.*

1.3 Problem Definition

With the increased attention of oil and gas industry on AC motor drives, the goal of this Ph.D. thesis is to examine the topics associated with the following general research question:

Can electric actuation systems replace and offer benefits compared to hydraulic powertrains for offshore drilling applications in a system perspective?

Since the offshore drilling equipment in general falls within the category of mechatronic systems, multidisciplinary approach is adopted to explore capabilities of its actuation system. Instead of focusing exclusively on the actuator's construction and design in isolation from the system it drives, a system-based design is followed which tries to improve the product performance from different viewpoints, considered simultaneously [95]. Therefore, the areas of modeling, identification, control, optimization, and design are studied to conduct investigations centered around the following set of research problems particularly relevant to the industry (consult Chapter 2 for evidence):

1. What modeling strategies are most suitable from the industrial point of view to simulate the offshore drilling equipment?

2. Which identification techniques are relevant to estimate parameters of such models and validate them against field data?

3. What benefits are obtained by using a scaled-down test bench to reproduce operation of a full-scale machine?

4. Which motion profiles and control strategies mitigate fatigue damage and vibration severity of electric powertrains?

5. Is it possible to decrease failure rate of AC motor drives by using sensorless control methods?

6. How can we increase flexibility and reduce conservatism in selection of electric drivetrain components?

7. How can we guarantee that an actuation system is optimally designed (e.g. maximum performance at minimum cost)?

8. How to predict temperature rise of an induction motor under arbitrary operating and ambient conditions?

9. Can this information be used to design tailor made electric actuation systems and enhance the existing dimensioning procedures?

Finally, this thesis recognizes the main driving factors which make electric powertrains become increasingly popular in offshore drilling operations and benchmarks their characteristic features with the ones of hydraulic drivetrains.

1.4 Outline and Contributions

The main contributions of this thesis are:

1. Development of an efficient optimization algorithm based on mixed integer programming (MIP) which allows for optimal selection of electric powertrain's components (namely, a motor, a drive, and a gearbox) from the manufacturers' catalogs.

2. Introduction of a method for evaluating temperature rise of an induction motor drive for an arbitrary overload magnitude, duty cycle, and ambient temperature in order to avoid relying on fragmentary information and rules of thumb provided in the catalogs concerning allowable thermal overloads.

3. Formulation of a systematic approach for selection of appropriate motion profiles for electric drivetrains, which permits to avoid the need to specify some machine requirements (such as operating speed or permissible load) *a priori* and offers the possibility to determine them as a result of fatigue and/or vibration severity minimization.

4. Verification of a sensorless method based on the extended Kalman filter (EKF) to estimate and control an induction motor operating under duty cycles characterized by offshore conditions to enhance motion control systems of drilling machines and reduce the number of sensors in their electric powertrains.

5. Comparative analysis of electrical and hydraulic actuation systems used in offshore drilling applications with an emphasis on cost, safety, environment, and automation capabilities.

6. Installation of laboratory equipment that enables to run scaled-down experiments to emulate operation of full-scale machinery.

In addition, the outline and contributions of each part of this thesis are summarized as follows.

Part I gives the relevant theoretical background and positions the thesis in a broader research perspective. In Chapter 2, the concept and methods of variable speed control of induction motor drives are discussed, and an overview on the current challenges associated with dimensioning and analysis of electric powertrains for offshore drilling applications is provided, particularly focusing on design optimization, motion control, and modeling strategies. In Chapter 3, characteristic features of hydraulic and electric actuation systems that are significant to their successful operation in offshore conditions are reviewed, and potential of these two solutions is assessed from the perspective of two emerging fields of application: subsea drilling/production and drilling systems automation.

Part II presents basic definitions and mathematical formulations from the fields of modeling and control of induction motors, design of electric actuation systems, and optimization techniques. The focus is on gathering in one place elementary knowledge that is necessary to model an induction motor drive and optimally select its components to satisfy sizing requirements and achieve design goals. Commonly used mathematical modeling and control methods for IMs are summarized in Chapter 4. Chapter 5 introduces state-of-the-art, industrially accepted

procedures for design of electric powertrains composed of variable frequency drives and induction motors, and identifies major shortcomings of these guidelines. Chapter 6 recapitulates fundamental notions, equations, and principles related to optimization methods, with particular attention to mixed integer programming as a solution approach to design optimization problems. A number of examples is given throughout Part II to better illustrate the discussed theory and demonstrate the relevance of the selected research methods.

Part III is devoted to the first area of contributions of this thesis: the reduction of failure rate of offshore drilling equipment by the integrated selection of motion control strategies aided by the the use of experimental testing and simulation tools. In Chapter 7, a method to identify parameters of an electric drivetrain is presented, and a laboratory setup is introduced in order to estimate the full-scale electromagnetic torque that must be delivered by a designed powertrain to meet the specification requirements. In Chapter 8, it is confirmed that the EKF algorithm can be successfully applied to estimate states of induction motors operating in drivetrains of full-scale offshore drilling equipment, which is particularly important from the reliability perspective, as it reduces the number of data acquisition devices that might potentially fail in harsh offshore conditions. Chapter 9 focuses on assessment of fatigue damage and vibration severity that an actuation system is exposed to in the presence of changing cyclic loads. Monitoring both the fatigue life and impact of vibrations over time enables to formulate a framework for systematic selection of motion profiles for a given machine which, in turn, has a potential to become an integral part of the drivetrain design process. This can extend the scope of dimensioning guidelines being currently in use to include considerations related to condition monitoring of equipment early in the design phase. The proposed methods do not seem to be associated with high implementation costs and allow for reducing uncertainties when designing and operating electric powertrains on offshore drilling rigs while being easily applicable in industrial environment.

Part IV focuses on two powerful approaches towards design of electric powertrains composed of frequency converters, induction motors, and mechanical transmission, however, the presented methodology is undoubtedly relevant to other actuation systems and applications. The optimization method introduced in Chapter 10 is based on mixed integer programming and enables to select from manufacturers' catalogs such a combination of drivetrain components that satisfies specification inequalities and offers the lowest value of the objective function. Contrary to commercial dimensioning software products, the proposed technique allows for selection of an optimal gear ratio, comparison of components from different producers, and determines the globally optimal design. In Chapter 11, a method to estimate temperature rise of an induction motor drive is developed based on identification of a first order thermal model derived from the popular loadability curves accessible in catalogs. The phenomenon of reduced torque availability at low speeds for self-ventilated IMs is captured, which enables evaluation of drivetrain thermal performance not only in the few scenarios that are typically covered by equipment manufacturers but in arbitrary overload conditions. This, in turn, makes it possible to investigate how realistic overload durations and magnitudes (as well as freely adjustable ambient temperature) affect motor drive's loadability. To our knowledge, such a degree of flexibility of the dimensioning process cannot be reached when relying exclusively on manufacturers' recommendations. The fact that the identification algorithm utilizes publicly available data reduces the need to contact suppliers for more specific information. The proposed method is verified against guidelines regarding permissible overloads specified in catalogs and standards, yielding the same thermal performance limits. These combined contributions improve the design process of electric actuation systems by allowing design engineers to select such drivetrain components that enable to shift operating conditions closer to design

constraints. Therefore, when the discussed strategy is followed, it is no longer necessary to depend to such extent on fragmentary information and rules of thumb which might result in unnecessarily over-dimensioned powertrains.

Part V contains additional material that improves ease of understanding of the results shown in this thesis. Chapter A presents an overview on both laboratory test benches and full-scale offshore drilling equipment that are used throughout this work to validate the proposed techniques and bolster their impact. Chapter B restates essential theory on modeling of dynamic mechanical systems, explains the workflow for simulation of the considered offshore drilling machine, and provides some numerical examples.

Concluding remarks are outlined at the end of every chapter in Parts III and IV. The summary of the results presented in this thesis is given in Chapter 12, together with the directions for possible further research on the discussed topics.

1.5 Publications

The work presented in this thesis was done in collaboration with others and is largely based on the following publications.

Chapter 3:

> W. Pawlus, M. Choux, and M. R. Hansen, "Hydraulic vs. Electric: A Review of Actuation Systems in Offshore Drilling Equipment," *Modeling, Identification, and Control*, vol. 37, no. 1, pp. 1–17, 2016. [265]

Chapter 7:

> W. Pawlus, M. Choux, M. R. Hansen, and G. Hovland, "Load Torque Estimation Method to Design Electric Drivetrains for Offshore Pipe Handling Equipment," *ASME Journal of Offshore Mechanics and Arctic Engineering*, vol. 138, no. 4, pp. 041301:1–9, 2016. [266]

Chapter 8:

> W. Pawlus, S. T. Kandukuri, G. Hovland, M. Choux, and M. R. Hansen, "EKF-based Estimation and Control of Electric Drivetrain in Offshore Pipe Racking Machine," *ICIT 2016 – IEEE International Conference on Industrial Technology*, pp. 153–158, 2016. [274]

Chapter 9:

> W. Pawlus, M. R. Hansen, M. Choux, and G. Hovland, "Mitigation of Fatigue Damage and Vibration Severity of Electric Drivetrains by Systematic Selection of Motion Profiles," *IEEE/ASME Transactions on Mechatronics*, In press, 2016. [271]

Chapter 10:

> W. Pawlus, D. Frick, M. Morari, G. Hovland, and M. Choux, "Drivetrain Design Optimization for Electrically Actuated Systems via Mixed Integer Programing," *IECON 2015 – 41st Annual Conference of the IEEE Industrial Electronics Society*, pp. 1465–1470, 2015. [270]

Chapter 11:

> W. Pawlus, H. V. Khang, and M. R. Hansen, "Identification of Induction Motor Thermal Model for Improved Drivetrain Design," *ICEM 2016 – IEEE International Conference on Electrical Machines*, In press, 2016. [276]

The following work related to the thesis was published and is referred to throughout the thesis:

Example 4.1:

W. Pawlus, M. Choux, G. Hovland, and H. V. Khang, "Parameters Identification of Induction Motor Dynamic Model for Offshore Applications," *MESA 2014 – IEEE/ASME 10th International Conference on Mechatronic and Embedded Systems and Applications*, pp. 1–6, 2014. [267]

Chapter B:

W. Pawlus, M. K. Ebbesen, M. R. Hansen, M. Choux, and G. Hovland, "Comparative Analysis of Numerical Models of Pipe Handling Equipment Used in Offshore Drilling Applications," *ICNAAM 2015 – 13th International Conference on Numerical Analysis and Applied Mathematics*, pp. 370013:1–4, 2016. [269]

W. Pawlus, M. Choux, G. Hovland, S. Øydna, and M. R. Hansen, "Modeling and Simulation of an Offshore Pipe Handling Machine," *SIMS 2014 – 55th Conference on Simulation and Modeling*, pp. 277–284, 2014. [268]

The following work related to the thesis was published but is only cited:

W. Pawlus, I. C. Inouva, S. Øydna, T. K. Wroldsen, and G. Hovland, "Next Generation Hardware-in-the-Loop Simulation Enables Advanced Testing of Offshore Hydraulic Systems," *ARTCE 2015 – IADC Advanced Rig Technology Conference and Exhibition*, pp. 1–7, 2015. [273]

W. Pawlus, M. R. Hansen, G. Hovland, and M. Choux, "Torque Peak Reduction and Overload Monitoring of Induction Motors in Offshore Drilling Operations," *ACEMP, OPTIM, ELECTROMOTION 2015 – IEEE International Joint Conference on Electrical Machines and Power Electronics, Optimization of Electrical and Electronic Equipment, and Advanced Electromechanical Motion Systems*, pp. 393–398, 2015. [272]

W. Pawlus, F. Liland, N. Nilsen, S. Øydna, G. Hovland and T. K. Wroldsen, "Optimization of a High Fidelity Virtual Model of a Hydraulic Hoisting System for Real-time Simulations," *IPTC 2014 – 8th International Petroleum Technology Conference*, pp. 1–11, 2014. [277]

Part I

Preliminaries

2 Theoretical Background

2.1 Variable Speed Drives

In majority of industrial applications there is at least one variable which affects the system performance [6]. Therefore, in order to achieve satisfactory output of the considered process, it is necessary to provide some form of control of that variable. In general, processes are divided into two main classes: material treatment and material transport, with each of these categories being composed of numerous sub-groups. Typical representative examples of processes are: chemical, pulp, paper, printing, power plants, mining, metal, plastic, heating, ventilation, air conditioning (HVAC), vehicle traction, marine propulsion, water treatment, etc. The need for variable speed control is what unifies them all. For instance, temperature and humidity in the room is what affects air flow requirements in air conditioning applications, which can be satisfied by regulating the supply and return air fans. There are many simple control methods that allow to adjust process variables, such as throttling or bypass control, however, high operating costs, difficulties to achieve optimal capacity, or risk of damage at startup are their main limiting factors [6]. Therefore, the best way to provide control in most systems is to use variable speed drive (VSD) [108]. VSDs that are particularly popular in the industrial sector are classified into four groups, according to [6]:

- Mechanical coupling – belt drives/gears are usually used to achieve mechanical variable speed control by moving pulleys/gears into appropriate positions to achieve desired transmission ratios – see for instance [42].

- Hydraulic coupling – controlling the volume of oil in the system by the means of pumps and valves makes it possible to regulate the speed difference between the driving and driven shafts [234].

- DC drive – direct current is changed to alternating current using a commutator and the motor supply voltage is varied on a DC converter to enable motor speed control [149].

- AC drive – frequency converter (controlled with electric signals) adjusts the frequency of the motor voltage which in turn affects its speed [34].

In mechanical and hydraulic VSDs, the control equipment (e.g. valve manifold) is situated between the actuator and the operated system. Hence, maintenance of such drivetrains becomes particularly difficult. On the other hand, in electrical VSDs, control systems are typically located far from the working machine. The list of benefits of electrical VSDs is longer [6]: lower maintenance costs, increased productivity, improved energy savings, and higher quality of the end product/process. As a result, as already described in Section 1.1, electrical VSDs dominate the market, with AC drives accounting for more than 60 % of the total VSD sales in Europe. In addition, the total growth of the electrical VSD market is exclusively caused by

the growth of the AC drives share by almost 10 % per year [6]. Stagnation (and in the long run – also reduction) of the DC drives percentage is mainly related to the fact that they utilize mechanical commutator and carbon brushes which complicate the motor structure and cause extra energy consumption and potential maintenance problems.

When VSDs are used to control AC drives, they are commonly referred to as variable frequency drives (VFDs) [146]. A typical VFD applied to control an induction motor is illustrated in Fig. 2.1. General purpose VFDs produced today are composed of four main parts [146]:

1. Input rectifier or converter – converts the AC voltage input into DC voltage and charges the capacitors in this part of the circuit. In the figure, the most common diode rectifier is shown which allows the current to flow only in the direction towards the load.

2. DC bus – acts as a power reservoir from which the VFD draws the output. If there is any regenerated energy from the load, it is either stored in the DC bus capacitors, dissipated on the brake resistor (if DC bus voltage exceeds the threshold of the control circuit) or fed back to the grid if insulated gate bipolar transistor (IGBT) rectifier is used [8].

3. Inverter – draws the power from the DC bus and creates the AC power supply, the frequency, amplitude, and phase of which are adjusted by the controller. The resulting output voltage is used to drive the electric motor.

4. Controller – is an integral part of a commercially available VFD. Sophistication of the control algorithm affects the dynamic performance, energy consumption, and overall productivity of the motor drive.
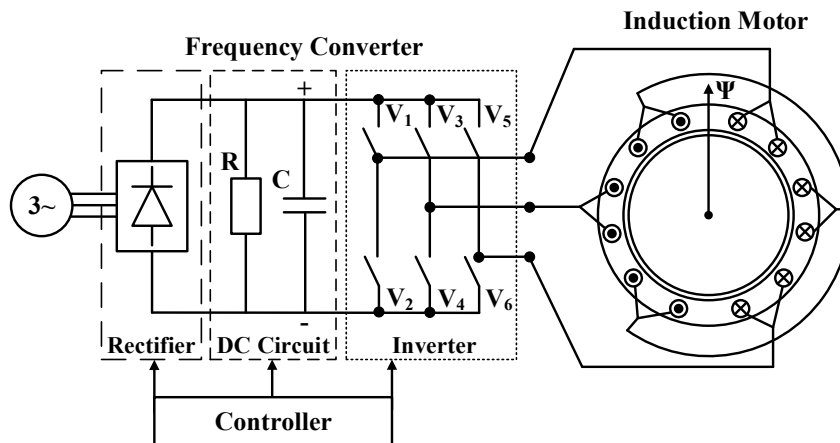
Figure 2.1: Variable frequency drive of induction motor [6].

As already discussed, induction motors are currently the most popular actuators in industrial applications. Compared with DC motors, they offer significant advantages, such as [73]: no commutator and brushes (for cage induction motors), ruggedness, lower rotor inertia, simpler maintenance and protection, smaller size and weight, and lower price. However, an induction motor is inherently a dynamic, recurrent, and nonlinear system, which makes it difficult to continuously control its performance without additional equipment, which, in turn, is by far more complex and costly than that of a DC machine. "There ain't no such thing as a free lunch" [115]. Therefore, it comes as no surprise that the extra effort to design and implement control systems of AC machines is the price to pay in order to benefit from the improvements they provide.

2.2 Control Methods for Induction Motors

Initial work on induction motors' control strategies can be traced back to the 1940's – some of the most significant contributions in this field are (see for instance [73] and the references therein):

1. Investigation of transient performance of induction motors using an analog computer in 1946 [348].

2. Invention of thyristor (or silicon-controlled rectifier) by Bell Laboratories in 1956 [55].

3. Application of rotating reference frames and space vectors to the study of induction motor transients in 1959 [188].

4. Evolution of various scalar control strategies since the 1960's [54].

5. Development of inverter circuit with pulse width modulation (PWM) in 1961 [229].

6. Formulation of field orientation principle in 1972 [46].

7. Introduction of direct self control (DSC)/direct torque control (DTC) in 1985 [97] and in 1986 [328].

8. Expansion of advanced control methods of induction motor drives since the 1990's [56].

2.2.1 Classification

Voltage and current supplied to an induction motor can be represented as sinusoidal function of either magnitude and frequency or magnitude and phase, according to [73]. Control methods of induction motors follow this classification and fall into two main categories, as illustrated in Fig. 2.2:

- Scalar control – based on adjusting magnitude and frequency of voltage.

- Vector control – based on adjusting magnitude and phase of voltage.

Control of magnitude and frequency (angular speed) of voltage, current, and flux linkage space vectors (which is done in scalar control) is valid only for steady state relationships, according to [178]. Consequently, the scalar control does not affect space vector position in transients. On the other hand, since vector control is based on relations valid for dynamic states, the orientation of the space vector can be controlled in both steady and transient states. The most common method of implementation of vector control is called field-oriented control (FOC) and was formulated by Hasse (indirect FOC) [134] and Blaschke (direct FOC) [47]. The underlying assumption behind this control principle is that IM equations are expressed in the rotor flux vector oriented coordinate system. Using these coordinates guarantees a linear relationship between current vector components and machine torque. In addition, similarly to DC machines, IM equations correspond to the decoupled torque generation and the reference flux amplitude is also reduced in the field-weakening range.

Although in the 1980's the trend was to standardize control systems based on the FOC methodology, Depenbrock [97] as well as Takahasi and Nogouchi [328] have proposed a new strategy that does not rely anymore on the analogy to DC machine control. The main idea behind the new method, called direct torque control (DTC), is to replace the averaging-based
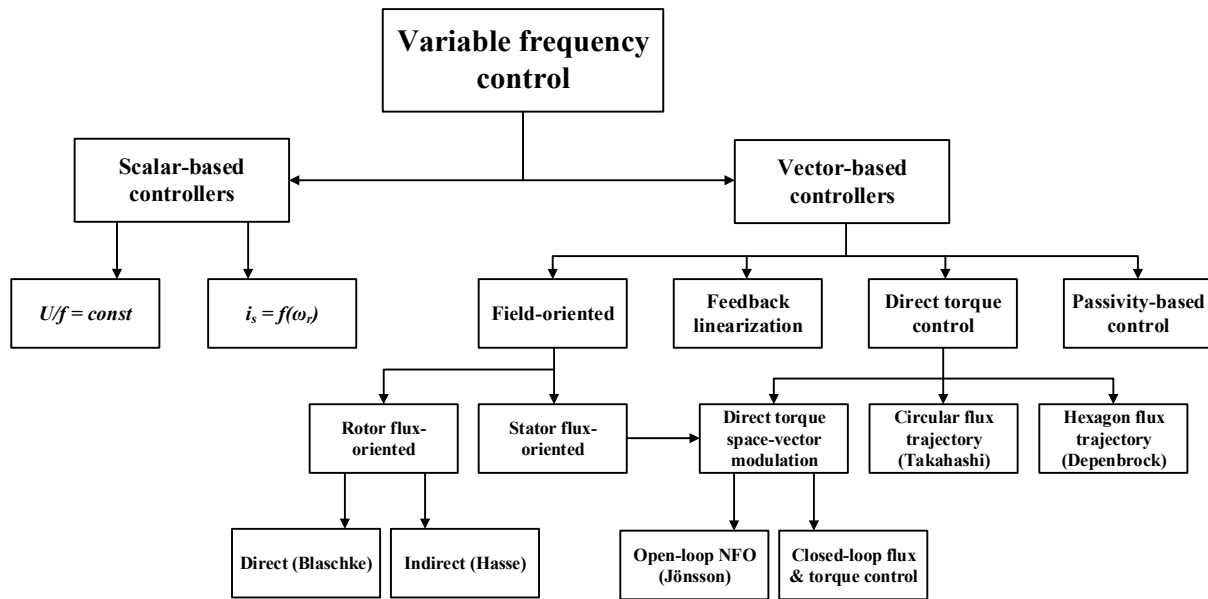
Figure 2.2: Classification of IM control methods [349].

decoupling control with the instantaneous bang-bang control, which corresponds to on-off operation of the voltage source inverter (VSI) semiconductor power devices [349]. The main advantages of DTC are simple structure, good dynamic behavior, and that it is inherently a motion-sensorless control method. Its drawbacks, such as variable switching frequency, high torque pulsation, and low-speed operation performance, however, necessitated development of improved IM control techniques. Therefore, space vector modulation (SVM) was introduced in [129] to eliminate the classical disadvantages of DTC. From the formal point of view, DTC-SVM can also be referred to as stator field-oriented control (SFOC). Similarly, natural field orientation (NFO) generates a rotating reference frame that is also aligned with the stator flux [171].

Another approach to decouple and linearize IM equations is to apply modern nonlinear control. Two common methods are feedback linearization control (FLC) described in [194] and [218] and passivity-based control (PBC) [179]. The former technique involves decoupling the speed and rotor flux amplitude by feedback, whereas the latter concept is based on the variation theory and energy shaping.

As far as industrial applications are concerned, scalar control, FOC, and DTC are the most popular types of control [5]. Depending on complexity of the controlled process, a decision is made whether to employ vector control or to use V/Hz mode. Nowadays, motor drives manufacturers provide a wide spectrum of VFDs offering both control strategies. Operation of automatic topside drilling equipment demands precise motion control, therefore commercially available frequency converters that utilize FOC or DTC are typically chosen for such applications.

2.2.2 Challenges in Offshore Drilling

Controlling induction motors without mechanical speed sensors is advantageous from both the cost and reliability points of view.[1] Reducing the number of data acquisition devices is particularly relevant for offshore drilling industry, since sensors operating in harsh conditions

---

1. Parts of this literature review are reproduced from publication [274].

which characterize this working environment are prone to failures or generating misleading measurements. Hence, lowering the number of data acquisition devices to control and monitor such systems without losing reliability and to improve the safety of personnel is highly desired.

Many authors have addressed the problem of sensorless motion control of induction motors using either a continuous-time model or a discrete-time model (see e.g. [19] and the references therein). Determination of rotor flux vector and motor speed is a typical challenge in such a type of control [70, 120, 365, 369]. A popular approach (almost considered to be an industrial standard in many fields [26]) to state estimation is based on the prediction filter proposed by Rudolf E. Kalman in 1960 [174]. His original idea has been further developed to become applicable to nonlinear systems, which makes the extended Kalman filter (EKF) widely used for control and estimation problems of induction motor drives as well [69, 137, 181]. There exist different variants of EKF and methods for tuning its parameters [35, 201, 312]. There are also other approaches to estimate motor states that are not based on Kalman filtering [79]. However, to our knowledge, the literature concerning EKF-based estimation and control of induction motors operating in drivetrains of offshore drilling machinery is limited. Since the need for speed/position sensorless control is particularly relevant for harsh operating environments [26], the EKF-based estimation and control method is applied in Chapter 8 to an electric actuation system operating on a drilling rig.

2.3   Design Aspects of AC Motor Drives

In this Section, some typical challenges associated with a general engineering design process are identified.[2] In addition, particular problems experienced when designing electric drivetrains for offshore drilling applications are recognized and their solutions proposed in this thesis are indicated.

2.3.1   General Considerations

The traditional sequential approach to product design considers each of the design stages separately. As a consequence, no information from later steps can be used in preliminary phases of product development. Therefore, evaluation of subsequent specification constraints and objectives becomes an iterative process, which has a negative impact on the overall efficiency of design activities. To address this problem, the so-called concurrent (or parallel) design approach is often followed which allows to integrate early in the design stage these requirements that come after in product development, according to [74]. It is well-known, that the ability to influence the final design is inversely proportional to the time spent in a project and that the cost of making such adjustments grows over time [227], as visualized in Fig. 2.3. Therefore, the design stage is often the most critical in many applications, as it predominantly affects both the total cost and functionality of the final product. As far as electrical actuation systems are concerned, it is always an initial phase of the design process (i.e. specification of requirements and selection of components) which allows for the highest level of design flexibility at the lowest cost. Hence, planning and design stages should receive a considerable amount of attention when developing electric powertrains, as any changes implemented later would result in a significant increase of cost and loss of design efficiency. This is why the unproductive time spent on iterative design approaches should be avoided and,

---

2.   Parts of the literature reviews presented throughout this Section are reproduced from publications [266, 270–272, 276].
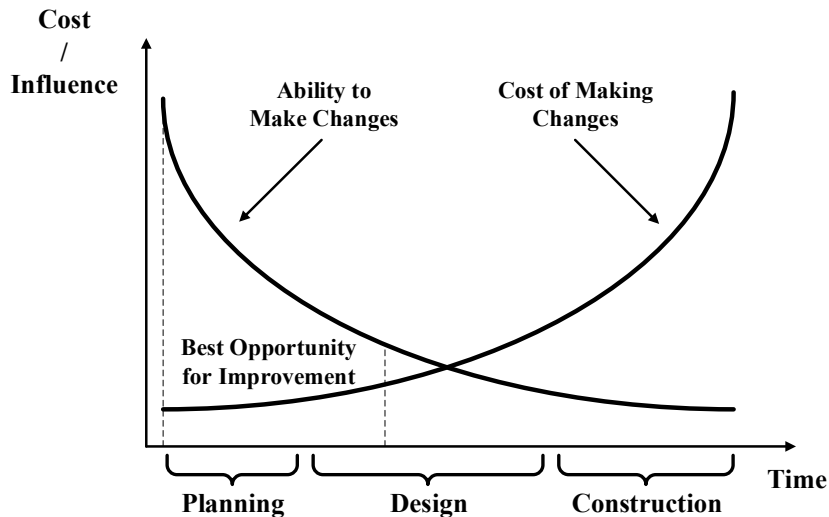
Figure 2.3: Cost of change vs. development – adapted from [227].

instead, these design techniques should be used that allow to effectively utilize the available engineering time. This is dictated by the increasing integration level of subsystems (e.g. sensors, actuators, control, etc.) with the remaining components (e.g. mechanical, electric, hydraulic, etc.) of a final product. Therefore, the growing synergy of equipment calls for solutions that allow for smooth and seamless increase of product functionality early in the design phase to detect potential failures and reduce unnecessary engineering efforts. One of the goals of this thesis is to investigate which aspects of design and operation of actuation systems of drilling equipment should be improved (and how) in order to come closer to a concurrent design paradigm, as explained further in the text.

2.3.2 Sizing of Components

Electrically actuated offshore drilling machines are often designed overly conservative which results in high initial investment and too costly maintenance. In case of uncertainty, it is safer to pick e.g. a larger motor than risk lack of machine performance or even the safety of personnel. Although imposing certain safety margins on a system is critical to compensate for unexpected events which are likely to occur in offshore environment, it is not acceptable to over-dimension drivetrain components due to the lack of information characterizing load conditions. Otherwise, the final solution would fail to meet some of the most important design objectives such as lowering the cost of an electric drivetrain or maximizing its efficiency. When the most significant phenomena such as dynamics or friction present in a designed machine are considered, determining the required motor performance turns out not to be a trivial task. Especially, when offshore conditions characterized by changing weather, strong wind, irregular heave motion, and induced cyclic loads are investigated.

One solution to optimal sizing of drivetrain components is adoption of a suitable selection procedure, as presented in [283] and [300], for instance. The techniques for design optimization proposed so far are also usually based on expert systems [81], genetic algorithms [204], particle swarm optimization [139], or other metaheuristic approaches and exact methods (such as e.g. branch and bound) [195]. In the offshore technology there are numerous examples of using optimization techniques to design structures or control related processes [44, 220, 248, 331]. In general, both everyday life and more complicated industrial cases involve optimization challenges – they range from easily solvable tasks to complex combinatorial problems [118,

123, 127, 148, 173, 283]. Even though mathematical programming models and optimization techniques have been widely used in many industrial applications [214, 292, 300, 356], much less work has been reported in using these tools in optimization of electrical actuation systems, especially in the offshore drilling industry [170]. The need to strengthen the expertise regarding design procedures and system analysis of the equipment which uses VFDs and induction motors is addressed in Chapter 10 where we introduce a method which aids the design of electric drivetrains and allows to choose optimally dimensioned powertrain components.

Successful application of design optimization methods, however, requires that all relevant information about load types and their magnitudes, as well as other design specifications and constraints are available [23, 67, 314]. In reality, the process of collecting these essential data is problematic, since design specifications are often influenced by factors that are burdensome to be specified *a priori* (e.g. friction or transient overloads). For topside drilling equipment, the occasional peak loads might lead to temporary loss of machine performance which may pose a threat to platform personnel. Therefore, it is particularly important to investigate these irregular scenarios in order to accurately determine the torque/force demand on actuation system rather than use rules of thumb and imprecise safety factors to account for intermittent overloads and friction. The information about the exact load profiles that must be withstand by the powertrain is critical for effective design process and to find an optimal solution. Although there are examples of online torque prediction [87, 263, 357], to the best of our knowledge, not much activity has been reported in offline estimation of load torque levels for offshore drilling machines. Thus, Chapter 7 proposes to fill this gap and presents a method to identify the required torque of a motor operating in offshore drilling equipment by performing scaled-down tests on an experimental setup and its virtual model.

2.3.3 Motion Control

Offshore drilling equipment is typically designed to handle high loads in harsh conditions. Because of potential risk factors, safety of offshore rig personnel is a top priority when planning functions of machinery and its layout on the drill floor. Therefore, it is of key importance to eliminate as many unexpected situations as possible when designing offshore machines. However, practical experience shows that some factors which influence performance of offshore drilling equipment are difficult to detect early in the design process. One of such examples is saturation of induction motors in transient state. Even though the maximum mechanical load is one of the criteria to consider when selecting components of electric drivetrains, in some exceptional cases the motor might not provide enough torque to compensate for the intermittent loads because of magnetic saturation effects. Solving this problem is not only related to definition of realistic design requirements but also to selection of appropriate trajectories that are used to control the offshore drilling equipment. According to [281], it is important that machine motions be smooth without any unwanted variations in the movement. Jerk (derivative of acceleration) directly influences and ensures smooth motion of a mechanism. Limiting its value is a well established strategy which reduces wear of equipment and improves tracking accuracy and speed. A trapezoidal velocity profile, which is popular among various industries because of its simplicity and straightforward implementation, is inherently associated with an infinite value of jerk. This has a negative impact on loads experienced by actuation systems where such a reference trajectory is used. In particular, infinite value of jerk is one of the reasons for excessive IM overload – and in some cases – saturation.

Some work has been done in the areas of thermal monitoring of induction motors [38] and improving their lifetime by using thermal model overload protection [290]. Similarly, overload

monitoring has been proven to be an effective tool to detect faults in induction motors as well, according to e.g. [237]. Induction motor failure analysis is a topic which is particularly relevant for oil and gas industry, since, as described in Chapter 3, the business moves towards all-electric drilling equipment and reliability-based maintenance. According to surveys presented in [50] and [335], stator winding and bearing are identified to be the components of an induction motor which are most prone to failures – see Fig. 2.4. Damages to the stator winding are mainly caused by overheating and deterioration of thermal insulation, whereas fatigue and vibration are primary reasons for bearing faults.
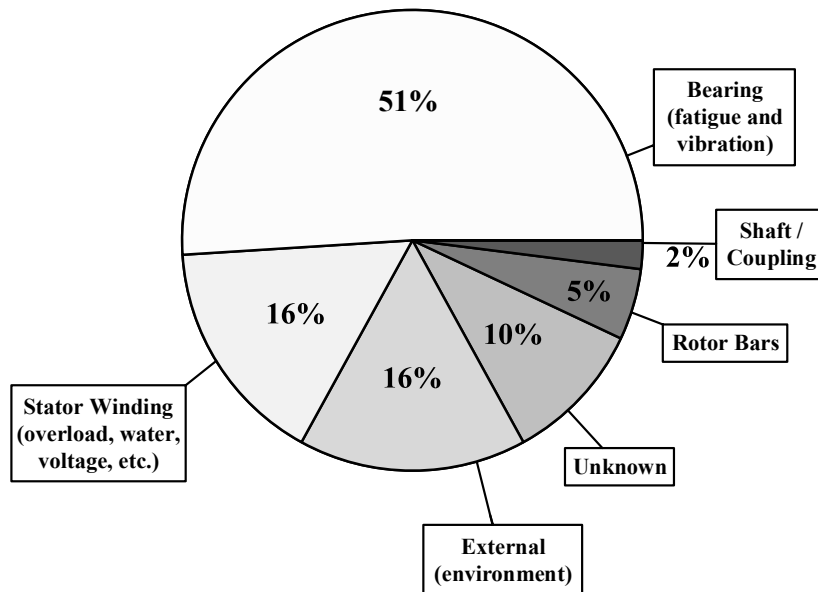
Figure 2.4: Distribution of failed components in an induction motor [271] – reproduced from [50].

There are many studies in the literature concerned with damage of structures, actuators fatigue and vibration mitigation – for instance [244, 296, 364] and the references therein. Particularly, evaluating an influence of motion profiles and the associated loads on drivetrain components has been popular in automotive applications [72, 199, 240]. Similar efforts are pursued nowadays with a special emphasis on propulsion systems and charging strategies for electric vehicles, as explained in [187] and [239]. Experiences from the renewable energy market, especially from the energy conversion systems [217], fault diagnostics and prognostics [175], and fatigue estimation methods of wind turbines [94] are also relevant for the offshore drilling equipment. Some techniques and methods could easily be adopted from both the automotive and wind energy applications and implemented to solve similar problems experienced by drivetrains of offshore drilling machines. There is evidence that selection of an appropriate motion profile for a powertrain can either solve or partially mitigate problems associated with fatigue damage and vibrations without the need to implement costly condition monitoring systems or redesigning drivetrains [231, 246, 247].

Therefore, Chapter 9 focuses on bearing faults and proposes a method to evaluate, and possibly reduce, damage caused to bearings in drivetrains equipped with induction motors. Four popular motion profiles are compared to benchmark their influence on both fatigue damage and vibration severity. The aim is to formulate the guidelines for systematic selection of reference input signals for motion control systems of industrial equipment. Even though the proposed methods and tools are well-known, the practical experience shows that they are not frequently used when designing drivetrains for offshore drilling applications.

2.3.4 Thermal Performance

As discussed in Section 1.1, the number of electric motor drives in industrial applications constantly grows. According to [342], despite reliability and successful operation of induction motors, their annual failure rate is estimated to be 3–5 % up to even 12 % in harsh applications. Statistics show (still up to date [238]) that motor bearing and stator winding insulation are the two components which fail the most frequently – see Table 2.1. The major reason of stator

IEEE study		EPRI study		Average
Failure contributor	**[%]**	**Failed Component**	**[%]**	**[%]**
Persistent Overload	4.20	Stator Insulation	23.00	**Electrical Failures**
Normal Deterioration	26.40	Turn Insulation	4.00	
		Bracing	3.00	
		Core	1.00	
		Cage	5.00	**33**
Electrical Total	**30.60**	**Electrical Total**	**36.00**	
High Lubrication	15.50	Sleeve Bearings	16.00	**Mechanical Failures**
Poor Lubrication	15.20	Antifriction Bearings	8.00	
		Thrust Bearings	5.00	
		Rotor Shaft	2.00	
		Rotor Core	1.00	**31**
Mechanical Total	**30.70**	**Mechanical Total**	**32.00**	
High Ambient Temp.	3.00	Bearing Seals	6.00	**Environmental, Maintenance & Other Failures**
Abnormal Moisture	5.80	Oil Leakage	3.00	
Abnormal Voltage	1.50	Frame	1.00	
Abnormal Frequency	0.60	Wedges	1.00	
Abrasive Chemicals	4.20			
Poor Ventilation	3.90			
Other Reasons	19.70	Other Components	21.00	**36**
Environmental & Other Total	**38.70**	**Maintenance & Other Total**	**32.00**	

Table 2.1: Motor reliability and major causes of failures [276] – adapted from [238].

damage is insulation failure, which is related to excessive heat and insufficient cooling. It is estimated, that particularly in offshore applications overheating and insulation breakdowns cause more than 30 % of all stator winding failures [335]. Since downtime in operation is often more expensive than motor drive replacement (especially in the offshore industry), proper protection is required to prevent drivetrain failures and to ensure both the safety of personnel and production objectives.

Motor thermal protection has been an important aspect of condition monitoring of electric actuation systems – see for instance [51] and [62] and the references therein. Currently, there are numerous examples of estimation of motors' lifetime expectancies based on their thermal performance [63], application of motor thermal protection strategies [222], thermal modeling of electric drivetrains [41, 347, 367], or design optimization driven by the need to reduce thermal overloads [52]. There are also examples of using a thermal analysis-based approach to design electric drivetrains – see for instance [158], or to derive the parameters of a first order thermal model of an induction motor drive using thermal limit curves – see for instance [370] and [371].

Since efficiency of a typical induction motor is in the range of 0.82–0.97 and that of a frequency converter 0.97–0.99 [6], thermal losses are inherently present in these machines and decisively affect their performance. According to [149], most induction motors produced

nowadays tend to be totally enclosed with a fan mounted on the shaft for self-ventilation. The internal air circulation, however, is not sufficient to allow them to operate continuously at low speeds without overheating. Hence, even though the VFD is able to make the motor deliver full torque at low speeds, such operation is not recommended without using an external cooling system. Heat management of industrial motor drives is therefore an important and broad research topic – see for instance [48, 165, 340, 345, 370] and the references therein. Especially manufacturers of electric motor drives recommend using guidelines based on thermal loadability when selecting components of industrial electric drivetrains [2, 10, 13, 146, 297, 310, 315]. These instructions are often provided in the form of the so-called loadability curves that illustrate the allowable motor torque at particular values of speed.

However, as far as we know, there is limited work done in the area of thermal modeling of motor drives based on these loadability curves. Although they are easily accessible in catalogs and are among fundamental design constraints of electric drivetrains, they are not sufficient alone to assess the duration of permissible overloads that a powertrain can withstand. Since one of the main design criteria is to prevent motor drives from reaching thermal protection limits [146], this has a critical impact on designing tailor-made electric actuation systems. Therefore, a technique based on the loadability curves to estimate motor temperature rise under various operating conditions and ambient temperatures is formulated in Chapter 11 in order to verify if a given drivetrain design does not violate the thermal restrictions specified in the IEC standard [154].

2.4   Modeling and Simulation of Drilling Equipment

The offshore drilling equipment produced nowadays is characterized by high level of techno-logical sophistication, high price and low production numbers [213]. Constructing full-scale prototypes of such machines is obviously too costly, which requires that the manufacturers have enough experience and skills to design and develop them without performing experiments on-site [31]. This, in turn, puts a lot of pressure on design engineers to correctly choose (early in the design phase) between such contradictory objectives as reliability, capacity, performance, and cost of the produced equipment. Therefore, virtual modeling tools that allow to test, redesign, adjust, and optimize a solution before it is manufactured attract more and more attention of the offshore industry [104].

Modeling and simulation software aids efforts of design engineers, enables detection of critical or possibly malfunctioning components of a designed system, and, generally speaking, improves the quality of the final product, according to [32]. In addition, what drives the more frequent use of simulation-based engineering techniques is an increasing level of automation of offshore drilling equipment, as discussed in more detail in Section 3.4.5. Nowadays, it is widely recommended to first test a developed control system in a virtual simulation environment against a reliable model, before deploying it on a real-world machine [167]. Hardware-in-the-loop (HIL) testing methods are recognized as particularly effective to disclose failure effects caused by software failures and design flaws [80]. According to [279], HIL testing is a dynamic method of testing of the control system software, where the actual software is executed on its native hardware. The control system software acts against the simulator which imitates the behavior of the actual equipment. To fully benefit from using this method, it is necessary to satisfy at least two contradictory conditions: 1) the model of the real-world machine has to be accurate (both in terms of inputs/outputs mapping and results fidelity) and 2) it has to be real-time (RT) compatible (e.g. to enable RT interaction of the human operator). Therefore, it is important to execute the modeling process wisely and thoroughly to focus on only these

functions of the system that are really relevant, and to avoid the temptation of modeling as many details as possible, just for the (apparent and misleading, of course) sake of making the model more accurate simply by increasing its level of complexity [208].

One of the topics that this thesis touches upon is modeling and simulation of dynamic mechanical systems based on multibody models [193]. The study of motion of bodies can be classified into two distinct parts [233]:

- Kinematics – which describes the motion of bodies without reference to the forces which either cause the motion or are produced as a result of the motion.

- Dynamics – which relates the action of forces on bodies to their resulting motions.

If the forces acting on a mechanical system are known, then the equations of motion can be solved to obtain the motion of the system [251]. This process is called forward dynamic analysis or just – forward dynamics. Contrary to that, if the objective is to find the forces that must act on the system to produce the required motion, such a process is referred to as the inverse dynamic analysis. Similarly, the kinematic problem usually consists of two sub-problems [196]. The forward (or direct) kinematics problem is to find the resulting motion of the machine given its actuators' or – generally speaking – joints' kinematic presets (e.g. input velocities), whereas the inverse kinematics problem is to determine the kinematic actuation signals that make the machine follow a predefined motion profile. Chapter B introduces the relevant theory and presents a case study of modeling a full-scale offshore pipe handling machine using both a commercial multibody software and analytical methods (aided by numerical solving software). The focus is to present the mathematical background that allows to create models of mechanical systems from scratch to double-check and troubleshoot potential glitches that might occur when using software products available on the market.

2.5 Mathematical Programming

This Section gives a general outlook on optimization techniques, introduces their common classification methodologies, and discusses two applications of these tools that are dealt with in this thesis.

Examples of optimization can be found virtually everywhere [253]: from portfolio creation, through engineering design, to reaching equilibrium in physical systems. Optimization techniques enable to solve problems in the domains of decision making and analysis of physical systems. Fundamental notions related to optimization methods are:

- objective – measure of the performance of a considered process/system/phenomenon/design, etc.; the goal is to achieve the best possible one,

- variable – characteristics of a system; the goal is to find these that minimize/maximize the objective,

- constraint – restrictions on variables; e.g. bounds on the required power of a motor,

- modeling – mathematical formulation of the considered system in terms of objectives, variables, and constraints; often the most critical step,

- algorithm – a method for finding an optimum of the given model; there are different algorithms (usually available nowadays as software products) for different types of optimization problems.

Remark 2.1. *The historical term from the 1940's, "mathematical programming", is still often used when referring to "optimization", according to [253]. Therefore, this thesis follows the convention of [253] and whenever calling an optimization problem a mathematical (or linear, quadratic, etc.) program, the intention is to retain this historical meaning rather than to evoke in the reader connotations with computer software.*

2.5.1 Brief History

The following events can be attributed to the development of the field of (linear) optimization, according to [316]: formulation of the method for solving systems of linear inequalities by Jean-Baptiste Joseph Fourier in 1827, research on resource allocation problems by Leonid V. Kantorovich in 1939, and work on linear optimization models in economics by Tjalling C. Koopmans in the 1940's (Kantorovich and Koopmans received the Nobel Prize in economic sciences in 1975 for their work). Actually, the problem of minimizing the cost of food to meet certain nutritional requirements is considered to be some of the earliest applications of linear programming techniques. It is also called the "Stigler Diet" problem named for George Stigler who also posed this question in 1939 to address the army's nutritional difficulties to feed soldiers at minimum cost [321] (the work of Kantorovich remained unknown in the West for several years). Stigler, however, solved this problem using heuristic techniques due to lack of satisfactory algorithms to deal with linear programs. It was not until 1947 when Dantzig developed the method, called simplex, for solving such problems and Laderman applied it to solve the original Stigler problem [92]. Interestingly, the initial Stigler's solution of 39.93 $ per year was very close to the optimal Laderman's solution of 39.69 $ per year. The computational effort of the latter one, however, was tremendous and amounted to 120 man-days using hand operated desk calculators [36]. The first software tools to solve optimization problems became available on the market at the end of the 1960's (some of the well-known companies are e.g. CPLEX and GUROBI co-founded by Robert Bixby later on).

2.5.2 Categories

Optimization problems can be classified according to properties of objective and cost functions, as well as the type of optimization variables, as described in [253]. A comprehensive explanation of each of the category listed below can be found in textbooks on optimization techniques, e.g. [53, 60, 253].

Continuous vs. Discrete

In some applications, the decision variables do not make sense if they are continuous, e.g. the number of shops to be opened (or a decision whether to open a shop at all). These problems are referred to as integer (or binary) programming problems and are separately discussed in Section 6.4. In general, continuous problems are considered to be easier to solve because information about the objective and constraints at a given point can be used to extract similar information about the vicinity of that point, as far as smooth functions are concerned. On the contrary, this is not applicable to discrete problems because two feasible points might drastically differ in terms of objective and constraints, even though they do not differ significantly in some other sense.

Constrained vs. Unconstrained

If there are no restrictions on optimization variables, such problems are called unconstrained. They might either be used to directly describe some practical problems (e.g. least-squares approximation) or to reformulate constrained optimization problems by removing the constraints and appropriately modifying the objective function. Constrained optimization problems, on the other hand, exhibit some limits on decision variables – they can either take the form of simple bounds or more complex relationships.

Global vs. Local

An ideal scenario for solving an optimization problem is to determine the global optimum, i.e. the solution that has the lowest objective function value among all feasible solutions. An important feature of convex programming problems is that all local solutions are global solutions as well. However, in many applications, finding a global optimum is difficult and not always possible. Especially, the general nonlinear problems might have local solutions that are not globally optimal. In practice, it is common to define the acceptable approximation limits for the local solutions and let the optimization algorithms find them numerically.

Convexity

The property of convexity is particularly important in optimization, as the convex optimization problems are considered to be effectively solvable in practice. The major challenge related to convex optimization is the ability to recognize convex optimization problems or these non-convex problems that can be reformulated into the convex ones. The focus of many research works is to develop effective methods for arriving at convex optimization problems, since this step is often critical to solve an original problem. In particular, solving nonlinear convex optimization programs is not yet a mature technology, however, it is expected that within a few years the consensus will be reached regarding the best method/methods [60]. Convex optimization programming and all related definitions are thoroughly discussed in Section 6.2.

Stochastic vs. Deterministic

In case where the model depends on parameters that are uncertain or not known at the time of formulation of an optimization problem, instead of approximating their values, it is often worthwhile to use additional information about the model and quantify parameters' uncertainty. Stochastic optimization deals with such problems by optimizing the expected performance of the model. There are two common approaches here: in chance-constrained optimization, it is assumed that the variables meet the constraints with a certain degree of probability, whereas in robust optimization, the constraints have to hold regardless of the values of the uncertain data. On the opposite, the problems which require that the models are completely known are called deterministic optimization problems and are considered in this thesis.

Multiparametric Programming

Variation of parameters in mathematical programs is typically handled in two ways: by performing sensitivity analysis to evaluate the impact of parameters' change on the solution and by utilizing (multi)parametric programming to determine the solution for a range of parameters [53]. The latter approach requires that the optimization problem is solved a number of

times for varying problem characteristics which can be translated into the dependence of the cost function and/or the constraints on the parameters that become additional inputs to the optimization problem [363]. The challenge is to establish relationships between the cost/constraint functions and the parameters, however, once it is done, this technique can be applied to solve a number of practical problems with optimal control of discrete-time dynamical systems or model predictive control (MPC) being some of the most typical examples ([53] and [258]).

Single- vs. Multiobjective

It often occurs in practice that an optimization problem is characterized by more than one objective function, e.g. simultaneous minimization of cost, volume, mass, and energy consumption of a designed machine. In order to solve such problems, it is essential to understand relative importance of different (often contradictory) objectives and quantify the associated trade-offs. Usually, there is no unique solution to such problems and the concept of noninferiority [360] (also referred to as Pareto optimality [71]) is used to define a front of points that cause improvement in one objective at the cost of degradation of another [224]. There are different techniques for solving multiobjective optimization problems (see e.g. [224] for a review of some common algorithms), however, the scope of this thesis is to focus on single-objective applications.

2.5.3 Applications

Optimization techniques have been used to solve a huge variety of practical problems and the list of applications is continuously growing [60]. The two trends when using optimization are either to consider it as an aid in decision making (which eventually still has to be made by a human) or let the embedded optimization algorithm perform necessary actions with no or limited human intervention. The latter field has recently flourished and become especially popular in automatic control applications, according to [102] and [103]. The list of areas where optimization techniques are used is impressive, with some of the most representative industries and applications being ([60] and [253]):

- Transportation – crew scheduling, fuel allocation, airport traffic planning, vehicle routing.

- Finance – portfolio selection, stock exchange operations, lease analysis.

- Process industries – plant logistics, expansion planning, chemical blending.

- Manufacturing – inventory management, job scheduling, production organization.

- Agriculture and forestry – farm land management, planting and harvesting models, pricing models, product distribution.

- Oil and gas/mining – sourcing and transportation logistics, production scheduling, operation management.

- Public utilities – electric power distribution, power generator scheduling, water resource management.

- And many more . . .

The two application areas of optimization techniques identified in [60] and particularly relevant for this thesis are device sizing and data fitting, as discussed in more detail in Chapters 5 and 6.

Device Sizing

Equipment dimensioning is a task of choosing the right parameters, sizes, or components of a system/product/machine, etc. In such applications, the variables can represent e.g. a set of available parts that can be selected from the catalogs, and the constraints can describe various engineering requirements, such as allowable torque or power levels, operating hours per day, or other specifications that must be met to achieve design goals. Usually, the objective is to minimize the cost of initial investment, however, some other typical goals might be to optimize the power consumption or keep the device as small as possible [60].

Data Fitting

Another popular example of using optimization methods is to establish a model, from a set of potential models, of a system/phenomenon/proces, etc. based on a collection of measured data. The variables of such a mathematical program are the parameters of the model, whereas the constraints normally represent the desired limits on the parameters or prior system information [60]. The cost function to be minimized is the discrepancy between the measured data and the response estimated by the model.

2.5.4 Artificial Intelligence Methods

One of the common difficulties related to solving optimization problems is that many real world phenomena or systems cannot be easily represented by reliable optimization models [60]. In addition, the time required to find a solution of a complex mathematical program might grow exponentially with the size of the problem [39]. Therefore, it is important to select appropriate numerical methods for solving optimization problems to mitigate the computational effort of the available hardware. The popular iterative algorithms (such as simplex, gradient, interior point, or branch and bound) permit to solve the optimization problem exactly or approximately with a possibility to assess the quality of the solution. Even though in many cases using them would be favorable, they might not be the best choice when solving complex and large-scale problems because of huge demands on computational power and time, the need to formulate an exact model of the considered problem, and troublesome implementation [60]. Therefore, the other approaches for solving optimization problems also receive substantial attention in the literature, especially the methods based on metaheuristics (e.g. evolutionary algorithms [319] or particle swarm optimization [216]) and artificial intelligence (e.g. expert systems based on "if-then" rules [136]), as they are known to tackle the above limitations, however, at the cost of no guarantee on solution's optimality.

Artificial Neural Networks

Artificial intelligence (AI) is understood as a merger of information technology and control engineering with an ultimate goal to resemble human intelligence [66]. Intelligent behavior is associated with such skills as the ability to adapt, learn new things, and establish complex relationships [353]. Some of the most prominent examples of the developed artificial intelligence methods are [353]:

- Artificial neural network (ANN) – developed since the 1940's [130], the method is inspired by the complexity of human brain. Basic building blocks (neurons) are interconnected with each other and form various architectures to mimic behavior of modeled systems.

- Support vector machine (SVM) – first proposed in 1992 [59], this technique is based on statistical learning and its objective is to estimate unknown dependencies between inputs and outputs from a set of exemplary data.

- Adaptive neuro-fuzzy inference system (ANFIS) – based on fuzzy logic introduced in the 1960's by Zadeh [361], it combines fuzzy logic and neural networks by using linguistic variables and structure of layers to approximate complex functions [368].

Artificial neural networks (ANNs) are considered to be one of the most popular tools among AI methods [66]. They find wide range of applications, especially in pattern recognition, market forecasting, estimation of process variables, engineering design, or – in general – optimization, in various industries such as automotive, finance, manufacturing, transportation, and many others [130].[3] Due to the inherently parallel operation of particular neurons, ANNs are easy to implement on modern graphics processing units (GPUs) that enable massive parallel computational power which, in turn, significantly speeds up the training process of the ANNs [203].

ANN's Architecture

Neurons of a network can be arranged in different patterns. It is common to group a few neurons in parallel, in a so-called layer, and connect them with the neurons in other layers. The number of neurons in the input layer is determined by the number of problem inputs, whereas the number of neurons in the output layer is equal to the number of problem outputs [130]. If all neurons in a given layer have connections with all neurons in a subsequent layer, such a network is called a fully connected multilayer network [66]. Normally, selection of the number of neurons and hidden layers (i.e. these between input and output layers) affects network's performance and is considered to be more art than science, however, there exist some rules of thumb and general recommendations for this subject that can be checked by the interested reader in textbooks on artificial neural networks, e.g. in [130]. The two common architectures of ANNs are called feedforward neural network (FNN), in which the information is propagated in the forward direction only, and recurrent neural network (RNN), which contains feedback paths and allows to store information for later use [66]. FNNs are commonly applied to solve parameters estimation or approximation problems [29], whereas RNNs deal effectively with speech/writing recognition or text generation [203].

ANN's Learning

Learning of a neural network is the process of selecting weights and biases of its particular neurons with the objective to achieve the best convergence of the network's response to the desired output [66]. The two broad categories of neural network learning rules are supervised and unsupervised learning. In supervised learning, the network outputs are compared to the target (desired) values for a given set of inputs and the weights and biases are adjusted such that the network's response is moved closer to the desired output [130]. The backpropagation algorithm (BPA), which is one of the most popular training techniques, falls within this category. On the other hand, in unsupervised learning, no feedback information is used to update the network's parameters [66]. Even though this approach might seem impractical at the first glance, there are algorithms which adopt it and solve such practical problems as, e.g. image compression or speech recognition, by categorizing the input patterns into a finite number of classes [130].

---

3. The list of applications of ANNs presented in [130] is actually quite similar to the one shown in Section 2.5.3 for general optimization problems.

ANN's Simulation

An important characteristic of a neural network trained using BPA is that no knowledge about the process or system it represents is required [66]. Therefore, ANN-based modeling and estimation techniques are considered to be "black-box" methods, since the network learns from the provided information rather than from analytical modeling. As a result, the network can be used to predict values of parameters or time-series data for a set of inputs that is different from the one used in the training stage. This feature makes ANNs particularly useful to deal with highly complex and/or nonlinear systems that are difficult to be modeled entirely from previous knowledge and physical insight [207], as presented in Chapters 6 and 7.

3 Review of Hydraulic and Electric Actuation Systems

This Chapter presents a survey on actuation systems encountered in offshore drilling applications.[4] Specifically, it focuses on giving a comparison of hydraulic and electric drivetrains along with detailed explanations of their advantages and drawbacks. A significant number of industrial case studies is examined in addition to the collection of academic publications, in order to accurately describe the current market situation. Some key directions of research and development required to satisfy increasing demands on powertrains operating offshore are identified. The impact of the literature and application surveys is further strengthened by benchmarking two designs of a full-scale pipe handling machine presented in Section A.3. Apart from other benefits, the electrically actuated machine reduces the total power consumption by 70 % compared to its hydraulically driven counterpart, as shown in Section A.3.2. It is concluded that electric actuation systems, among other advantages, in general offer higher efficiency and flexibility, however, in some specific applications (such as energy accumulation or translational motion control) hydraulic powertrains are favorable.

3.1 Introduction

3.1.1 Historical Perspective

Electrification of onshore drilling rigs started in the 1930's [295]. The overall trend back then was to shift from steam power to internal combustion engine power. However, despite the substantial cost of the equipment and the general fear of electricity that existed then, in several cases DC transmission was used [293]. The reason for internal combustion engine fitted rigs to become prevalent was their portability and improved efficiency, as compared to steam power solutions. The situation changed in the 1950's due to a significant number of new offshore locations. Placement of machinery in such applications was dictated by vessel design and did not allow for such flexibility as for conventional land rigs, hence it excluded both steam power and internal combustion engines. What solved the problem was to apply locomotive traction type direct current (DC) equipment which paved the way for future development of electrified drill rigs, as reported in [323], for instance. Initially, the generator was placed onshore and the electrical power was transmitted to the platform via submarine cable. Since then, many improvements have been made in designing optimized electric power systems for drilling and production platforms [83].

The history of electrification in the offshore drilling industry begins in 1947 when the first offshore platform was installed off the coast in Louisiana in 8 *m* of water [322]. Although at that time the need for electrical systems was limited (e.g. to navigation systems), further

---

4. This Chapter is reproduced (with minor changes) from publication [265].

discoveries of oil and gas led to location of platforms further offshore. This in turn necessitated an increase in electricity generation on platforms to meet growing requirements to include living quarters and associated amenities (cooking, air conditioning, lighting, etc.) offshore. Traditionally, starting from the 1950's, gas turbines or engines were used for power generation and – by coupling to mechanical drives – for load handling [346]. An alternative approach is to use electric power to supply machinery which manipulates the payload and to apply a separate energy source (typically gas turbines) for power generation. This solution is the most popular nowadays. Normally, actuation types which take advantage of electric motors are variable frequency drives (VFDs) and hydraulic drives, as described in [346].

3.1.2 State-of-the-Art

The idea to use gas turbines as prime movers to turn alternating current generators which drive all major drilling components of offshore rigs has a well-proven track record in the industry [18]. Traditionally, the solution that provided for speed control was to apply a fluid coupling, i.e. a hydro-kinetic device with a primary rotor (a pump to add energy to the fluid) connected to the power source and a secondary rotor (to extract stored energy from the fluid) connected to the driven machine [22]. This solution, referred in this thesis to as a hydraulic actuation/drivetrain, owes its popularity to a number of factors. According to [166], fluid power systems are capable of providing high forces at high power levels simultaneously to several actuating locations in a flexible manner. This results in higher torque/mass ratios than those available from electric motors, particularly at high levels of torque and power [33]. Another advantage of a hydraulic actuation system is that any heat generated at the load is automatically transferred to another location away from the point of heat generation by the hydraulic fluid itself and effectively removed by means of a heat exchanger [347]. These features together with total automation capabilities and accessibility as well as explosion proofness made hydraulic drives a primary solution for offshore drilling equipment since the 1960's.

However, for some applications the disadvantages of fluid power systems are more significant than their benefits. Due to friction and nonlinearities of valves, variations in fluid viscosity, and stiffness, fluid power systems are more nonlinear than electrical actuation systems and more prone to oscillations. These negative factors cause additional difficulties for a control system design [32]. Other challenges include leakage, noise, or difficulties in synchronization of several degrees of freedom [31]. Finally, when the necessary accessories are included, fluid power systems might be by far more expensive and less portable than electrical actuation systems. In the past it was not possible to replace hydraulic actuators by alternating current (AC) drives due to the limited control features the latter solution offered. Even though when Blaschke introduced a novel method to control AC motors in [46], it was not an industrially mature technology yet. Moreover, although DC drives provided sufficient control characteristics, they were not desired solutions neither due to high cost, maintenance, and risk of spark generation.

Nevertheless, enhanced control strategies of AC motor drives and recent advancements in power electronics (mainly development of semiconductor switching devices that started in the 1980's) made VFDs more popular and accessible [97, 120, 263, 336]. Cost-effectiveness of VFDs and use of convenient power source distinguish them from other types of actuation systems. They are especially suitable for petrochemical industry, since there is virtually no risk of electric spark generation or arcing. The main advantages of VFDs are high reliability, high robustness, easy maintenance, long life and low cost [189, 309, 327]. These are the reasons for electric powertrains to become increasingly popular in the offshore drilling business. A typical drivetrain which uses electrical variable speed drives is illustrated in Fig. 3.1.
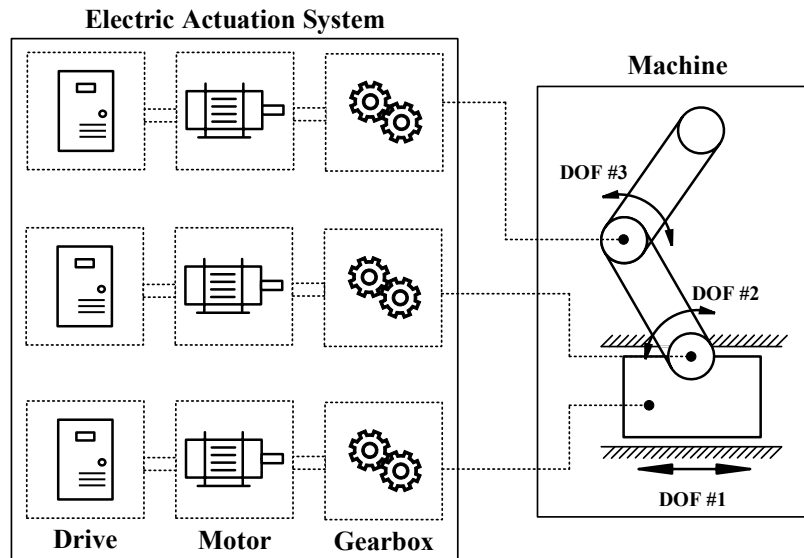
Figure 3.1: Conceptual representation of electric actuation system.

3.2 Electric Motor Drives in Offshore Applications

3.2.1 Overview

A number of successful examples shows that oil and gas producing plants may now rely to a higher degree on electric drives – see for instance [116, 268, 286, 335]. Advantages and disadvantages of both hydraulic and electric top drive systems with a special emphasis on their performance and productivity are outlined in [351]. Since in hydraulic actuation systems energy changes its form more often, their overall efficiency is lower compared to electrically driven machines. According to [351], for the same top drive application the electrical system is more efficient by nearly 21 %. In addition, the key to reliability of the hydraulic system is cleanliness of oil. This of course involves additional expenses on appropriate filtration in both high pressure and return systems, as well as on a reservoir that will maintain clean oil.

Hydraulic drives take the major lead in applications where high power density is required [261]. To address the issue of generating high power from linear actuators, a concept of a permanent magnet linear actuator combined with a double gas spring is introduced in [339]. Similarly, a hammer drilling system driven by a tubular reciprocating translational motion PMSM is presented in [365]. Gas springs make it possible for the piston to oscillate at high frequency. In addition, permanent magnets allow to produce large electromagnetic force, which, combined with large stroke lengths, is particularly useful in drilling applications. A similar concept, based on magnetic lead screw (MLS), can be utilized in ocean wave power extraction to convert low speed, high force power to high speed, low force power [143].

A problem of controlling wellhead gate valves by hydraulic actuators is described in [294]. So far, they were operated from a pneumatically powered control panel which used electrically driven compressors to generate the instrument air. Not only such a solution was found to be inefficient due to losses associated with energy conversion but it was maintenance intensive as well. Therefore, an all-electric system that uses electric gate-valve actuators was proposed to overcome these historical difficulties. It eliminated the risk of leakage of fluid/gas, provided a clean power source, and made control and response times independent of temperature and fluid/gas displacement. Conceptually, the all-electric system contains fewer subsystems –

see Fig. 3.2. Although there are additional accessories that have to be considered with this solution (e.g. harmonics reduction systems mentioned in Section 3.2.3), the resulting increase in system complexity is still lower than for the other actuation types. The reason is that this supplementary equipment does not necessitate extra energy conversion processes and is usually built-in in commercial products that are to be used anyway (e.g. harmonic filters on VFDs).
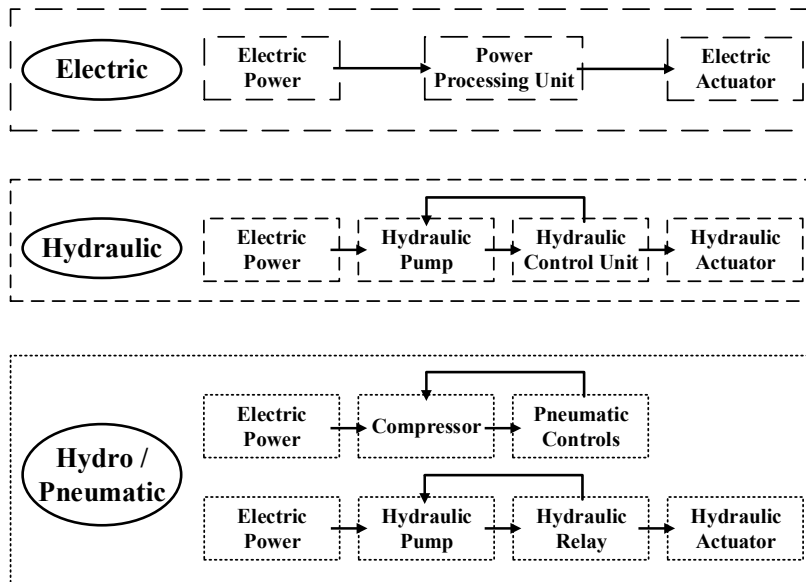
Figure 3.2: Comparison of complexity levels of popular types of actuation systems [294].

Smooth control and relatively silent operation that variable speed AC drives provide is recognized in shipping and marine sectors as well [305]. Recently, all-electric vessels have become increasingly popular with dynamic positioning (DP) systems receiving special attention – see for instance [355] and the references therein. A solution with a variable pitch propeller and a fixed rotational speed has been the most popular so far. What is more beneficial, however, is to fix pitch propeller and control the rotational speed instead, since in majority of cases the thrust needed is minimal (which reduces the shaft speed) [200]. This results in lower energy consumption, as the electrical systems only require the power that is needed for the work, contrary to hydraulic drives which normally provide full torque at all speeds, causing the supply to operate at full power at all times.

As exploration of new offshore oil and gas fields is moving into deeper waters, marine operations related to development, completions, and production activities require more power and design of optimal power generation systems ([89] and [221]). Since technology which enables well control in ultra-deepwater has emerged, there is observed the trend to move all infrastructure subsea. It was already in the 1990's when it was recognized that an all-electric control system for subsea well control would be simpler and less expensive compared to a conventional electro-hydraulic control system [169]. Some advantages of using this new solution are: higher flexibility when expanding an existing system, removal of significant environmental, technical, and economical problems associated with hydraulic fluids, and possibility to develop marginal fields at large distances from processing facilities. The topic of subsea systems and installations deserves a closer attention when seen from the perspective of electric powertrains, and is therefore widely discussed in Section 3.4.4. Another field that is expected to play a key role in the future and which is related to electric actuation systems is drilling automation [291], covered in Section 3.4.5.

3.2.2 Challenges in Design and Operation

One of the challenges that arises with an increased use of electric motor drives in offshore applications is susceptibility to poor power quality in the form of voltage notches and over-voltage ringing [140]. Such distortion might lead to failures in other equipment connected to the power distribution bus. It is therefore important to apply harmonic mitigation techniques such as filters discussed in [140] and [141] to ensure no power-quality problems. We elaborate more thoroughly on this topic in Section 3.4.1. Similarly, pressure oscillations in wells, caused by heave motion, present a serious threat to personnel and the environment, and a risk of a significant economic damage in case of loss of the well. Hence, appropriate vibration and oscillation mitigation techniques have to be applied to suppress pressure fluctuations [17]. Drilling of complex curved boreholes in order to access unconventional reservoirs of oil and gas is associated with an additional problem of increased drag losses while drilling. To prevent borehole spiraling, a model-based control strategy is developed in [192], for instance. Not only guarantees the method the stable generation of complex curved boreholes, but it also requires only the limited measurement data.

When designing electric drivetrains, an extra effort should be made to select an appropriate motor type. Generally speaking, induction motors are the most frequent in use because of their simple and rugged construction, and simple installation and control [88]. Synchronous motors, on the other hand, offer slightly higher efficiencies than that of induction motors, especially at low speed. They are particularly useful in high power and/or low speed applications, and usually have higher power density compared to induction motors (at the cost of higher price).

Electrically actuated offshore drilling machines are often designed overly conservative, as discussed in Section 2.3.2. Of course, sensible over-dimensioning to account for unexpected events which are likely to occur in offshore environment is acceptable. What should not be tolerated, however, is to over-dimension drivetrain components due to the lack of information characterizing load conditions. To address this problem, in Chapter 7 an approach is presented to estimate the required full-scale motor torque using a scaled-down experimental setup and its computational model. In addition, to reduce conservatism when designing electric powertrains, a method to optimally choose elements of drivetrains from manufacturers' catalogs is proposed in Chapter 10.

3.2.3 Summary

The following main advantages of electric actuation systems are identified for offshore drilling operations [16] (refer to Section A.3.2 for evidence):

1. Reduced fuel/energy consumption – especially when there is a large variation in load demand.

2. Less space occupation – increase of rig's payload due to the lack of hydraulic power unit (HPU) and extra control elements (valves).

3. Flexibility in location of actuators – electric power is supplied through cables, therefore an actuator could be placed independently of the location of the power generator.

4. Lowered noise – optimized operation of power generators.

5. Improved control features – accessible speed control of AC motor drives and limited nonlinearity of the system.

6. High positioning accuracy – convenient control of motion profiles.

7. No risk of leakages – removal of hoses, pipes, tanks, valves, pumps, etc.

8. Fewer maintenance tasks – no need to replace worn out hydraulic components and to retune control systems.

9. Regenerative braking – the kinetic energy can be recovered as electricity directly by the frequency converter.

These benefits have to be, however, weighted up against the following drawbacks:

1. Lower power density – hydraulic actuators develop relatively large forces/torques for comparatively small devices.

2. Fail-safe brake – in case of power loss, a mechanical brake has to hold the load.

3. Extra components – harmonics reduction systems, transformers, extra cooling, etc.

4. Stall conditions – it is dangerous to operate an electric motor continuously at full load and low speed.

3.3 Hydraulic Powertrains – Recent Developments

There are many unique features of hydraulic drivetrains pointed out in [234] that are still relevant when compared to other types of control. The most significant ones are:

1. The fluid carries away the generated heat to a convenient heat exchanger.

2. It acts as a lubricant as well and extends life of drivetrain components.

3. Hydraulic actuators are characterized by relatively large force densities.

4. Torque to inertia ratios are large which results in high acceleration capabilities.

5. Actuators can directly be used for dynamic braking (with relief valves protection).

6. They can be operated under continuous, intermittent, reversing, and stalled conditions without damage.

7. Higher stiffness results in little drop in speed as loads are applied.

8. Energy storage is relatively straightforward with hydraulic/pneumatic accumulators.

9. Natural damping due to the compressibility of the hydraulic oil. This behavior makes the hydraulic actuators more tolerant of impact (shock) loads.

Apart from numerous proven examples of using hydraulic powertrains in the offshore drilling applications – see for instance [30] and the references therein – we would like to discuss some recent developments and innovative solutions that make hydraulic systems a vigorous competitor to all-electric drivetrains [254].

An area that attracts significant attention of the industry is the use of VFD-fed IMs in fluid pumping applications [164]. It is considered to be more efficient solution for achieving adjustable flow rates compared to old-fashioned (but still popular) method to drive pumps by

three-phase IMs operating at fixed speeds. However, what still might occur at low speeds and high static heads is that pumps run at efficiencies that are far from the optimum. Therefore, adjusting the flow rate and total head within the best efficiency region of the pump by using appropriate induction motor control strategies becomes a challenge [172]. Additional design factors such as serial or parallel connections of pumps and motors have to be considered to achieve the best possible system performance [245]. Some other recent innovations to achieve low-cost, low-maintenance, and high-efficiency hydraulic solutions, involve fast switching digital valves [299], robust control of hydraulic linear drives [307], or optimal design of hydrostatic transmissions [278].

Finally, the conventional drilling rigs are known to waste the deposited potential energy during hoisting/lowering operations and active/passive heave compensation. However, there are efforts to store this energy in the form either available as pressure boost in hydraulic systems or electricity induced during regenerative braking [211]. So far, the capabilities of hydraulic/pneumatic accumulators are superior to energy storage options that modern battery systems offer [40]. Especially, when offshore operating conditions characterized by high loads/inertias and heave motion are considered.

3.4   Comparative Analysis

Some of the additional aspects that might affect selection of an actuation method (hydraulic vs. electric) are discussed below. The list is by no means complete, however, it highlights some of the supplementary factors which should be considered and which are different from the indicators and features discussed in Sections 3.2 and 3.3.

3.4.1   Safety and Environment

Actuation systems that provide for high fuel efficiency and lower emissions are preferred nowadays to mitigate the greenhouse effect and address environmental concerns of governments and various agencies [181]. Standard HPUs which supply fluid flow in hydraulic actuation systems are known to have higher power demands than all-electric systems. This results in higher energy consumption and CO_2 emissions [325]. The effect of reduced environmental footprint is more pronounced for applications utilizing VFDs when operating at load conditions different than the rated [182]. Hence, variable speed electric drivetrains not only improve efficiency of driven equipment and allow for continuous process control over a wide range of speeds, but also decrease the emissions of greenhouse gases [358]. In addition, the problem which completely disappears in applications involving the use of electric powertrains is leakage from hydraulic pipes, hoses, pumps, etc. [294].

According to [287], the major sources of noise on drilling rigs are ventilation ducts, generators, hydraulic pumps, and the drawworks on the rig floor. The study revealed that the noise in offshore applications is a complex issue both in terms of vibration and structural noise as well as personnel noise exposures. It is therefore essential not only to install acoustic panels or enclosures in highly sensitive areas (e.g. to protect personnel in their living quarters), but also to substitute/upgrade equipment producing too much acoustic emission. Replacing hydraulic drivetrains or moving them away from personnel working areas is identified as a key factor in [287] to improve noise control on offshore production platforms and drilling rigs.

Additional critical safety issue related to an increasing use of electric drives in marine applications (e.g. electric propulsion or offshore drilling operations) is harmonic distortion [142]. Since VFDs draw current in a nonlinear or sinusoidal manner, they can introduce excessive

levels of both current and voltage harmonics. Harmonics are dangerous especially in oil refineries and oil production platforms, i.e. in zones 1 and 2 of explosive atmospheres ([155] and [156]) described thoroughly in Section 5.1.2. Degradation of bearing lubrication caused by rotors overheated by harmonics might lead to frictional sparking. Similarly, a risk of explosion increases as quality of shaft seals decreases. Therefore, specific requirements are given in the standards in an attempt to protect against this risk and to keep voltage distortion below acceptable levels, as shown for instance in [15, 100, 153, 154]. Typically, the techniques to mitigate total harmonic voltage distortion (THDv) involve application of filters or active front-end (AFE) drives which became a common industrial practice [235]. Finally, to ensure safe load handling/parking in case of loss of electrical power, proper brake mechanisms have to be applied. Traditionally, mechanical friction brakes that are costly and require maintenance have been used for AC motor drives [176]. They are a well-proven solution still used in many industrial applications [186]. On the other hand, drive-by-wire systems without mechanical backup become increasingly popular in automotive and aerospace industries [159]. They are based on a number of redundant control systems that transfer electrical commands to electromechanical actuators, resulting eventually in a scheme that is usually not fail-safe but has fault-tolerant properties. In this regard, hydraulic actuators are more convenient to operate, since it is enough to design a fail-safe circuit which ensures that the actuator (e.g. a hydraulic cylinder) will stand still in case of a hydraulic line rupture or power loss [284].

3.4.2 Cost and Maintenance

In [311], an individual cost of major parts of various transmission systems is compared. Already in 1951, for a rig under question, the electric transmission turned out to be slightly more cost-effective than the widely spread mechanical drives. In addition, the cost of initial investment did not indicate the maintenance savings that result from the reduction of engine shock loads or overload, and the elimination of many chain drives and clutches. Similarly, such intangible effects on drilling costs and safety of operation as simple control, the ability to meter all loads, or the reduction of engine noise at the derrick floor were impossible to be accurately assessed but they generally speak in favor of electric transmissions.

Nowadays, the initial investment of electric and hydraulic drives in offshore drilling applications is in most cases comparable. There are of course some examples when one solution is cheaper than the other [351]. However, given an increasing number of electric actuation systems in various industries [84], it is expected that the cost of variable speed drives, motors, and associated power electronics systems will further decrease. For instance, in [294], it is estimated that the total cost savings for an all-electric system controlling well production exceed 200 000 $ per well compared to the traditional pneumatic/hydraulic system. The savings that are not included in this amount come from reduction of maintenance and service personnel and are difficult to be precisely assessed.

Similarly, there is evidence that all-electric systems are more compact and flexible than their hydraulic counterparts [30]. This directly translates to cost savings, since, according to [83], platform deck area is valued at approximately 600–6 000 $/$ft^2$, depending on the platform location, and for every pound in weight saved, 1–5 $ of structural material is saved. Serious maintenance tasks require stopping platform production. The cost of this operation ranges from 37 500 $/$h$ for small Gulf of Mexico platforms to 187 500 $/$h$ for large North Sea platforms. It is therefore essential to limit service and maintenance activities to an absolute minimum – something that is within the reach when using all-electric solutions.

3.4.3 Arctic Operations

According to [85], shrinking global energetic supplies and a continuously growing demand on all kinds of fuels (especially on crude oil, natural gas, and oil-products) brought attention of international community to an enormous hydrocarbonic potential of the Arctic. Despite temporary interruptions and market difficulties, fossil fuels remain the dominant form of global energy, accounting for almost 80 % of total energy supplies by 2035 [61]. In particular, the global oil demand is predicted to increase by almost 20 Mb/d (millions of barrels per day) within the same time period. The Arctic Ocean is ranked at the first place among all global waters with respect to presence of oil and gas resources [372]. It is estimated that in the Arctic there is 25–30 % of global deposits of natural gas and 10–15 % of global deposits of crude oil. Drilling activities have already started in Pechora [282] and Barents [359] Seas, just to name the two most famous examples. Therefore, the Arctic Ocean is definitely going to play a key role in the near future when it comes to the shape of the global energy outlook.

Oil and gas production in the Arctic depends on a complex set of variables [133]. Harsh winters with extreme temperatures and year-round ice represent highly challenging conditions for the oil and gas industry. A few more factors that make drilling in the Arctic particularly difficult are: thick ice cover present for 4–12 months per year, frequent storms and strong gales, low temperatures reaching from $-20\,°C$ to $-60\,°C$, high seismic activity, and floating ice floes capable of destroying virtually every offshore installation. On top of that, governments are not willing to give out drilling licenses without proper consideration of the environmental impact of drilling in highly sensitive regions. Therefore, it is strongly recommended that the petroleum enterprises in the years to come invest in technology which makes exploratory drilling less difficult, more cost-effective, and environment friendly.

As already mentioned in Section 3.2, AC motors controlled by VFDs are characterized by improved control features, reduced energy consumption, higher reliability over time, as well as minimal routine and preventive maintenance. These features, together with lower emissions and eliminated risk of oil leakages to sea water, cause VFDs to have a better impact on the environment, and directly correspond to the above mentioned strict requirements for actuation systems which are to be used in the Arctic environment.

3.4.4 Subsea Infrastructure and Control Systems

The trend of moving the production into deeper water and areas with hostile weather conditions has been recognized already in the 1970's [303]. Operation of control valves in subsea equipment, such as blowout preventers (BOPs), satellite trees, and complex manifold systems, requires suitable control systems. In addition, extra signals, such as production pressures and valves positions, have to be made available to control system so that it can detect adverse conditions and perform its automatic shut-down in case of serious failures. Normally, the following subsystems are needed for a successful operation of a subsea control system: hydraulic power, communication, and electrical power. In the beginning of the 1980's there were no known examples of application of electrical energy to directly operate subsea systems, according to [285]. This, however, has completely changed over 2–3 decades. For instance, the first all-electric subsea system in the Dutch sector of the North Sea has been already in operation in the 2000's [14]. A few reasons for electric actuation systems to become dominant over traditional hydraulic solutions in subsea equipment are: increased precision, increased energy efficiency, fewer converting processes, reduced risk of pollution, less potential failure points, smaller footprint, short response time, improved operability, extended monitoring possibilities,

and enhanced maintenance, with the only drawback being identified as the limited track record. This, however, can be justified by the relatively new state of technology, and − given many advantages this solution offers − is going to change in the future. In addition, the overall trend is not only to replace/supplement the existing hydraulic subsea control systems with all-electric actuators but to move the production facilities from the sea surface into seabed, as mentioned e.g. in [1]. The electric actuation systems will certainly play a key role in such facilities operating in the Arctic, given the challenges described in Section 3.4.3 [135].

3.4.5 Drilling Systems Automation

The level of automation in the drilling industry is still relatively low compared to other industries. It was only in the last decade when significant amount of research and development initiatives have been started in this field [64]. Automation can be defined as reduction of workload of human operators by introduction of control systems and information technology. It goes one step beyond mechanization which only replaced human power by mechanical power. Obviously, automation of all stages of drilling process is a challenging task. To better understand different levels of automation and the role of the driller in such environment, Table 3.1 summarizes possible modes of automation based on automation strategies from the aviation industry. The driller should be able to switch between different modes of automation so that at all times he/she is the absolute authority of the operation. Experiences from other industries show that increasing the mode of automation increases the overall operational and economic performance of the controlled process.

> **Remark 3.1.** *The word "automation" must not be used interchangeably with "autonomy", since these two notions have totally different meaning, as it is clear from Table 3.1.*

The oil and gas industry has always striven to improve both the safety and profitability of drilling operations. Reaching these goals have recently become more difficult due to increased challenge and risk of recovering today's harder-to-reach reserves [304]. Due to these obstacles, a need to automate drilling systems has emerged in order to improve rate of penetration (ROP) and repeatability of drilling process, as well as to mitigate risks associated with health, safety, and environment (HS&E). In addition, as more experienced people retire from the industry, it is necessary to find ways to access the expertise regardless of human factors. A number of successful examples to reduce mean time between failure (MTBF), improve safety, performance, quality, reliability, consistency, and interoperability thanks to automation of drilling processes is presented in [96].

However, to realize the vision of fully automated (and some day − autonomous) drilling operations, one should think of using such components and subsystems that acquire, process, provide information, and automatically execute instructions within a common information-sharing framework. Hence, automated control of drilling process can only be achieved with seamless communication and interoperability of various portions of the complete drilling package [304]. These features have to be supported by reliable decision-making systems to integrate real-time data with optimal control actions [298].

Therefore, from the perspective of drilling automation, the favorable approach would be to unify and integrate different subsystems of drilling process, software solutions, and types of actuation systems. This is especially applicable when considering the fact that the level of complexity and integration of various parts of offshore installations constantly grows [313]. Since offshore drilling machines driven by fully electric powertrains simplify design of actuation

Mode	Management Mode	Automation Functions	Driller Functions
6	Autonomous Operation	Fully autonomous operation.	No particular function. Operation goals are self-defined. Monitoring is limited to fault detection.
5	Management by Exception	The automation system chooses operations and defines operation goals, informs the driller, and monitors responses on critical decisions.	The driller is informed of the system intent. Must consent to critical decisions only. May intervene by reverting to lower mode of management.
4	Management by Consent	The automation provides coordinated control of multiple control loops.	The driller feeds the automation system with a chosen operation, operation goals, and desired values for key variables.
3	Management by Delegation	The automation system provides closed loop control of individual tasks.	The driller decides setpoints for the individual control loops. Some tasks are still performed manually.
2	Shared Control	The automation system could interfere to prevent the driller from exceeding specified boundaries.	Envelope protection systems are enabled. Decision support/advisory systems are available.
1	Assisted Manual Control	Provides down-hole information trends and detects abnormal conditions in the well. Does not intervene.	The driller has direct authority over all systems. Decision-making is computer aided.
0	Direct Manual Control	Warnings and alarms only.	The driller has direct authority over all systems. Unaided decision-making.

Table 3.1: Modes of automation in drilling control systems [64].

systems, they are more likely to faster reach certain levels of automation than their hydraulically actuated counterparts.

One step towards an increasing level of drilling automation is simulation-based engineering [277]. Allowing the model of a designed system to grow to cover the complete process and all scenarios is necessary in order to test more sophisticated control algorithms in a virtual simulation environment before applying them on full-scale machinery [104]. Such approach facilitates product development and shortens commissioning time by making it possible to immediately implement each subsystem of automation engineering in simulation.

3.5   Future Trends

It is expected that electric actuation systems will constitute an increasing share of powertrain solutions in offshore drilling applications in the future. In particular, more attention should be devoted to selection of the best motor type for a given application – e.g. induction vs. permanent magnet motors (PMMs). According to [65], on average, PMM uses 20 % less energy than IM in applications that have high power demand. Therefore, it is anticipated that the number of installations equipped with such machines will increase so that the industry will formulate best practices and recommendations for selection of the optimal motor type given particular specification requirements.

In addition, considering the amount of research that is currently being done to develop linear electromagnetic actuators characterized by high power density and continuous force control [181], it is predicted that hydraulic linear actuators might become less popular. Many

components, such as hydraulic pump, valve module, and connecting hoses, as well as relatively slow response times, are the negative features of hydraulic cylinder blocks. Their electromagnetic counterparts, on the other hand, already offer improved dynamic response, high accuracy, high efficiency, environmentally friendly design, and clean work area [131]. The only limiting factor is their lower power density but this is likely to improve considering their increasing popularity among various industries [48].

Finally, judging by the interest that the international community developed for the Arctic resources, it is highly probable that subsea production sites will dominate the drilling landscape in the years to come. Such solutions are desirable as they reduce or eliminate the surface production platforms, improve cost-effectiveness, and lower threat to personnel [89]. For the same reasons, drilling automation and robotic systems are expected to play a key role and significantly change the way we understand and design drilling and production processes today [27]. In both applications, all-electric systems would be superior to hydraulic drivetrains, given their advantages discussed in Sections 3.4.4 and 3.4.5 [318].

3.6 Conclusion

This Chapter presents a survey on actuation systems in offshore drilling applications. Contrary to previous works, this study is focused on electrically driven equipment and is not concerned with one specific machine design but, instead, it tries to focus on drilling equipment in general. In addition, not only academic publications are reviewed but – what we believe is equally important – a significant number of industrial case studies and research activities. In order to draw an informative picture describing the undergoing shift from hydraulically to electrically actuated drilling machines, state-of-the-art in both the research front and the industrial applications is presented. Such an approach gives more credibility to the findings shown in this thesis, since many industrial examples from the market are also discussed. Finally, the results of comparative analysis of hydraulic and electric drivetrains, based on theoretical studies as well as on literature and application surveys, are confirmed by the conclusions coming from analyzing a case study of electrification of the actuation system of a full-scale pipe handling machine presented in Section A.3.

Electric powertrains offer higher efficiencies, lower emissions, improved maneuverability and positioning accuracy, reduced environmental impact, smaller footprint, as well as lighter and more compact drivetrain designs, just to name a few of their advantages. Although hydraulic actuation systems are still prevalent in some specific applications (e.g. well-established hydraulic linear drives, energy accumulators, or higher power density in general), it is expected that electric drivetrains will become increasingly popular. This is dictated by the progressive move of production into more hostile and remote environments, where the benefits of the latter solution are dominant. Likewise, the developing need for robotic drilling systems, or automated drilling in general, as well as an increasing attention that the subsea systems attract, all call for efficient, easy to maintain, and reliable powertrains.

Part II

Research Methodology

4 Induction Motor Fundamentals

Schematic representation of a two-pole, three-phase symmetrical induction machine is shown in Fig. 4.1. It is assumed that the stator windings are identical and have the same electrical resistance R_{sw} [219]. Similarly, the rotor windings are considered to be alike and characterized by the resistance R_{rw}. The equivalent turns for stator and rotor windings are expressed as N_{sw} and N_{rw}, respectively. In addition, the air gap is assumed to be uniform and both windings are approximated as sinusoidally distributed ones. Typically, induction motors are classified
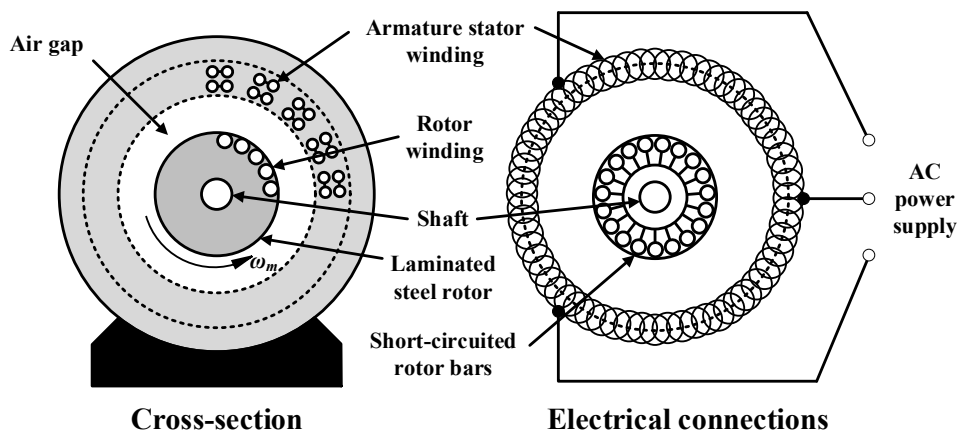
Figure 4.1: Three-phase induction motor [219].

according to the type of rotor's construction [111]. Two most common classes are: squirrel cage and wound rotor. In both cases the rotor consists of a stack of silicon steel laminations with evenly spaced slots punched around the circumference [149]. Cage rotor is by far the most popular nowadays. This is attributed to its simple construction: all rotor slots contain solid longitudinal bars which are connected together at both ends and short-circuited by rings. The construction of the cage might be two-fold: the rotor winding may be composed of individual conducting bars and rings combined together, or it may be a single element produced by die casting. Since the rotor circuit is not externally accessible, the motor is robust but its control becomes more complex [111]. The other motor type, wound rotor, has one significant difference compared to the squirrel cage motor: its rotor winding is made of separately insulated coils which are connected together at collector rings. Hence, the rotor circuit itself is open and its connection to slip rings make it possible to adjust resistance of each phase. This feature was extensively used before the advent of VFDs, as it enabled control of motor by using the slip ring and associated control gear, which was particularly justified for high-power machines. Currently, however, comparatively few such machines are produced (and only in large sizes) but many still remain in operation [149].

According to [111], a rotating magnetic field is generated by the stator that carries a sinusoidal current of supply frequency ω_s. The magnetic field induces the currents in the rotor

bars. The induced currents produce opposite fluxes which contribute to torque generation in the rotor. As a result, the rotor starts turning with mechanical speed ω_m which makes rotor currents oscillate at frequency $\omega_2 = \omega_s - p\omega_m$ which is called slip frequency and is caused by the difference between the stator (synchronous) frequency ω_s and rotor electrical speed $\omega_r = p\omega_m$. Number of pole pairs p decides about how fast ω_r changes compared to ω_m. The electromagnetic torque produced by the induction machine is proportional to ω_2.

4.1 Modeling Workflow and Assumptions

The following assumptions are adopted in this thesis when modeling induction machines [111]:

1. Proportionality of fluxes and corresponding induced currents.

2. Constancy of self- and mutual inductances.

3. Disregarding iron losses.

4. Neglecting saturation effects.

5. Symmetry, uniformity, and smoothness of air gap.

6. Symmetry of stator and rotor windings in the three-phase supply.

Modeling of induction motor consists of two steps: 1) application of electromagnetic laws to the different windings and 2) formulation of equations of motion (EOMs) for the rotor that drives the mechanical load. The challenge associated with the first step is that even though the equations describing motor currents, voltages, and fluxes in the three-phase system are informative, their complexity makes it difficult to implement them on real control hardware [132]. Therefore, it is a common practice to transform motor variables from the physical three-phase system (a, b, c) to a fictive rotating frame, two-phase system. Within this approach the following three strategies of orientation of the artificial frame are the most popular (refer to Fig. 4.2 for illustration of the discussed systems):

1. Coordinate system rotating with the stator frequency: $\omega_1 = \omega_s$. This (d, q) frame is called synchronous reference frame. It is more convenient to analyze than a general reference frame rotating with an arbitrary speed.

2. Coordinate system rotating with the rotor flux: $\omega_1 = \dot{\rho}$. Aligning the d-axis of the synchronous frame $(\omega_1 = \omega_s)$ with the rotor flux is an assumption which is called perfect field orientation. It is often used to further simplify analysis and modeling of induction motor.

3. Coordinate system fixed to the stator: $\omega_1 = 0$. This frame is called stationary or (α, β) frame. Such representation of the system is highly nonlinear (which is shown in the following part of the text) but it is beneficial from the intelligibility point of view [219]: it explicitly shows that the control input voltages $(u_{s\alpha}, u_{s\beta})$ have a direct effect on the stator currents $(i_{s\alpha}, i_{s\beta})$, which in turn indirectly affect both motor speed ω_m and the rotor flux $\mathbf{\Psi}_r$.

In all three cases, the transformation of stator variables is assumed, since this is the convention that is followed in the thesis. However, it is also possible to work exclusively on rotor variables but then the transformation angles become $\theta_1 = \theta_s - \theta_r$ for rotating frame (d, q) and $\theta_1 = \theta_r$
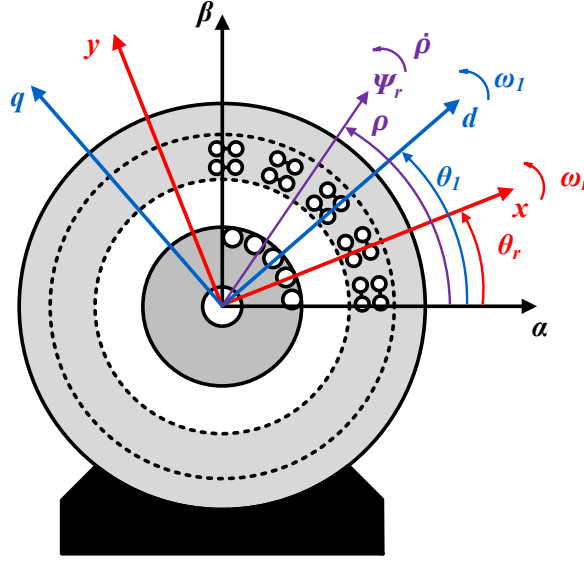
Figure 4.2: Rotating frames diagram for induction motor.

for fixed frame (α, β). The considered angles are derived from their respective rotational speed values

$$\theta = \int \omega \, dt + \theta_0. \tag{4.1}$$

4.2 Park Transformations

In order to transform the three-phase current/voltage system (a, b, c) to an arbitrarily chosen two-phase reference frame involving two orthogonal windings, the so-called Park transformation is used [111]. While both systems produce the same magnetomotive force (MMF), the latter one is simpler to analyze and implement in real-time applications. The original Park transformation dates back to 1929 and is defined as [46]

$$\begin{bmatrix} i_d \\ i_q \\ i_0 \end{bmatrix} = \frac{n_1}{n_2} \underbrace{\begin{bmatrix} \cos(-\theta_1) & \cos\left(-\theta_1 + \frac{2\pi}{3}\right) & \cos\left(-\theta_1 - \frac{2\pi}{3}\right) \\ \sin(-\theta_1) & \sin\left(-\theta_1 + \frac{2\pi}{3}\right) & \sin\left(-\theta_1 - \frac{2\pi}{3}\right) \\ K_0 & K_0 & K_0 \end{bmatrix}}_{\mathbf{P}(\theta_1)} \begin{bmatrix} i_a \\ i_b \\ i_c \end{bmatrix} \tag{4.2}$$

which can be expressed in the vector form as (it holds for voltages and fluxes as well)

$$\mathbf{i}_{dq0} = \mathbf{P}(\theta_1)\mathbf{i}_{abc} \tag{4.3}$$

$$\mathbf{u}_{dq0} = \mathbf{P}(\theta_1)\mathbf{u}_{abc} \tag{4.4}$$

$$\mathbf{\Psi}_{dq0} = \mathbf{P}(\theta_1)\mathbf{\Psi}_{abc}. \tag{4.5}$$

Similarly, inverse transforms are used to convert (d, q) frame variables back to (a, b, c) coordinates

$$\mathbf{i}_{abc} = [\mathbf{P}(\theta_1)]^{-1} \mathbf{i}_{dq0} \tag{4.6}$$

$$\mathbf{u}_{abc} = [\mathbf{P}(\theta_1)]^{-1} \mathbf{u}_{dq0} \tag{4.7}$$

$$\mathbf{\Psi}_{abc} = [\mathbf{P}(\theta_1)]^{-1} \mathbf{\Psi}_{dq0}. \tag{4.8}$$

Values of n_1, n_2, and K_0 are assigned depending on whether the Park transformation preserving energy or amplitudes is chosen. Their detailed derivation for both cases is presented in [111] and omitted here for the sake of brevity.

Another popular notation is described in [132] and adopted in this thesis: space vectors, i.e. these that change angle of rotation, are denoted by superscript "s", whereas for their transformed counterparts this superscript is omitted. The transformation removes the rotation of the vector with respect to the reference frame which allows to rewrite (4.3)-(4.5) as

$$\mathbf{i} = \mathbf{P}(\theta_1)\mathbf{i}^s \tag{4.9}$$

$$\mathbf{u} = \mathbf{P}(\theta_1)\mathbf{u}^s \tag{4.10}$$

$$\mathbf{\Psi} = \mathbf{P}(\theta_1)\mathbf{\Psi}^s \tag{4.11}$$

and modify the inverse transforms accordingly

$$\mathbf{i}^s = [\mathbf{P}(\theta_1)]^{-1} \mathbf{i} \tag{4.12}$$

$$\mathbf{u}^s = [\mathbf{P}(\theta_1)]^{-1} \mathbf{u} \tag{4.13}$$

$$\mathbf{\Psi}^s = [\mathbf{P}(\theta_1)]^{-1} \mathbf{\Psi}. \tag{4.14}$$

Then, the space vectors in transformed coordinates can be expressed in the component form which, in an exemplary case of a synchronous frame, is

$$\mathbf{i} = i_d + j i_q \tag{4.15}$$

$$\mathbf{u} = u_d + j u_q \tag{4.16}$$

$$\mathbf{\Psi} = \Psi_d + j \Psi_q. \tag{4.17}$$

This notation is particularly useful in modeling induction motors for control applications, as presented in Chapters 7 and 8.

Since the first application of the stationary reference frame to induction motor modeling in 1938 [320], limitations caused by modeling assumptions and inaccuracies have been identified and improvements have been proposed to enhance fidelity of this approach (see for instance [191] and [324]). As a result, representation of induction motor in two-phase reference frame can be found in most literature on electrical machines nowadays [132].

4.2.1 Park Transformation Preserving Energy

In the first variant, the three free parameters are selected so that the power remains the same when passing from the three-phase system to the two-phase system [111]. Then, $n_1/n_2 = \sqrt{2/3}$ and $K_0 = 1/\sqrt{2}$ which make the Park matrix become

$$\mathbf{P}(\theta_1) = \sqrt{\frac{2}{3}} \begin{bmatrix} \cos\left(-\theta_1\right) & \cos\left(-\theta_1 + \dfrac{2\pi}{3}\right) & \cos\left(-\theta_1 - \dfrac{2\pi}{3}\right) \\[2mm] \sin\left(-\theta_1\right) & \sin\left(-\theta_1 + \dfrac{2\pi}{3}\right) & \sin\left(-\theta_1 - \dfrac{2\pi}{3}\right) \\[2mm] \dfrac{1}{\sqrt{2}} & \dfrac{1}{\sqrt{2}} & \dfrac{1}{\sqrt{2}} \end{bmatrix} \tag{4.18}$$

and its inverse

$$[\mathbf{P}(\theta_1)]^{-1} = \sqrt{\frac{2}{3}} \begin{bmatrix} \cos\left(-\theta_1\right) & \sin\left(-\theta_1\right) & \dfrac{1}{\sqrt{2}} \\[2mm] \cos\left(-\theta_1 + \dfrac{2\pi}{3}\right) & \sin\left(-\theta_1 + \dfrac{2\pi}{3}\right) & \dfrac{1}{\sqrt{2}} \\[2mm] \cos\left(-\theta_1 - \dfrac{2\pi}{3}\right) & \sin\left(-\theta_1 - \dfrac{2\pi}{3}\right) & \dfrac{1}{\sqrt{2}} \end{bmatrix}. \tag{4.19}$$

Setting the angle $\theta_1 = 0$ in the above equations results in the Park matrix becoming a linear transformation, commonly called Concordia matrix [111]

$$\mathbf{K} = \sqrt{\frac{2}{3}} \begin{bmatrix} 1 & -\dfrac{1}{2} & -\dfrac{1}{2} \\[2mm] 0 & \dfrac{\sqrt{3}}{2} & -\dfrac{\sqrt{3}}{2} \\[2mm] \dfrac{1}{\sqrt{2}} & \dfrac{1}{\sqrt{2}} & \dfrac{1}{\sqrt{2}} \end{bmatrix}, \qquad \mathbf{K}^{-1} = \sqrt{\frac{2}{3}} \begin{bmatrix} 1 & 0 & \dfrac{1}{\sqrt{2}} \\[2mm] -\dfrac{1}{2} & \dfrac{\sqrt{3}}{2} & \dfrac{1}{\sqrt{2}} \\[2mm] -\dfrac{1}{2} & -\dfrac{\sqrt{3}}{2} & \dfrac{1}{\sqrt{2}} \end{bmatrix}. \tag{4.20}$$

4.2.2 Park Transformation Preserving Amplitudes

This transformation is followed in the remaining part of the thesis to stay consistent with reference [132] on induction motor modeling. It entails two conditions: 1) the homopolar current i_0 is the same as the arithmetic mean value of the currents (i_a, i_b, i_c) and 2) the components of the two-phase current (i_d, i_q) have the same amplitude as those of the three-phase current (i_a, i_b, i_c) [111]. These requirements are satisfied when $n_1/n_2 = 2/3$ and $K_0 = 1/2$ which results in the following Park matrix

$$\mathbf{P}(\theta_1) = \frac{2}{3} \begin{bmatrix} \cos\left(-\theta_1\right) & \cos\left(-\theta_1 + \dfrac{2\pi}{3}\right) & \cos\left(-\theta_1 - \dfrac{2\pi}{3}\right) \\[2mm] \sin\left(-\theta_1\right) & \sin\left(-\theta_1 + \dfrac{2\pi}{3}\right) & \sin\left(-\theta_1 - \dfrac{2\pi}{3}\right) \\[2mm] \dfrac{1}{2} & \dfrac{1}{2} & \dfrac{1}{2} \end{bmatrix} \tag{4.21}$$

and its inverse

$$[\mathbf{P}(\theta_1)]^{-1} = \begin{bmatrix} \cos\left(-\theta_1\right) & \sin\left(-\theta_1\right) & 1 \\[2mm] \cos\left(-\theta_1 + \dfrac{2\pi}{3}\right) & \sin\left(-\theta_1 + \dfrac{2\pi}{3}\right) & 1 \\[2mm] \cos\left(-\theta_1 - \dfrac{2\pi}{3}\right) & \sin\left(-\theta_1 - \dfrac{2\pi}{3}\right) & 1 \end{bmatrix}. \tag{4.22}$$

In a special case of the stationary (d, q) frame, also referred to as (α, β) frame, the transformation angle $\theta_1 = 0$ yields the so-called Clarke matrices

$$\mathbf{K} = \frac{2}{3} \begin{bmatrix} 1 & -\dfrac{1}{2} & -\dfrac{1}{2} \\ 0 & \dfrac{\sqrt{3}}{2} & -\dfrac{\sqrt{3}}{2} \\ \dfrac{1}{2} & \dfrac{1}{2} & \dfrac{1}{2} \end{bmatrix}, \qquad \mathbf{K}^{-1} = \begin{bmatrix} 1 & 0 & 1 \\ -\dfrac{1}{2} & \dfrac{\sqrt{3}}{2} & 1 \\ -\dfrac{1}{2} & -\dfrac{\sqrt{3}}{2} & 1 \end{bmatrix}. \tag{4.23}$$

4.3 Equivalent Circuits

It is common to represent induction motor in the form of an equivalent electrical circuit [149]. Such representation provides a natural way to assess both dynamic and steady-state performance of a motor, facilitates controller design, and improves understanding of motor's operation by substantially simplifying its modeling and simulation [132]. Since the construction of the wound rotor induction motor is clearly similar to that of the three-phase transformer (stator and rotor windings correspond to the primary and secondary windings of a transformer), their equivalent circuits are conceptually the same [149].

4.3.1 T-equivalent Circuit

The traditional circuit of the induction machine is called T-equivalent circuit and is shown in Fig. 4.3. As there are three inductances connected in a "T", hence its name. The parameters
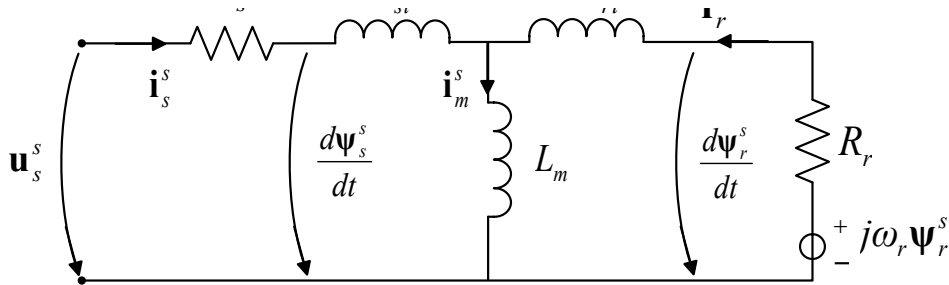
Figure 4.3: Dynamic T-equivalent circuit of induction motor.

of this system are: stator and rotor resistances (R_s, R_r), mutual inductance L_m, as well as stator and rotor leakage inductances (L_{sl}, L_{rl}). Sometimes values of stator $L_s = L_{sl} + L_m$ and rotor $L_r = L_{rl} + L_m$ inductances can be found in the catalogs instead. The space vector of stator voltage $\mathbf{u}_s^s$ is an input to the model, whereas the stator, rotor, and mutual current space vectors are variables and are denoted by $\mathbf{i}_s^s$, $\mathbf{i}_r^s$, and $\mathbf{i}_m^s$, respectively.[5] The mutual (magnetizing) current vector $\mathbf{i}_m^s = \mathbf{i}_s^s + \mathbf{i}_r^s$ decides about the value of the air-gap flux under linear magnetic conditions [132]

$$\mathbf{\Psi}_a^s = L_m \mathbf{i}_m^s. \tag{4.24}$$

---

5. This thesis follows the notation of [132] where superscripts "s" are used for space vectors and subscripts (e.g. "r" for rotor) are used for designation of coordinates.

Similarly, the stator/rotor flux space vectors are found by adding the air-gap flux and the stator/rotor leakage flux, and are equal to

$$\mathbf{\Psi}_s^s = L_m \mathbf{i}_m^s + L_{sl} \mathbf{i}_s^s \tag{4.25}$$

$$\mathbf{\Psi}_r^s = L_m \mathbf{i}_m^s + L_{rl} \mathbf{i}_r^s. \tag{4.26}$$

According to [132], the induction machine represented by the T-equivalent circuit is described by the following equations

$$\frac{d\mathbf{\Psi}_s^s}{dt} = \mathbf{u}_s^s - R_s \mathbf{i}_s^s \qquad \text{(stator)} \tag{4.27}$$

$$\frac{d\mathbf{\Psi}_r^s}{dt} = j\omega_r \mathbf{\Psi}_r^s - R_r \mathbf{i}_r^s \quad \text{(rotor)} \tag{4.28}$$

which, after combining with (4.25) and (4.26), become

$$\mathbf{u}_s^s = R_s \mathbf{i}_s^s + L_{sl}\frac{d\mathbf{i}_s^s}{dt} + L_m\frac{d\mathbf{i}_m^s}{dt} \tag{4.29}$$

$$j\omega_r \mathbf{\Psi}_r^s = R_r \mathbf{i}_r^s + L_{rl}\frac{d\mathbf{i}_r^s}{dt} + L_m\frac{d\mathbf{i}_m^s}{dt}. \tag{4.30}$$

4.3.2 Inverse-Γ-equivalent Circuit

According to [132], the model illustrated in Fig. 4.3 is physically relevant, however, its dynamic analysis and controller design might become burdensome due to its over-parametrization. Since the three currents $\mathbf{i}_m^s = \mathbf{i}_s^s + \mathbf{i}_r^s$ are not linearly independent, it is sufficient to use only one leakage inductance, not two. By defining new rotor variables

$$\mathbf{\Psi}_R^s = b\mathbf{\Psi}_r^s, \qquad \mathbf{i}_R^s = \frac{\mathbf{i}_r^s}{b} \tag{4.31}$$

where the transformation factor $b = L_m/L_r$ is chosen, the leakage inductance on the rotor side is removed, the total leakage becomes referred to the stator side only, and the inverse-Γ-equivalent circuit shown in Fig. 4.4 is obtained. Then, with the magnetizing current being
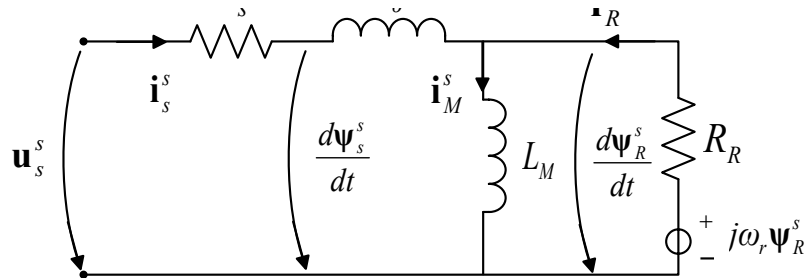
Figure 4.4: Dynamic inverse-Γ-equivalent circuit of induction motor.

equal to $\mathbf{i}_M^s = \mathbf{i}_s^s + \mathbf{i}_R^s$, the flux equations become

$$\mathbf{\Psi}_s^s = L_\sigma \mathbf{i}_s^s + L_M \mathbf{i}_M^s \tag{4.32}$$

$$\mathbf{\Psi}_R^s = L_M \mathbf{i}_M^s. \tag{4.33}$$

The new parameters: transformed magnetizing inductance L_M, total leakage inductance L_σ, and transformed rotor resistance R_R are defined based on the parameters of the T-equivalent circuit

$$L_M = \frac{L_m^2}{L_r} \tag{4.34}$$

$$L_\sigma = L_s - L_M \approx L_{sl} + L_{rl} \tag{4.35}$$

$$R_R = \left(\frac{L_m}{L_r}\right)^2 R_r. \tag{4.36}$$

Since the stator flux remains the same as in the case of the T-equivalent model, the new rotor equation is

$$\frac{d\mathbf{\Psi}_s^s}{dt} = \mathbf{u}_s^s - R_s \mathbf{i}_s^s \qquad \text{(stator)} \tag{4.37}$$

$$\frac{d\mathbf{\Psi}_R^s}{dt} = j\omega_r \mathbf{\Psi}_R^s - R_R \mathbf{i}_R^s \qquad \text{(rotor).} \tag{4.38}$$

By substituting (4.32) and (4.33) into (4.37) and (4.38), the following equations which characterize the inverse-Γ-equivalent circuit are obtained

$$\mathbf{u}_s^s = R_s \mathbf{i}_s^s + L_\sigma \frac{d\mathbf{i}_s^s}{dt} + L_M \frac{d\mathbf{i}_M^s}{dt} \tag{4.39}$$

$$j\omega_r \mathbf{\Psi}_R^s = R_R \mathbf{i}_R^s + L_M \frac{d\mathbf{i}_M^s}{dt}. \tag{4.40}$$

4.3.3 Torque Production

In the new (d, q) frame, the initial electromagnetic system describing the induction machine (three equations for stator voltages and the other three for rotor voltages) is simplified into a four equations system (or three equations system for field-oriented coordinates) [111]. The remaining equation describes the rotor behavior in the presence of mechanical loads and follows the Newton's second law

$$T_a = J\frac{d\omega_m}{dt} = T_{em} - T_{ext} - T_{frict} \tag{4.41}$$

where T_a denotes the accelerating torque, J is the shaft moment of inertia, T_{em} is the electromagnetic torque, and the load torque $T_l = T_{ext} + T_{frict}$ is composed of the external torque and the friction torque, respectively. The electromagnetic torque can be derived either from the energy balance [111]

$$T_{em} = \frac{\partial W_{mag}}{\partial \theta_r} \quad \text{where} \quad W_{mag} = \frac{1}{2}\left([\mathbf{i}_{sabc}]^T [\mathbf{\Psi}_{sabc}] + [\mathbf{i}_{rabc}]^T [\mathbf{\Psi}_{rabc}]\right) \tag{4.42}$$

or from the mechanical power P_{mech} developed by the motor

$$T_{em} = p\frac{P_{mech}}{\omega_s} \quad \text{where} \quad P_{mech} = [\mathbf{u}_{sabc}]^T [\mathbf{i}_{sabc}] + [\mathbf{u}_{rabc}]^T [\mathbf{i}_{rabc}]. \tag{4.43}$$

Equations (4.42) and (4.43) are simplified and expressed in the (d, q) frame as (refer to [111] and [219] for detailed derivation)

$$P_{mech} = (\psi_{sd} i_{sq} - \psi_{sq} i_{sd})\frac{d\theta_s}{dt} + (\psi_{rd} i_{rq} - \psi_{rq} i_{rd})\frac{d\theta_r}{dt} \tag{4.44}$$

$$P_{mech} = \frac{3}{2}\frac{L_m}{L_r}(\psi_{rd} i_{sq} - \psi_{rq} i_{sd})\frac{d(\theta_s - \theta_r)}{dt}. \tag{4.45}$$

Hence, the electromagnetic torque produced by induction motor becomes

$$T_{em} = \frac{3}{2}\frac{L_m}{L_r}p\left(\psi_{rd}i_{sq} - \psi_{rq}i_{sd}\right). \tag{4.46}$$

4.4 State Space Models

Since coordinates systems that are the most common in the analysis of induction motors are these associated with the stator frequency and fixed to the stator [111], the state space models presented in the thesis will follow this convention. In addition, since the T-equivalent circuit is preferred by motor drives manufacturers [132], the formulated models are expressed using its parameters. It is, however, possible to develop similar equations utilizing the inverse-Γ-equivalent circuit parameters and new rotor variables by taking advantage of (4.34)-(4.36) and (4.31), respectively.

4.4.1 Rotating (d, q) Frame

Typically, either a stationary reference frame or an oriented rotating frame are used in the analysis of induction machine. Since sets of equations that characterize these two systems share many similarities, it is not required to derive them separately. Instead, first the equations for a rotating frame are developed and, from these general equations, state space models for particular frames are formulated [191]. Such a time-varying (d, q) frame model which rotates at the synchronous speed ω_s is formulated according to [111] and [219] as

$$\begin{cases} \dfrac{di_{sd}}{dt} = -\gamma i_{sd} + \omega_s i_{sq} + \dfrac{\beta}{\tau_r}\psi_{rd} + p\omega_m\beta\psi_{rq} + \dfrac{u_{sd}}{\sigma} \\[2mm] \dfrac{di_{sq}}{dt} = -\gamma i_{sq} - \omega_s i_{sd} - p\omega_m\beta\psi_{rd} + \dfrac{\beta}{\tau_r}\psi_{rq} + \dfrac{u_{sq}}{\sigma} \\[2mm] \dfrac{d\psi_{rd}}{dt} = \dfrac{L_m}{\tau_r}i_{sd} - \dfrac{\psi_{rd}}{\tau_r} + \left(\omega_s - p\omega_m\right)\psi_{rq} \\[2mm] \dfrac{d\psi_{rq}}{dt} = \dfrac{L_m}{\tau_r}i_{sq} - \left(\omega_s - p\omega_m\right)\psi_{rd} - \dfrac{\psi_{rq}}{\tau_r} \\[2mm] \dfrac{d\omega_m}{dt} = \dfrac{3}{2}\mu p\left(\psi_{rd}i_{sq} - \psi_{rq}i_{sd}\right) - \dfrac{T_l}{J} \end{cases} \tag{4.47}$$

where stator currents (i_{sd}, i_{sq}), rotor fluxes (ψ_{rd}, ψ_{rq}), and motor speed (i.e. mechanical rotor speed) ω_m are the states, motor voltages (u_{sd}, u_{sq}) are the control inputs, whereas rotor inertia J, stator and rotor inductances (L_s, L_r), mutual inductance L_m, stator and rotor resistances (R_s, R_r), and the number of pole pairs p are the parameters. The following reparametrization is used to simplify the notation [219]

$$\mu = \frac{L_m}{JL_r}, \quad \tau_r = \frac{L_r}{R_r}, \quad \sigma = L_s\left(1 - \frac{L_m^2}{L_sL_r}\right), \quad \beta = \frac{L_m}{\sigma L_r}, \quad \gamma = \frac{R_s}{\sigma} + \frac{\beta}{\tau_r}L_m. \tag{4.48}$$

The transformation angle $\theta_1 = \theta_s$ is used in (4.21) and (4.22) to convert variables from the (a, b, c) frame to the (d, q) frame and vice versa. The state space model (4.47) could be even more generalized by assuming a reference frame rotating with an arbitrary speed (not associated with neither stator nor rotor coordinates) as explained in [191]. Even though such representation is crucial to understand the concept of rotating frames and to arrive at the remaining particular models, it is intentionally not included here to avoid highly theoretical derivation.

4.4.2 Stationary (α, β) Frame

By assuming the reference frame associated with the stator, the transformation angle becomes zero (both $\theta_1 = 0$ and $\omega_1 = 0$) which simplifies (4.47) by removing the synchronous speed ω_s from the equations. Then, the continuous-time induction motor model in the (α, β)-coordinates (stationary frame), represented by the T-equivalent circuit illustrated in Fig. 4.3 is formulated as [219, 341]

$$
\begin{cases}
\dfrac{di_{s\alpha}}{dt} = -\gamma i_{s\alpha} + \dfrac{\beta}{\tau_r}\psi_{r\alpha} + p\omega_m\beta\psi_{r\beta} + \dfrac{u_{s\alpha}}{\sigma} \\[2ex]
\dfrac{di_{s\beta}}{dt} = -\gamma i_{s\beta} - p\omega_m\beta\psi_{r\alpha} + \dfrac{\beta}{\tau_r}\psi_{r\beta} + \dfrac{u_{s\beta}}{\sigma} \\[2ex]
\dfrac{d\psi_{r\alpha}}{dt} = \dfrac{L_m}{\tau_r}i_{s\alpha} - \dfrac{\psi_{r\alpha}}{\tau_r} - p\omega_m\psi_{r\beta} \\[2ex]
\dfrac{d\psi_{r\beta}}{dt} = \dfrac{L_m}{\tau_r}i_{s\beta} + p\omega_m\psi_{r\alpha} - \dfrac{\psi_{r\beta}}{\tau_r} \\[2ex]
\dfrac{d\omega_m}{dt} = \dfrac{3}{2}\mu p\left(\psi_{r\alpha}i_{s\beta} - \psi_{r\beta}i_{s\alpha}\right) - \dfrac{T_l}{J}
\end{cases}
\tag{4.49}
$$

where stator currents $(i_{s\alpha}, i_{s\beta})$, rotor fluxes $(\psi_{r\alpha}, \psi_{r\beta})$, and motor speed ω_m are the states, motor voltages $(u_{s\alpha}, u_{s\beta})$ are the control inputs, whereas parameters of the system are the same as in the case of the rotating frame model (4.47). Transformation of variables between (a, b, c) and (α, β) frames is achieved by utilizing Clarke matrices (4.23). Although the stationary frame-based model allows to avoid confusion typically associated with the rotating reference frames and selection of the proper transformation angle [206], it suffers from rather complex expression of the produced electromagnetic torque

$$
T_{em} = \frac{3}{2}\frac{L_m}{L_r}p\left(\psi_{r\alpha}i_{s\beta} - \psi_{r\beta}i_{s\alpha}\right)
\tag{4.50}
$$

and nonlinear terms $\omega_m\psi_{r\alpha}$ and $\omega_m\psi_{r\beta}$ [219]. These factors might potentially cause difficulties for implementing controller hardware and software. Therefore, in some cases, in order to model IM, it is more beneficial to use the rotating frame being aligned with the rotor flux.

4.4.3 Oriented (d, q) Frame

When the transformation angle is chosen such that the d-axis of the reference frame coincides with the rotor flux $\boldsymbol{\Psi}_r^s$, the so-called rotor-flux-oriented model is obtained [111]. This is achieved when $\omega_1 = \dot\rho$, which analytically is equivalent to letting $\boldsymbol{\Psi}_r = \psi_{rd}$ and $\dot\psi_{rq} = \dot\psi_{rq} = 0$. Hence, the model becomes a fourth order model

$$
\begin{cases}
\dfrac{di_{sd}}{dt} = -\gamma i_{sd} + \omega_1 i_{sq} + \dfrac{\beta}{\tau_r}\psi_{rd} + \dfrac{u_{sd}}{\sigma} \\[2ex]
\dfrac{di_{sq}}{dt} = -\gamma i_{sq} - \omega_1 i_{sd} - p\omega_m\beta\psi_{rd} + \dfrac{u_{sq}}{\sigma} \\[2ex]
\dfrac{d\psi_{rd}}{dt} = \dfrac{L_m}{\tau_r}i_{sd} - \dfrac{\psi_{rd}}{\tau_r} \\[2ex]
\dfrac{d\omega_m}{dt} = \dfrac{3}{2}\mu p\left(\psi_{rd}i_{sq}\right) - \dfrac{T_l}{J}
\end{cases}
\tag{4.51}
$$

with the speed of the rotating (d, q) frame being equivalent to the rotor flux speed [111]

$$\omega_1 = \frac{d\theta_1}{dt} = \dot{\rho} = p\omega_m + \frac{L_m}{\tau_r}\frac{i_{sq}}{\psi_{rd}}. \tag{4.52}$$

The field-oriented model is the most advantageous from the control point of view [219], as it clarifies that the direct current component i_{sd} exclusively decides about the dynamics of the rotor flux modulus ψ_{rd} and indirectly affects the electromagnetic torque production

$$T_{em} = \frac{3}{2}\frac{L_m}{L_r}p\left(\psi_{rd}i_{sq}\right) \tag{4.53}$$

through ψ_{rd} itself, whereas the quadrature current component i_{sq} directly controls the electromagnetic torque, which in turn determines the rotor mechanical speed ω_m dynamics [219]. Conceptually, this reasoning is similar to the torque production mechanism in a DC machine. However, the rotor flux is not readily available for measurement and has to be estimated, which complicates the analysis of AC machines [132].

Remark 4.1. *In the particular case of modeling induction motor using both perfect field orientation and inverse-Γ-equivalent circuit, the electromagnetic torque produced by the motor becomes*

$$\begin{aligned}
T_{em} &= \frac{3}{2}\frac{L_m}{L_r}p\left(\psi_{rd}i_{sq} - \psi_{rq}i_{sd}\right) \\
&= \frac{3}{2}p\left(\psi_{Rd}i_{sq} - \psi_{Rq}i_{sd}\right) \\
&= \frac{3}{2}p\left(\psi_{Rd}i_{sq}\right)
\end{aligned} \tag{4.54}$$

since, recall (4.31), $\psi_{Rd} = (L_m/L_r)\psi_{rd}$ and $\psi_{Rq} = (L_m/L_r)\psi_{rq} = 0$. Similarly, the slip frequency can be expressed as

$$\begin{aligned}
\omega_2 &= \frac{L_m}{\tau_r}\frac{i_{sq}}{\psi_{rd}} = \frac{L_m R_r}{L_r}\frac{i_{sq}}{\psi_{rd}} \\
&= \frac{L_m R_r}{L_r}\frac{L_m}{L_r}\frac{i_{sq}}{\psi_{Rd}} \\
&= R_R\frac{i_{sq}}{\psi_{Rd}}.
\end{aligned} \tag{4.55}$$

4.5   Control Aspects

There are two common objectives in controlling AC motor [111]: 1) to maintain a given torque level no matter what the speed of the machine is (e.g. traction drives for electric vehicles [129]) and 2) to achieve certain motor speed (or position) in the presence of load variations (e.g. payload hoisting with given acceleration [266]). The latter case is more complex, as speed control makes it necessary not only to produce enough electromagnetic torque to overcome the load torque, but also to develop sufficient accelerations of the rotor to meet the desired dynamic performance of the controlled equipment. A typical control strategy that is applicable to a general AC motor is illustrated in Fig. 4.5. However, given the scope of the thesis, closer attention is given in the remaining part of the text to control issues of induction motors only.

To produce a given torque in an AC induction motor, it is necessary to provide a sufficient level of rotor magnetization, i.e. a sufficiently high rotor flux magnitude [111]. Therefore, flux and current control are important challenges to be solved in both torque and speed control applications. The motor supply voltages are normally obtained from the binary inverter
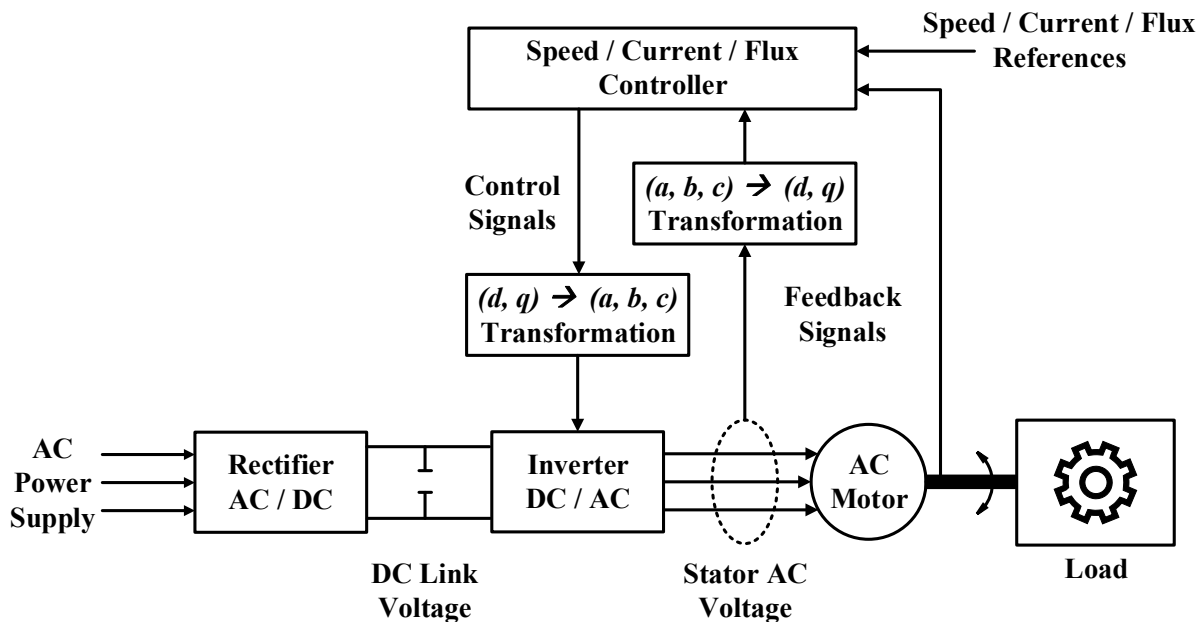
Figure 4.5: Basic control strategy of AC motor: state-feedback control [111].

control signals (that command conduction nodes on and off) by using the pulse width modulation (PWM) technique. It is also possible to control the rectifier (to regulate the DC voltage or regenerate power to the grid) but this is not always required in industrial applications. What adds to the complexity of AC motor control is its nonlinearity and high dimension of its mathematical model. These challenges are tackled by projecting three-phase variables (a, b, c) on a two-phase fictive reference frame (d, q), as discussed in Section 4.2. Some other techniques involve state- and output-feedback linearization, Lyapunov control, sliding-mode control or passivity-based control [160, 180, 260, 306, 344]. Similarly, the basic control scheme shown in Fig. 4.5 can be enhanced by applying e.g. adaptive output-feedback control, fault-tolerant control, control with optimized flux, or power factor correction [111]. However, as this thesis deals with industrial applications of AC motor control, particular attention is given to these vector control strategies that are dominant in commercially available VFDs, i.e. field-oriented control (FOC) and direct torque control (DTC).

4.6 Vector Control Methods

In a separately excited DC machine, magnitude of the armature current is proportional to the produced torque and directly controlled by using power electronic converters [111]. In AC machines, on the other hand, speed/torque control is realized by controlling both magnitude and phase of the three-phase current/voltage signals. In DC machines, the orientation of the field flux and the armature MMF is fixed by commutator and brushes, whereas AC machines demand external control to fix this orientation. Otherwise, the oscillatory dynamic response rises due to the varying space angle between different fields caused by loads and transients [111]. FOC controls this angle, as it tries to maintain the 90 ° angle between particular field components in order to emulate DC machine and provide de-coupling control. In FOC, the currents i_{sd} and i_{sq} are analogous to the field current i_f and armature current i_a of the DC motor and, therefore, the produced electromagnetic torque can be expressed as

$$T_{em} = K_{AC}\psi_{rd}i_{sq} = K_{DC}i_f i_a = K'_{AC}i_{sq}i_{sd} \tag{4.56}$$

where K is constant for a given motor. Since these two currents can be independently controlled, to keep the analogy with a DC machine, the current i_{sd} is kept constant, whereas the torque is varied by controlling the i_{sq} component. We can distinguish two fundamental methods of FOC based on acquisition of the flux vector angle [111]: 1) the direct method which is based on measurement or estimation of the magnitude and position of the flux vector and 2) the indirect method which takes advantage of the slip relation.

4.6.1 Direct Field-oriented Control

Fig. 4.6 shows an exemplary representation of the direct vector control scheme for an inverter-fed induction motor drive [111]. The torque command signal that generates the i_{sq}^{ref} current
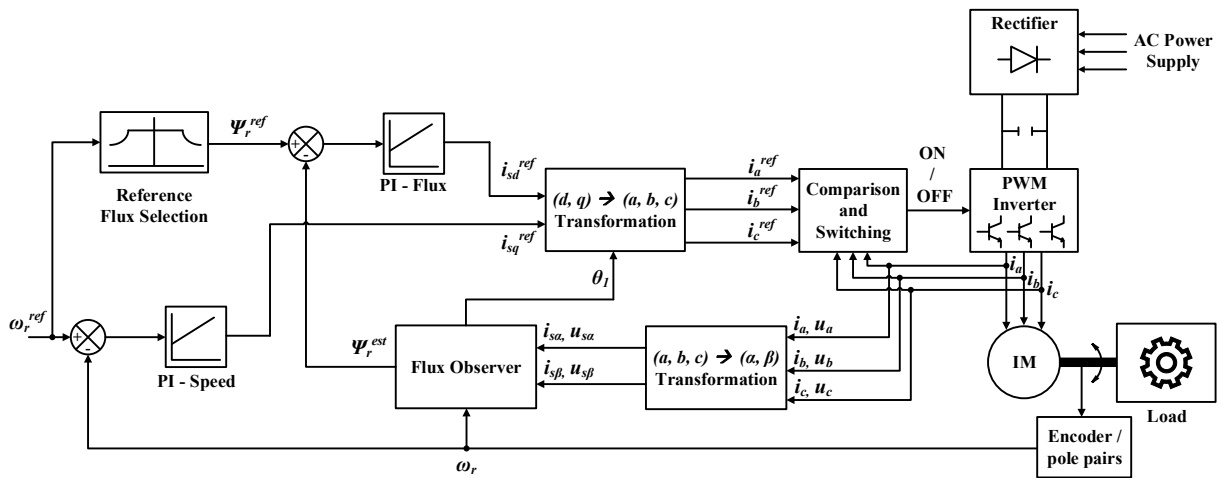
Figure 4.6: A possible implementation of rotor flux-oriented direct vector control for a current regulated PWM-fed induction motor [77].

reference is obtained from the speed control loop, whereas the reference current i_{sd}^{ref} is produced by the flux control loop. Both these currents are converted to the stationary reference frame by taking advantage of the transformation angle estimated by the flux observer. Since the rotor flux is not directly available for measurement, it is obtained from the air-gap flux. The air-gap flux, on the other hand, can either be measured by using such sensors as e.g. Hall probes or search coils, or estimated from machine variables such as stator voltage, current, and speed [168]. There are different methods to estimate rotor flux and the corresponding transformation angle – see for instance [25, 259, 343]. Normally, motor variables are converted to the stationary frame before they are used in the flux estimator [90]. Also, the reference flux Ψ_r^{ref} is chosen based on the operating conditions in either constant torque or constant power region [77]. Finally, for current-fed PWM inverter, the line currents have to be controlled so that they follow the current reference.

4.6.2 Indirect Field-oriented Control

An alternative to estimation of the flux position is to utilize rotor voltage equations in a synchronously rotating reference system to derive slip relation (4.55) by assuming that the rotor flux is exclusively aligned with the *d*-axis of the reference frame [111]. The block diagram of a typical indirect vector-controlled induction motor drive is illustrated in Fig. 4.7. The reference current signals i_{sq}^{ref} and i_{sd}^{ref} are converted to the stator (a, b, c) frame in the same way as in the case of direct field orientation. Similarly, the quadrature current component i_{sq}^{ref} is adjusted to
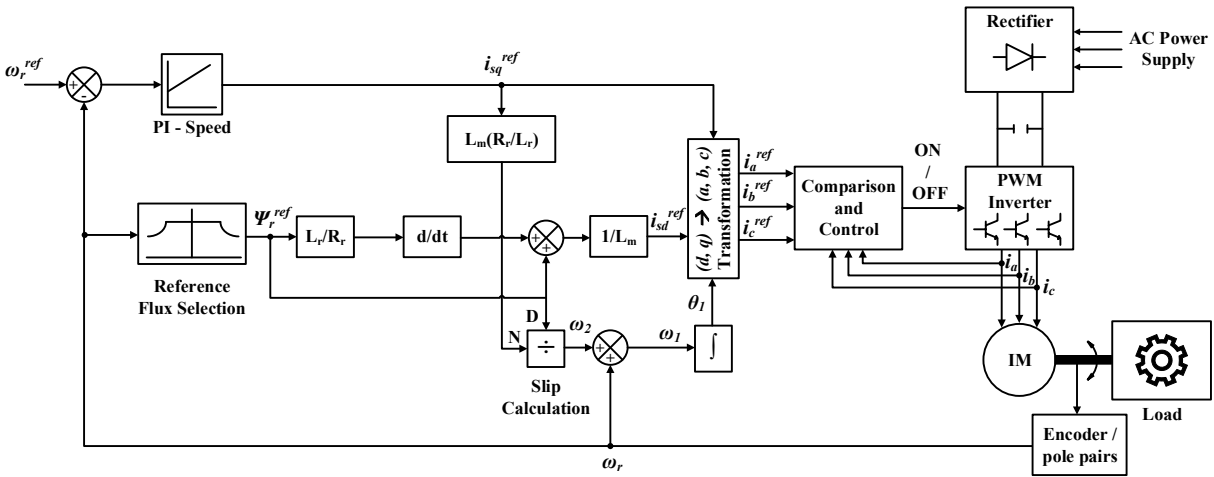
Figure 4.7: A possible implementation of rotor flux-oriented indirect vector control for a current regulated PWM-fed induction motor [77].

provide the desired torque, whereas the direct current component i_{sd}^{ref} is necessary to meet the flux requirement ($i_{sd}^{ref} = \psi_{rd}^{ref}/L_m$ in steady-state). Although the performance of indirect FOC (also referred to as flux feedforward control) is strongly affected by calculation of the slip value (which depends on machine parameters that might be different than the actual values [77]), this method is particularly popular due to its simple concept and avoiding estimation of the rotor flux vector. IFOC is applied in Chapter 7 to emulate operation of full-scale motors on an experimental test bench.

4.6.3 Sensorless Control

Sensorless vector control is in principle the same as vector control but without any speed and flux sensors [111], as illustrated in Fig. 4.8. The benefits of skipping a mechanical speed
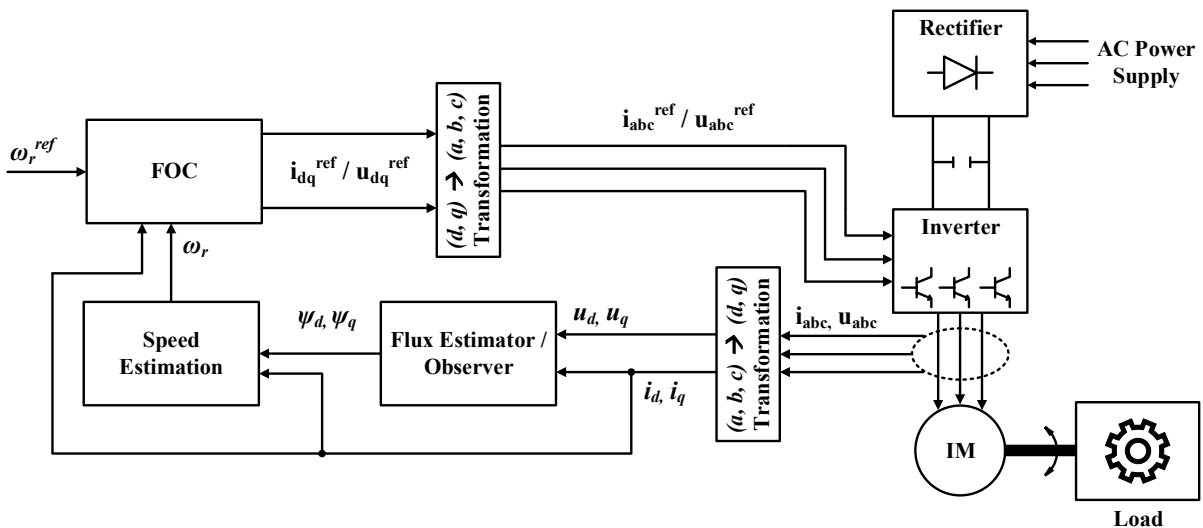
Figure 4.8: Simple block diagram of sensorless vector control system [111].

encoder are obvious: reduced cost, less reliability problems, and no extra mounting arrangements, just to name a few. Machine terminal voltages and currents can be applied to estimate speed/flux signals by using a number of methods, e.g. slip calculation, synthesis from machine

state equations, speed adaptive flux observer, extended Kalman filter (EKF), or slot harmonics [58]. Typical problems associated with these techniques are estimation near zero speed and dependency on machine parameters. Some recent variants of EKF, such as unscented Kalman filter [163] or bi-input EKF [35], effectively tackle the above challenges [19]. In addition, injection of high frequency signals in order to subject the motor to transient conditions can also serve to detect motor speed/position in the low speed range where IM becomes an unobservable system ([145] and [183]). Necessary and sufficient observability conditions for IM are covered for instance in [19] and [69] and in the references therein. In general, a sufficient condition for observability loss is when the excitation voltage frequency is zero and the motor is operating at constant speed [69]. Since the applications that are dealt with in this thesis do not involve lasting low speed operations, the formulation of EKF is followed in Chapter 8, as its well-proven track record makes it the most popular nonlinear state estimator [163].

4.6.4 Direct Torque Control

The concept of direct torque control (DTC) was developed in the late 1980's ([98] and [328]), and subsequently patented and commercialized in the 1990's by ABB. The basic scheme of DTC is shown in Fig. 4.9 where both the flux and torque are controlled by a hysteresis controller ([77] and [336]). It can be shown that the electromagnetic torque generated by the machine
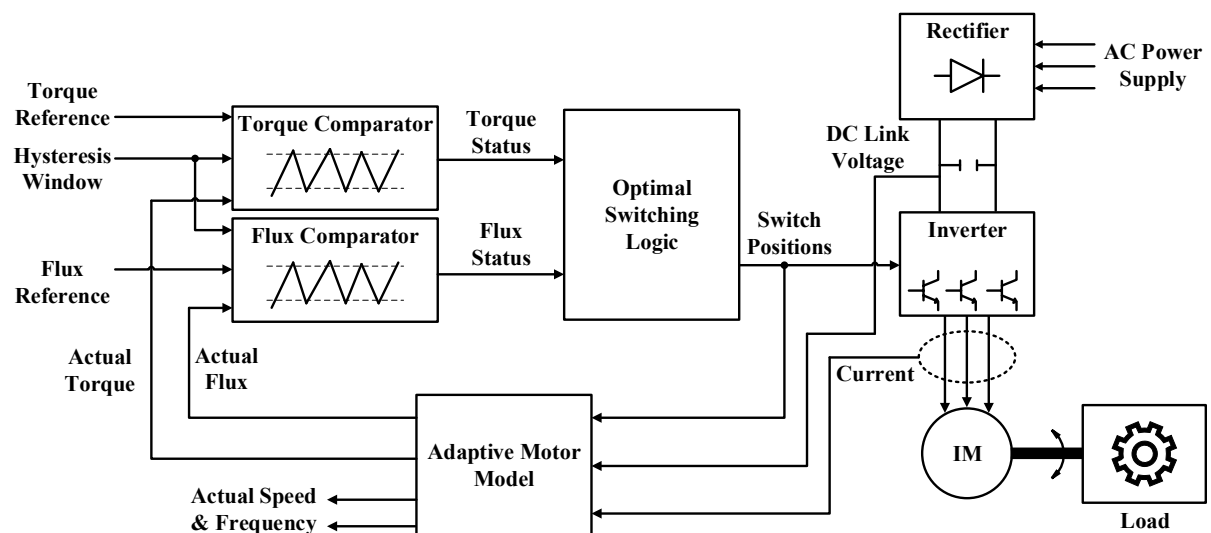
Figure 4.9: Direct torque control (DTC) scheme [77].

is proportional to the product of the stator flux Ψ_s, rotor flux Ψ_r, and the angle between them [111]. Stator flux (which is the main controlled variable) is directly controlled by the stator voltage u_s. This method is inherently sensorless, as the adaptive motor model estimates the actual torque, stator flux, shaft speed, and frequency from the motor current, line voltage, and power switch positions input data [77]. An optimal switching flux vector selection table is applied to get rid of the delays associated with the PWM. The role of this look-up table is to select the most appropriate voltage vector to satisfy the torque and flux demands [111]. Not only the DTC scheme has faster response than the FOC, but it also simplifies IM control, as there are no PI regulators, current control loops, vector transformations, nor PWM blocks. In addition, the need to use a physical speed sensor on the shaft is completely eliminated. The limitation of this method, however, is that the feedback signals are estimated from the motor model which makes the control performance sensitive to variations in machine parameters

and which causes tracking problems at low speeds [111]. These problems have recently been addressed by using e.g. improved switching logic, discrete space vector modulation (SVM) techniques, or adaptive hysteresis-band control [257].[6]

Example 4.1 presents experimental results of controlling IM using IFOC.

Example 4.1 (Simulation of a Vector Controlled Motor)

This Example is fully reproduced from article [267]. A model of a vector controlled induction motor based on the inverse-Γ-equivalent circuit is experimentally validated using the development platform described in Section A.1. Some typical simulation results are illustrated in Fig. 4.10.

(a) Amplitude $i_q^{ref} = 0.4$ A.

(c) Amplitude $n^{ref} = 1800$ rpm.

(b) Amplitude $i_q^{ref} = 0.5$ A.

(d) Amplitude $n^{ref} = 2400$ rpm.
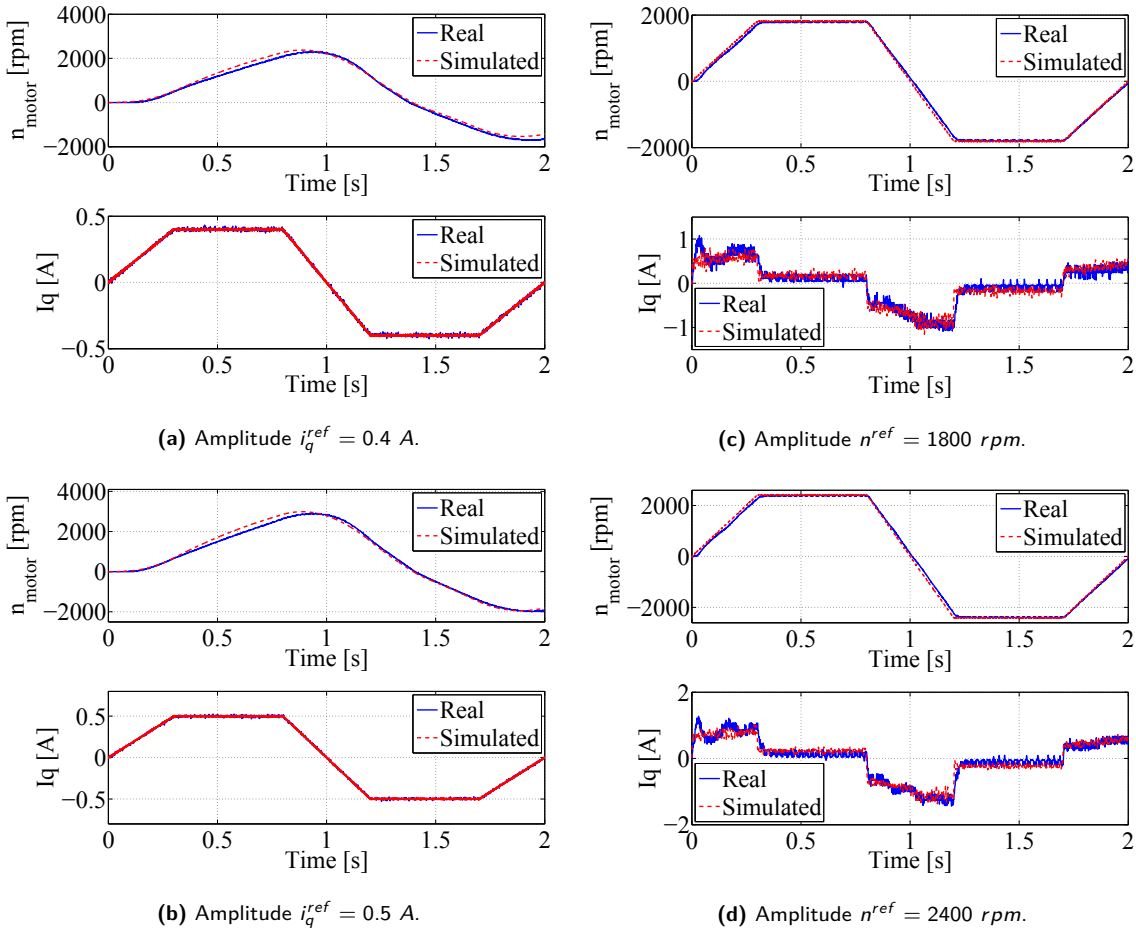
Figure 4.10: Simulation results of an induction motor with indirect field oriented control (IFOC): (a) and (b) – current control; (c) and (d) – speed control [267].

The obtained speed and current profiles indicate that the simulation model of the motor produces results which closely resemble the field data recorded on the experimental motor. The IFOC method is used as a case study here, however, depending on the application, available sensors, or design specifications, other discussed control methods can be implemented on the laboratory setup shown in Section A.1.

---

6. Although the application of DTC to IM control is not further exploited in this thesis, its basic principles are presented, since the experimental setup described in Section A.2 is composed of two ABB ACS800 drives that are controlled using this strategy.

5 Design of Electric Drivetrains

As discussed in Section 2.3.1, it is worthwhile to spent time on dimensioning and designing drivetrains and execute that process as thoroughly as possible because this may lead to substantial cost savings in the overall product development perspective. Selecting components of powertrains requires consideration of multiple factors and constraints, according to [7]. Typically, information regarding the whole system has to be synthesized and aspects such as electric supply, driven machine, environmental conditions, as well as specifications of motors and drives have to be examined. What makes this task complicated is that almost always there is involved an engineering trade-off between the desired performance and the total cost of the final design [34]. This thesis deals with the selection of components of an electric drivetrain composed of a frequency converter, an induction motor, and a gearbox.

5.1 Design Procedure

When dimensioning an electric powertrain, it is essential to guarantee that both the motor and the drive are correctly rated to perform satisfactorily under the anticipated circumstances [34]. The correct type and size of the motor provide its sufficient output torque, speed, and accuracy for the considered load and environmental conditions, whereas the correct type and size of the inverter ensure that its output voltage, current, and frequency satisfy the demands of the selected motor.

5.1.1 Main Selection Criteria

The general steps for dimensioning the motor and the frequency converter are illustrated in Fig. 5.1 and summarized as follows [7]:

1. Examine the **initial conditions** such as the mains supply voltage and frequency.

2. Go through the **process requirements** to determine the torque demand, speed range, or type of load.

3. Select the **motor** which produces enough continuous torque and withstands process overloads. In addition, its thermal loadability must not be exceeded.

4. Select the **frequency converter**. Its current and power ratings are determined by the motor and initial conditions. Potential short term overloadability must be considered as well.

Remark 5.1. *Normally, the design procedures described by motor drives manufacturers do not include selection of mechanical transmission. Instead, these guidelines assume that the gear ratio is known when dimensioning the motor drive (e.g. [7] or [315]). However, to claim that a*
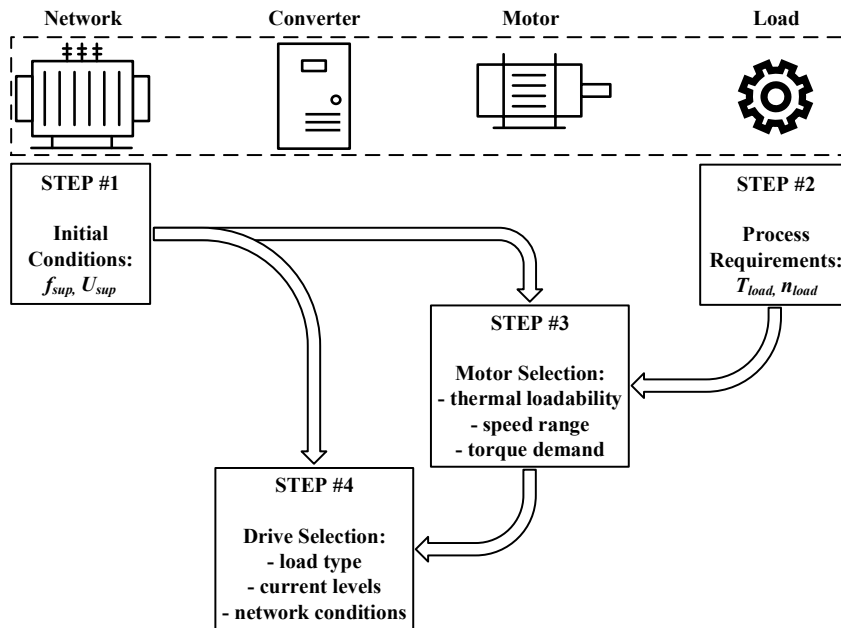
Figure 5.1: Schematic representation of the dimensioning procedure applicable to industrial electric drivetrains – adapted from [7].

given design of electric drivetrain is optimal, it should include optimal selection of gearbox as well [270]. Therefore, without violating the design procedure described above, the choice of the transmission ratio should be made simultaneously with the selection of the motor. Details on how this can be implemented in the design procedure are presented in Chapter 10.

5.1.2 Additional Concerns

A complete checklist covering most of the factors that need to be considered when dimensioning an electric powertrain is quite extensive and apart from such obvious criteria like torque, speed, and power requirements, it also encompasses such detailed points as:[7] environmental conditions, allowable mechanical resonance, permissible noise levels, control cable specifications, maintenance considerations, harmonics/electromagnetic inference (EMI), ventilation/enclosures, explosive atmospheres, or braking and regenerative action. It is self-explanatory that properties like e.g. earthing and shielding requirements have to be taken care of in the design stage but are not likely to drastically affect the final selection of drivetrain components (they would rather introduce some minor changes to additional accessories or supplementary equipment). Therefore, this thesis studies the effect of only these features that, according to [7], are identified to be the most relevant when designing a typical industrial powertrain, as demonstrated in Chapters 10 and 11. However, the two last points in the list above deserve particular attention, as they might fundamentally affect the final design of a drivetrain.

Explosive Atmospheres

In 1994 the European Union has adopted the ATEX Directive 94/9/EC, recently replaced with the updated ATEX Directive 2014/34/EU, which regulates usage of electrical equipment in hazardous areas. It defines health and safety requirements as well as conformity assessment

---

7. Refer e.g. to [34] and [149] for a detailed discussion on each of the listed items.

procedures for electrical products to enter the EU market [106]. What this legislation practically means is that only the equipment that is "Ex" certified (i.e. complies with the ATEX Directive) can be used in explosive atmospheres. The directive classifies the zones from the IEC/EN60079 standard (see for instance [155]) into similar categories, each designating whether it is gas (G) or dust (D) present in the atmosphere. The three zones/categories which characterize explosive atmospheres (and which, naturally, are common on oil and gas rigs) are [11]:

- Zone 0/20 or category 1G/1D – permanent presence of explosive atmosphere.

- Zone 1/21 or category 2G/2D – incidental presence of explosive atmosphere during normal duty.

- Zone 2/22 or category 3G/3D – presence of explosive atmosphere only by accident but not during normal duty.

This naturally limits the number of induction motor drives that can be installed on both offshore and onshore drilling rigs. Normally, no electrical motors are allowed in zone 0. Zones 1 and 2, on the other hand, require using motors that exhibit one of the following additional protection features [243]:[8]

- increased safety (denoted as "e"),

- flameproof enclosure (denoted as "d"),

- pressurized enclosure (denoted as "p"),

- protection by enclosure (denoted as "t"),

- non-sparking design (denoted as "nA").

Especially the flameproof motors ("Ex d") and these with the increased safety design ("Ex e") are popular in the oil and gas industry [11]. The flameproof enclosure ("Ex d") guarantees that a potential explosion inside the motor is not transmitted to the surrounding explosive atmosphere. Usually, such motors are heavier than their "regular" counterparts and require special design of shafts and bearings which form a part of the flameproof joint [243]. On the other hand, the increased safety design motors ("Ex e") are not allowed to include any sparking or arcing parts, as their enclosure is not strong enough to resist a possible explosion. According to [243], squirrel cage IMs are typically the most suitable for this type of protection, however, there are a few commercial examples of PMSMs which are "Ex" certified as well.

Since only these components that are "Ex" certified can be used in offshore/onshore drilling applications, the design process becomes more troublesome, as it might turn out that the solutions which satisfy the requirements and objectives do not comply with the ATEX Directive.

Braking and Regenerative Action

To reduce the speed of the motor, the kinetic energy accumulated in the system during the operation in the *M*-1 and *M*-3 quadrants (consult Fig. 5.5) has to be removed and converted to other form of energy, which normally poses a significant challenge for high inertia loads [34]. There are three usual ways of slowing down or stopping an electric variable speed drive system [34]:

---

8. The list includes some of the most common definitions. Please refer e.g. to [117] for a more comprehensive overview.

1. Coast to stop – the kinetic energy is dissipated in the load itself.

2. Mechanical braking – the kinetic energy is transformed to heat on friction brakes.

3. Electrical braking – the kinetic energy is converted to electrical energy which is then either fed back to the supply or dissipated as heat in the motor or a resistance.

In some applications, it is sufficient to stop the drive by removing the power and letting the machine coast to a stop. This is adequate for e.g. conveyors or fans [34]. In other cases, where shortening the braking time is required, the traditional approach is to use mechanical braking. Of course, this solution is not desired due to e.g. excessive maintenance of the frictional mechanical brakes. Therefore, nowadays, it is the electrical braking that is the most popular option in VFDs. It offers significant advantages compared to the mechanical braking such as wear reduction, more accurate speed control, or potential energy recovery. The disposal of the excess electrical energy is normally achieved through the following operations [34]:

- DC braking – energy (heat) dissipation in the rotor.

- Flux braking – energy (heat) dissipation in the stator.

- Dynamic braking – energy (heat) dissipation in an external resistor.

- Regenerative braking – recovering the energy by the supply.

Details on each braking method can be found, for instance, in [34] and are omitted here. Since, in principle, induction motors can equally well be operated as generators, it is up to the frequency converter to decide what to do with the excess energy in *G*-2 and *G*-4 quadrants of motor operation: whether to recover or dissipate it, as it is discussed in Section 5.2.3. Regenerative action of VFDs is normally a costly option and, therefore, its usage should be motivated by justified reasons. It is often not just the desire to recover the energy which makes design engineers choose this option, but rather a necessity to achieve a certain dynamic performance [149]. Typically, non-regenerative drives are characterized by an asymmetrical transient speed response, which means that in the case of high speed demand it is possible to quickly provide the extra kinetic energy. On the other hand, when a lower speed is desired, what often happens is that the drive reduces the torque to zero and lets the speed coast down [149]. These features can be improved by using high performance regenerative drives which allow for rapid reverse operation and quick removal of the kinetic energy.

Remark 5.2. *Current-source inverters (CSIs) enable regenerative braking, whereas voltage-source inverters (VSIs) require costly modifications to the rectifier module to fed back the energy to the supply [34].*

5.2 Torque-speed Characteristics

To pick the right motor for handling a given mechanical load one needs to recognize both the electromagnetic torque developed by the motor and its operating speed [34]. The so-called torque-speed curves (or characteristic curves) are the basis of illustrating how the motor torque changes over the speed range. They can be derived both experimentally and analytically (using equivalent circuit models or any other simulation techniques, e.g. finite element analysis). The output torque of the motor connected to the supply with rated voltage and frequency (direct-on-line: DOL) is shown in Fig. 5.2. In addition, an exemplary load torque profile is presented
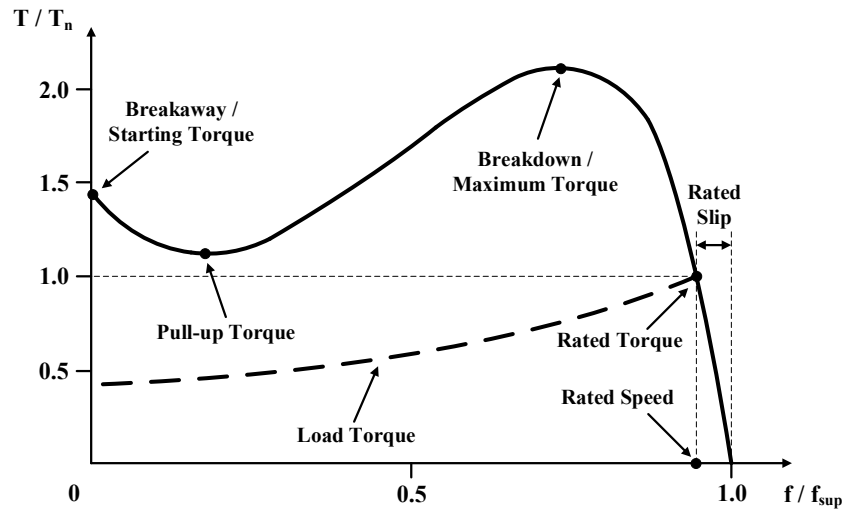
Figure 5.2: Torque-speed characteristic curve of a three-phase AC induction motor [34].

as a dashed line. The necessary condition for the motor to start is that its breakaway torque exceeds the initial load torque. To make the motor accelerate, its torque must be higher than the load torque. The motor torque reaches its peak value at the breakdown point and thereafter, for the increasing values of speed, it is gradually reduced until it stabilizes at the point where the load torque is equal to the motor torque (in Fig. 5.2, the load torque is equal to the rated torque) [34]. For higher loads, the motor speed is reduced, slip increases, and more torque is developed. The range between the maximum torque and synchronous speed is considered to be the stable operating range of the motor [7]. If the maximum torque is exceeded, the machine would stall.

5.2.1 Variable Speed Operation

It is possible to derive a family of torque-speed curves similar to the one illustrated in Fig. 5.2. A straightforward approach is to adjust the voltage at each frequency so that their ratio V/Hz is kept constant up to the base speed [149]. This is illustrated in Fig. 5.3a. Both slope of these curves and their breakdown torque are almost identical in the operating region close to
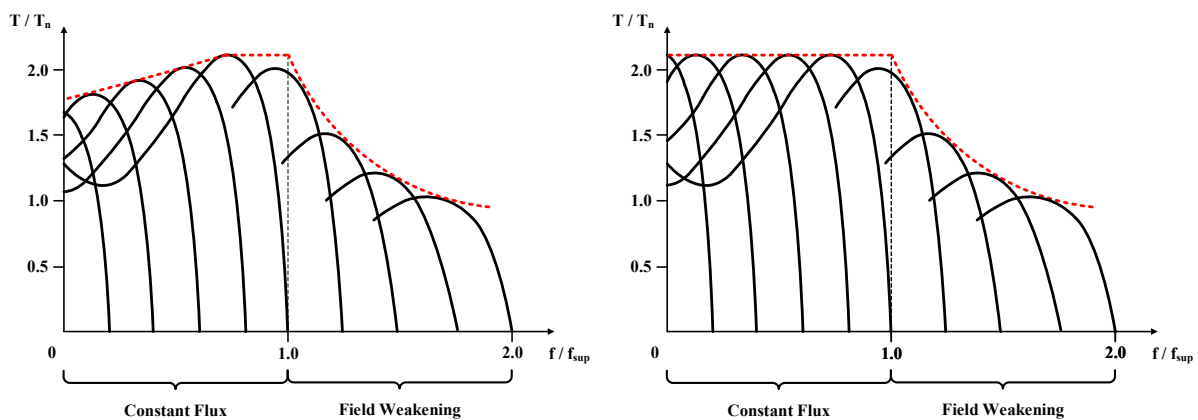
(a) Constant V/Hz ratio up to base speed ($f_{sup} = 50\ Hz$) and constant voltage at higher frequencies.

(b) Constant flux up to base speed ($f_{sup} = 50\ Hz$) and constant voltage at higher frequencies.

Figure 5.3: Typical torque-speed curves for inverter-fed induction motor [149].

the base speed. For low speeds, however, the voltage drop over the stator resistance becomes significant as the applied voltage is reduced [149]. The negative consequences of such simple V/Hz control are decreased flux and less available torque at low speeds. These features might be improved by applying the so-called voltage boost technique. The V/Hz ratio is increased at low frequencies to restore the flux that was previously missing. Modern control methods, such as the ones discussed in Section 4.6, for instance, automatically boost the voltage as compared to the linear V/Hz characteristic. An exemplary set of torque-speed curves for a motor drive with improved performance at low speeds is shown in Fig. 5.3b. The region below the nominal frequency presented in Fig. 5.3 is referred to as a constant flux range, whereas the region above the rated frequency is called the field weakening range [7]. In the latter one, the stator voltage reaches its maximum value [34]. Consequently, the air gap flux is reduced which limits the output torque.

Even though the curves illustrated in Fig. 5.3 explicitly state what torques can be produced by the motor at different values of speed, they convey no information regarding continuous operation of the motor at a given point of interest [149]. It is this knowledge, however, that is particularly relevant from the design engineer's point of view and, therefore, it deserves a separate discussion.

5.2.2 Inverter's Imposed Limitations

A fundamental safety feature of an inverter is to keep the drive currents within certain protection limits so that neither switching devices nor the motor are damaged, according to [149]. The values of the current limits are selected differently by different manufacturers, however, the general rule is that the drive output currents cannot exceed the values that would cause excessive heating of both the inverter and the motor. Normally, catalogs provide only a few discretized overload definitions which specify duration, frequency, and magnitude of the permissible overloads, as discussed in more detail in Section 11.3.1. Since modern control strategies allow to control independently flux- and torque-producing components of the motor current, it is self-explanatory that the current limits of the drive impose upper limits on the allowable motor torque [149]. Theoretically, up to the base speed, the permissible torque will be limited by its rated value, as indicated in Fig. 5.4. Above the base speed, on the other hand, the flux decreases inversely proportional to the speed and, since the stator current is thermally limited too, the load torque capacity of the motor is also reduced inversely with the speed. Therefore, to develop the full rated current (and the appropriately weakened torque), the motor has to operate with higher slips compared to the region below the rated speed [149]. Normally, when the speed of the motor exceeds the base speed by two, the voltage drop over the stator leakage inductance decreases the available torque so much that the constant power operation of the motor is not possible anymore.

The breakdown (maximum) torque of the motor is proportional to the square of the magnetic flux: $T_b \propto \Psi^2$, hence, it can be considered constant in the constant flux range [7]. However, due to the field weakening, the maximum torque is reduced and it is inversely proportional to the square of the frequency: $T_b \propto (f_{sup}/f)^2$. Similarly, the continuous motor torque also decreases in the constant power region but this time the relationship is linear: $T_m^{cont} \propto (f_{sup}/f)$.

> **Remark 5.3.** *The maximum motor torque T_b is available for short term overloads, as illustrated in Fig. 5.4. Frequency converters, however, typically further limit this torque to approx. 70 % of T_b [7].*

In addition to the limitations imposed by the inverter, there is also one important limitation caused by the motor itself: its cooling capacity. Contrary to majority of industrial DC motors
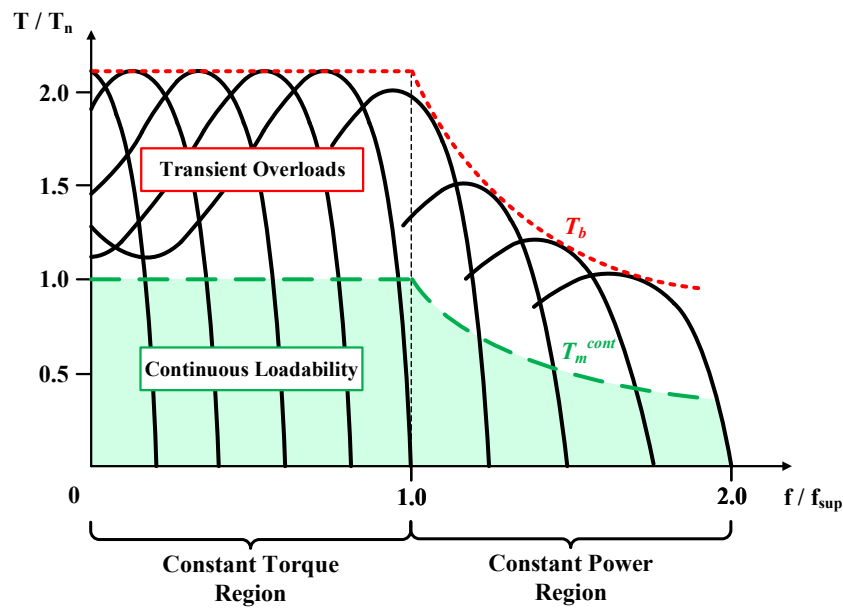
Figure 5.4: Influence of inverter on motor loadability in constant torque and constant power regions [34].

which typically come with an external air blower to guarantee continuous operation with full torque at lower speeds, squirrel cage induction motors are usually totally enclosed with the only fan mounted on the motor shaft [149]. Its role is to blow air over the outer case to avoid spot heating but since these motors are primarily designed to operate continuously at base speed, such cooling is not sufficient at low frequencies when the efficiency of the cooling fan is significantly lower. It is, of course, possible to produce full motor torque at low speeds but then the stator and rotor losses will be anyway the same as at the base speed which will cause the motor to overheat if operated long enough [149]. Therefore, manufacturers derate the continuous output torque for lower speeds if there is no external cooling system connected to the motor (by the way, the most popular solution is to use an auxiliary fan) [34].

> **Remark 5.4.** *As discussed in Section 5.1.2, what is particularly relevant for the offshore drilling industry when it comes to induction motors, is that they could easily be enclosed in flameproof or waterproof enclosures. Since this operation is more cost-effective for AC squirrel cage IMs than for DC machines, it comes as no surprise why the former solution is preferred in such applications nowadays [34].*

5.2.3 Four-quadrant Capability

An induction motor can also be operated as a generator, especially when the breaking, reverse direction of operation, or – in general – the speed reduction is required [149]. Therefore, a family of torque-speed curves for the other three quadrants of motor operation can be derived analogously to the curves presented in Fig. 5.4. The shaded regions of Fig. 5.5 represent allowable continuous loadability in the motor quadrants (*M*-1 and *M*-3), whereas the dashed black lines indicate breaking/regeneration during deceleration (*G*-2 and *G*-4). The characteristic curves in the reverse motoring range (*M*-3) are obtained by mirroring the curves from the forward motoring range (*M*-1).
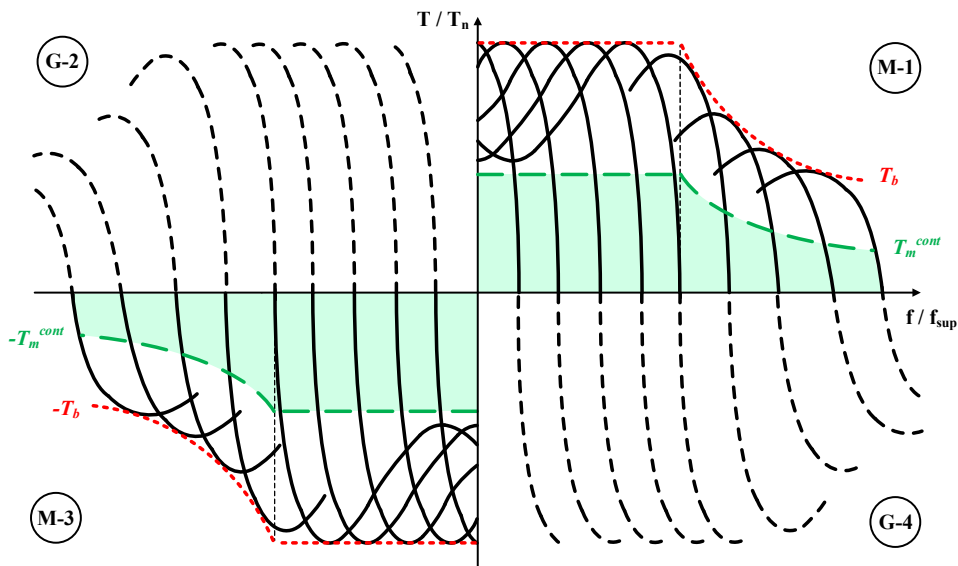
Figure 5.5: Torque-speed curves in four quadrants of induction motor operation [34].

5.3 Loadability of Inverter-fed Induction Motor

The most important selection criterion of an AC motor is to ensure that it does not become overloaded or stall over the entire speed range and under any load conditions [34], as discussed in Section 5.2. To avoid violating the temperature limits of the motor, the mechanical load it experiences must stay below its torque capacity. When the motor is connected to the power supply direct-on-line (DOL), it is normally sufficient to verify that the motor torque at the rated speed is above the load torque. In this case, only the operation at the fixed speed is possible. On the other hand, if the motor speed is supposed to vary, the available torque usually changes as well. Then, in order to ensure that the motor produces enough torque to overcome the mechanical load, the complete speed range has to be investigated. The continuous load torque capacity (loadability) of an inverter-fed squirrel cage induction motor is usually lower than its rated torque due to [34]:

1. **At all speeds**, harmonic currents cause additional heating in the motor which reduces its load capacity. This is caused by nonsinusoidal drive output currents which occur even with modern PWM inverters characterized by high switching frequencies.

2. **At speeds below base speed**, lower fan speed reduces its cooling capacity which decreases the motor's continuous loadability. If no manufacturer's specific data are provided, it can be assumed that the torque available at standstill is equal to approx. 40 % of the rated torque. To improve stator cooling and increase load capacity at low speeds, an auxiliary cooling fan can be used. This solution, however, might not entirely solve the overheating problem, since the rotor losses are usually higher and more difficult to dissipate than the stator losses.

3. **At speeds above base speed**, the weakened air gap flux reduces the output torque capability of the motor.

The loadability curve illustrated in Fig. 5.6 summarizes the above three comments. Inverter-fed IMs can experience only such steady loads that stay below the solid line representing the maximum available continuous torque T_m^{cont}. In the constant flux range, motors can produce
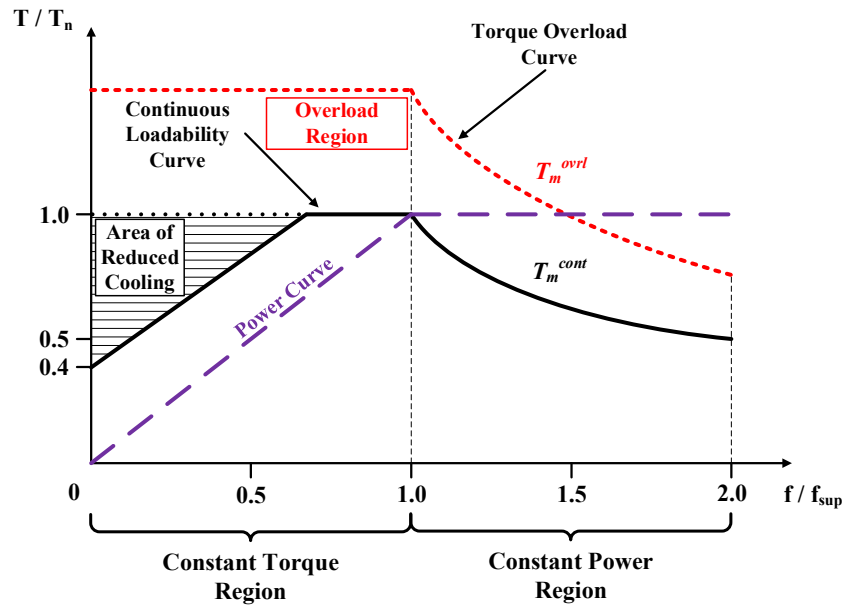
Figure 5.6: An exemplary load torque capacity (loadability) over the speed range of an inverter-fed induction motor [34].

higher torque levels (up to the rated torque) provided that an external cooling method is used. Motors can also handle torques that go above the continuous loadability only if they do not violate the overload torque limit T_m^{ovrl} and do not last for too long. Overloads are typically encountered at motors' startup or during the transients when certain accelerations have to be reached. The duration of the allowed overload depends on e.g. the overload magnitude or speed and cannot be extracted from the loadability curves alone, as it is discussed in more detail in Section 11.3.1.

In addition, Fig. 5.6 presents the equivalent load power capacity curve [34]. In the region below the base speed, the available power of the motor increases linearly to the rated power at the base speed. This region is referred to as the constant torque region. In the constant power region, on the other hand, further increase of power is not possible and the power remains constant for speed values above the base speed. This name is attributed to the analogy with a DC motor: as the torque in the field weakening range decreases, the motor can be operated at the constant power. In practical applications, however, the power available in the field weakening range might also be limited by the breakdown torque [315].

The loadability curves of commercially available motors are typically somewhat different from the exemplary curves shown in Fig. 5.6. Manufacturers follow proprietary motor designs, use particular control methods, or apply various materials, all of which affects the final shape of the loadability curves – compare for instance [13, 297, 310, 315]. However, in general, one type of loadability curve is applicable to a given class of motors which greatly simplifies drivetrain design activities. Real loadability curves for an inverter-fed AC induction motor are presented in Example 5.1.

Example 5.1 (Conventional Loadability Curves)
When a motor is subjected to the action of an uninterrupted duty cycle (i.e. S1 continuous duty from the IEC standard [154]), its thermal torque limits define allowable loads it can be exposed to over the complete speed control range. Such exemplary loadability curves from [315] are reproduced in Fig. 5.7.
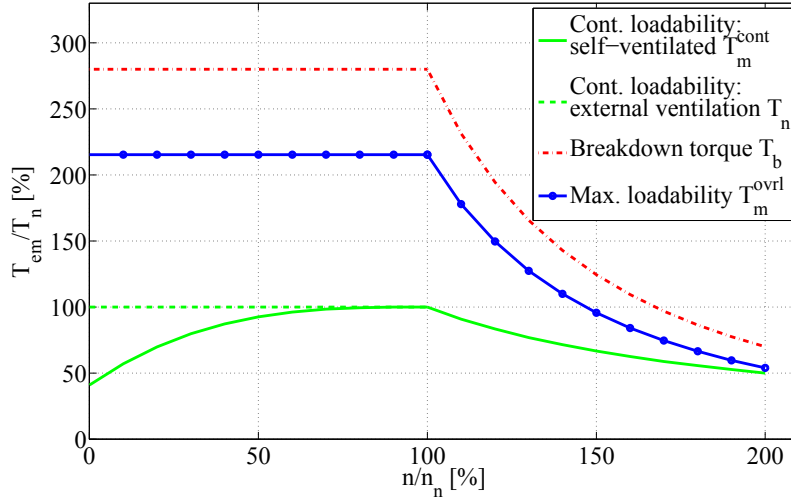
Figure 5.7: Thermal torque limits for VFD-controlled induction motor – reproduced from [315].

The normalized values of the illustrated permissible continuous loadability curves for a self-ventilated machine are characterized by the following equations, according to [315]

$$\begin{cases} T_m^{cont}/T_n = 0.59 \cdot (n/n_n)^3 - 1.77 \cdot (n/n_n)^2 + 1.77 \cdot (n/n_n) + 0.41 & \text{if } n \leq n_n \\ T_m^{cont}/T_n = 1/n & \text{if } n > n_n. \end{cases} \quad (5.1)$$

When the external cooling is used, the continuous loadability in the region below the rated speed is equal to the full motor torque $T_m^{cont} = T_n$. The maximum loadability curves are obtained by reducing the catalog value of the breakdown torque T_b by 1.3 [315]

$$\begin{cases} T_m^{ovrl}/T_n = T_b/T_n/1.3 & \text{if } n \leq n_n \\ T_m^{ovrl}/T_n = T_b/T_n/1.3 \cdot (1/n)^2 & \text{if } n > n_n. \end{cases} \quad (5.2)$$

What is important to notice is that there is no uniformity among the manufacturers regarding the allowable overload specifications as well: recall $T_m^{ovrl} = 0.7 \cdot T_b$ from Remark 5.3 suggested by [7] and compare it with $T_m^{ovrl} = T_b/1.3$ advised by [315]. Therefore, the loadability curves seem to be a promising tool to extract the synthesized producer-specific information relevant for drivetrain design, since individual pieces of manufacturers data are typically not publicly available (e.g. detailed geometry of a motor).

5.4 Mechanical Loads

The correct definition of the specification requirements is an essential part of any drivetrain design procedure. As illustrated in Fig. 2.3, any faults at this stage might turn out to be extremely costly to be eliminated at later phases of product development. Therefore, it is of such importance to properly analyze the mechanical system in order to accurately determine the levels of loads to be sustained by the dimensioned powertrain. As far as the actuation systems composed of IMs are concerned, their output torque is considered to be sufficient when it [34]:

- exceeds the breakaway load torque,

- is able to accelerate a given load from standstill to the required speed within the desired time,

- surpasses the mechanical load during continuous operation by a sufficient safety margin within a given speed range and under all conditions,

- does not result in violation of the thermal ratings of electrical components.

The fundamental information about the mechanical system required when designing an electric drivetrain for variable speed applications is summarized in these three bullet points [34]:

- The **load torque** – its type, magnitude, duration.

- The **speed range** – its boundary and base values.

- The **inertia** – what load is actually seen by the motor.

5.4.1 Classification of Load Types

In a very general classification, loads can be divided into two main categories: constant torque and variable torque [149]. Certain load patterns are characteristic for particular applications, which makes it possible to distinguish some common steady-state load types. A comprehensive list of them can be found in any textbook on practical aspects of variable speed drives, for instance in [34]. In this thesis, only the most popular load types are presented, as illustrated in Fig. 5.8.

1. Constant Torque	2. Quadratic Torque	3. Constant Power	4. Starting Torque
Handling fixed volumes, e.g: - conveyors - compressors.	**Most common load type, e.g:** - pumps - fans.	**Changing geometry, e.g:** - rollers - winders.	**High torque at low speed, e.g:** - extruders - screw pumps.
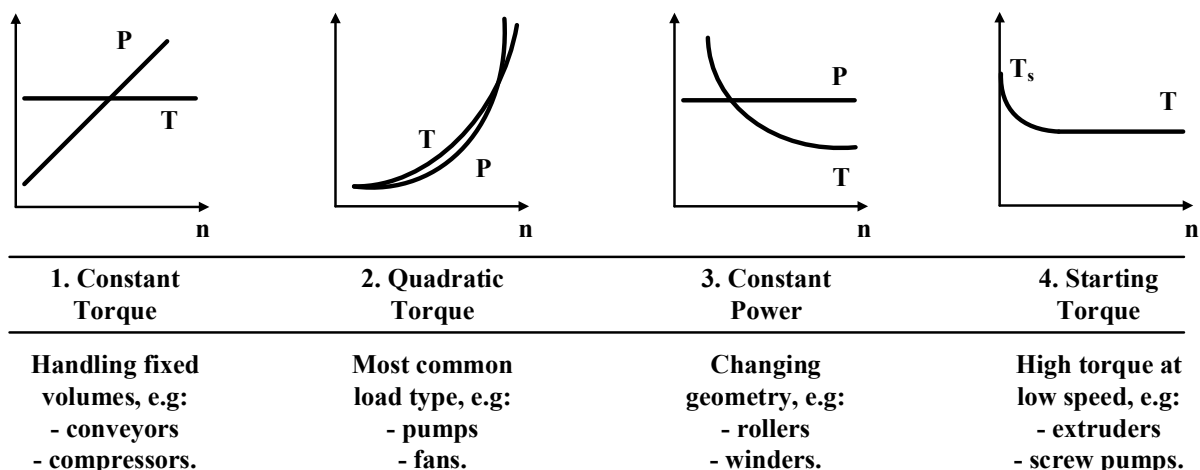
Figure 5.8: Torque and power curves for popular load types [7].

It is primarily the load torque coming from the machine which decides about both the size of the motor and its cost [34]. A rule of thumb is that the cost of the motor is approximately proportional to its rated torque capacity (not power!). Therefore, it is essential to investigate not only what loads and inertias characterize the mechanical system but – most importantly – what loads and inertias are actually experienced by the motor. When such mechanical elements as gearboxes or conveyors are present, the loads on the machine must be converted to torques acting on the motor shaft [34]. Some of the most popular transmission components are compiled in Table 5.1 together with the corresponding basic conversion formulas.
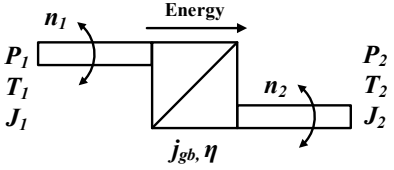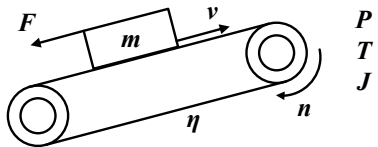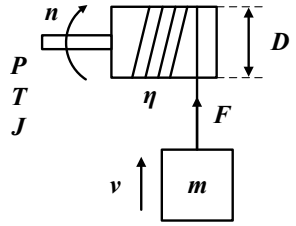
Gearbox	
 Figure 5.9: Gear with efficiency η and gear ratio $j_{gb} = \dfrac{n_1}{n_2}$.	$P_1 = \dfrac{P_2}{\eta}$ $T_1 = \dfrac{T_2}{\eta} \cdot \dfrac{n_2}{n_1}$ $J_1 = J_2 \cdot \left(\dfrac{n_2}{n_1}\right)^2$
Conveyor	
 Figure 5.10: Conveyor with payload mass m.	$P = \dfrac{Fv}{\eta}$ $T = \dfrac{F}{\eta} \cdot \dfrac{v}{2\pi n}$ $J = m \cdot \left(\dfrac{v}{2\pi n}\right)^2$
Winch	
 Figure 5.11: Winch with drum diameter D.	$P = \dfrac{Fv}{\eta}$ $T = \dfrac{F}{\eta} \cdot \dfrac{D}{2}$ $J = m \cdot \left(\dfrac{D}{2}\right)^2$

Table 5.1: Typical mechanical elements used in conversion of loads to motor shaft values [34].

The overload specifications might be superimposed on the steady-state profiles illustrated in Fig. 5.8. Depending on the desired duty cycle, their duration and magnitude might vary. In these cases, it is crucial to guarantee that not only the continuous loadability of the motor is not exceeded by the steady-state machine load but also that the machine overloads do not cause excessive heating of the motor drive. According to [7], to partially account for the intermittent overloads it is often convenient to use their root-mean-square (RMS) value when computing the continuous mechanical load.

Different aspects of drivetrains' dimensioning discussed in this Chapter are based on the case study of a popular winch mechanism demonstrated in Example 5.2.

Example 5.2 (Winch Drive)
The hoisting system shown in Fig. 5.12 is composed of a winch/drum, gearbox, motor, frequency converter, and the payload. The torque demanded by the mechanical system changes with the load on the hook, but not with the speed of hoisting [149]. Therefore, this application falls within the first category of load types presented in Fig. 5.8.
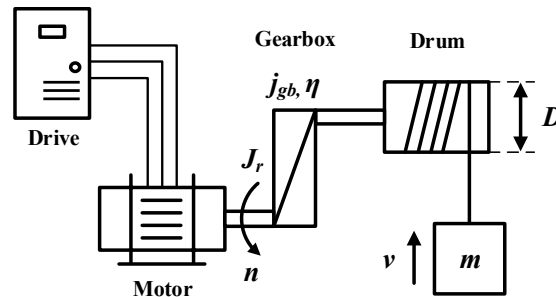
Figure 5.12: Hoisting system driven by a motor – a constant torque load application [149].

The following numerical values are chosen to describe the system:

Parameter	Value
Payload mass	$m = 1500$ [kg]
Drum diameter	$D = 1$ [m]
Efficiency	$\eta = 0.8$ [−]
Gearbox ratio	$j_{gb} = 80$ [−]
Rotor inertia	$J_r = 0.35$ [$kg\,m^2$]

Table 5.2: Numerical data of the mechanical system.

By using the formulas summarized in Table 5.1, the effective mass moment of inertia is computed as (J_L is the inertia of the load seen by the motor)

$$J_{eff} = J_r + J_L \tag{5.3}$$

$$J_{eff} = J_r + \frac{m}{j_{gb}^2} \cdot \left(\frac{D}{2}\right)^2 = 0.4086 \ kg\,m^2. \tag{5.4}$$

An interesting observation is that for the assumed parameters of the mechanical system, it is still the rotor inertia J_r that dominates the effective inertia J_{eff}. For the same reason, the drum inertia is not considered here, as the relatively high value of gear ratio j_{gb} makes it negligible when referred to the motor side.

5.4.2 Constant Torque Loads

The first load type shown in Fig. 5.8 is represented by a constant torque over the entire speed range [34]. It is commonly applied to drive such equipment as conveyors or positive displacement pumps due to the constant torque and increasing power demands which characterize this type of machinery. The following factors have to be considered when designing drivetrains operating under such load circumstances [34]:

- Although in theory the starting motor torque should be the same as the load torque at full speed, in practice the former is usually higher because of the breakaway and acceleration torque requirements.

- Running the motor at high torque (i.e. above the continuous loadability curve) and low speed might cause severe damage due to motor overloads if no separate cooling is used.

- The risk of stalling the motor at speeds above the base speed must be taken into account when operating in the field weakening range.

The solutions developed by the manufacturers that focus on the above problems are discussed in Sections 5.2.2 and 5.3 and not repeated here. What should be emphasized, however, is the fact that addressing the issues such as the stator voltage drop at low frequencies, short term current overloadability, or motor drive thermal protection is mainly attributed to the frequency converters. Therefore, the variable speed AC induction motor drives are not only characterized by the features discussed in Section 2.1, but they also allow for improved flexibility and more options for optimization when designing electric actuation systems.

Examples 5.3 and 5.4 present two case studies of identifying mechanical loads for the winch drive.

Example 5.3 (Mechanical Requirements – Occasional Overload)

Let us consider the winch drive system presented in Example 5.2. As already discussed, the steady state load torque T^{ss} is constant in this application, whereas the acceleration torque T^{acc} depends on the desired hoisting speed and time. If an exemplary hoisting speed of $v = 1.3 \ m/s$ together with the acceleration time interval $t^{acc} = 3 \ s$ are considered, these two load torques are computed as, respectively ($g = 9.81 \ m/s^2$ is the gravity constant)

$$T^{ss} = \frac{mg}{\eta j_{gb}} \cdot \frac{D}{2} = 115 \ Nm \tag{5.5}$$

$$T^{acc} = \frac{\omega}{t^{acc}} \cdot \left(J_r + \frac{J_L}{\eta} \right) = 29 \ Nm \tag{5.6}$$

where the speed of the motor that corresponds to the desired linear hoisting speed can easily be obtained both in $[rad/s]$ and $[rpm]$

$$\omega = \frac{v}{D/2} \cdot j_{gb} = 208 \ rad/s \tag{5.7}$$

$$n = \omega \cdot \frac{60}{2\pi} = 1987 \ rpm. \tag{5.8}$$

Hence, the total torque experienced by the motor during overloads becomes

$$T^{ovrl} = T^{ss} + T^{acc} = 144 \ Nm. \tag{5.9}$$

Similarly, the power levels that the motor has to deliver in both continuous and overload operations are

$$P^{cont} = T^{ss} \cdot \omega = 24 \ kW \tag{5.10}$$

$$P^{ovrl} = T^{ovrl} \cdot \omega = 30 \ kW. \tag{5.11}$$

In this Example, the mechanical torque demand is dominated by the steady-state torque and the acceleration period is intermittent and does not occur frequently [149]. Therefore, it is allowed to consider the steady-state torque as the continuous mechanical load: $T^{cont} = T^{ss}$. However, as illustrated in Example 5.4, as soon as a specific duty cycle is requested, the continuous mechanical load T^{cont} for which the motor should be rated must include the RMS value of the desired load profile ([7] and [12]).

Example 5.4 (Mechanical Requirements – Frequent Overload)
For the steady-state T^{ss} and maximum T^{ovrl} torque demands computed in Example 5.3 and summarized in Fig. 5.13a we assume the duty cycle illustrated in Fig. 5.13b. It visualizes a case of overloading the motor drive for 2 *min* every 3 *min* with the maximum mechanical torque T^{ovrl}.

(a) Torque-speed requirements. **(b)** Continuous loadability demand T^{cont} for given duty cycle.
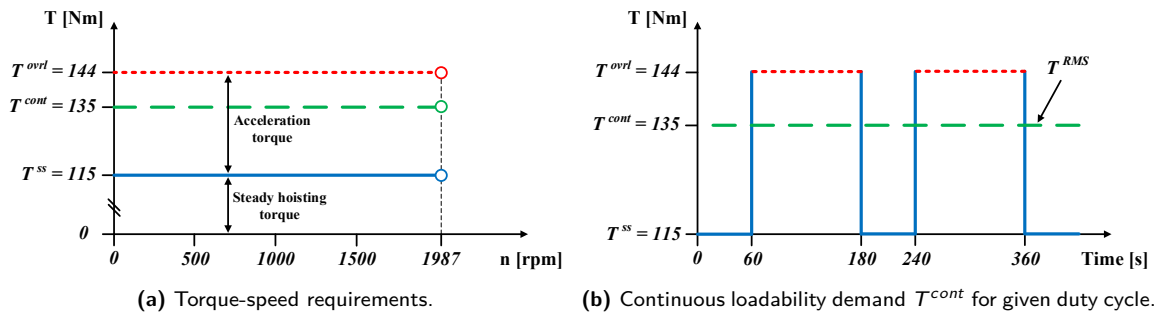
Figure 5.13: Arbitrary operating conditions in hoist application.

Whether such a load profile is realistic or not for the considered winch mechanism, is of secondary importance here. What is important, however, is that according to catalogs and manufacturers' guidelines (for instance [7, 12, 13]), the continuous loadability of the motor must exceed not only the steady-state torque T^{ss} but also the RMS value of the desired duty cycle. Therefore, the motor has to continuously deliver at least $T^{cont} = T^{RMS}$, which in the current Example is found to be 135 Nm, according to the definition of RMS of function f

$$f_{RMS} = \sqrt{\frac{1}{t_2 - t_1} \int_{t_1}^{t_2} |f(t)|^2 \, dt} \tag{5.12}$$

for the time interval bounded by $t_1 < t < t_2$. Therefore, the minimum continuous power rating of the motor in the analyzed example becomes

$$P^{cont} = T^{cont} \cdot \omega = 28 \ kW \tag{5.13}$$

which is by 17 % higher than P^{cont} computed using the steady-state load torque T^{ss}. Obviously, this difference corresponds exactly to the percentage of increase of T^{cont} with respect to T^{ss} and explains why more powerful motors should be selected for operation in frequent overload conditions. As illustrated in Fig. 5.13, the maximum torque T^{ovrl} and power P^{ovrl} demands remain the same as in Example 5.3. A convenient way to characterize the overload OL and RMS magnitudes is to express the maximum and continuous torques as percentages of the steady-state torque

$$OL = \frac{T^{ovrl}}{T^{ss}} \cdot 100 \ \% = 125 \ \% \tag{5.14}$$

$$RMS = \frac{T^{cont}}{T^{ss}} \cdot 100 \ \% = 117 \ \%. \tag{5.15}$$

Such notation is followed by some manufacturers (e.g. [7, 12, 13]) and is helpful in the dimensioning stage.

Remark 5.5. *RMS of a periodic function is the same as RMS of its one period so it does not take into account the absolute duration of the load profile (e.g. RMS of an overload profile with a given magnitude would be the same no matter if the load is experienced for 2 min every 3 min or for 4 min every 6 min). Therefore, the so-called RMS10 value is sometimes recommended by manufacturers [12], which is the RMS value computed over a 10 min interval instead of over a complete duty cycle. If the RMS10 value is greater than the default RMS, it should then be used to compute the continuous mechanical capacity and to avoid underestimating the actual loads during the initial 10 min of operation.*

5.4.3 Variable Torque Loads

The most representative example of the variable torque machine loads is depicted by the second variant in Fig. 5.8 which exhibits a quadratic torque and cubic power characteristics. It is common to assume that this load type is the least complicated to handle, since usually the required initial torque is lower that the motor starting torque and the mechanical torque demand increases with the speed [34]. The additional features listed below are typically associated with the quadratic torque loads ([34] and [149]):

- Although, in general, the mechanical torque demand is proportional to the square of the speed, this does not always hold at low speeds, since usually fans and pumps have a significant static friction or breakaway torque that must be exceeded when starting.

- Nevertheless, in many applications, the required starting current is still low, which eliminates the need to accommodate for the overload capacity of the inverters during acceleration.

- As a consequence, it is normally not a problem to run the motor for long periods and low speeds.

- However, if the operating speeds above the base speed are required, a special care should be taken not to exceed the available motor power, since the load power increases cubically with the speed.

Manufacturers normally take advantage of the reduced performance requirements for quadratic torque applications and recommend using drives with lower output specifications to improve cost-effectiveness of VSDs for pumps and fans [34]. In fact, in many cases it is sufficient to use utility-fed IMs for fans which are expected to operate continuously at rated speed [149].

By comparing the constant and variable load types, the evident difference is observed when it comes to the power-speed relationships [149]. In applications characterized by the quadratic torque demands, if the motor is rated for continuous operation at full speed, the load it will experience at half speed will be significantly lower (around 12 % of the rated power if there is negligible starting torque). On the other hand, when the constant torque application is considered, reducing the motor speed by half gives the reduction of the power rating by only 50 %. Therefore, there is typically no need for external cooling of inverter-fed IMs driving fan-type loads at low speed.

5.4.4 Inertia Matching

Apart from handling steady-state loads, an electric drivetrain is typically expected to provide sufficient dynamic acceleration torque, which is affected by the acceleration requirements (magnitude and duration) as well as by the moment of inertia of the load [34], as shown in Example 5.3. The acceleration torque is necessary for the machine to increase its operating speed. Its shape, together with the machine moment of inertia, affects the torque and, naturally, the size and cost of the motor. The dynamic torque contribution is computed as

$$T^{acc} = J_{eff} \cdot \alpha = J_{eff} \cdot \frac{\Delta\omega}{\Delta t} = J_{eff} \cdot \frac{2\pi}{60} \cdot \frac{n_2 - n_1}{\Delta t} \tag{5.16}$$

where J_{eff} $[kg\,m^2]$ is the effective mass moment of inertia seen by the motor, α $[rad/s^2]$ is the angular acceleration, $\Delta\omega$ $[rad/s]$ is the desired speed change, and Δt $[s]$ is the time it takes to

accelerate from speed n_1 to n_2 (these are given in $[rpm]$ for convenience). Hence, the torque delivered by the motor during acceleration T_m^{ovrl} must satisfy the combined steady-state T^{cont} and overload T^{acc} conditions

$$T_m^{ovrl} \geq T^{cont} + T^{acc} \tag{5.17}$$

$$T_m^{ovrl} \geq T^{ovrl}. \tag{5.18}$$

As summarized in Table 5.1, the effective moment of inertia J_{eff} which the motor actually feels can be adjusted by the transmission (let us assume it is represented by the gear ratio j_{gb}). According to [149], if the design objective is to maximize the acceleration (or, in other words, minimize the acceleration time), it turns out that the optimal gear ratio is the one that makes the referred inertia of the load J_L equal to the inertia of the motor J_r, where $J_{eff} = J_r + J_L$ (or $J_{eff} = J_1 + J_2/j_{gb}^2$ when using the notation from Table 5.1). By connecting the motor to the input shaft 1 of the gearbox shown in Table 5.1, the following motor acceleration α_1 is arrived at[9]

$$T^{acc} = J_{eff} \cdot \alpha_1 \tag{5.19}$$

$$T^{acc} = \left(J_1 + \frac{J_2}{j_{gb}^2} \right) \cdot \alpha_1 \tag{5.20}$$

$$\alpha_1 = \frac{T^{acc}}{J_1 + \dfrac{J_2}{j_{gb}^2}} \tag{5.21}$$

which yields the value of time needed to accelerate to a certain speed ω (recall that $\alpha_1 = j_{gb}\alpha_2$)

$$t = \frac{\omega}{\alpha_2} = \frac{j_{gb} J_1 + \dfrac{J_2}{j_{gb}}}{T^{acc}} \cdot \omega. \tag{5.22}$$

By taking the partial derivative of (5.22)

$$\frac{\partial \left(j_{gb} J_1 + \dfrac{J_2}{j_{gb}} \right)}{\partial j_{gb}} = 0 \tag{5.23}$$

it becomes possible to compute the optimal value of gear ratio [78]

$$j_{gb} = \sqrt{\frac{J_2}{J_1}} \tag{5.24}$$

or the optimal motor inertia

$$J_1 = \frac{J_2}{j_{gb}^2} \tag{5.25}$$

that will minimize the acceleration time. It is important to note, however, that it might turn out that some specification constraints like e.g. the maximum required speed, might not be satisfied if the above inertia matching principles are followed [149]. In addition, the fact that the motor inertia (or gear ratio) minimizes the acceleration time does not necessarily mean that this solution is optimal from the cost perspective [270]. Therefore, it is recommended to include selection of the optimal gear ratio in the drivetrain design procedure which is one of the contributions of Chapter 10.

---

9. For the sake of simplicity, the efficiency losses are not considered.

5.5 Dimensioning of Frequency Converter and Motor

The most important steps that have to be followed when selecting an induction motor and a frequency converter are listed in Section 5.1. In practice, they mean that the motor has to deliver enough torque to overcome mechanical loads over a given duty cycle, whereas the drive has to provide sufficient current and power to make it possible for the motor to do its job. Selection of the components depends upon the required speed range, loadability curves, ventilation method, supply voltage, voltage drop due to e.g. cables, or other power losses. As commented on in Section 5.1, the focus of this thesis is to study these criteria that mainly decide about the size of a drivetrain. Therefore, the specification constraints regarded as industrially accepted guidelines are extracted from [7]. For motors, they are formulated as [12]

$$\text{Motor torque} \begin{cases} T_m^{cont} & \geq T^{cont} \\ T_m^{ovrl} & \geq T^{ovrl} \end{cases} \tag{5.26a}$$

$$\text{Motor power} \begin{cases} P_m^{cont} & \geq P^{cont}. \end{cases} \tag{5.26b}$$

Therefore, for a successfully chosen motor, its loadability is equal to or exceeds the mechanical load – this applies to motor continuous T_m^{cont} and maximum T_m^{ovrl} loadability and mechanical steady-state load T^{cont} and overload T^{ovrl}. Considering the power constraints (5.26b) allows to include the effect of speed on motor loadability. The ultimate goal is to prevent the motor from overheating due to excessive loads.

On the other hand, the essential specifications for drives are summarized as [12]

$$\text{Drive current} \begin{cases} I_d^{cont} \geq I_m^{cont} \\ I_d^{ovrl} \geq I_m^{ovrl} \end{cases} \tag{5.27a}$$

$$\text{Drive power} \begin{cases} P_d^{ovrl} \geq P_m^{ovrl}. \end{cases} \tag{5.27b}$$

Likewise, the continuous drive current I_d^{cont} should be equal to or exceed the continuous motor current I_m^{cont} (analogically, the same applies to the overload scenario). Also, an additional criterion is that the maximum motor supply power P_m^{ovrl} should remain lower than what the drive can provide P_d^{ovrl}. Finally, the thermal capacity of the drive must not be violated.[10]

The drivetrain dimensioning process is best understood when illustrated on an example. Therefore, in the following part of this Section, it is shown how the above guidelines can be applied in practice: Example 5.5 presents a procedure for picking the right motor, whereas Example 5.6 demonstrates how to choose the appropriate frequency converter.

---

10. The topic of thermal protection of motor drives is studied in Chapter 11.

Example 5.5 (Selection of Motor)
For the mechanical system presented in Example 5.2 and characterized by the working conditions and duty cycle illustrated in Example 5.4, the following specification inequalities have to be satisfied when selecting a motor [7]

$$\text{Motor torque} \begin{cases} T_{m,min}^{cont} & \geq T_{min}^{cont} = 135 \ Nm \\ T_{m,base}^{cont} & \geq T_{base}^{cont} = 135 \ Nm \\ T_{m,min}^{ovrl} & \geq T_{min}^{ovrl} = 144 \ Nm \\ T_{m,base}^{ovrl} & \geq T_{base}^{ovrl} = 144 \ Nm \end{cases} \tag{5.28a}$$

$$\text{Motor power} \begin{cases} P_{m,min}^{cont} & \geq P_{min}^{cont} = 0 \ kW \\ P_{m,base}^{cont} & \geq P_{base}^{cont} = 28 \ kW \end{cases} \tag{5.28b}$$

where the minimum speed of the motor is assumed to be $n_{min} = 0 \ rpm$ (the motor starts from standstill) and the base speed is $n_{base} = 1987 \ rpm$. In fact, as long as the torque demands are considered simultaneously with the speed requirements in (5.28a), the relative motor power excess resulting from (5.28b) would be identical to the relative motor torque excess, as presented in Chapter 10.

In this Example, the electric supply delivers $U_{sup} = 400 \ V$ at $f_{sup} = 50 \ Hz$. For the sake of simplicity, let us assume that we examine only two variants of a 4-pole induction motor M3BP 200 MLA 4 from catalog [13], characterized by the rated power $P_n = 30 \ kW$ matching the continuous mechanical power demand at the base speed P_{base}^{cont}. The resulting loadabilities of these two motors are shown in Fig. 5.14.

| (a) Temperature rise class B. | (b) Temperature rise class F. |
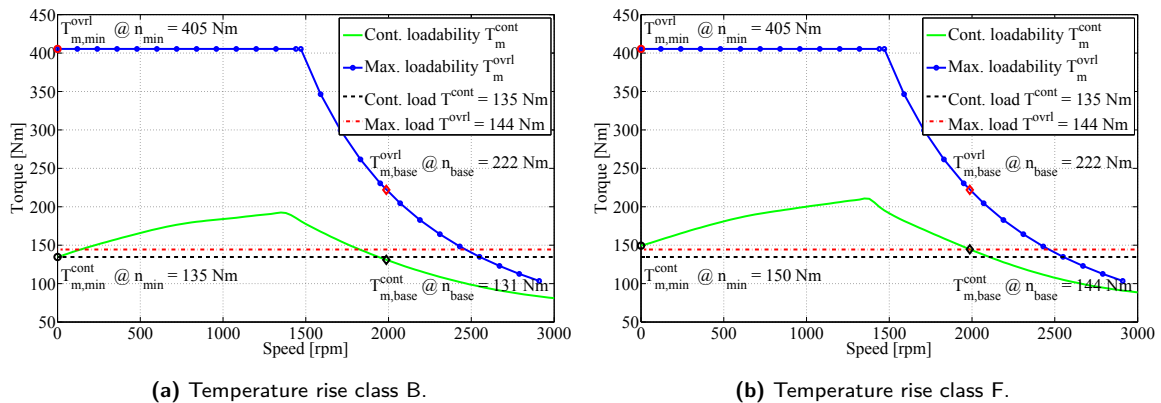
Figure 5.14: Verification of the loadability curves for the M3BP 200 MLA 4 motor from catalog [13].

Clearly, the motor produced in the rise class B is not sufficient for the considered application, since its continuous loadability at n_{base} is less than the required continuous mechanical load ($131 \ Nm < 135 \ Nm$). The resulting safety margins for both motors are summarized below:

Torque [Nm]	Class B motor			Class F motor		
	Required	Result	Margin	Required	Result	Margin
$n_{min} = 0 \ rpm$	135	135	0 %	135	150	11 %
$n_{base} = 1987 \ rpm$	135	131	−3 %	135	144	7 %
Overload [Nm]						
$n_{min} = 0 \ rpm$	144	405	181 %	144	405	181 %
$n_{base} = 1987 \ rpm$	144	222	54 %	144	222	54 %

Table 5.3: Resulting safety margins for the M3BP 200 MLA 4 motor – adapted from [12].

The choice of the F class motor seems to be more reasonable if no additional objectives (such as e.g. initial cost) are considered. During operation up to the base speed, overloading the F class motor would not be a problem, since in this range even $T_m^{cont} > T^{ovrl}$! On the other hand, exceeding the continuous loadability curve T_m^{cont} for speed values greater than n_{base} is allowed only for limited time periods and as long as the overload remains below the maximum loadability curve T_m^{ovrl} [7]. An attempt to asses whether the overload limits are violated or not involves thermal analysis of the motor drive and is presented in Chapter 11 (together with the definition of motor insulation and rise classes).

Remark 5.6. *Although the overload torque T^{ovrl} in Example 5.5 is relatively low compared to the continuous torque T^{cont} and the loadability differences between classes B and F are not significant, they are enough to illustrate the point: improved thermal capacity of the motor increases its mechanical loadability.*

Example 5.6 (Selection of Frequency Converter)

Fundamental conditions that must be met by the frequency converter to satisfactorily drive a given induction motor are summarized as [7]

$$\text{Drive current} \begin{cases} I_d^{cont} \geq I_m^{cont} \\ I_d^{ovrl} \geq I_m^{ovrl} \end{cases} \tag{5.29a}$$

$$\text{Drive power} \begin{cases} P_d^{ovrl} \geq P_m^{ovrl} \end{cases} \tag{5.29b}$$

where the currents delivered by the drive during continuous I_d^{cont} and overload I_d^{ovrl} operations must exceed motor currents I_m^{cont} and I_m^{ovrl} in these respective regions. Similarly, the resulting maximum drive power P_d^{ovrl} should be sufficiently high to overcome the required electrical motor power in the worst case load scenario: P_m^{ovrl}. For the considered M3BP 200 MLA 4 motor from Example 5.5 we have

$$P_m^{ovrl} = \frac{P_{base}^{ovrl}}{\eta_m} = 32 \ kW \tag{5.30}$$

where $\eta_m = 0.932$ is the motor efficiency and $P_{base}^{ovrl} = 30 \ kW$ – recall (5.11). According to [7], the following approximated formulas are used to compute motor currents in constant flux and field weakening ranges for continuous and maximum loads, respectively

$$\text{Constant flux} \begin{cases} I_{m,cf} = I_n \left(\frac{T_{load}}{T_n}\right) & \text{if } 0.8 \cdot T_n \leq T_{load} \leq 0.7 \cdot T_b : \\ \\ I_{m,cf}^{cont} = I_n \left(\frac{T_{base}^{cont}}{T_n}\right) \\ I_{m,cf}^{ovrl} = I_n \left(\frac{T_{base}^{ovrl}}{T_n}\right) \end{cases} \tag{5.31a}$$

$$\text{Field weakening} \begin{cases} I_{m,fw} = I_n \left(\frac{T_{load}}{T_n} \cdot \frac{n}{n_n}\right) & \text{if } 0.8 \cdot T_n \left(\frac{n_n}{n}\right) \leq T_{load} \leq 0.7 \cdot T_b \left(\frac{n_n}{n}\right)^2 : \\ \\ I_{m,fw}^{cont} = I_n \left(\frac{T_{base}^{cont}}{T_n} \cdot \frac{n}{n_n}\right) \\ I_{m,fw}^{ovrl} = I_n \left(\frac{T_{base}^{ovrl}}{T_n} \cdot \frac{n}{n_n}\right). \end{cases} \tag{5.31b}$$

Since for the M3BP 200 MLA 4 motor selected in Example 5.5 the operating speed is $n_{base} = 1987 \ rpm$, the rated speed $n_n = 1480 \ rpm$, the rated torque $T_n = 193 \ Nm$, and the rated current $I_n = 55.3 \ A$, the desired motor currents are computed in the field weakening range as $I_{m,fw}^{cont} = 52 \ A$ and $I_{m,fw}^{ovrl} = 55 \ A$. The remaining criterion is to assess what maximum power can be delivered by the drive, according to [10]

$$P_d^{ovrl} = \sqrt{3} \cdot U_{sup} \cdot I_{hd} \cdot (OL_{hd}/100) \cdot PF \tag{5.32}$$

where I_{hd} is the drive heavy duty current, OL_{hd} is the heavy duty overload allowing 150 % of overload for 1 min / 5 min at 40 $^\circ C$, and PF is the motor power factor. There are two drive candidates from catalog [10] that seem to match the motor power demands: ACS800-01-0030-3 (nominal power without overload $P_{d,n} = 30 \ kW$) and ACS800-01-0040-3 (nominal power without overload $P_{d,n} = 37 \ kW$). By using the catalog data from [10] and [13], the maximum powers of these two drives are computed as

$$P_{d,0030}^{ovrl} = \sqrt{3} \cdot 400 \ V \cdot 37 \ A \cdot (150/100) \cdot 0.84/1000 = 32 \ kW \tag{5.33}$$

$$P_{d,0040}^{ovrl} = \sqrt{3} \cdot 400 \ V \cdot 49 \ A \cdot (150/100) \cdot 0.84/1000 = 43 \ kW. \tag{5.34}$$

Hence, even though the continuous and overload current specifications of the drive ACS800-01-0030-3 exceed the motor demands ($I_{d,0030}^{cont} = 55 \ A$ and $I_{d,0030}^{ovrl} = 72 \ A$), its power is identical to the maximum required motor power P_m^{ovrl} which makes it a feasible but risky choice. Therefore, the bigger drive ACS800-01-0040-3 appears to be more appropriate alternative in the considered example (its current rating is even higher: $I_{d,0040}^{cont} = 72 \ A$ and $I_{d,0040}^{ovrl} = 86 \ A$).

5.6 Concluding Comments

Although the drivetrain dimensioning approach presented in Examples 5.5 and 5.6 is recommended by the manufacturers (e.g. [10, 12, 13, 315]), it is somewhat conservative and suffers from the following (most important) limitations:

1. **Highly iterative process**: an example is the computation of the overload mechanical torque – for calculation of T^{ovrl} we assumed $J_r = 0.35 \ kgm^2$ in Example 5.3 and we cheated, since we deliberately made it close to the inertia of the selected motor $J_r = 0.309 \ kgm^2$ in Example 5.5. In reality, however, the rotor inertia is unknown until the motor is selected so it has to be guessed before the scope is narrowed down to a few motors only. So, the selection of the rotor inertia affects the maximum load, which affects the motor selection and, hence, the rotor inertia! A solution would be to automatically update the load conditions to tailor them for the available motors.

2. **Isolation from the mechanical system**: e.g. the gear ratio between the motor and the machine has to be assumed *a priori*, whereas, ideally, it should also be optimized.

3. **Time consumption**: even though the manufacturers provide the software to aid drivetrain dimensioning, these tools just speed up the necessary computations and evaluate the most critical design constraints. Finding an optimal (or actually even a sub-optimal) combination of components using this technique requires performing the aforementioned analysis a number of times. The dimensioning process should, therefore, be automated to avoid the excessive manual interventions of design engineers.

4. **Lack of optimality**: one of the few properties of equipment which is typically understood by top management in companies: price, is kept out of the picture. Therefore, comparing the prices of different designs has to be done manually. Needless to say, this is far from minimizing the objective function (e.g. cost) to find the solution that not only meets the requirements but is also the cheapest possible.

5. **Proprietorship**: selection of one crucial drivetrain element normally determines the supplier company for the remaining parts (at least usually in offshore drilling applications). Although the reasons might be reasonable (e.g. better service and warranty options, purchase discounts, etc.), it should be possible to quickly evaluate both the performance and cost of solutions produced by different manufacturers to clearly quantify the expected benefits/losses of choosing a given contractor.

6. **Poor flexibility**: e.g. when selecting the frequency converter in Example 5.6 the heavy-duty overload is assumed, though the desired duty cycle in Fig. 5.13b is different.

7. **Problematic evaluation of overloads**: permissible durations of overloads are classified into the discrete sets of operating conditions which makes it impossible to fully analyze the temperature rise in drivetrains under arbitrary duty cycles.

8. **Cryptic thermal performance indicators**: the software selection tools supplied by the manufacturers additionally check the drive temperature margins but this operation cannot be reproduced without an access to such proprietary data as e.g. mass, dimensions, or specific heat capacity of heat sinks applied in frequency converters. Therefore, to compensate for these shortcomings, the selection of induction motor drives should involve analysis and modeling of heat flow using the available catalog data.

This thesis addresses all of the above points:

1–5 are solved in Chapter 10.

6–8 are solved in Chapter 11.

The combined effect of these contributions allows to formulate an automated selection procedure that yields an optimal drivetrain configuration. In addition, it becomes possible to model the temperature rise of a motor drive using openly accessible information in order to improve dimensioning of electric powertrains and reduce unnecessary conservatism when choosing their components.

6 Optimization Techniques

Optimization techniques are used to find a set of decision variables x, which can be somehow regarded as optimal, according to [53, 60, 224]. Usually, this involves minimization or maximization (using a change of sign) of a property or feature of a system that depends on x. An optimization problem is generally formulated as [53]

$$\begin{aligned} \underset{x}{\text{minimize}} \quad & f(x) \\ \text{subject to} \quad & x \in X \subseteq \mathcal{X} \end{aligned} \tag{6.1}$$

which is often further simplified to

$$\min_{x \in X \subseteq \mathcal{X}} f(x) \tag{6.2}$$

where the vector x collects the decision variables, the set $\mathcal{X}$ is the domain of the decision variables, the set $X \subseteq \mathcal{X}$ is the constraint set and describes the feasible decisions, and the objective function $f : \mathcal{X} \to \mathbb{R}$ assigns a cost $f(x)$ to each decision x [122].[11]

6.1 Fundamental Notions

Solving problem (6.2) is equivalent to computing the least possible cost $f^\star$ [53]

$$f^\star = \min_{x \in X} f(x). \tag{6.3}$$

The number $f^\star$ is considered to be the optimal value of problem (6.2) when

$$f(x) \geq f(x^\star) = f^\star \ \forall x \in X, \ \text{with } x^\star \in X. \tag{6.4}$$

If the optimal value $f^\star = -\infty$, problem (6.2) is unbounded below. If the set X is empty, the problem is said to be infeasible and, by convention [53], $f^\star = +\infty$. The problem is unconstrained if $X = \mathcal{X}$. Apart from minimizing the objective function, usually one is also interested in finding the optimal solution, i.e. the one whose associated cost is equal to the optimal value: $x^\star \in X$ with $f(x^\star) = f^\star$. The set of optimal solutions (there might be more that one solution!) is denoted as [53]

$$\arg \min_{x \in X} f(x) = \{x \in X : f(x) = f^\star\}. \tag{6.5}$$

The solution $x^\star$ is called an optimizer (or global optimizer/optimal solution). The term minimizer (or global minimizer) can also be used when describing specifically an optimizer of a minimization problem.

A feasibility problem is a process of detecting if the set of feasible solutions is empty or not and finding a point which is feasible. A feasible solution is the vector $x \in X$ which satisfies all constraints.

---

11. The convention followed in this Chapter assumes that vectors and matrices are denoted by plain (not boldface) letters, according to [53] and [60].

6.1.1 Continuous Problem

If the problem domain $\mathcal{X}$ is a subset of the finite-dimensional Euclidean vector-space $\mathbb{R}^n$, such an optimization problem is referred to as a continuous problem. Then, the general optimization problem (6.2) can be rewritten in a more common form as [60]

$$
\begin{aligned}
\min_{x} \quad & f_0(x) \\
\text{s.t.} \quad & f_i(x) \leq d_i, \ i = 1, \ldots, k \\
& h_j(x) = b_j, \ j = 1, \ldots, p \\
& x \in \mathcal{X}.
\end{aligned}
\tag{6.6}
$$

The vector $x = (x_1, ..., x_n)$ is the optimization/decision variable of the problem defined in the domain of the objective function $\mathcal{X} \subseteq \mathbb{R}^n$, the function $f_0 : \mathbb{R}^n \to \mathbb{R}$ is the objective function, the functions $f_i : \mathbb{R}^n \to \mathbb{R}, i = 1, ..., k$, and $h_j : \mathbb{R}^n \to \mathbb{R}, j = 1, ..., p$ are the constraint functions, and the constants $b_1, ..., b_p$ and $d_1, ..., d_k$ are the limits for the constraints, according to [53, 60, 122]. A vector $x^\star$ is called optimal, or a solution of the problem (6.6), if it yields the lowest objective value among all vectors that satisfy the constraints. An optimization problem of such a general form is called a continuous nonlinear program.

Standard Form

There are various ways of formulating optimization problems [53]. The convention of minimizing the cost function is presented in (6.6) with the right-hand side of the inequality and equality constraints bounded by variable bounds. However, typically numerical methods of solving optimization problems require that the right-hand side of constraints is equal to zero [102]. According to [53], any problem in different form can be written in a standard form

$$
\begin{aligned}
\min_{x} \quad & f_0(x) \\
\text{s.t.} \quad & f_i(x) \leq 0, \ i = 1, \ldots, k \\
& h_j(x) = 0, \ j = 1, \ldots, p \\
& x \in \mathcal{X}
\end{aligned}
\tag{6.7}
$$

where the constraint functions $f_i(x)$ and $h_j(x)$ are modified accordingly. Example 6.1 illustrates this process.

> **Example 6.1 (Box Constraints)**
> The optimization problem where $x \in \mathbb{R}^n$ is the variable [60]
>
> $$
> \begin{aligned}
> \min_{x} \quad & f_0(x) \\
> \text{s.t.} \quad & l_i \leq x_i \leq u_i, \ i = 1, \ldots, n
> \end{aligned}
> \tag{6.8}
> $$
>
> is constrained by variable bounds (or box constraints). The problem can be expressed in standard form as
>
> $$
> \begin{aligned}
> \min_{x} \quad & f_0(x) \\
> \text{s.t.} \quad & l_i - x_i \leq 0, \ i = 1, \ldots, n \\
> & x_i - u_i \leq 0, \ i = 1, \ldots, n
> \end{aligned}
> \tag{6.9}
> $$
>
> with total number of inequality constraints equal to $2n$
>
> $$
> f_i(x) = l_i - x_i \quad if \quad i = 1, \ldots, n \tag{6.10}
> $$
> $$
> f_i(x) = x_{i-n} - u_{i-n} \quad if \quad i = n+1, \ldots, 2n. \tag{6.11}
> $$

Excluding Equality Constraints

Optimization problems are often considered in the form without equality constraints (i.e. when $p = 0$) [53]

$$
\begin{aligned}
\min_{x} \quad & f_0(x) \\
\text{s.t.} \quad & f_i(x) \leq 0, \ i = 1, \ldots, k \\
& x \in \mathcal{X}.
\end{aligned}
\tag{6.12}
$$

A method to replace equality constraints with inequality constraints without compromising on accuracy and efficiency of the optimization algorithm is discussed in [53] and omitted here. The point is, however, that even though some advanced numerical solvers perform that operation automatically, this is not always advisable. The negative effect of this transformation might be that the problem becomes more difficult to understand and analyze or even some of its properties can be affected (like sparsity, when the variable x has large dimension) – see for instance [53] and [60] for a detailed discussion on this topic.

Local Optimality

Instead of achieving a global optimum, an optimization algorithm might in some cases settle in a local optimum only. x is said to be locally optimal for problem (6.6) if there exists an $R > 0$ such that $z = x$ is optimal for [53]

$$
\begin{aligned}
\min_{z} \quad & f_0(z) \\
\text{s.t.} \quad & f_i(z) \leq d_i, \ i = 1, \ldots, k \\
& h_j(z) = b_j, \ j = 1, \ldots, p \\
& \|z - x\|_2 \leq R \\
& z \in \mathcal{X}.
\end{aligned}
\tag{6.13}
$$

The point x is referred to as a local optimizer (or local minimizer) and it minimizes $f(z)$ in a feasible neighborhood of x defined by $\|z - x\|_2 \leq R$ where the *2-norm* is the usual Euclidean length

$$
\|x\|_2 = \left(\sum_{i=1}^{n} |x_i|^2 \right)^{\frac{1}{2}}.
\tag{6.14}
$$

Lagrange Duality

In order to find a locally optimal solution, the knowledge of the global optimum is still required, as shown in (6.13). The primal problem (6.6) has an associated Lagrange dual problem, which can be used to certify optimality of a primal feasible solution [363]. The difference between a primal feasible and a dual feasible solution is referred to as a duality gap. Under certain conditions, the duality gap is zero and values of these two solutions are equal (it is called strong duality) [102]. A popular method of constraint qualification to prove strong duality is Slater's condition [60]. Therefore, duality is an indirect way of evaluating the accuracy of the locally optimal solution. Lagrange duality theory which is necessary to derive optimality conditions is thoroughly discussed in [53] and skipped in this thesis. The essential material relevant for this aspect is also compiled in [102].

Optimality Conditions

In order for a point x to be considered as an optimizer, it must satisfy certain analytical conditions for optimality [60]. Necessary and sufficient optimality conditions for unconstrained and constrained problems together with a thorough theoretical background are comprehensively presented in [53] and [60]. The two most commonly used conditions are Slater's condition (constraint qualification) and Karush-Kuhn-Tucker (KKT) condition (global optimality). The interested reader is referred to e.g. [363] for a practical summary of definitions and theorems associated with these optimality requirements.

6.1.2 Integer and Mixed Integer Problem

If optimization problem (6.2) has a finite domain $\mathcal{X}$, it is called combinatorial or discrete [53]. If $x \in \{0,1\}^n$ or $x \in \mathbb{Z}^n$ (integers), the problem is said to be integer [122]. In addition, if we assume that some decision variables x apart from being binary or integer (x_b) also belong to a real Euclidean space (x_c)

$$\mathcal{X} \subseteq \{[x_c, x_b] : x_c \in \mathbb{R}^{n_c}, x_b \in \{0,1\}^{n_b}\} \tag{6.15}$$

the problem is called a mixed integer program (MIP) and can be formulated as [53]

$$
\begin{aligned}
\min_{[x_c, x_b]} \quad & f_0(x_c, x_b) \\
\text{s.t.} \quad & f_i(x_c, x_b) \leq 0, \ i = 1, \ldots, k \\
& h_j(x_c, x_b) = 0, \ j = 1, \ldots, p \\
& x_c \in \mathbb{R}^{n_c}, x_b \in \{0,1\}^{n_b} \\
& [x_c, x_b] \in \mathcal{X}
\end{aligned}
\tag{6.16}
$$

where f_0, f_i, and h_j are real-valued functions defined over $\mathcal{X}$. All properties, terminology, and definitions discussed so far are applicable to combinatorial, integer, and mixed integer optimization problems as well.

6.2 Convex Optimization

The optimization problem (6.6) is considered to be convex if the cost function f_0 is convex on the domain $\mathcal{X}$ and the set of feasible decisions X is a convex set [53]. The interested reader is referred to any textbook on optimization techniques (for instance [53] and [60]) for theory related to convex sets and functions. In this thesis, however, the focus is rather on application of optimization methods, therefore, the convex optimization problem is directly formulated as [60]

$$
\begin{aligned}
\min_{x} \quad & f_0(x) \\
\text{s.t.} \quad & f_i(x) \leq d_i, \ i = 1, \ldots, k \\
& a_j^T x = b_j, \ j = 1, \ldots, p \\
& x \in \mathcal{X}
\end{aligned}
\tag{6.17}
$$

where the functions $f_0, \ldots, f_k : \mathbb{R}^n \to \mathbb{R}$ are convex, i.e. satisfy [60]

$$f_i(\alpha x + \beta y) \leq \alpha f_i(x) + \beta f_i(y) \tag{6.18}$$

for all $x, y \in \mathbb{R}^n$ and all $\alpha, \beta \in \mathbb{R}$ with $\alpha + \beta = 1$, $\alpha \geq 0$, and $\beta \geq 0$. In addition, the equality constraint functions $h_j(x) = a_j^T x - b_j$ must be affine. An affine set is a convex set defined as [122]

$$\mathcal{X} = \{x \in \mathbb{R}^n : Ax = b\}, \tag{6.19}$$

which allows to gather the affine equality constraints into matrix A and rewrite (6.17) in a more common form

$$\begin{aligned}
\min_{x} \quad & f_0(x) \\
\text{s.t.} \quad & f_i(x) \leq 0, \ i = 1, \ldots, k \\
& Ax = b, \ A \in \mathbb{R}^{p \times n} \text{ and } b \in \mathbb{R}^p \\
& x \in \mathbb{R}^n.
\end{aligned} \tag{6.20}$$

Therefore, simply put, an affine function includes a linear function and a constant. Also, affinity is similar to the concept of linearity but generalized to Euclidean n-dimensional spaces. An important advantage of convex optimization problems is that local optimizers are also global optimizers which is proven in [53], for instance. Therefore, it is sufficient to compute a local minimum of (6.17) to be guaranteed the global optimality of the solution. Although reformulating an optimization problem in convex form might be difficult or not always possible, it is worth the effort [122]. Many non-convex problems can be solved by iterating between the solutions of convex sub-problems which has a practical significance when solving optimization problems numerically [102].

6.2.1 Linear Programming

Optimization problem (6.17) is called a linear program (LP) if the objective and constraint functions are linear (affine, to be more general), i.e. satisfy [60]

$$f_i(\alpha x + \beta y) = \alpha f_i(x) + \beta f_i(y) \tag{6.21}$$

for all $x, y \in \mathbb{R}^n$ and all $\alpha, \beta \in \mathbb{R}$. Therefore, we may say that convexity is more general than linearity: in (6.18) the inequality sign is used, contrary to equality sign in (6.21), and (6.18) is valid only for some specific values of α and β. As a consequence, convex optimization is generalization of linear programming, as any linear program falls within the class of convex optimization problems.

Standard Forms

For affine cost and constraint functions, the general form of a linear program is written as [60]

$$\begin{aligned}
\min_{x} \quad & c^T x \\
\text{s.t.} \quad & Gx \leq d \\
& Ax = b
\end{aligned} \tag{6.22}$$

where $x \in \mathbb{R}^n$, $c \in \mathbb{R}^n$, $G \in \mathbb{R}^{k \times n}$, $A \in \mathbb{R}^{p \times n}$, $d \in \mathbb{R}^k$, and $b \in \mathbb{R}^p$. Sometimes, a constant w is used in the objective function, $c^T x + w$, which makes the function affine, however it has no effect on the optimal solution when minimizing the linear cost function $c^T x$ [60]. An alternative representation of (6.22) includes only equality constraints and positive variables [53]

$$\begin{aligned}
\min_{x} \quad & c^T x \\
\text{s.t.} \quad & Ax = b \\
& x \geq 0.
\end{aligned} \tag{6.23}$$

Standard manipulations described in [60] allow to convert (6.22) to (6.23), and vice versa. Also, LPs are easily tractable in practice so there exists a great variety of solution methods and software tools to handle such problems [363].

Feasible Point

Finding a feasible point, i.e. the one that satisfies the constraints without considering the cost function (recall Section 6.1), is equivalent to solving the optimization problem with zero objective function [122]

$$
\begin{aligned}
\min_{x} \quad & 0 \\
\text{s.t.} \quad & Gx \leq d \\
& Ax = b.
\end{aligned}
\tag{6.24}
$$

Example 6.2 presents a typical LP optimization problem.

Example 6.2 (Diet Problem)

A diet problem is one of the standard applications of linear programming – recall Section 2.5.1. Let us assume that there are n different ingredients which can be chosen in $x_1, \ldots, x_n$ quantities [60]. Each ingredient j contains an amount a_{ij} of nutrient i, and is characterized by a cost c_j. The goal is to formulate the cheapest diet that satisfies the minimum nutritional requirements $b_1, \ldots, b_m$ for all m different nutrients. This problem can be formulated as the following LP [60]

$$
\begin{aligned}
\min_{x} \quad & c^T x \\
\text{s.t.} \quad & Ax \geq b \\
& x \geq 0.
\end{aligned}
\tag{6.25}
$$

An interesting example of this problem is presented in [316], where the exact amounts of nutrients in the diet are required. This leads to linear equality constraints and makes the optimization problem analytically solvable for some numerical data presented below

$$
\begin{aligned}
\min_{x} \quad & 20x_1 + 50x_2 + 70x_3 \\
\text{s.t.} \quad & x_1 + 2x_2 + 5x_3 = 15 \\
& 3x_1 + 20x_2 + 40x_3 = 100 \\
& x_1, x_2, x_3 \geq 0.
\end{aligned}
\tag{6.26}
$$

There are two nutritional requirements: $b_1 = 15$ and $b_2 = 100$ (e.g. in $[kg]$) in (6.26) and three different types of foods: x_1, x_2, x_3, to select from, associated with their respective cost: $c_1 = 20, c_2 = 50, c_3 = 70$ (e.g. in $[\$]$). The composition of each nutrient in a given food type is described by matrix

$$
A = \begin{bmatrix} 1 & 2 & 5 \\ 3 & 20 & 40 \end{bmatrix}.
$$

By expressing the equality constraints in terms of x_1

$$
x_2 = 1.25x_1 - 5 \tag{6.27}
$$
$$
x_3 = -0.7x_1 + 5 \tag{6.28}
$$

and modifying the objective function, the following rearranged problem is obtained

$$
\begin{aligned}
\min_{x} \quad & 33.5x_1 + 100 \\
\text{s.t.} \quad & x_1 \geq 0 \\
& x_1 \geq 4 \\
& x_1 \leq \frac{50}{7} \approx 7.14.
\end{aligned}
\tag{6.29}
$$

Since the objective coefficient of x_1 is positive, the optimal solution is found by selecting the least possible x_1, i.e. $x_1^\star = 4$. Therefore, the optimal solution of the original problem (6.26) is

$$x^\star = [4, 0, 2.2]^T,$$

since $x_2^\star = 1.25 \cdot 4 - 5 = 0$ and $x_3^\star = -0.7 \cdot 4 + 5 = 2.2$. Finally, the optimal objective function becomes $f^\star = 33.5 \cdot 4 + 100 = 234$ \$ which is the lowest possible cost of the diet according to given nutritional requirements.

6.2.2 Quadratic Programming

Optimization problem (6.17) is called a quadratic program (QP) if the constraints are affine and the cost function is convex quadratic [60]

$$
\begin{aligned}
\min_{x} \quad & \frac{1}{2}x^T P x + q^T x \\
\text{s.t.} \quad & Gx \leq d \\
& Ax = b
\end{aligned}
\tag{6.30}
$$

where $x \in \mathbb{R}^n$, $P = P^T > 0 \in \mathbb{R}^{n \times n}$, $q \in \mathbb{R}^n$, $G \in \mathbb{R}^{k \times n}$, $A \in \mathbb{R}^{p \times n}$, $d \in \mathbb{R}^k$, and $b \in \mathbb{R}^p$. Similarly to (6.22), a constant term w might be included in the objective function, however, it can be omitted if one is exclusively interested in the optimizer [53]. Also, if $P = 0$ in (6.30), an LP problem is obtained.

Typically, the complexity of solving a convex QP is comparable to solving an LP [363]. Some popular solution methods are e.g. active-set, gradient, or interior-point methods [253]. QPs play an important role as sub-problems in general constrained programming methods and they can be used to represent many real-world optimization problems [363]. A demonstration of using a QP to solve a typical engineering problem is illustrated in Example 6.3.

Example 6.3 (Least-squares Problem)
The problem of minimizing the convex quadratic function

$$\min_{x} \|Ax - b\|_2^2 \tag{6.31}$$

is a simple example of an unconstrained QP and is also called least-squares approximation or regression analysis [60]. It is found in numerous applications, see for instance parameters identification in Chapter 7. The objective of (6.31) can be represented as a sum of squares of residuals which results in the following least-squares approximation problem

$$\min_{x} \|Ax - b\|_2^2 = r_1^2 + r_2^2 + \cdots + r_m^2 \tag{6.32}$$

which can be solved analytically by representing the cost to be minimized as the convex quadratic function [60]

$$f(x) = x^T A^T A x - 2b^T A x + b^T b \tag{6.33}$$

and by taking its gradient

$$\nabla f(x) = 2A^T A x - 2A^T b = 0. \tag{6.34}$$

Therefore, point x minimizes f if and only if

$$A^T A x = A^T b \tag{6.35}$$

$$x = \underbrace{\left(A^T A\right)^{-1} A^T}_{A^\dagger} b \tag{6.36}$$

where $A^\dagger$ is called the pseudo-inverse matrix and (6.36) has a unique solution if the columns of matrix A are independent [60]. Gradient is defined for a real-valued function $f : \mathbb{R}^n \to \mathbb{R}$ as the transpose of its derivative $Df(x)$ [60]

$$\nabla f(x) = Df(x)^T. \tag{6.37}$$

Since derivative $Df(x)$ is a $1 \times n$ matrix, i.e. a row vector, its transpose is a column vector in $\mathbb{R}^n$. Components of (6.37) are partial derivatives of f

$$\nabla f(x)_i = \frac{\partial f(x)}{\partial x_i}, \ i = 1, \ldots, n. \tag{6.38}$$

When extra linear constraints (here represented as lower and upper bounds) are added to (6.31), the problem is called constrained regression [60]

$$
\begin{aligned}
\min_x \quad & \|Ax - b\|_2^2 \\
\text{s.t.} \quad & l_i \leq x_i \leq u_i, \ i = 1, \ldots, n
\end{aligned}
\tag{6.39}
$$

and cannot be solved analytically anymore. Techniques for numerically solving optimization problems are discussed in Section 6.3.

6.3 Numerical Optimization Methods

In general (except for some simple cases), an analytical solution of optimization problem (6.6) does not exist [53]. To tackle this issue, an approximated solution is usually computed using iterative algorithms [102]. The process starts from an initial guess x_0 and a sequence of $x_m, m = 0, \ldots, m_{max}$ is computed such that

$$x_{m+1} = \Upsilon \left(x_m, f_0, \mathcal{X} \right) \tag{6.40}$$

where Υ is an update rule that is selected depending on a particular optimization method. The algorithm terminates after a finite number of iterations m_{max} (or earlier, if the desired accuracy has already been obtained) and yields an estimated minimizer that satisfies

$$|f_0(x_{m_{max}}) - f_0(x^\star)| \leq \epsilon \ \text{ and } \ \text{dist}(x_{m_{max}}, \mathcal{X}) \leq \delta \tag{6.41}$$

where

$$\text{dist}(x, \mathcal{X}) = \min_{y \in \mathcal{X}} \|y - x\| \tag{6.42}$$

is the shortest distance between a point and a set in $\mathbb{R}^n$ measured by the norm $\| \cdot \|$, and parameters ϵ and δ represent the allowable tolerances for optimality and feasibility, respectively [102]. There is a huge number of algorithms for solving unconstrained and constrained optimization problems – refer to [102] and the references therein for a comprehensive overview. The role of this Section is to briefly present only some fundamental methods of solving (6.20). The selection of the most suitable algorithm for a given application depends on the desired accuracy, speed, and problem complexity. Advantages and disadvantages of each technique are elaborated on in [53] and [102]. Since problems of type (6.16) are particularly relevant for this thesis, the techniques for solving them are discussed separately in Section 6.4.3.

6.3.1 Unconstrained Optimization

Techniques for solving unconstrained (i.e. $\mathcal{X} = \mathbb{R}^n$ – recall Section 6.1) smooth optimization problems

$$\min_x \ f_0(x) \tag{6.43}$$

where $f_0 : \mathbb{R}^n \to \mathbb{R}$ is convex and continuously differentiable, have been in use for centuries (Newton, Cauchy, Gauss, just to name a few who proposed iterative methods for moving towards an optimum) [102]. The two most common approaches (discussed below) for solving such problems are based on the so-called descent method in which the next iterate x_{i+1} is obtained from the current state x_i by taking a step of size $h_i > 0$ along a certain descent direction Δx_i [102]

$$x_{i+1} = x_i + h_i \Delta x_i. \tag{6.44}$$

Gradient Method

The classic gradient method is applicable to convex, unconstrained optimization problems with a smooth cost function. An important property of the gradient evaluated at x_i, is that it points into the direction of the steepest local ascent, which allows to apply the anti-gradient direction as a descent direction [53] (for simplicity we can replace f_0 from (6.43) by f)

$$\Delta x_i = -\nabla f(x_i). \tag{6.45}$$

Therefore, the descent expression (6.44) can be reformulated as the following gradient update rule

$$x_{i+1} = x_i - h_i \nabla f(x_i) \tag{6.46}$$

which actually results from minimizing a quadratic function (see [102] for detailed derivation). Selection of the step size h_i is a crucial part of this strategy and is based on the so-called L-smoothness property of a twice continuously differentiable function f (see [53] for derivation)

$$\|\nabla^2 f(x)\| \leq L \tag{6.47}$$

where $L > 0$ is the so-called Lipschitz constant. Then, the constant step size is selected to be

$$h_i = \frac{1}{L} \tag{6.48}$$

and the algorithm is repeated m times until one of the following stopping criteria is met

$$f(x_m) - f(x^\star) \leq \epsilon_1 \tag{6.49}$$

$$\|x_m - x_{m-1}\| \leq \epsilon_2 \tag{6.50}$$

where ϵ_1 and ϵ_2 are user-defined tolerances.

> **Remark 6.1.** *Gradient method for unconstrained systems presented above can also be extended to constrained problems – refer to exhaustive explanations in [53] and [102].*

Newton's Method

A numerical approach to finding the roots of a differentiable function f is referred to as a Newton–Raphson method and is explained in Section B.8. In optimization, however, one uses the Newton's method to find the roots of the derivative of a twice differentiable function f [102]. It is more quickly converging algorithm than the gradient method, since it uses the second-order information of f – the so-called Hessian $\nabla^2 f$, contrary to using the first-order information in the former approach. By introducing appropriate assumptions and limitations

concerning properties of the function f (covered in [53]), the Newton's method can be summarized as minimization of the second-order approximation (Taylor expansion) of the function f at the current state x_i

$$x_{i+1} = \arg\min_x f(x_i) + \nabla f(x_i)^T (x - x_i) + \frac{1}{2}(x - x_i)^T \nabla^2 f(x_i)(x - x_i). \tag{6.51}$$

Therefore, the so-called Newton direction

$$\Delta x_i = - \left(\nabla^2 f(x_i)\right)^{-1} \nabla f(x_i) \tag{6.52}$$

is obtained which is used to compute the next iterate

$$x_{i+1} = x_i - h_i \left(\nabla^2 f(x_i)\right)^{-1} \nabla f(x_i) \tag{6.53}$$

using the step size $h_i > 0$. Techniques such as line search (or backtracking line search) can be applied to find the appropriate value of h_i and are presented in details in [60].

6.3.2 Constrained Optimization

In this Section, the two most popular techniques (typically encountered in both free and commercial software products [102]) to find solution of constrained optimization problems are briefly presented. There exist other approaches as well (e.g. already mentioned gradient projection or alternating minimization methods) but since they are not as common, they are out of the scope of this thesis.

Interior Point Methods

The name of these techniques originates from the way the solution is achieved: an interior point (i.e. the point which strictly satisfies the inequality constraints) is selected as a starting point and the solution follows a so-called central path to the optimal solution, according to [363]. To follow the central path, only the feasible iterates that strictly satisfy the inequality constraints are chosen.

Interior point methods (IPMs) are classified into two groups: barrier methods, which were the first practically relevant algorithms for linear programming, and primal-dual methods, which are modern and most commonly applied nowadays [53]. The principal concept behind the barrier method is to transform the constrained convex optimization problem (6.20) into an unconstrained one (in terms of inequalities) by taking advantage of the so-called barrier function $\Phi_f : \mathbb{R}^n \to \mathbb{R}$ [102]

$$\begin{aligned} x^\star(\mu) \in \arg\min_x \quad & f_0(x) + \mu \Phi_f(x) \\ \text{s.t.} \quad & Ax = b \end{aligned} \tag{6.54}$$

where $\mu > 0$ is called barrier parameter and function Φ_f is typically selected to be the log barrier function [363]

$$\Phi_f(x) = - \sum_{i=1}^{k} \ln(-f_i(x)). \tag{6.55}$$

The domain, continuous gradient, and continuous Hessian of this function are [53]

$$\{x \in \mathbb{R}^n : f_i(x) < 0 \ \forall \ i = 1, \ldots, k\} \tag{6.56}$$

$$\nabla \Phi_f(x) = \sum_{i=1}^{k} \frac{1}{-f_i(x)} \nabla f_i(x) \tag{6.57}$$

$$\nabla^2 \Phi_f(x) = \sum_{i=1}^{k} \frac{1}{f_i(x)^2} \nabla f_i(x) \nabla f_i(x)^T + \frac{1}{-f_i(x)} \nabla^2 f_i(x). \tag{6.58}$$

Such formulation of the barrier problem allows to use the previously described Newton's method. The logarithmic barrier function is the most commonly applied in practical implementations of barrier methods [53]. Selection of parameters and detailed description of this technique are presented e.g. in [253].

On the other hand, primal-dual methods solve problem (6.20) by computing the Karush-Kuhn-Tucker (KKT) conditions mentioned in Section 6.1.1 by a modified version of Newton's method [102]. The basic concept is to linearize the relaxed KKT conditions and solve the modified Newton's procedure at each iteration [363]. There are different interior point algorithms, described comprehensively in [354], however, the one that is particularly well-suited for practical implementations is Mehrotra's algorithm [232].

Active Set Methods

Another method for solving the problem

$$\begin{aligned} \min_{x} \quad & f_0(x) \\ \text{s.t.} \quad & x \in X \end{aligned} \tag{6.59}$$

where $X \subset \mathbb{R}^n$, is called an active set method [53]. As the name indicates, the major idea is to determine the set of active constraints for the optimal solution. This is achieved by selecting an initial set of active constraints and iteratively improving it until the optimal active set is found which ultimately yields the optimum [363]. An i-th inequality constraint $f_i(z) \leq 0$ is considered to be active at a feasible point x if $f_i(x) = 0$. If $f_i(x) < 0$, then the constraint $f_i(z) \leq 0$ is inactive at x. Therefore, equality constraints are always active for all feasible points [53]. Also, a constraint can be redundant if it does not affect the feasible set.

Active set methods are widely described in the literature on optimization techniques, e.g. in [53] and [253]. The reason these methods are only briefly mentioned in this Section is that different algorithms (namely: interior point and branch and bound discussed in Section 6.4.3) are used to solve problems of the nature presented in this thesis (i.e. nonlinear programming in Chapter 11 and mixed integer programming in Chapter 10, respectively).

6.3.3 Software Tools

There is a huge variety of software tools for solving optimization problems [122]. A popular approach is to formulate an optimization problem in a mathematical language and pass it to the solver [102]. The list below summarizes some of the most widely used:

- Modeling languages:
  - YALMIP: language consistent with MATLAB syntax for modeling convex and non-convex optimization problems [209],

- CVX: MATLAB-based modeling system for convex optimization ([125] and [124]),
- AMPL: proprietary software, compatible with majority of solvers [113].

- Standalone solvers:
  - MATLAB: solving wide range of optimization problems (practically useful for LP and QP: functions `linprog`/`quadprog`) [224],
  - CPLEX: commercial product, industry standard for (MI)LP [151],
  - CVXOPT: free software package for convex optimization based on the Python programming language [21].

- Solvers for embedded platforms:
  - CVXGEN: generation of custom code for small LP or convex QP problems ([225] and [226]),
  - FORCES Pro: tool for generating decision-making software [103].

Tools and solvers listed above differ in terms of accuracy, availability (free vs. commercial), ease of use, etc. In this thesis, YALMIP modeling software is interfaced with MATLAB to solve MIP problems using CPLEX solver.

6.4 Mixed Integer Programming

As mentioned in Section 6.1.2, optimization problems that include a mixture of discrete and continuous decision variables are referred to as mixed integer programming (MIP) problems. In this Section, special attention is given to classification of MIPs depending on the type of domain of optimization variables as well as to the solution of design optimization problems using combinatorial approach [270] vs. modeling of logical decisions as linear inequalities [39]. Given the scope of the thesis (application of MIP to design optimization), the discussion is limited to mixed integer linear programs (MILPs) only.[12]

6.4.1 Logical Constraints as Mixed Integer Linear Inequalities

Modeling and controlling systems characterized by interfering physical laws, logical rules, and operating conditions have been recognized as a challenge and received substantial amount of attention since at least the 1990's [126]. Transforming propositional logic into linear inequality constraints that involve both integer and continuous variables was a significant contribution in this field and enabled to obtain mixed logical dynamical (MLD) systems described by linear dynamic equations constrained by mixed integer inequalities [39]. The most prominent examples of MLD systems are hybrid systems (i.e. the ones that integrate logic-based discrete dynamics and continuous dynamics with events and mode switches), finite state machines, constrained linear systems, or nonlinear systems which can be linearized at different operating points by convex piecewise linear functions [39].

To describe a hybrid system in a form compatible with optimization software, there are two main steps that have to be followed [53]:

1. Reformulation of logic rules into linear integer inequalities.

---

12. In general, it is recommended to convert nonlinear optimization problems (which are difficult to solve) into simpler, linear problems [39].

2. Translation of continuous and logical parts of the system into linear mixed integer dependencies.

Therefore, the goal is to arrive at a system represented by continuous and Boolean variables that is constrained by linear equalities and inequalities. Dealing with such a compact model is usually more efficient than studying separate continuous systems in each discrete operating region.

Step no.1 above is solved by defining a polyhedral set P for a given Boolean formula $F(p_1, p_2, \ldots, p_n)$ such that a set of binary values $\{\delta_1, \delta_2, \ldots, \delta_n\}$ satisfies the Boolean formula F in P [53]

$$F(p_1, p_2, \ldots, p_n) \text{ ``TRUE''} \iff A\delta \leq B, \ \delta \in \{0,1\}^n \tag{6.60}$$

where the binary integer variable δ_i is associated to each Boolean variable p_i such that

$$\{\delta_i = 1\} \iff p_i = \text{TRUE}. \tag{6.61}$$

Some of the most popular Boolean relations are summarized in Table 6.1 together with their corresponding linear constraints, according to [39, 53, 350].

Relation	Boolean	Linear Constraints
AND	$\delta_1 \wedge \delta_2$	$\delta_1 \geq 1$
		$\delta_2 \geq 1$
OR	$\delta_1 \vee \delta_2$	$\delta_1 + \delta_2 \geq 1$
NOT	$\neg \delta_1$	$(1 - \delta_1) \geq 1$
XOR	$\delta_1 \oplus \delta_2$	$\delta_1 + \delta_2 = 1$
IMPLY	$\delta_1 \to \delta_2$	$\delta_1 - \delta_2 \leq 0$
IFF	$\delta_1 \leftrightarrow \delta_2$	$\delta_1 - \delta_2 = 0$
ASSIGN		$\delta_1 + (1 - \delta_3) \geq 1$
$\delta_3 = \delta_1 \wedge \delta_2$	$\delta_3 \leftrightarrow \delta_1 \wedge \delta_2$	$\delta_2 + (1 - \delta_3) \geq 1$
		$(1 - \delta_1) + (1 - \delta_2) + \delta_3 \geq 1$

Table 6.1: Common Boolean relations and their corresponding linear constraints [53].

On the other hand, to address step no.2, it is necessary to establish mixed integer linear inequalities, i.e. linear inequalities which contain both continuous variables $x \in \mathbb{R}^n$ and logical variables $\delta \in \{0, 1\}$. It can be shown (refer to [39] and [53] for proofs and derivation) that for a linear real-valued function $f : \mathbb{R}^n \to \mathbb{R}$ defined over a bounded set $x \in \mathcal{X}$, a product of logical and continuous variables $\delta f(x)$ can be replaced by an auxiliary real variable

$$y = \delta f(x) \tag{6.62}$$

which satisfies

$$[\delta = 0] \to [y = 0] \tag{6.63}$$

$$[\delta = 1] \to [y = f(x)]. \tag{6.64}$$

According to [39], by defining

$$M = \max_{x \in \mathcal{X}} f(x) \tag{6.65}$$

$$m = \min_{x \in \mathcal{X}} f(x) \tag{6.66}$$

it becomes possible to express $y = \delta f(x)$ as a set of linear inequalities

$$y \leq M\delta \tag{6.67}$$
$$y \geq m\delta \tag{6.68}$$
$$y \leq f(x) - m(1 - \delta) \tag{6.69}$$
$$y \geq f(x) - M(1 - \delta). \tag{6.70}$$

As shown later in Example 6.6, such a formulation enables efficient solution of optimization problems which involve mixed integer decision variables. One of the software tools that allows for modeling hybrid systems using the discussed approach is e.g. HYSDEL [337].

6.4.2 Common Formulations

The three most popular formulations of MILPs are binary, integer, and mixed integer programs. They find many practical applications, with modeling and controlling MLD systems [39] and decision-making being some of the most prominent examples [197].

Binary Programming

The most frequent decision-making schemes (also in our daily life) are based on alternatives. It can be shown that a more or less complex set of variables can be used to reduce every decision to a set of alternatives (as long as the number of states of the system is finite), according to [177]. Boolean algebra operating on binary variables is particularly useful to represent such problems, since the simplest reasoning behind the concept of an alternative is that either a decision is made or not, which is equivalent to 0–1 interpretation. A general nonlinear MIP (6.16) can be reformulated into the following linear program with binary variables [53]

$$
\begin{aligned}
\min_{x} \quad & c^T x \\
\text{s.t.} \quad & Gx \leq d \\
& Ax = b \\
& x_i \in \{0, 1\}, \quad i = 1, \ldots, n
\end{aligned}
\tag{6.71}
$$

where $x \in \{0, 1\}^n$ is the decision variable, $c \in \mathbb{R}^n$ is the cost function to be minimized, $G \in \mathbb{R}^{k \times n}$ and $A \in \mathbb{R}^{p \times n}$ are the constraint matrices, and $d \in \mathbb{R}^k$ and $b \in \mathbb{R}^p$ are the constraint vectors. An illustration of a binary linear program is presented in Example 6.4.

Example 6.4 (Payload Optimization)
There are seven types of goods that can be transported between a warehouse and a shop – their mass, volume, and profit are summarized below:

Payload Type	Mass $[kg]$	Volume $[m^3]$	Profit [\$]
1	400	0.9	300
2	600	2.3	700
3	900	2.5	200
4	1000	1.4	600
5	200	1.1	400
6	2000	3.6	1500
7	700	2.7	1100

Table 6.2: Numerical data for the payload optimization problem.

Only one type of each good can be carried by a truck such that its maximum payload capacity of 4100 *kg* and volume capacity of 11 *m³* are not exceeded. In addition, due to the safety reasons, cargo type 1 cannot be transported simultaneously with cargo type 2, and if cargo type 5 is taken, cargo type 3 has to be carried as well. The question is, which types of goods should be shipped from the warehouse to the shop so that the potential profit is maximized?

The problem is formulated as the following binary linear program

$$\min_{x} \quad \underbrace{-[300 \ 700 \ 200 \ 600 \ 400 \ 1500 \ 1100]}_{c^T_{(1\times7)}} \cdot \underbrace{\begin{bmatrix} x_1 \\ \dots \\ x_7 \end{bmatrix}}_{x_{(7\times1)}}$$

$$\text{s.t.} \quad \underbrace{\begin{bmatrix} 400 & 600 & 900 & 1000 & 200 & 2000 & 700 \\ 0.9 & 2.3 & 2.5 & 1.4 & 1.1 & 3.6 & 2.7 \end{bmatrix}}_{G_{(2\times7)}} \cdot \underbrace{\begin{bmatrix} x_1 \\ \dots \\ x_7 \end{bmatrix}}_{x_{(7\times1)}} \leq \underbrace{\begin{bmatrix} 4100 \\ 11 \end{bmatrix}}_{d_{(2\times1)}} \tag{6.72}$$

$$x_1 + x_2 = 1$$
$$x_5 - x_3 \leq 0$$
$$x_i \in \{0, 1\}, \quad i = 1, \dots, 7.$$

Problem (6.72) is implemented in YALMIP modeling language and solved using CPLEX solver as shown below.

```
% Data
mass = [400 600 900 1000 200 2000 700]; % [kg]
vol = [0.9 2.3 2.5 1.4 1.1 3.6 2.7]; % [m^3]
profit = [300 700 200 600 400 1500 1100]; % [$]

% Variables
x = binvar(7,1); % decision if cargo is taken or not (0-1)

% Objective
obj = -profit*x; % objective to maximize profit

% Constraints
const = [ mass*x <= 4100; % mass constraints
          vol*x <= 11; % volume constraints
          x(1) + x(2) == 1; % either 1 or 2 (XOR)
          x(5)-x(3) <= 0; % 5 -> 3 (IMPLY)
        ];

% Options
ops = sdpsettings('solver','cplex'); % select CPLEX solver

% Solution
sol = optimize(const,obj,ops); % solve the problem
solution = find(value(x))'; % indices of the optimal solution
total_profit = -value(obj); % total profit
total_mass = mass*value(x); % mass of the carried goods
total_vol = vol*value(x); % volume of the carried goods

% Output
solution =  1  4  6  7
total_profit = 3500
total_mass = 4100
total_vol = 8.6000
```

Therefore, to maximize the cost of the carried cargo and to avoid violating the payload and volume constraints, goods x_1, x_4, x_6, x_7 have to be transported by the truck. The total profit then becomes 3500 $.

Integer Programming

In applications where the modeled quantities are integers, the domain of (6.71) is expanded. Such applications normally involve problems associated with production rates (e.g. number of cars, houses etc.) or, in general, these, where fractional solutions are not acceptable (e.g. number of employees, capital budgeting, etc.) [177]. A binary linear program (BLP) (6.71) is rewritten as an integer linear program (ILP) [53]

$$
\begin{aligned}
\min_{x} \quad & c^T x \\
\text{s.t.} \quad & Gx \leq d \\
& Ax = b \\
& x_i \in \mathbb{Z}, \quad i = 1, \dots, n
\end{aligned}
\tag{6.73}
$$

only by changing the domain of the decision variable to integers $x \in \mathbb{Z}^n$ (the remaining symbols are defined as for (6.71)). Formulation of and solution strategy for a typical integer linear programming problem are shown in Example 6.5.

Example 6.5 (Production Optimization)
A paper mill produces rolls of paper in four different widths: 10 cm, 20 cm, 30 cm, and 40 cm. Each day, the paper mill is supposed to deliver to a customer at least

- 700 rolls of 10 cm width,
- 1500 rolls of 20 cm width,
- 1700 rolls of 30 cm width,
- 2300 rolls of 40 cm width.

Each paper roll that is used in the production process is 1 m wide and 100 m long. The paper mill can cut the raw rolls according to 8 different methods summarized below:

Cutting Method	Rolls				Wasted Width [m]
	10 cm	20 cm	30 cm	40 cm	
1	5	2	0	0	0.1
2	0	2	2	0	0
3	0	1	1	1	0.1
4	2	0	0	2	0
5	0	0	3	0	0.1
6	1	1	1	1	0
7	6	0	1	0	0.1
8	0	4	0	0	0.2

Table 6.3: Cutting methods, the corresponding amounts of produced rolls, and generated waste.

Task 1
The first objective is to minimize the total number of 1×100 m rolls required to meet the daily production goals. This problem can be formulated as the following integer linear program

$$
\min_{x} \quad \sum_{i=1}^{8} x_i
$$

$$
\text{s.t.} \quad \underbrace{\begin{bmatrix} 5 & 0 & 0 & 2 & 0 & 1 & 6 & 0 \\ 2 & 2 & 1 & 0 & 0 & 1 & 0 & 4 \\ 0 & 2 & 1 & 0 & 3 & 1 & 1 & 0 \\ 0 & 0 & 1 & 2 & 0 & 1 & 0 & 0 \end{bmatrix}}_{G_{(4 \times 8)}} \cdot \underbrace{\begin{bmatrix} x_1 \\ \dots \\ x_8 \end{bmatrix}}_{x_{(8 \times 1)}} \geq \underbrace{\begin{bmatrix} 700 \\ 1500 \\ 1700 \\ 2300 \end{bmatrix}}_{d_{(4 \times 1)}}
\tag{6.74}
$$

$$
\begin{aligned}
& x_i \in \mathbb{Z}, \quad i = 1, \dots, 8 \\
& x_i \geq 0, \quad i = 1, \dots, 8
\end{aligned}
$$

---

which is solved by using YALMIP and CPLEX as presented below.

```
% Data
rolls_10 = [5 0 0 2 0 1 6 4];   % number of 10cm-rolls from a 1m-roll
rolls_20 = [2 2 1 0 0 1 0 4];   % number of 20cm-rolls
rolls_30 = [0 2 1 0 3 1 1 0];   % number of 30cm-rolls
rolls_40 = [0 0 1 2 0 1 0 0];   % number of 40cm-rolls
waste = [0.1 0 0.1 0 0.1 0 0.1 0.2];  % wasted width of a 1m-roll [m]

% Variables
x = intvar(8,1); % number of standard 1m-rolls being cut in 8 different ways

% Objective
obj = sum(x); % minimize the number of standard 1m-rolls

% Constraints
const = [ rolls_10*x >= 700; % daily production goal #1
          rolls_20*x >= 1500; % daily production goal #2
          rolls_30*x >= 1700; % daily production goal #3
          rolls_40*x >= 2300; % daily production goal #4
          x >= 0; % only positive solution
        ];

% Options
ops = sdpsettings('solver','cplex'); % select CPLEX solver

% Solution
sol = optimize(const,obj,ops); % solve the problem
solution = value(x)'; % number of 1m-rolls cut in a given way
total_rolls = sum(value(x)); % optimal amount of 1m-rolls
total_waste = waste*100*value(x); % total waste [m^2]
% Particular numbers of produced rolls
rolls_10_no = rolls_10*value(x); % 10cm-rolls
rolls_20_no = rolls_20*value(x); % 20cm-rolls
rolls_30_no = rolls_30*value(x); % 30cm-rolls
rolls_40_no = rolls_40*value(x); % 40cm-rolls

% Output
solution =  0   750   0   1150   67   0   0   0
total_rolls = 1967
total_waste = 670
rolls_10_no = 2300
rolls_20_no = 1500
rolls_30_no = 1701
rolls_40_no = 2300
```

Given the daily production requirements, the most efficient ways of cutting the raw rolls into the final products are methods 2, 4, and 5. The least number of 1×100 *m* rolls that has to be processed by the paper mill is hence $1967 = 750 + 1150 + 67$. The particular amounts of produced rolls are:

- 10 *cm* rolls: 2300,

- 20 *cm* rolls: 1500,

- 30 *cm* rolls: 1701,

- 40 *cm* rolls: 2300,

and significantly exceed only the production goal for 10 *cm* rolls: $2300 > 700$.

Task 2
An interesting observation is made when instead of minimizing the total number of rolls, we minimize the total waste generated by the paper mill. To achieve that, the cost function of problem (6.74) is modified to be

$$\min_x \quad \underbrace{[0.1\ 0\ 0.1\ 0\ 0.1\ 0\ 0.1\ 0.2]}_{c^T_{(1\times 8)}} \cdot \underbrace{\begin{bmatrix} x_1 \\ ... \\ x_8 \end{bmatrix}}_{x_{(8\times 1)}} \qquad (6.75)$$

and the relevant portion of YALMIP code is updated as well:

```
% Objective
obj=waste*100*x; % minimize surface area of waste

% Output
solution =  0  850  0  1150  0  0  0  0
total_rolls = 2000
total_waste = 0
rolls_10_no = 2300
rolls_20_no = 1700
rolls_30_no = 1700
rolls_40_no = 2300
```

Indeed, the surface area of the wasted paper is 0 m^2. However, the total number of rolls required to achieve this objective is higher when compared to the case in which the goal was to minimize the amount of the required resource: 2000 vs. 1967 raw paper rolls, respectively. This is similar to the well-known more-for-less paradox in linear programming [76]. In the considered example, the daily production goals are achieved at lower expense when minimizing the cost (even though the waste is higher!) rather than when minimizing the waste. Of course, it is only a seeming paradox because the available methods of cutting raw paper rolls are what affect the solution. As expected, when minimizing the waste (i.e. increasing the efficiency), the overall production output should increase. This is confirmed by obtaining additional 200 20 cm rolls:

- 10 cm rolls: 2300,
- 20 cm rolls: 1700,
- 30 cm rolls: 1700,
- 40 cm rolls: 2300,

which could be e.g. sold to a different customer to increase the paper mill's income (which, depending on the price of 20 cm rolls, might potentially exceed the investment of using 33 extra 1×100 m rolls). This simple example illustrates superiority of the efficient utilization of goods (**Task 2**) over direct allocation approach (**Task 1**). Therefore, the optimal solution should always be understood to be optimal in the sense of given constraints and cost function.

Mixed Integer Programming

The most common problems which MIP helps to solve are these which involve not only some decision-making (e.g. whether to build a factory or not) but also quantification of optimization variables (e.g. to achieve a certain production output). Typical examples of application are crew assignment for airlines, electronic circuits design, development of telecommunication networks [177], or modeling and control of hybrid systems [39]. A mixed integer linear program (MILP) is obtained from (6.71) by letting some decision variables to be continuous [53]

$$\begin{aligned} \min_{x} \quad & c^T x \\ \text{s.t.} \quad & Gx \leq d \\ & Ax = b \\ & x \in \{0,1\}^{n_b} \cup \mathbb{R}^{n-n_b} \end{aligned} \quad (6.76)$$

where the index n_b denotes the number of binary optimization variables. Mixed integer linear programming problem is illustrated in Example 6.6. The same problem is then reformulated as a combinatorial binary linear program and solved in Example 6.7. Obviously, these examples are significantly simplified compared to a more realistic case study of drivetrain dimensioning presented in Chapter 10. Nevertheless, they present two common approaches for dealing with optimal selection of components from a discrete set of data, discussed in more detail in [215] and [270], respectively.

Example 6.6 (Motor and Gearbox Selection – Mixed Integer Approach)
Let us consider a simple actuation system composed of a motor and a gearbox, as presented in Table 5.1. A constant mechanical torque required by a driven machine is $T_{load} = 440 \ Nm$. The task of a design engineer is to select such a combination of a motor and a gearbox that will deliver the required torque and be as cheap as possible. For the sake of simplicity, only five motors ($k = 5$) are chosen to be available:

Motor Number	1	2	3	4	5
Rated Torque T [Nm]	2	5	10	20	30
Cost c [\$]	200	400	600	800	1000

Table 6.4: Set of available motors.

Therefore, the selection of a motor is a binary problem. The permissible gear ratio j_{gb} is real-valued and defined on an interval $j_{gb} \in [m, M]$ where $m = 30$ and $M = 180$. The cost of the gearbox is assumed to be proportional to its gear ratio

$$c_{gb} = \frac{10}{3} j_{gb}. \tag{6.77}$$

The necessary design condition is that the torque delivered by the drivetrain is equal to or exceeds the load torque

$$j_{gb} T_i \geq T_{load} \quad \text{where} \quad i = 1, 2, \ldots, 5. \tag{6.78}$$

By using the principles formulated in Section 6.4.1, an auxiliary real-valued variable $y_i = j_{gb} T_i x_i$ is introduced and the optimization problem is expressed as the following mixed integer linear program

$$\min_{x} \quad \underbrace{[200 \ 400 \ 600 \ 800 \ 1000]}_{c^T_{(1 \times 5)}} \cdot \underbrace{\begin{bmatrix} x_1 \\ \ldots \\ x_5 \end{bmatrix}}_{x_{(5 \times 1)}} + c_{gb}$$

$$\text{s.t.} \quad \sum_{i=1}^{5} y_i \geq T_{load}$$

$$\begin{bmatrix} y_1 \\ \ldots \\ y_5 \end{bmatrix} \leq 180 \cdot \begin{bmatrix} T_1 x_1 \\ \ldots \\ T_5 x_5 \end{bmatrix}$$

$$\begin{bmatrix} y_1 \\ \ldots \\ y_5 \end{bmatrix} \geq 30 \cdot \begin{bmatrix} T_1 x_1 \\ \ldots \\ T_5 x_5 \end{bmatrix}$$

$$\underbrace{\begin{bmatrix} y_1 \\ \ldots \\ y_5 \end{bmatrix}}_{y_{(5 \times 1)}} \leq j_{gb} \cdot \underbrace{\begin{bmatrix} T_1 \\ \ldots \\ T_5 \end{bmatrix}}_{T_{(5 \times 1)}} - 30 \cdot \underbrace{\begin{bmatrix} T_1 \cdot (1 - x_1) \\ \ldots \\ T_5 \cdot (1 - x_5) \end{bmatrix}}_{T(1-x)_{(5 \times 1)}} \tag{6.79}$$

$$\begin{bmatrix} y_1 \\ \ldots \\ y_5 \end{bmatrix} \geq j_{gb} \cdot \begin{bmatrix} T_1 \\ \ldots \\ T_5 \end{bmatrix} - 180 \cdot \begin{bmatrix} T_1 \cdot (1 - x_1) \\ \ldots \\ T_5 \cdot (1 - x_5) \end{bmatrix}$$

$$j_{gb} \in \mathbb{R} \ \cap \ j_{gb} \in [30, 180]$$

$$y_i \in \mathbb{R}, \quad i = 1, \ldots, 5$$

$$x_i \in \{0, 1\}, \quad i = 1, \ldots, 5$$

$$\sum_{i=1}^{5} x_i \leq 1$$

which is solved by implementing the code provided below in YALMIP modeling language.

```
% Data
T = [2 5 10 20 30]; % motor torque [Nm]
cost_T = [200 400 600 800 1000]; % motor cost [$]
T_load = 440; % required load torque [Nm]
```

```
% Variables
x = binvar(5,1); % binary variable for motor selection
j_gb = sdpvar(1,1); % continuous variable to find gear ratio
y = sdpvar(5,1); % auxiliary continuous variable y=j_gb*T'*x

% Objective
obj = cost_T*x+10/3*j_gb; %  minimize drivetrain cost

% Constraints
const = [ sum(y) >= T_load; % maintain the load torque
          y <= 180*T'.*x; % constraints to define variable y
          y >= 30*T'.*x;
          y <= j_gb*T'-30*T'.*(ones(5,1)-x);
          y >= j_gb*T'-180*T'.*(ones(5,1)-x);
          30 <= j_gb <= 180; % allowable gearbox ratios
          sum(x) <= 1; % no more than one motor is selected
        ];

% Options
ops = sdpsettings('solver','cplex'); % select CPLEX solver

% Solution
sol = optimize(const,obj,ops); % solve the problem
solution = find(value(x)); % index of the optimal motor
motor_torque = T(solution); % motor torque value
j_gearbox = value(j_gb); % selected gear ratio
drivetrain_torque = motor_torque*j_gearbox; % total delivered torque
total_cost = value(obj); % total cost

% Output
solution = 2
motor_torque = 5
j_gearbox = 88.0000
drivetrain_torque = 440
total_cost = 693.3333
```

The motor 2 characterized by the rated torque $T_2 = 5\ Nm$ is selected as the optimal choice. The gearbox ratio that in combination with the picked motor minimizes the drivetrain cost is found to be $j_{gb} = 88$. Either a manufacturer that produces such a gearbox has to be found, or a similar gear ratio has to be selected from the available suppliers. The latter solution would naturally require recomputation of the total provided torque and the total drivetrain cost. The drivetrain delivers the torque of $j_{gb} \cdot T_2 = 88 \cdot 5 = 440\ Nm$ which is exactly equal to the required mechanical torque. Of course, it is possible to include additional safety margins in the final design by constraining the delivered drivetrain torque to be e.g. a few percent greater than the load torque. The total cost of the designed system amounts to $c_2 + c_{gb} = 400 + 10/3 \cdot 88 = 693.33$ \$.

Example 6.7 (Motor and Gearbox Selection – Combinatorial Approach)
Instead of finding a continuous value of gear ratio, let us consider the case when, similarly to a motor, it has to be selected from catalogs (which is actually a more common scenario in industrial environment). Both the mechanical requirements and the list of motors to choose from are considered to be the same as in Example 6.6. In addition, the following six gearboxes ($k_{gb} = 6$) are available:

Gearbox Number	1	2	3	4	5	6
Gear Ratio j_{gb} $[-]$	30	60	90	120	150	180
Cost c_{gb} [\$]	100	200	300	400	500	600

Table 6.5: Set of available gearboxes.

The solution strategy is to evaluate all possible combinations n of motors and gearboxes and assign to each combination a binary variable $x_i, i = 1, 2, \ldots, n$. By doing so, rather than picking separately an optimal motor and an optimal gearbox, what is selected first is their optimal combination which, obviously, can be further decomposed to identify the particular motor and gearbox. In the considered example, the total number of possible solutions is $n = k \cdot k_{gb} = 5 \cdot 6 = 30$. Therefore, the cost of each combination ($c_{c,i}, i = 1, 2, \ldots, 30$) is found by adding the particular cost of a motor ($c_i, i = 1, 2, \ldots, 5$) and a gearbox

$(c_{gb,i}, i = 1, 2, \ldots, 6)$ and creating a vector of all possible costs. Similarly, the resulting torque values

$$T_c = j_{gb} \cdot T \tag{6.80}$$

are grouped in a vector $(T_{c,i}, i = 1, 2, \ldots, 30)$. Such a combinatorial problem can be formulated as the following integer linear program

$$
\min_{x} \quad \underbrace{[300\ 400\ 500\ 600\ 700\ 800\ 500\ \ldots\ 1600]}_{c_{c(1 \times 30)}^T} \cdot \underbrace{\begin{bmatrix} x_1 \\ \ldots \\ x_{30} \end{bmatrix}}_{x_{(30 \times 1)}}
$$

$$
\text{s.t.} \quad \underbrace{[60\ 120\ 180\ 240\ 300\ 360\ 150\ \ldots\ 5400]}_{T_{c(1 \times 30)}^T} \cdot \underbrace{\begin{bmatrix} x_1 \\ \ldots \\ x_{30} \end{bmatrix}}_{x_{(30 \times 1)}} \geq T_{load} \tag{6.81}
$$

$$x_i \in \{0, 1\}, \quad i = 1, \ldots, 30$$

$$\sum_{i=1}^{30} x_i \leq 1.$$

Clearly, (6.81) contains less inequality constraints than problem (6.79) and, in general, is simpler to formulate. The only difficulty is a systematic creation of vectors containing all possible combinations of torque, cost, etc. but, as shown below, this challenge is easily solved when implementing the optimization problem in software.

```matlab
% Data
j_gb = [30 60 90 120 150 180]; % gear ratio [-]
T = [2 5 10 20 30]; % motor torque [Nm]
cost_j_gb = [100 200 300 400 500 600]; % gearbox cost [$]
cost_T = [200 400 600 800 1000]; % motor cost [$]
T_load = 440; % required load torque [Nm]

% Evaluate all possible combinations
% Drivetrain torque
T_c_m = j_gb'*T; % matrix
T_c = T_c_m(:)'; % vector
% Combined cost
[X,Y] = meshgrid(cost_T,cost_j_gb);  % prepare vectors for adding their elements
cost_c_m = X+Y; % matrix
cost_c = cost_c_m(:)'; % vector

% Variables
x = binvar(numel(T_c),1); % binary variable for motor and gearbox selection

% Objective
obj=cost_c*x; % minimize drivetrain cost

% Constraints
const = [ T_c*x >= T_load; % maintain the load torque
          sum(x) <= 1; % no more than one combination is selected
        ];

% Options
ops=sdpsettings('solver','cplex'); % select CPLEX solver

% Solution
sol=optimize(const,obj,ops); % solve the problem
solution = find(value(x)); % index of the optimal combination
[sol_gearbox,sol_motor]=ind2sub(size(T_c_m),solution); % index of gearbox and motor
motor_torque=T(sol_motor); % motor torque value
j_gearbox=j_gb(sol_gearbox); % selected gear ratio
drivetrain_torque = motor_torque*j_gearbox; % total delivered torque
total_cost = value(obj); % total cost

% Output
solution = 9
sol_gearbox = 3
```

```
sol_motor = 2
motor_torque = 5
j_gearbox = 90
drivetrain_torque = 450
total_cost = 700
```

The combination that is found to be optimal is designated by the index $i = 9$. After decomposing it into particular indices of motors and gearboxes, it turns out that the same motor ($T_2 = 5\ Nm$) is selected as in Example 6.6. Also, the gearbox 3 picked from a discrete set of permissible gearboxes is characterized by the gear ratio $j_{gb,3} = 90$ which is close to $j_{gb} = 88$ found when solving mixed integer linear program (6.79). Consequently, the torque delivered by the current actuation system is 10 Nm greater than the required mechanical load. Finally, the total drivetrain cost is almost identical to the one computed in Example 6.6 (tabulated gearbox cost follows the previous relationship $c_{gb} = 10/3 \cdot j_{gb}$).

6.4.3 Solution Techniques

In general, mixed integer programs are non-convex which causes a significant difficulty to obtain their solutions [53]. MIP problems are categorized as NP-complete (non-deterministic polynomial-time complete), which means that in the worst case, the solution time would grow exponentially with the problem size [289]. There are several algorithms that are capable of solving these problems despite their combinatorial nature. Some of the most commonly used are [39]: cutting plane methods, decomposition methods, logic-based methods, brute force approach and branch and bound methods. The brute force approach is the most straightforward, whereas the branch and bound is the most efficient [53].

Brute Force Approach

Brute force method is illustrated on an example of the following mixed integer linear program

$$
\begin{aligned}
\min_{[x_c, x_b]} \quad & c_c^T x_c + c_b^T x_b \\
\text{s.t.} \quad & G_c x_c + G_b x_b \leq d \\
& x_c \in \mathbb{R}^{n_c}, x_b \in \{0, 1\}^{n_b}
\end{aligned}
\tag{6.82}
$$

where the notation follows the one of (6.16) and (6.71). When one of the binary variables $x_b \in \{0, 1\}^{n_b}$ is fixed, i.e. $\overline{x}_b$, the MILP becomes a linear program (LP) [53]

$$
\begin{aligned}
\min_{x_c} \quad & c_c^T x_c + \left(c_b^T \overline{x}_b \right) \\
\text{s.t.} \quad & G_c x_c \leq d - G_b \overline{x}_b \\
& x_c \in \mathbb{R}^{n_c}.
\end{aligned}
\tag{6.83}
$$

The solution strategy is to enumerate the 2^{n_b} integer values of the variable x_b and solve the resulting LPs. Comparison of the computed 2^{n_b} optimal objective functions yields the optimizer and the optimal cost of the original problem (6.82) [53].

Branch and Bound

The most widely used method for solving MIP problems is referred to as branch and bound [39]. The first step within this technique is to "relax" the binary constraints (i.e. $\{0, 1\} \rightarrow [0, 1]$). Then, the resulting optimization problem (linear or nonlinear) is solved and its solution is

considered to be the lower bound on the optimal cost [53]. The upper bound on the optimal cost is obtained by finding a feasible solution to the original problem. The branch and bound method chooses one of the variables that have non-integer solutions and "branches" to create two new subproblems in accordance with a tree search. A solution is considered to be improved, if it is constrained tighter than the others. The process is repeated until the final solution is found which meets all of the integer constraints [53]. Branch and bound algorithm is much more efficient than the brute force approach, as it allows to exclude from further exploration whole subtrees if the resulting subproblem is infeasible or if an integer solution is arrived at [53].

A comprehensive description of the branch and bound algorithm (and also its variations such as e.g. branch and cut method) can be found in any textbook on mixed integer programming, e.g. in [197] or [256]. In particular, book [110] gives a broad overview on algorithms to solve MIP problems.[13] The commercially available solver CPLEX is especially well-suited for solving mixed integer programming problems and it uses the branch and cut technique (refer to solver documentation [150] for additional information). As mentioned in Section 6.3.3, CPLEX solver is used in this thesis to solve an optimal drivetrain design problem presented in Chapter 10.

6.5 Nonlinear Optimization

The scope of this brief Section is not to thoroughly elaborate on various challenges related to nonlinear programming, but rather to communicate that solving nonlinear optimization problems is usually associated with the lack of guarantees on global optimality of the solution.[14] A popular area of application of optimization techniques is identification of unknown model's parameters based on full-scale data. Therefore, a case study of a nonlinear system is presented in Example 6.8 and a method for identifying its parameters is discussed in Example 6.9.

6.5.1 Basics

A general optimization problem can be formulated by rewriting (6.2) as [60]

$$
\begin{aligned}
\min_{x} \quad & f_0(x) \\
\text{s.t} \quad & f_i(x) \leq d_i, \ i = 1, \ldots, k.
\end{aligned}
\tag{6.87}
$$

All symbols are defined according to (6.6) except for the domain of variable x which is not constrained to be continuous here. Optimization problem (6.87) is referred to as a nonlinear program (NLP). In NLP, objective or constraint functions are not linear, but not known to be convex [60]. In general, NLPs are difficult to deal with and there are no universal (i.e. working no matter what) methods to solve (6.87).

Often, a compromise has to be made between accuracy of the solution and computational time. The methods that focus on local optimization are especially popular in some engineering applications where the benefit of achieving a "good enough" result is already significant [60]. However, apart from compromising on global optimality, local optimization methods require an initial guess which in many cases is critical and can strongly affect the local optimum. Therefore, using local optimization techniques requires experimenting with the selection of

---

13. There are other, strictly heuristic (metaheuristic), methods such as e.g. genetic algorithms, that aim to find a "good enough" solution to MIP problems, however, these methods give no guarantee on solution's optimality [256].

14. The reader interested in this particular subject is referred to textbooks on nonlinear optimization, e.g. [110, 197, 253, 256, 332].

Example 6.8 (LuGre Friction Model)

A representative and fairly popular example of a nonlinear system is the LuGre (Lund-Grenoble) friction model [68]. It captures the dynamic friction effects, such as varying breakaway force or hysteresis, by approximating friction as a phenomenon originating from contacting bristles [82]. The friction force F_{frict} in this model is expressed as [68]

$$F_{frict} = \sigma_0 z + \sigma_1 \frac{dz}{dt} + \sigma_2 v \qquad (6.84)$$

$$\frac{dz}{dt} = v - \frac{|v|}{g(v)} z \qquad (6.85)$$

where z denotes the average deflection of the bristles, σ_0 is the bristle stiffness, σ_1 is the damping coefficient, and σ_2 is the viscous coefficient. Function g is selected so that it describes the Stribeck effect, namely

$$g(v) = \frac{1}{\sigma_0} \left(F_C + (F_S - F_C) \exp \left(- \left(\frac{v}{v_s} \right)^2 \right) \right) \qquad (6.86)$$

where F_C is the Coulomb friction, F_S is the stiction force, and v_s is the Stribeck velocity. Parameters σ_2, F_C, F_S, and v_s describe static friction effects, whereas parameters σ_0 and σ_1 characterize dynamic friction.

(a) Speed. **(b)** Friction force. **(c)** Hysteresis loop.
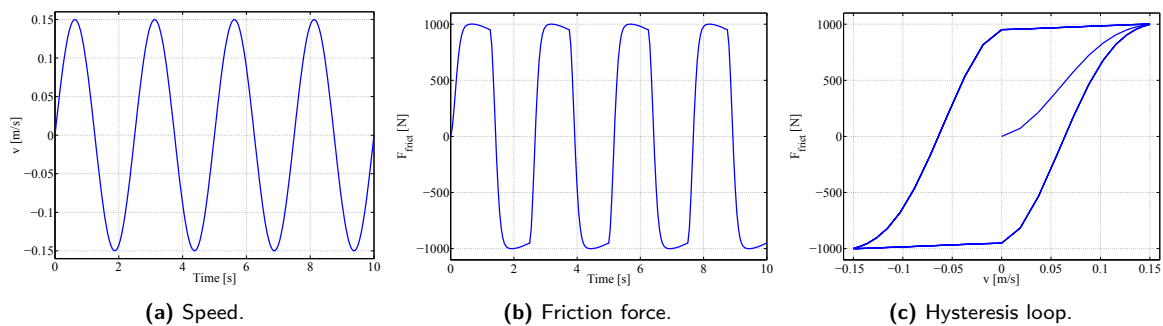
Figure 6.1: Reference data set used for identification of the LuGre model's parameters.

Numerical values of the LuGre model's parameters considered in this Example are assumed based on [82] and are slightly modified as summarized below:

Parameter	σ_0 [N/m]	σ_1 [Ns/m]	σ_2 [Ns/m]	F_c [N]	F_s [N]	v [m/s]
Value	100000	1050	350	1450	950	0.005

Table 6.6: Reference parameters of the LuGre friction model – adapted from [82].

An arbitrary speed profile $v = 0.15 \cdot \sin(2\pi t \cdot 0.4)$ m/s shown in Fig. 6.1a is selected as an input to (6.84) and the resulting friction force together with the obtained hysteresis loop are illustrated in Figs. 6.1b and 6.1c, respectively. These plots serve as reference data in Examples 6.9 and 6.10 to evaluate feasibility of different parameters identification techniques. The metrics used to quantify the accuracy of the models to reproduce field data are discussed in Remark 6.2 and the general identification strategy adopted in Examples 6.9 and 6.10 is briefly commented on in Remark 6.3.

algorithm, tuning its parameters, and picking the right starting point. According to [60], this resembles more art than technology and the author of this thesis has nothing more to add to this statement.

In some cases, however, a global solution of (6.87) can be found at the cost of efficiency. According to [60], a typical engineering application is verification of a safety-critical system in which optimization problem (6.87) is the problem of finding worst case values of the systems' parameters. If they are acceptable in a given process or design, the system can be certified as

safe (relative to parameter variations).

In this thesis, finding solutions of nonlinear optimization problems is handled in two ways: 1) when solving a nonlinear optimization problem in Chapter 11, the goal is to find the solution that is "sufficiently good" and 2) when dimensioning an electric drivetrain in Chapter 10, a set of assumptions and limitations is introduced to linearize the default nonlinear optimization problem in order to arrive at the global optimum.

Remark 6.2. *Fidelity of estimated data can be conveniently evaluated by using two popular metrics: variance accounted for (VAF) and root-mean-square error (RMSE) [266]. According to [28] and [301], VAF is defined as*

$$VAF = \left(1 - \frac{var(y_i - \hat{y}_i)}{var(y_i)} \right) \cdot 100 \ \% \tag{6.88}$$

where y_i is the reference signal, $\hat{y}_i$ is the estimated signal, and var is defined as variance of signal (also known as square of standard deviation)

$$var(y) = \frac{1}{n-1} \sum_{i=1}^{n} (y_i - \bar{y})^2 \tag{6.89}$$

where $\bar{y} = \frac{1}{n} \sum_{i=1}^{n} y_i$. The formula for RMSE is well-known

$$RMSE = \sqrt{\frac{\sum_{i=1}^{n} (y_i - \hat{y}_i)^2}{n}} \tag{6.90}$$

and is composed of both the sum of squared errors

$$SSE = \sum_{i=1}^{n} (y_i - \hat{y}_i)^2 \tag{6.91}$$

and the mean squared error

$$MSE = \frac{1}{n} \sum_{i=1}^{n} (y_i - \hat{y}_i)^2 . \tag{6.92}$$

For VAF being equal to 100 %, the fit of experimental or simulation results to reference data logs is assumed to be perfect [266]. On the other hand, RMSE represents an average deviation between the observed and predicted values given in the units of measurement. Consequently, the predicted signal is considered to be identical to the reference one if $RMSE = 0$. In addition, keeping track on the relative percentage error

$$y_i^{err} = \frac{y_i - \hat{y}_i}{max(|y|)} \cdot 100 \ \% \tag{6.93}$$

might give a better insight into the error signal itself – i.e. whether it is growing over time or stays within the given limits. Normalizing the error to the maximum absolute value of signal, $max(|y|)$, can equally well be replaced by normalizing it to e.g. its mean value $\bar{y}$, depending on the application.

6.5.2 Solution Methods

Finding a locally optimal solution of a convex optimization problem is equivalent to discovering its global optimum, as discussed in Section 6.2. Typical examples of such problems are LP, QP, but also NLP problems with convex objective function and constraints. However, when NLP problems are non-convex, finding their solution becomes a complicated task. Not only

because there might be local optima shadowing truly optimal solution but also due to the computational demands that grow rapidly with complexity of the problem [53].

Numerical methods for solving unconstrained NLP problems can be broadly classified into two main groups, depending on whether the derivative information of the optimization problem is required or not [224]. Methods based on function evaluations (e.g. Nelder-Mead search method [242]) are practical only if a problem is characterized by many discontinuities and is highly nonlinear. On the other hand, gradient-based methods perform much better if the derivatives (first order for general gradient method and second order for Newton's method) of the minimized function are continuous.

Constrained optimization problems are usually converted to simpler subproblems which are solvable and serve as the basis of an iterative process [224]. Techniques that involve using a penalty function and solving a sequence of unconstrained optimization problems are considered to be inefficient nowadays (recall barrier methods from Section 6.3.2). The techniques that are more common are called interior point methods. They are based on primal-dual algorithms which involve numerical evaluation of KKT optimality conditions and offer improved performance when compared to barrier methods [53].

According to [224], some of the most common algorithms for solving constrained and unconstrained nonlinear optimization problems are:

- Unconstrained NLP:
    - Quasi-Newton – avoids computing Hessian ∇^2 numerically,
    - Nelder-Mead – heuristic search method,
    - trust region – approximates minimized function in its neighborhood.

- Constrained NLP:
    - interior point – solution of KKT conditions,
    - active set – finds optimum by evaluation of active constraints,
    - sequential quadratic programming (SQP) – mimics Newton's method for unconstrained optimization.

Description, advantages, and drawbacks of each method can be found in the literature on numerical methods in optimization (e.g. in [53, 224, 253, 354]) and are omitted here. As described in Section 6.3, the two most prominent methods for solving constrained optimization problems are active set and interior point methods. In this thesis, MATLAB optimization toolbox [224] and function `fmincon` with interior point algorithm are applied to solve the parameters identification problem formulated as NLP, as shown in Chapter 11.

Remark 6.3. *Even though the static friction parameters σ_2, F_C, F_S, and v_s of the LuGre model (6.84) can be identified separately by performing static friction tests, in Examples 6.9 and 6.10 both static and dynamic parameters are identified simultaneously to better illustrate capabilities of the discussed estimation techniques.*

6.6   Feedforward Neural Network

Apart from the optimization methods discussed above, a popular approach to deal with estimation and identification problems is to apply artificial neural networks, as mentioned in Section 2.5.4. Therefore, although artificial neural networks are not classified as optimization

Example 6.9 (Parameters Identification as Nonlinear Optimization Problem)
Details on how to implement a nonlinear optimization problem for parameters identification are presented in Chapter 11 and are omitted here. The main point is to minimize the sum of squared errors (SSE) between the reference and estimated signals to find such parameters of the model that produce the model's output as similar to the original one as possible.
Here, the friction force from Example 6.8 is corrupted with some white Gaussian noise and is used as reference data in the optimization problem. The solution strategy is to apply the `fmincon` solver with the interior-point algorithm from MATLAB optimization toolbox [224]. In the considered scenario, the solution was found after 81 iterations when the size of the last change in location where the objective function was evaluated (the so-called step size tolerance) went below the requested tolerance. In such a case, there is a possibility of achieving a local minimum, since the first-order optimality measure (based on KKT conditions and thoroughly explained in [253]) is not less than the desired optimality tolerance [224].
The friction force predicted by the identified model is illustrated in Figs. 6.2a and 6.2b and closely reproduces the reference signal. Fig. 6.2c shows the relative percentage error between the reference and estimated friction profiles which does not exceed 8 % of the maximum force during the entire duration of simulation.

| (a) Force. | (b) Hysteresis loop. | (c) Relative percentage error. |
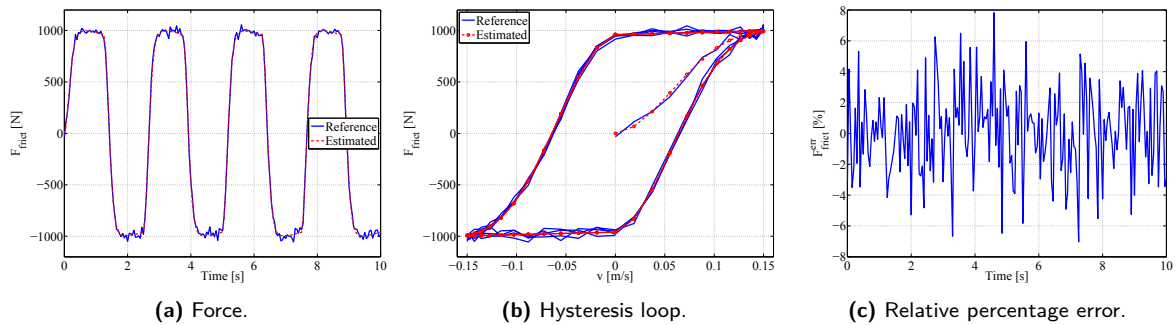
Figure 6.2: Identification results of the LuGre model's parameters based on nonlinear programming.

Exact values of the LuGre model's parameters identified in this Example are listed below:

Parameter	Reference	Estimated	Estimation Interval
$\sigma_0 \; [N/m]$	100000	103660	$0 - 110000$
$\sigma_1 \; [Ns/m]$	1050	867	$0 - 10000$
$\sigma_2 \; [Ns/m]$	350	246	$0 - 3000$
$F_c \; [N]$	1450	2723	$0 - 3000$
$F_s \; [N]$	950	960	$0 - 2000$
$v_s \; [m/s]$	0.005	0.003	$0 - 1$

Table 6.7: Parameters of the LuGre friction model estimated by nonlinear programming.

Even though some estimated parameters (especially $\hat{F}_C$) diverge from the reference values, the estimated friction force accurately replicates the original friction profile. The upper and lower bounds of the parameters have to be indicated together with the initial values (all set to 1 in this Example) in order for the solver to proceed with the optimization routine [224].
Finally, the accuracy of the established model is evaluated by using the following metrics:

VAF [%]	RMSE [N]
99.9	29.6

Table 6.8: Numerical assessment of parameters estimation results' fidelity.

The original friction force is ideally reproduced by the estimated model (VAF is almost 100 % and RMSE is low and mainly attributed to the Gaussian noise). This indicates the potential of the proposed strategy to sufficiently well identify models of nonlinear systems when the focus is on the overall response rather than on particular parameters.

techniques, fundamental information is provided here regarding a particular class of ANNs especially suited for identification purposes: a feedforward neural network.

A multi-layer perceptron network (also-called feedforward back-propagation network, abbreviated simply as FNN) is widely used for approximation problems (see for instance [128] or [368]).[15] Typically, an input layer, several hidden layers, and output layer are building blocks of the network. All nodes (i.e. neurons) are connected with each other in a sequential manner along the layers. The output of a single neuron is equal to [66]

$$s_j = \sum_{i=1}^{N} w_{ji}x_i + b_j. \tag{6.94}$$

A complete list of transfer functions that can be used inside a single neuron is given in [66]. In this thesis, the sigmoid activation function

$$y_j = f(s_j) = \frac{1}{1 + e^{-s_j}} \tag{6.95}$$

is applied in hidden layers together with a linear function in the output layer. According to [130], such a configuration provides for efficient approximation of functions with minor discontinuities. The back-propagation algorithm (BPA) is used to adjust the weights of the connections in the network [302]. It utilizes a gradient descent optimization method known as the delta rule which is described by the following equations ([66] and [275])

Delta rule: $\quad \Delta w_{ji}(t_k) = \eta\delta_j x_i$ $\tag{6.96}$

New weight: $\quad w_{ji}(t_k) = w_{ji}(t_{k-1}) + \Delta w_{ji}(t_k)$ $\tag{6.97}$

Output layer: $\quad \delta_j = y_j(1 - y_j)(d_j - y_j)$ $\tag{6.98}$

$$J = \frac{1}{2}\sum_{j=1}^{M}(d_j - y_j)^2 \tag{6.99}$$

Other layers: $\quad [\delta_j]_l = [y_j(1 - y_j)]_l \left[\sum_{j=1}^{N} w_{ji}\delta_j\right]_{l+1}$ $\tag{6.100}$

where x_i – inputs, w_{ji} – weight value for jth layer and ith input, Δw_{ji} – weight increment, b_j – bias for a neuron, d_j – desired outputs, y_j – actual outputs, M – total number of neurons, N – total number of inputs, t – time instant, k – indexing variable, J – performance index (cost function) – here represented as a mean squared error (MSE), f – activation function, η – learning rate, and l – particular layer's index. The weights are adjusted for a given set of inputs. Then, for new inputs the information is fed forward through the network again to compute the errors at the output layer. The BPA process continues until one of the following criteria is met [66]: 1) the cost function J reaches an acceptable value; 2) a maximum iteration count is exceeded; 3) a training-time period is exceeded. There is obviously a risk that local minima might be achieved if conditions no.2 or no.3 are met. In these cases, the BPA should be restarted and if the obtained results are still not satisfactory, another training set should be used [66]. Similarly, the cost function might not reach the goal value but settle at a different point if no improvement in data accuracy is observed for a given number of consecutive iterations.

A demonstration of application of FNN to parameters identification is presented in Example 6.10. In this thesis, MATLAB neural networks toolbox [223] is used to implement and solve neural networks problems.

---

15. This Section is partially based on publication [267].

Example 6.10 (Parameters Identification Using Feedforward Neural Network)
To illustrate how an FNN can be used to estimate parameters of a model, let us consider the same workflow and ANN as presented in Chapter 7. The LuGre model from Example 6.8 is used to provide the reference data for network training and simulation. To make the data more realistic (and the identification process more difficult), the friction force from Fig. 6.1b is corrupted with some white Gaussian noise. For network training, the maximum iteration count is set to 100 with the goal objective function $MSE^\star = 0$. In the considered example, the network training stopped quite fast, only after 13 iterations, since the MSE did not reach the goal 0 value and no improvement in further minimizing it was achieved after 5 validation checks.
The friction force estimated by the established model is illustrated in Figs. 6.3a and 6.3b and closely tracks the reference profile. Fig. 6.3c shows the relative percentage error between the reference and estimated signals which stays within 10 % of the maximum force during the entire duration of simulation.
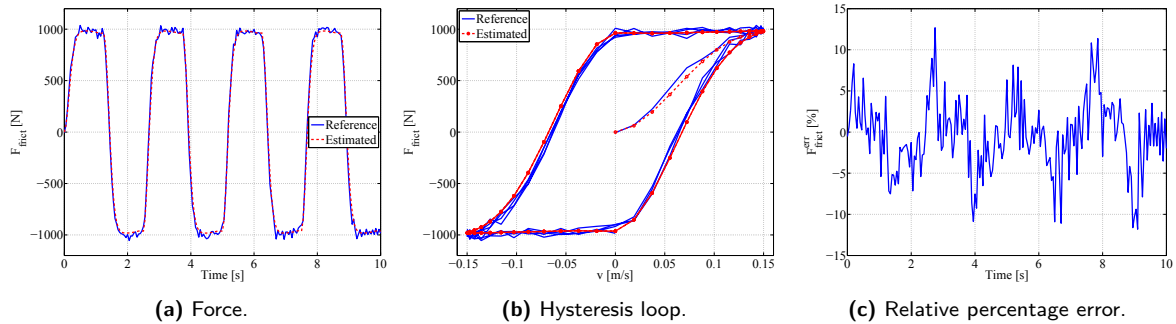

| (a) Force. | (b) Hysteresis loop. | (c) Relative percentage error. |

Figure 6.3: Identification results of the LuGre model's parameters based on FNN.

Specific parameters of the LuGre model identified by the FNN are listed below:

Parameter	Reference	Estimated	Estimation Interval
$\sigma_0 \ [N/m]$	100000	94897	$90000 - 110000$
$\sigma_1 \ [Ns/m]$	1050	740	$700 - 1100$
$\sigma_2 \ [Ns/m]$	350	234	$150 - 650$
$F_c \ [N]$	1450	1242	$1200 - 1500$
$F_s \ [N]$	950	949	$800 - 1100$
$v_s \ [m/s]$	0.005	0.020	$0.001 - 0.021$

Table 6.9: Parameters of the LuGre friction model estimated by FNN.

It is observed that although there are some minor differences between the reference and estimated parameters, the response of the established friction model correctly reproduces the original friction force. The so-called estimation interval has to be specified by the user in order for the FNN to know from which range of parameters it can pick the solutions [223]. For the solution to converge, the intervals above are selected in the trial and error method and are much tighter than the ones shown in Example 6.9. Obviously, this is the limitation of this approach, since a relatively strict approximation of parameters is required *a priori* before running the actual identification routine. This is not practical in cases when no such knowledge is available or when it is required not only to accurately reproduce the model's output but also to find exact model's parameters.
Finally, the performance metrics of the identified model are computed to be:

VAF [%]	**RMSE** [N]
99.7	45.5

Table 6.10: Numerical assessment of parameters estimation results' fidelity.

High value of VAF and relatively low value of RMSE (compared to the maximum friction force) obtained in this Example demonstrate that parameters of nonlinear models can be estimated by using the ANN-based methods.

6.7   Discussion

The most important observations coming from the analysis of Examples 6.6, 6.7, 6.9, and 6.10 are briefly discussed below.

6.7.1   Optimal Design Problems

Example 6.6 presents a solution of a design optimization problem based on reformulation of the original problem into a set of mixed integer linear inequalities. A similar approach to design optimization is adopted e.g. in [215]. It is undoubtedly efficient and, in general, it allows for solving nonlinear mixed integer programs. However, as Example 6.6 shows, even a relatively simple problem requires a rather extensive mathematical formulation when following this technique. Not to mention a tedious process of implementing the optimization problem in a solver software when no modeling language is used.

Therefore, the same problem of drivetrain dimensioning is presented in Example 6.7, but this time, a more straightforward solution strategy is proposed. This attractive alternative is to investigate all possible solutions. Then, the solver finds these that are feasible and selects the one that offers the lowest objective function. Such an approach seems to be more practical in applications where the number of variables is not too high and there are no strict demands on computational time (for drivetrain dimensioning it does not matter if the optimal configuration of components is found within 1 *s* or 1 *h*). Both methods require approx. 100 *ms* to arrive at the solution on a desktop PC given the exemplary numerical data. Although (6.81) looks less complex than (6.79), a possible mitigation of computational effort should not be taken for granted in this case, as it is typically the number of variables, not constraints, that make MIP more demanding for a solver [53]. An illustration on how to solve a more realistic design optimization problem using this approach is presented in Chapter 10.

6.7.2   Parameter Estimation Problems

Error signals, VAF, and RMSE of the identified friction models are similar to each other regardless of the applied estimation technique. Whether it is the approach based on nonlinear optimization programming shown in Example 6.9 or the FNN-based estimation technique illustrated in Example 6.10, the simulated models closely track the reference data. In both cases, however, the identified parameters are not unique: each time the neural network is simulated or the optimization problem solved, a different set of friction model's parameters is produced (even without Gaussian noise). This is attributed to the local optimality limitation of both estimation methods discussed in Section 6.5.1. However, the differences between values of parameters arrived at in various simulation runs are much smaller when using the `fmincon` function (it has higher "repeatability"). Also, in this case, the lower and upper bounds on parameters do not have to be as tight as when using the FNN-based method. Therefore, formulating a parameters estimation problem as a nonlinear optimization problem seems to be more accurate, practical, and do not require precise knowledge about the physical system *a priori*. Evaluation of both neural networks and nonlinear programming techniques to identify parameters of nonlinear models based on real-world data is presented in Chapters 7 and 11, respectively.[16]

---

16. After the FNN-based method was found to be insufficient in Chapter 7, the nonlinear optimization programming was used for a different problem in Chapter 11.

Part III

Modeling, Simulation, and Control of Electric Drivetrains in Offshore Drilling Applications

7 Assessment of Machine Load Torque

As discussed in the brief survey in Section 2.3.2, one of the main design objectives for electric drivetrains operating in offshore drilling equipment is to keep them as small, yet as effective, as possible, to minimize space they occupy on drill floor and maximize their performance.[17] However, practical experience shows that typically choices made by design engineers are too conservative due to the lack of enough data characterizing load conditions. This results in too costly and too heavy selected components. Therefore, in this Chapter, we present a method to estimate required full-scale motor torque using a scaled-down experimental setup presented in Section A.1 and its computational model. The gripper arm of the offshore vertical pipe handling machine introduced in Section A.4 is selected as a case study for which the practical significance of this work is demonstrated. The presented method has a potential to aid design of electrically actuated offshore drilling equipment and help design engineers choose correctly dimensioned drivetrain components.

7.1 Modeling and Control of Induction Motor

7.1.1 Perfect Field Orientation

The experimental IMs from Section A.1 are modeled using the inverse-Γ-equivalent circuit introduced in Section 4.3.2. The set of equations that describe motor behavior in synchronous reference frame is obtained by substitution of

$$\mathbf{i}_R^s = \mathbf{i}_M^s - \mathbf{i}_s^s = \frac{\mathbf{\Psi}_R^s}{L_M} - \mathbf{i}_s^s \tag{7.1}$$

together with (4.39) and (4.40) in (4.37) and (4.38), according to [132]

$$L_\sigma \frac{d\mathbf{i}_s}{dt} = \mathbf{u}_s - (R_s + R_R + j\omega_1 L_\sigma)\mathbf{i}_s + \left(\frac{R_R}{L_M} - j\omega_r\right)\mathbf{\Psi}_R \tag{7.2}$$

$$\frac{d\mathbf{\Psi}_R}{dt} = R_R\mathbf{i}_s - \left(\frac{R_R}{L_M} + j\omega_2\right)\mathbf{\Psi}_R \tag{7.3}$$

where $\mathbf{i}_s = i_{sd} + ji_{sq}$ is the stator current vector, $\mathbf{u}_s = u_{sd} + ju_{sq}$ is the stator voltage vector, $\mathbf{\Psi}_R = \psi_{Rd} + j\psi_{Rq}$ is the rotor flux vector, $\omega_1 = \omega_s$ is the stator frequency, $\omega_2 = \omega_1 - \omega_r$ is the slip frequency. Parameters of the model are defined as in Fig. 4.4. Under the assumption of perfect field orientation, described in Section 4.4.3, the (d, q) reference frame is aligned with the rotor flux of the induction motor, so that $\mathbf{\Psi}_R$ becomes real-valued: $\mathbf{\Psi}_R = \psi_{Rd}$ and $\psi_{Rq} = 0$. The electromagnetic torque equation is expressed in terms of current and flux as (recall Remark 4.1) [132]

$$T_{em} = \frac{3}{2}p\left(\psi_{Rd}i_{sq}\right). \tag{7.4}$$

---

17. This Chapter is reproduced (with minor changes) from publication [266].

Finally, the equation of motion of the induction motor (4.41) is rewritten here for convenience

$$T_a = J\frac{d\omega_m}{dt} = T_{em} - T_{ext} - T_{frict}.$$ (7.5)

According to [132], it can be shown that the actual and reference d-axis rotor fluxes are, respectively (in the constant flux region):

$$\psi_{Rd} = \frac{i_{sd}L_M}{1 + s\tau_r}$$ (7.6)

$$\psi_{Rd}^{ref} = \left| \frac{L_M}{1 + j\omega_2\tau_r} \right| I_n$$ (7.7)

where s is the Laplace variable, $\tau_r = L_M/R_R$ is the rotor time constant, and I_n is the rated motor current. By keeping the rotor flux ψ_{Rd} constant, the torque developed by the motor (7.4) can be controlled by adjusting the value of i_{sq}. The speed of the oriented (d, q) frame is obtained from (4.52) and, for the inverse-Γ-equivalent circuit, becomes

$$\omega_1 = \frac{d\theta_1}{dt} = \omega_r + \omega_2$$ (7.8)

$$\omega_1 = p\omega_m + R_R\frac{i_{sq}}{\psi_{Rd}}.$$ (7.9)

Therefore, to model induction motor in the oriented frame, it is sufficient to substitute (7.9) and $\Psi_R = \psi_{Rd}$ in (7.2) and (7.3). The discussed control strategy could easily be expanded by adding the speed control loop which is included in the schematics shown in Fig. 7.1. To convert the measured currents to (d, q) reference frame (and vice versa) Park transformations (4.21) and (4.22) are used. Finally, the desired voltage levels u_{sa}^{ref}, u_{sb}^{ref}, and u_{sc}^{ref} are passed to the pulse width modulation (PWM) and switching logic sections which control the motor.
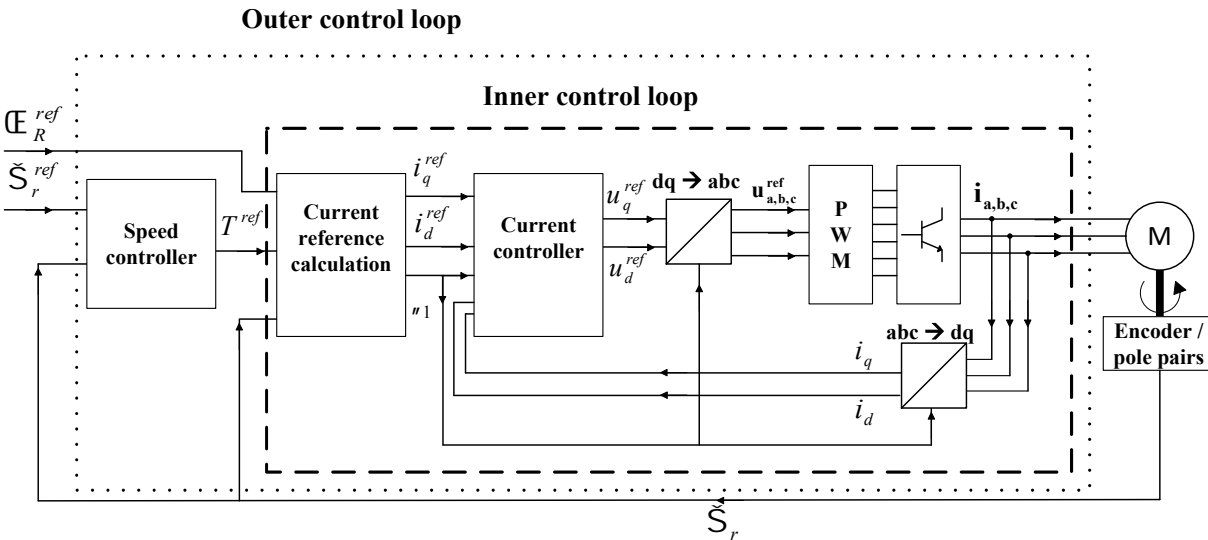

Figure 7.1: Indirect field-oriented control of induction machine [267].

7.1.2 Mechanical Friction

Friction plays an essential role in control systems design, according to [68]. It can lead to many unwanted phenomena such as tracking errors or undesired stick-slip motion. To find the most

suitable friction representation for an induction motor, two approaches are analyzed: static and dynamic friction. For a static model, a simple Coulomb and viscous friction is studied, whereas for a dynamic model, a popular LuGre friction is selected for benchmarking purposes.

Static Friction

There is evidence [268] that even a simplified friction model (only Coulomb) satisfactorily describes combined friction phenomenon for a setup composed of an induction motor and a mechanical system. However, sign (signum) function typically present in this model does not provide for smooth enough detection of velocity direction switching as it has discontinuity at zero speed. Therefore, it is decided to use tanh (hyperbolic tangent) function for this purpose, as it allows for both smoother transition between speed directions and adjustment of slope close to zero. Hence, the static friction model becomes:

$$T_{frict,static} = \begin{cases} \tanh\left(k\omega_m\right)\left(|\omega_m|\, b_{neg} + T_{C,neg}\right) & \text{if } \omega_m \leq 0 \\ \tanh\left(k\omega_m\right)\left(|\omega_m|\, b_{pos} + T_{C,pos}\right) & \text{if } \omega_m > 0 \end{cases} \tag{7.10}$$

where b is viscous coefficient and T_C is Coulomb friction torque, both defined for negative and positive speeds. Factor k controls the slope of the tanh function in the vicinity of zero speed, so, in other words, it determines how fast the friction model responds to changes in velocity direction.

Dynamic Friction

As already discussed in Example 6.8, LuGre model captures most friction phenomena that are of interest for feedback control, according to [68] and [205]. For convenience, the translational model from Example 6.8 is reformulated here to become applicable to rotational systems. The varying friction torque T_{frict} from (7.5) characterized by the LuGre friction model is expressed as [68]

$$T_{frict,dynamic} = \sigma_0 z + \sigma_1 \frac{dz}{dt} + \sigma_2 \omega_m \tag{7.11}$$

$$\frac{dz}{dt} = \omega_m - \frac{|\omega_m|}{g(\omega_m)} z \tag{7.12}$$

where z denotes the average deflection of the bristles, σ_0 is the bristle stiffness, σ_1 is the damping coefficient, and σ_2 is the viscous coefficient. Function g is selected so that it describes the Stribeck effect, namely:

$$g(\omega_m) = \frac{1}{\sigma_0}\left(T_C + (T_S - T_C)\exp\left(-\left(\frac{\omega_m}{\omega_s}\right)^2\right)\right) \tag{7.13}$$

where T_C is the level of Coulomb friction, T_S is the value of the stiction torque, and ω_s is the Stribeck velocity.

7.2 Friction Parameters Identification

7.2.1 Static Friction

To identify parameters of the Coulomb and viscous friction model (7.10), the well-known method of running a motor at a constant speed and monitoring the corresponding torque is

applied. The static friction identified for the experimental setup is illustrated in Fig. 7.4a. Static friction parameters are identified using the least squares estimation technique characterized by the following equations

$$T_{frict} = b\omega_m + T_C \tag{7.14}$$

$$= \begin{bmatrix} \omega_m & 1 \end{bmatrix} \begin{bmatrix} b \\ T_C \end{bmatrix}$$

$$\begin{bmatrix} T_{frict,1} \\ T_{frict,2} \\ T_{frict,3} \\ ... \\ T_{frict,n} \end{bmatrix} = \begin{bmatrix} \omega_{m,1} & 1 \\ \omega_{m,2} & 1 \\ \omega_{m,3} & 1 \\ ... \\ \omega_{m,n} & 1 \end{bmatrix} \begin{bmatrix} b \\ T_C \end{bmatrix}. \tag{7.15}$$

which could be expressed as

$$\mathbf{T}_{frict} = \mathbf{\Phi}\mathbf{q} \tag{7.16}$$

where vector $\mathbf{T}_{frict}$ contains all values of friction torque recorded during the experiment (n samples) and vector $\mathbf{q}$ stores the parameters to be identified. The identification process itself is conducted by performing the following matrix operations (recall linear least squares estimation discussed in Section 6.2.2)

$$\mathbf{\Phi}^T\mathbf{T}_{frict} = \mathbf{\Phi}^T\mathbf{\Phi}\mathbf{q} \tag{7.17}$$

$$\left(\mathbf{\Phi}^T\mathbf{\Phi}\right)^{-1}\mathbf{\Phi}^T\mathbf{T}_{frict} = \mathbf{q}. \tag{7.18}$$

Friction parameters $\mathbf{q}$ are found by computing the product of the so-called pseudo-inverse matrix $\left(\mathbf{\Phi}^T\mathbf{\Phi}\right)^{-1}\mathbf{\Phi}^T$ and friction torque values $\mathbf{T}_{frict}$. The term $\tanh(k\omega_m)$ is omitted here, as it has no influence on identified parameters. Also, the identification process is performed separately for the negative speed range, yielding b_{neg} and $T_{C,neg}$, and for the positive speed range, yielding b_{pos} and $T_{C,pos}$. Parameters identified for the scaled-down experimental setup from Section A.1 are summarized in Table 7.1. As shown in Fig. 7.4a, in the vicinity of zero speed there is observed the Stribeck effect. However, to keep the friction model easy to implement in a virtual modeling software, this phenomenon is neglected. Another reason for this is that in the scope of the current work it is primarily to reproduce the conditions when the VPR gripper arm motors run with higher speeds and are outside of the region where the Stribeck effect occurs.

Parameter	Value
Viscous friction coefficient (negative speed) b_{neg}	$1.92 \cdot 10^{-4}$ [Nm s/rad]
Coulomb friction (negative speed) $T_{C,neg}$	$-9.50 \cdot 10^{-3}$ [Nm]
Viscous friction coefficient (positive speed) b_{pos}	$1.96 \cdot 10^{-4}$ [Nm s/rad]
Coulomb friction (positive speed) $T_{C,pos}$	$1.24 \cdot 10^{-2}$ [Nm]

Table 7.1: Identified parameters of the Coulomb and viscous model for the development platform motors [266].

7.2.2 Dynamic Friction

A method to identify parameters of a dynamic friction model is based on [267]. We assume that for the dynamic friction model the positive static friction parameters are used wherever

applicable (namely, $\sigma_2 = b_{pos}$ and $T_C = T_{C,pos}$), since differences among absolute values of these parameters depending on the speed range are not significant (recall Table 7.1). In addition, the parameters describing the Stribeck effect (T_S and ω_s) are identified from the static friction curve illustrated in Figure 7.4a. The remaining two dynamic friction parameters (σ_0 and σ_1) are identified using the approach based on artificial neural networks. The theoretical background on feedforward back-propagation neural network is given in Section 6.6. Steps illustrated in Fig. 7.2 are to be followed to establish, train, and validate the FNN in order to make it capable of identifying parameters of the LuGre dynamic friction model. The
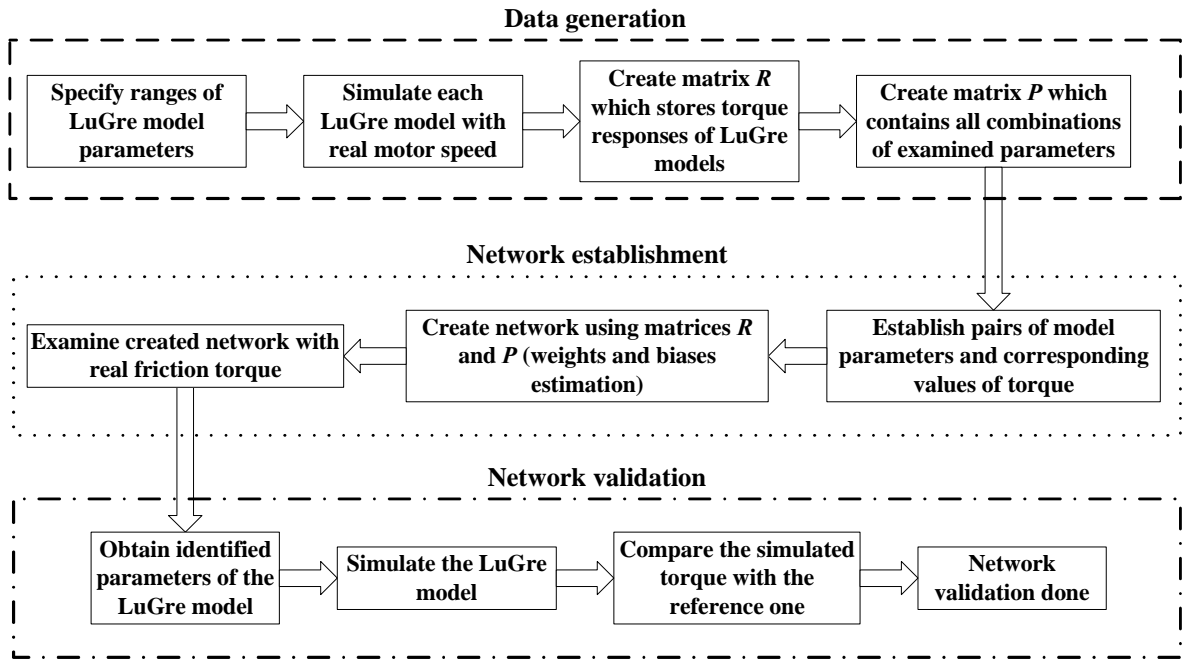
Data generation

| Specify ranges of LuGre model parameters | ⟹ | Simulate each LuGre model with real motor speed | ⟹ | Create matrix **R** which stores torque responses of LuGre models | ⟹ | Create matrix **P** which contains all combinations of examined parameters |

Network establishment

| Examine created network with real friction torque | ⟸ | Create network using matrices **R** and **P** (weights and biases estimation) | ⟸ | Establish pairs of model parameters and corresponding values of torque |

Network validation

| Obtain identified parameters of the LuGre model | ⟹ | Simulate the LuGre model | ⟹ | Compare the simulated torque with the reference one | ⟹ | Network validation done |

Figure 7.2: Procedure to establish and validate the neural network to identify parameters of the LuGre friction model [267].

structure of the designed network is illustrated in Fig. 7.3. In the trial and error method it was decided to select two hidden layers with sigmoid activation functions. The number of neurons for each layer is $l_1 = 5$ and $l_2 = 10$, respectively. Length of the time-domain friction torque vector depends on the applied sampling rate and duration of the experiment. Network training stops when there is no improvement in lowering the mean squared error (MSE) value. This is controlled by performing validation checks at subsequent points having the same value of MSE. For the current problem, the best validation performance of the network is achieved at epoch 34 and is equal to $MSE = 4.89 \cdot 10^{-5}$ $(Nm)^2$, as illustrated in Fig. 7.4b. According to [68], simulation of mechatronic systems with a full LuGre model is computationally demanding due to the fact that the model can become too stiff if large values of σ_0 and σ_1 are used. To avoid this problem, it is decided to leave selection of these parameters purely to the identification algorithm, without considering their physical meaning (high stiffness and damping of microbristles). Releasing these constraints results in mitigation of the computational effort at the cost of loss of simulation accuracy in the vicinity of zero speed. In this region, the friction torque for decreasing speed becomes higher than the friction torque for increasing speed, which is opposite to what happens for higher values of absolute motor speed. However, as shown in Fig. 7.4c, the identified LuGre model represents well the overall behavior of the reference friction. Its estimated parameters are summarized in Table 7.2. A drawback of this approach is that parameters identification based on neural networks produces different results
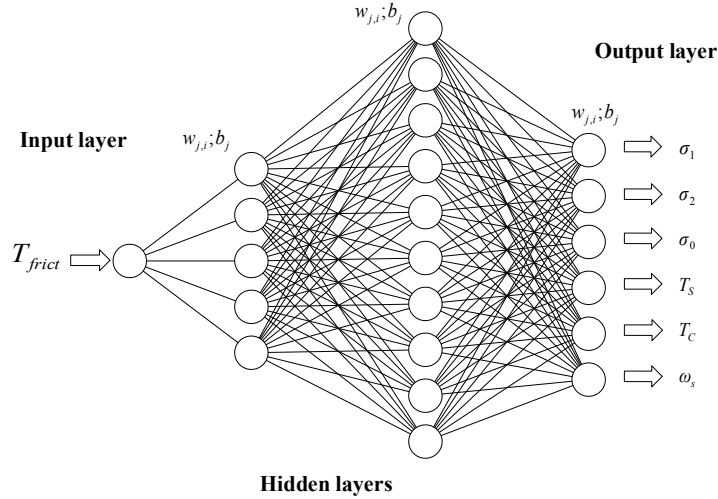
Figure 7.3: Structure of the feedforward neural network [267].

each time a network is simulated. Therefore, network training and simulation processes have to be repeated a few times before satisfactory results are achieved.

Parameter	Value
Bristle stiffness σ_0	$5.10 \cdot 10^{-4}$ $[Nm/rad]$
Damping coefficient σ_1	$4.30 \cdot 10^{-4}$ $[Nm\ s/rad]$
Viscous friction σ_2	$1.96 \cdot 10^{-4}$ $[Nm\ s/rad]$
Stiction torque T_S	$1.40 \cdot 10^{-2}$ $[Nm]$
Coulomb friction T_C	$1.24 \cdot 10^{-2}$ $[Nm]$
Stribeck velocity ω_s	15.71 $[rad/s]$

Table 7.2: Identified parameters of the LuGre friction model for the development platform motors [266].

Fig. 7.4d shows friction values estimated by both the static and dynamic models. They are benchmarked against the real friction computed for the test bench during an arbitrary experiment. It is observed that the friction profile produced by the LuGre model corresponds better to the reference, real world friction. However, in terms of both amplitude and phase values, static and dynamic friction models are equivalent. In addition, according to [68], the real benefit of using dynamic friction models is observed in applications with high precision positioning and low velocity tracking, which is not the case for VPR. Considering the cumbersome identification process of the dynamic friction model and limited benefits it offers in the current application, we conclude that it is sufficient to use the friction model described by static maps between velocity and friction force. It represents satisfactorily major phenomena that are of our interest from the application point of view and it is easy to implement in a typical industrial environment where the trade-offs between engineering time, financial effectiveness, model complexity, and results accuracy have to be continuously made.

7.2.3 Friction in the Full-scale Machine

To relate the friction identified for the experimental setup (shown in Section A.1) to friction identified for the VPR gripper arm as seen by the winch motor (shown in Section A.4), the linear scaling factors are used [268]. Therefore, the combined friction model for the VPR
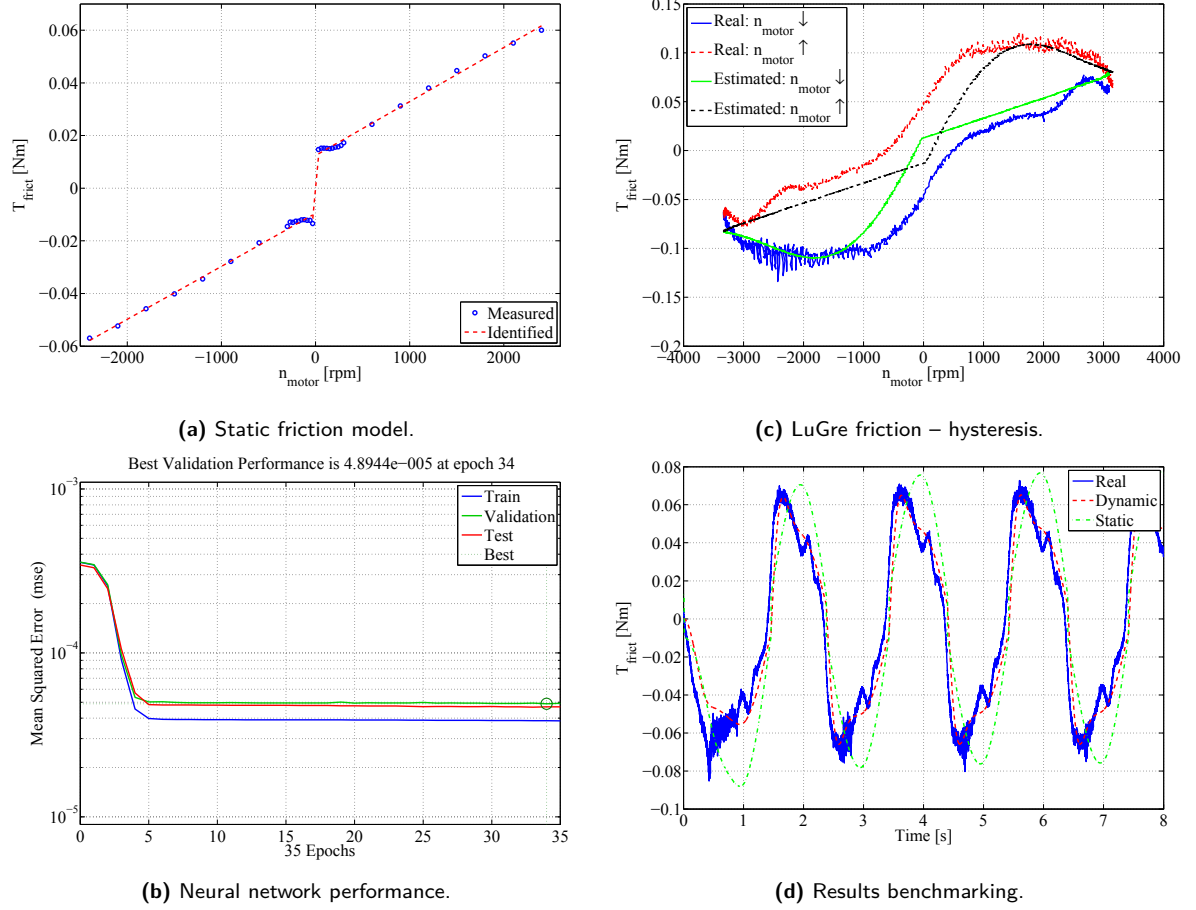
(a) Static friction model.

(c) LuGre friction – hysteresis.

(b) Neural network performance.

(d) Results benchmarking.

Figure 7.4: Establishment of friction models [266].

winch motor becomes

$$T_{fr,real} = \begin{cases} \tanh\left(k\omega_{real}\right)\left(|\omega_{real}|\,b_I + T_{C,I}\right) & \text{if } \omega_{real} \leq 0 \\ \tanh\left(k\omega_{real}\right)\left(|\omega_{real}|\,b_{II} + T_{C,II}\right) & \text{if } \omega_{real} > 0 \end{cases} \tag{7.19}$$

where ω_{real} is speed of the winch motor and new friction coefficients are defined as

$$b_I = r_I b_{neg} \tag{7.20}$$
$$b_{II} = r_{II} b_{pos} \tag{7.21}$$
$$T_{C,I} = r_{III} T_{C,neg} \tag{7.22}$$
$$T_{C,II} = r_{IV} T_{C,pos}. \tag{7.23}$$

Linear friction scaling factors $r_I, r_{II}, r_{III}, r_{IV} > 0$ are found in the trial and error method to achieve the best possible convergence of the experimental results to the full-scale data logs. This is an inevitable effort that needs to be taken if one wants to tune and validate either an experimental setup or a simulation model *a posteriori*, i.e. against the data recorded in reality. Once it is done for various operating points and payloads, the identified scaling factors could be interpolated to represent friction levels in similar type of equipment and different load conditions.

7.3 Scaled-down Experiments for Mechanical Load Estimation

An introduction on how the development platform test bench depicted in Fig. A.1 can be used to reproduce operation of a full-scale winch motor of the VPR gripper arm illustrated in Fig. A.13 is presented in Section A.1. The focus of the current Section is to discuss in more detail the mathematical foundation of the proposed scaling techniques and present the associated numerical results for running the scaled-down experiments to emulate operation of the full-scale offshore drilling equipment.

7.3.1 Scaling of Operating Conditions

Performing scaled-down experiments to imitate behavior of full-scale systems is common among different industries and applications – see for instance [107, 308, 329]. Using rated parameters of motors (especially the torque) to scale between different operating conditions is probably one of the simplest approaches [43], also followed in this thesis. In addition, since the motors installed in the test bench shown in Section A.1 are much smaller than their corresponding full-scale counterparts, it is more likely that they will saturate if the scaling is only based on the rated torques [138]. To avoid that, an additional linear scaling factor $m > 0$ is used.

The reference speed $n_{ref,exp}$ that the experimental induction motor is supposed to follow is expressed as

$$n_{ref,exp} = \frac{n_{ref,real}}{m} \tag{7.24}$$

where $n_{ref,real}$ is the reference speed of the full-scale motor. According to (7.5), the load torque that the experimental induction motor needs to overcome in order to reproduce operation of the reference full-scale induction motor becomes

$$T_{ext} = \frac{1}{m} \left(T_{st,exp} + T_{dyn,exp} + T_{fr,exp} \right). \tag{7.25}$$

The static torque experienced by the full-scale winch motor is directly related to the total payload mass m_{tot}, drum radius r_d and gearbox ratio j_{gb} (note division by 2 because of two wire portions)

$$T_{st,real} = \frac{m_{tot}g}{2j_{gb}} \cdot r_d \tag{7.26}$$

where g is the gravity constant and the total mass m_{tot} is composed of the payload (pipe) mass m_p, mass of the machine itself m_{mech} and mass of the sheave m_s

$$m_{tot} = m_p + m_{mech} + m_s. \tag{7.27}$$

Consequently, the scaled-down static torque becomes (we divide by 2 because in reality there are two winch motors)

$$T_{st,exp} = \frac{T_{st,real}}{2} \cdot \frac{T_{n,exp}}{T_{n,real}} \tag{7.28}$$

where $T_{n,exp}$ is the rated torque of the experimental motor and $T_{n,real}$ is the rated torque of the full-scale motor. The dynamic torque component is related to the effective mass moment of inertia seen by the motor and its angular acceleration $\dot{\omega}_{real}$

$$T_{dyn,real} = J_{eff}\dot{\omega}_{real}. \tag{7.29}$$

The effective mass moment of inertia J_{eff} is calculated for the VPR winch axis as (recall Table 5.1)

$$J_{eff} = \frac{r_d^2 m_{tot}}{j_{gb}^2} + 2J_{m,real} \tag{7.30}$$

where $J_{m,real}$ is the real motor inertia (the inertia of drum and gearbox are neglected). To determine the scaled-down dynamic torque, the rated torque values and the number of motors connected to the drivetrain in the real machine have to be considered

$$T_{dyn,exp} = \frac{T_{dyn,real}}{2} \cdot \frac{T_{n,exp}}{T_{n,real}}. \tag{7.31}$$

The combined friction present in the gripper arm and its drivetrain is also scaled down using the rated torque of motors

$$T_{fr,exp} = T_{fr,real} \cdot \frac{T_{n,exp}}{T_{n,real}}. \tag{7.32}$$

This is justified, since as shown in Section 7.2.3, it is possible to express the full-scale friction $T_{fr,real}$ as a linear combination of the friction identified for the experimental setup T_{frict}.

In order to compare experimental results with full-scale data logs, it is needed to perform scaling up of the results. This is done in a straightforward way. The scaled up speed is

$$n_{su,exp} = mn_{exp} \tag{7.33}$$

where n_{exp} is the actual speed of the experimental motor. Similarly, the scaled up combined electromagnetic torque of the VPR gripper arm drivetrain is given by

$$T_{su,exp} = 2mT_{em,exp} \cdot \frac{T_{n,real}}{T_{n,exp}}. \tag{7.34}$$
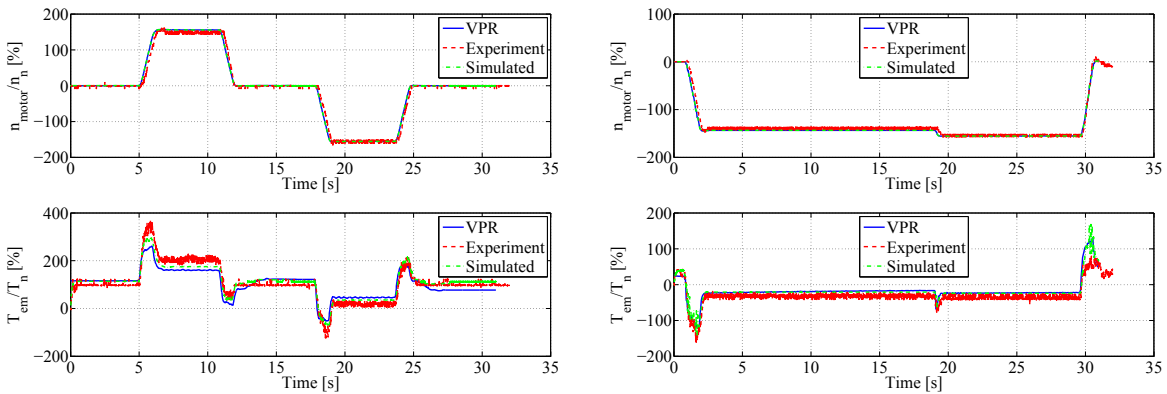
7.3.2 Numerical Results

Data used for validation of the proposed method have been recorded during a regular machine operation when a pipe that was handled was hoisted and lowered to certain positions. The reference four hoisting scenarios are reproduced by performing scaled-down experiments on the test bench and by running its virtual model in a simulation environment. Scaled-down real-world velocity input signals are used in both experiment and simulator to excite the motors. Simultaneously, the load motor follows the torque profile that represents scaled-down load conditions experienced by motors in the real machine. The resulting electromagnetic torques are recorded, scaled up, and benchmarked against full-scale torques developed in the same load scenarios by VPR winch motors. Scaling principles are based on Section 7.3.1. Figs. 7.5a-7.5d present results of running scaled-down experiments.

Both torque and speed profiles are normalized with respect to the nominal torque T_n and speed n_n of the motors used in the real machine. Mass of the payload m_p which winch motors need to manipulate is expressed in terms of the so-called safe working load m_{swl}, which defines a typical load being handled by the machine during regular operation. Profiles of the required motor torque estimated by both the experimental setup and its computational model stay in close accordance with the torque developed by the VPR gripper arm motors. In addition, in Fig. 7.5c a case is presented where the full-size motor has been saturated due to too high currents resulting from excessive acceleration demands. The resulting load torque is still well estimated, since the experimental motor follows the saturated speed profile of the full-scale machine.
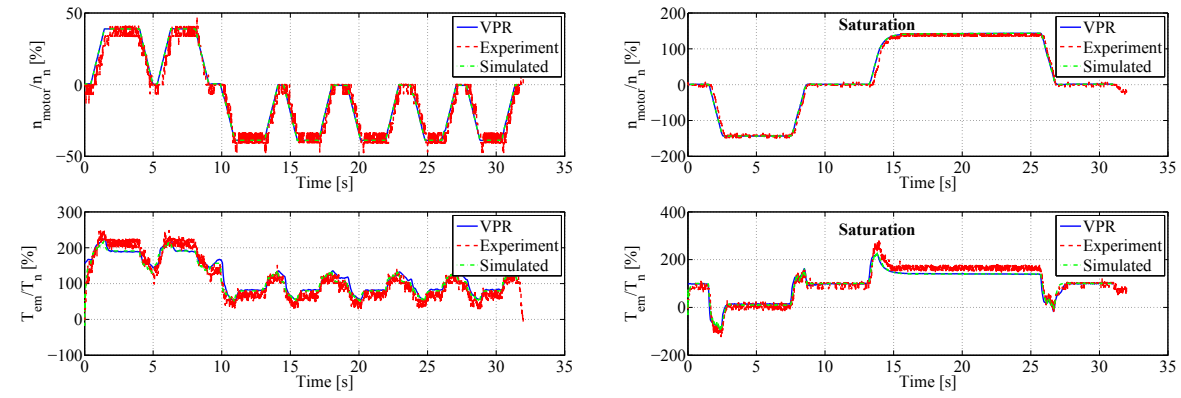
(a) Case *I*: $m_p = 100\% \cdot m_{swl}$ and absolute speed amplitude $n = 39\% \cdot n_n$.

(b) Case *II*: $m_p = 100\% \cdot m_{swl}$ and absolute speed amplitude $n = 155\% \cdot n_n$.

(c) Case *III*: $m_p = 37\% \cdot m_{swl}$ and absolute speed amplitude $n = 143\% \cdot n_n$.

(d) Case *IV*: $m_p = 0\% \cdot m_{swl}$ and absolute speed amplitude $n = 155\% \cdot n_n$.

Figure 7.5: Comparative analysis of winch motor operation [266].

In the current work, the variance accounted for (VAF) metric, defined in Remark 6.2, is used to assess if operation of the real-world winch motor is correctly represented. Resulting values of VAF for all the analyzed load scenarios are shown in Table 7.3. It is clear that the simulator predicts the correct levels of motor torque with more than 90 % of accuracy in almost all the four load cases. The results of running experiments on the scaled-down test bench also produce high degree of fidelity – more than 85 % of accuracy in three scenarios out of four. The presented method estimates not only the maximum value of the required full-scale motor torque but also a complete profile of demanded electromagnetic torque including the effects of static and dynamic loads as well as friction. The reason why it is the simulator that yields more accurate torque predictions than the experimental setup is that it does not include the effects of some real-world phenomena related to data acquisition (e.g. signal noise) which decide about the quality of results in the case of real hardware.

Load case	Experiment	Simulation
Case *I*	89.1 %	94.4 %
Case *II*	71.3 %	87.9 %
Case *III*	86.0 %	96.4 %
Case *IV*	87.1 %	91.3 %

Table 7.3: Results accuracy evaluation – VAF values.

7.4   Conclusion

This Chapter presents a method to estimate profiles of electromagnetic torque needed to be supplied by induction motors under offshore load conditions. This helps to assess with a higher degree of confidence what levels of torque should be delivered by drivetrains where such motors operate. Contrary to previous works, the techniques shown here are specifically applied to electric motors operating in offshore drilling machines, however, they could easily be adapted to other types of actuation systems and industries. The discussed methods are based on representing real-world load circumstances by adjusting them to a scaled-down test bench. By running such a minimized version of offshore drilling equipment operation, the torque developed by an experimental induction motor is scaled up, giving the profile of the torque needed to be produced by a full-scale motor. As a consequence, the proposed method mitigates the effort of design engineers to select the best combination of components of an electrical actuation system, as it allows to explicitly specify the required drivetrain torque over a duty cycle.

The advantage of the proposed load torque estimation technique is the possibility to assess the level of torque required by the motor in a given application, without a need to build a machine's prototype or conduct costly on-site tests, once the model validation has been done. In the future, similar scaled-down tests should be performed on an experimental setup composed of larger motors to further validate the proposed approach. Finally, another full-scale machine should be investigated in order to estimate the levels of torque/force which its actuators have to generate to meet design specifications by interpolating the already identified scaling factors.

8 EKF-based Estimation and Control of Induction Motor

A typical challenge for electric drivetrains is to reduce the number of sensors required for control action or system monitoring.[18] This is particularly important for electric motors operating in offshore conditions, since they work in hostile environment which often damages data acquisition systems, as mentioned in Section 2.2.2. Therefore, this Chapter deals with verification and validation of the extended Kalman filter (EKF) for sensorless indirect field-oriented control (IFOC) of an induction motor operating in offshore conditions. The EKF is employed to identify the speed of the induction motor based on the measured stator currents and voltages. The estimated speed is used in the motor speed control mode instead of a physical encoder signal. In addition, we utilize a stationary frame model of the induction machine to assess the fidelity level of the EKF-based estimation of rotor fluxes. The experimental setup is used to validate the accuracy of the EKF-based state estimation and motor speed control. The importance of the current work is demonstrated on an example of a full-scale offshore drilling equipment. Real-world speed and load profiles sustained by the gripper arm of the vertical pipe handling machine shown in Section A.4 are scaled down and reproduced on the experimental setup presented in Section A.1. The proposed EKF algorithm accurately estimates both speed and electromagnetic torque experienced by the reference full-scale electric drivetrain, creating a potential to reduce the number of data acquisition devices in similar type of equipment. Although the EKF-based control of IMs is well-known, the novelty of this work is to apply this technique with the goal to control topside drilling equipment.

8.1 Discrete-time IM Model

According to [341], the main design steps for a speed-sensorless induction motor drive implementation using the discretized EKF algorithm are as follows:

1. Selection of the time-domain IM model.

2. Discretization of the IM model.

3. Determination of the noise and state covariance matrices.

4. Implementation and tuning of the discretized EKF algorithm.

In this Chapter, we consider an induction motor model in the (α, β)-coordinates (stationary frame discussed in Section 4.4.2), represented by the T-equivalent circuit illustrated in Fig. 4.3, and characterized by static mechanical friction (7.10). To enable hardware implementation of

---

18. This Chapter is reproduced (with minor changes) from publication [274].

the proposed EKF-based control scheme, the continuous-time model (4.49) is converted to the discrete-time model of the form [73]

$$x_{n+1} = A_n x_n + B_n u_n$$
$$y_n = C_n x_n. \tag{8.1}$$

Discretization is accomplished by the series expansion, approximated as ([201] and [202])

$$A_n = I + A T_s + \frac{A^2 T_s^2}{2!} + \frac{A^3 T_s^3}{3!} + \cdots \approx I + A T_s$$
$$B_n = B T_s + \frac{B^2 T_s^2}{2!} + \frac{B^3 T_s^3}{3!} + \cdots \approx B T_s \tag{8.2}$$

where the system, input, and output matrices of the continuous system are denoted by A, B, C, and those of the discrete system by A_n, B_n, C_n, respectively. According to [73], the output matrix of both systems is equivalent ($C_n = C$). The sampling period T_s, which defines the frequency of taking measurements, should be significantly shorter than the dynamics of the system. The discrete form (8.1) of the induction motor equation is derived from (4.49):

$$
\underbrace{\begin{bmatrix} i_{s\alpha}^{n+1} \\ i_{s\beta}^{n+1} \\ \psi_{r\alpha}^{n+1} \\ \psi_{r\beta}^{n+1} \\ \omega_m^{n+1} \end{bmatrix}}_{x_{n+1}} = \underbrace{\begin{bmatrix} 1-\gamma T_s & 0 & \frac{\beta}{\tau_r}T_s & p\omega_m\beta T_s & 0 \\ 0 & 1-\gamma T_s & -p\omega_m\beta T_s & \frac{\beta}{\tau_r}T_s & 0 \\ \frac{L_m}{\tau_r}T_s & 0 & 1-\frac{T_s}{\tau_r} & -p\omega_m T_s & 0 \\ 0 & \frac{L_m}{\tau_r}T_s & p\omega_m T_s & 1-\frac{T_s}{\tau_r} & 0 \\ -\frac{3}{2}p\mu T_s\psi_{r\beta} & \frac{3}{2}p\mu T_s\psi_{r\alpha} & 0 & 0 & 1 \end{bmatrix}}_{A_n} \underbrace{\begin{bmatrix} i_{s\alpha}^{n} \\ i_{s\beta}^{n} \\ \psi_{r\alpha}^{n} \\ \psi_{r\beta}^{n} \\ \omega_m^{n} \end{bmatrix}}_{x_n}
$$

$$
+ \underbrace{\begin{bmatrix} \frac{T_s}{\sigma} & 0 & 0 \\ 0 & \frac{T_s}{\sigma} & 0 \\ 0 & 0 & 0 \\ 0 & 0 & 0 \\ 0 & 0 & -\frac{T_s}{J} \end{bmatrix}}_{B_n} \underbrace{\begin{bmatrix} u_{s\alpha}^{n} \\ u_{s\beta}^{n} \\ T_l^{n} \end{bmatrix}}_{u_n} \tag{8.3}
$$

$$
\underbrace{\begin{bmatrix} i_{s\alpha}^{n} \\ i_{s\beta}^{n} \end{bmatrix}}_{y_n} = \underbrace{\begin{bmatrix} 1 & 0 & 0 & 0 & 0 \\ 0 & 1 & 0 & 0 & 0 \end{bmatrix}}_{C_n} \underbrace{\begin{bmatrix} i_{s\alpha}^{n} \\ i_{s\beta}^{n} \\ \psi_{r\alpha}^{n} \\ \psi_{r\beta}^{n} \\ \omega_m^{n} \end{bmatrix}}_{x_n} .
$$

In order to transform currents and voltages measured in the physical three-phase system (a, b, c) to the (d, q)-coordinates (and vice versa), the Park transformations (4.21) and (4.22) are used. Actually, since the transformation angle is equal to zero $(\theta_1 = 0)$ for the stationary-frame model, these matrices are reduced to Clarke matrices (4.23) which are linear transformations only.

8.2 Extended Kalman Filter

8.2.1 Sensorless Control Scheme

The control strategy adopted in the current study is briefly characterized in Section 4.6.3 and illustrated in Fig. 8.1. In principle, it is almost identical to the one discussed in Section 7.1.1 and presented in Fig. 7.1. The assumption of perfect field orientation enables to control the
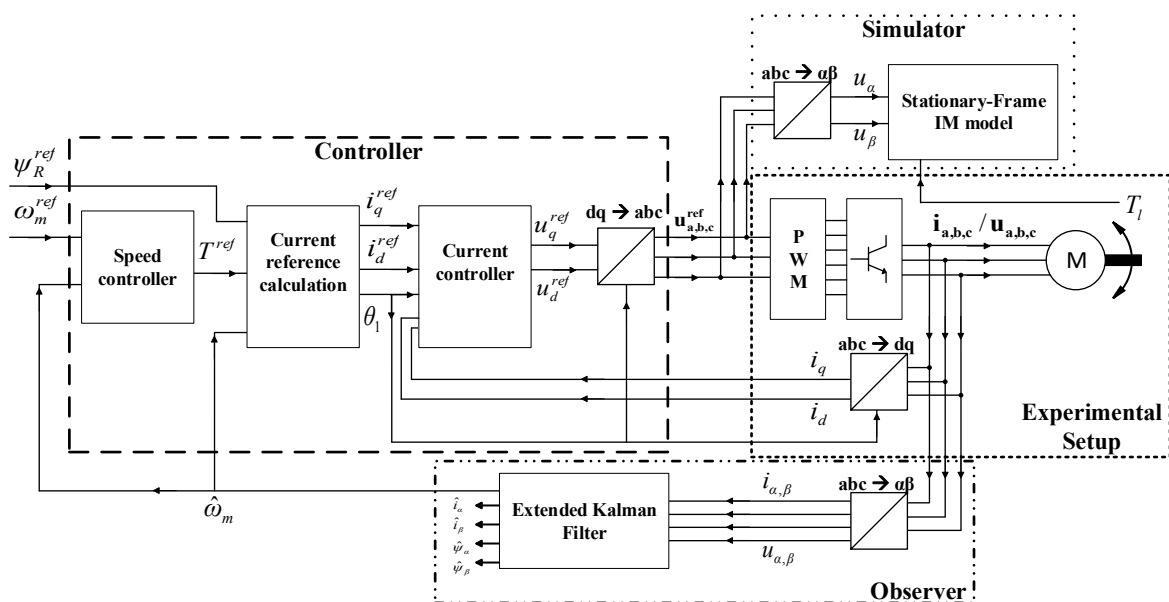

Figure 8.1: Sensorless indirect field-oriented control of induction motor [274].

quadrature current component i_{sq} which directly affects the electromagnetic torque produced by the motor. Hence, by keeping the flux ψ_{rd} constant (indirectly, i.e. by controlling the current i_{sd} – recall (7.6) and (7.7)), the torque is controlled by adjusting i_{sq}, according to the torque equation (4.53)

$$T_{em} = \frac{3}{2} \frac{L_m}{L_r} p \left(\psi_{rd} i_{sq} \right).$$

(8.4)

In this study, PI controllers are used for controlling both currents: i_{sq} and i_{sd} [132]. In addition, the discussed torque control mode is expanded to the speed control, as shown in Fig. 8.1. The output of the PI speed controller becomes a torque set point T^{ref}. The EKF is applied in sensorless control to provide the motor speed feedback signal $\hat{\omega}_m$, instead of using a physical sensor. The IM model that is used by EKF is also formulated in the stationary reference frame and presented in Section 8.2.2. The reference voltage signals generated by the current controller $\left(u_{sd}^{ref}, u_{sq}^{ref} \right)$ are converted to $\left(u_{s\alpha}^{ref}, u_{s\beta}^{ref} \right)$, which in turn are used to excite the stationary frame model of the induction motor (8.3). This way it is proven that even though the controller is implemented in the (d, q)-coordinates, it can be successfully

used (after coordinates transformations) to regulate operation of the model formulated in the (α, β) frame. The associated simulation results are shown in Section 8.3.2.

8.2.2 Formulation

An alternative way of representing a three-phase induction motor (4.49) is to consider only its dynamic electrical model with four state variables: stator currents $(i_{s\alpha}, i_{s\beta})$ and rotor fluxes $(\psi_{r\alpha}, \psi_{r\beta})$. An extended model is obtained if the motor speed is included as a state variable by using an augmented system matrix [73]. This formulation is particularly useful for motor speed estimation problems, as it does not involve modeling of mechanical friction nor load torque acting on the motor, hence it is followed in this thesis. In general, the discrete-state model and the output model are defined for a nonlinear system as

$$\dot{x}(t) = f\left[x(t), u(t), t\right] + G(t)w(t) \qquad \text{(System)} \qquad (8.5)$$
$$y(t) = h\left[x(t), t\right] + v(t) \qquad \text{(Measurement)}.$$

The induction motor extended model is formulated based on (8.5) as [202]

$$\dot{x} = Ax + Bu + G(t)w(t) \qquad \text{(System)} \qquad (8.6)$$
$$y = Cx + v(t) \qquad \text{(Measurement)}$$

which takes the following form after discretization – recall (8.1), (8.2), and (8.3)

$$x_n = \begin{bmatrix} i_{s\alpha}^n \\ i_{s\beta}^n \\ \psi_{r\alpha}^n \\ \psi_{r\beta}^n \\ \omega_m^n \end{bmatrix} ; \quad A_n = \begin{bmatrix} 1 - \gamma T_s & 0 & \dfrac{\beta}{\tau_r} T_s & p\omega_m \beta T_s & 0 \\[2mm] 0 & 1 - \gamma T_s & -p\omega_m \beta T_s & \dfrac{\beta}{\tau_r} T_s & 0 \\[2mm] \dfrac{L_m}{\tau_r} T_s & 0 & 1 - \dfrac{T_s}{\tau_r} & -p\omega_m T_s & 0 \\[2mm] 0 & \dfrac{L_m}{\tau_r} T_s & p\omega_m T_s & 1 - \dfrac{T_s}{\tau_r} & 0 \\[2mm] 0 & 0 & 0 & 0 & 1 \end{bmatrix}$$

$$u_n = \begin{bmatrix} u_{s\alpha}^n \\ u_{s\beta}^n \end{bmatrix} ; \quad y_n = \begin{bmatrix} i_{s\alpha}^n \\ i_{s\beta}^n \end{bmatrix} ; \quad B_n = \begin{bmatrix} \dfrac{T_s}{\sigma} & 0 \\[2mm] 0 & \dfrac{T_s}{\sigma} \\[2mm] 0 & 0 \\[2mm] 0 & 0 \\[2mm] 0 & 0 \end{bmatrix} ; \quad C_n = \begin{bmatrix} 1 & 0 & 0 & 0 & 0 \\ 0 & 1 & 0 & 0 & 0 \end{bmatrix} \qquad (8.7)$$

where $G(t)$ is the noise-weight matrix, $w(t)$ is noise matrix of state model (system noise), and $v(t)$ is noise matrix of output model (measurement noise). The covariance matrices Q and R of these noises are defined as [312]

$$Q = \text{cov}(w) = E\{ww^T\} \qquad (8.8)$$
$$R = \text{cov}(v) = E\{vv^T\}. \qquad (8.9)$$

The extended Kalman filter is an extension of the standard Kalman algorithm to nonlinear systems. It is a recursive state estimator that is applicable to multi-input multi-output systems in which measurement and process noises are present. It utilizes the stochastic state-space model together with the plant's inputs and outputs to give optimal estimates of the states in the sense of minimizing their mean-squared error ([35] and [79]). Since the motor speed increases the dimension of the state vector, the state-space model becomes nonlinear (speed is both a state and a parameter in the system matrix $A(\omega_m)$) [181]. Hence, the nonlinear-state model is relinearized at each new time instant by applying the EKF algorithm to estimate motor states. The EKF-based estimation is normally composed of the following stages ([184] and [201]):

I Prediction

1) State:
$$\hat{x}(k+1|k) = f\left(\hat{x}(k|k), u(k)\right) \tag{8.10}$$

2) Error Cov. Matrix:
$$\hat{P}(k+1|k) = F(k)\hat{P}(k|k)F^T(k) + Q \tag{8.11}$$

II Filtering

3) Kalman Filter Gain:
$$K(k+1) = \frac{\hat{P}(k+1|k)H^T(k)}{H(k)\hat{P}(k+1|k)H^T(k) + R} \tag{8.12}$$

4) State Estimation:
$$\hat{x}(k+1|k+1) = \hat{x}(k+1|k) + K(k+1)\epsilon(k+1) \tag{8.13}$$

5) Error Cov. Matrix:
$$\hat{P}(k+1|k+1) = \left[I - K(k+1)H(k)\right]\hat{P}(k+1|k) \tag{8.14}$$

where $(k|k)/(k+1|k)$ denotes a prediction at time $k/k+1$ based on data up to time k and

$$F(k) = \left.\frac{\partial f\left(x(k), u(k)\right)}{\partial x^T(k)}\right|_{x(k)=\hat{x}(k|k)} \tag{8.15}$$

$$H(k) = \left.\frac{\partial h\left(x(k)\right)}{\partial x^T(k)}\right|_{\hat{x}(k+1|k)} \tag{8.16}$$

$$\epsilon(k+1) = y(k+1) - h\left(\hat{x}(k+1|k), k\right). \tag{8.17}$$

Based on (8.5), (8.7), (8.15), and (8.16) the matrices $F(k)$ and $H(k)$ are determined to be [73]

$$F(k) = \begin{bmatrix} 1 - \gamma T_s & 0 & \dfrac{\beta}{\tau_r}T_s & p\omega_m^k\beta T_s & p\beta T_s\psi_{r\beta}^k \\[2mm] 0 & 1 - \gamma T_s & -p\omega_m^k\beta T_s & \dfrac{\beta}{\tau_r}T_s & -p\beta T_s\psi_{r\alpha}^k \\[2mm] \dfrac{L_m}{\tau_r}T_s & 0 & 1 - \dfrac{T_s}{\tau_r} & -p\omega_m T_s & -pT_s\psi_{r\beta}^k \\[2mm] 0 & \dfrac{L_m}{\tau_r}T_s & p\omega_m^k T_s & 1 - \dfrac{T_s}{\tau_r} & pT_s\psi_{r\alpha}^k \\[2mm] 0 & 0 & 0 & 0 & 1 \end{bmatrix} \tag{8.18}$$

$$H(k) = \begin{bmatrix} 1 & 0 & 0 & 0 & 0 \\ 0 & 1 & 0 & 0 & 0 \end{bmatrix}. \tag{8.19}$$

Finally, the electromagnetic torque estimated by the EKF algorithm is computed as [219]

$$\hat{T}_{em} = \frac{3}{2}\frac{L_m}{L_r}p\left(\hat{\psi}_{r\alpha}\hat{i}_{s\beta} - \hat{\psi}_{r\beta}\hat{i}_{s\alpha}\right). \tag{8.20}$$

For the state estimator to converge, its observability property is essential. For the induction motor model, sufficient observability conditions are provided in the literature for both continuous-time and discrete-time models – see for instance [19] and [69].

8.3 Experimental Results

8.3.1 Implementation Details

In the current work, the gripper arm actuated by the winch hoisting system shown in Section A.4 is selected as a case study and its vertical motion (i.e. winch hoisting/lowering) is reproduced by the scaled-down experimental setup presented in Section A.1. The EKF algorithm is implemented in a simulation environment and the simulation results are compared with the experimental data. The focus of this work is to:

1. Validate the proposed EKF-based speed estimation.

2. Investigate the accuracy of flux estimation.

3. Reproduce the scaled-down operation of a full-scale offshore drilling machine.

Since the state variables have different magnitudes (rotor flux amplitude could be 1 Wb and motor speed might reach 300 rad/s), the diagonal elements of the system covariance matrix should be selected separately for different states, depending on their order of magnitude. Hence, the system and measurement noise covariance matrices become, respectively

$$Q = \text{diag}\left(\begin{bmatrix} \zeta & \zeta & \zeta & \zeta & \xi \end{bmatrix}\right) \tag{8.21}$$
$$R = \text{diag}\left(\begin{bmatrix} \rho & \rho \end{bmatrix}\right) \tag{8.22}$$

where $\zeta = 1 \cdot 10^{-6}$, $\xi = 10$, and $\rho = 1 \cdot 10^{-9}$ are found in the trial and error process, according to the rule of thumb which advices to assign greater values to ξ, since the estimated speed typically experiences greater variations than the other state variables [73]. The sampling time which produces satisfactory results is $T_s = 1 \cdot 10^{-5}$ s.
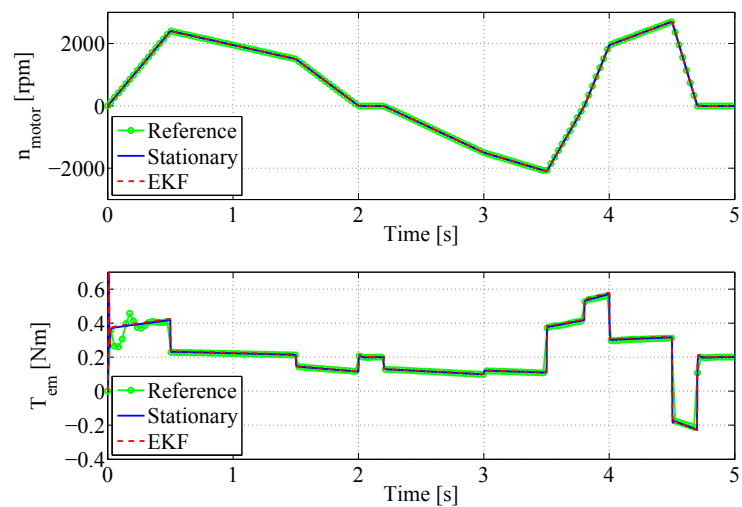
8.3.2 Verification

To verify the performance of the EKF, the IM model (8.3) is run in the speed control mode with the reference speed signal illustrated in Fig. 8.2c in the presence of the constant external torque $T_{ext} = 0.2$ Nm and static friction T_{frict} (7.10) identified in Section 7.2.1. The speed control loop is closed using the speed signal estimated by the EKF algorithm. The EKF-based speed sensorless IFOC presented in Fig. 8.1 is simulated on a computer by replacing the experimental hardware with a discrete induction motor model. The resulting stator currents ($i_{s\alpha}, i_{s\beta}$), rotor fluxes ($\psi_{r\alpha}, \psi_{r\beta}$), motor speed ω_m, and electromagnetic torque T_{em} are compared with the ones that the EKF estimates based on stator currents and voltages only. Actually, the current signals ($i_{s\alpha}, i_{s\beta}$) are directly available by transforming the measured currents (i_{sa}, i_{sb}, i_{sc}), therefore, current estimation by EKF is redundant. All the estimation results are identical to the reference signals, as shown in Fig. 8.2.
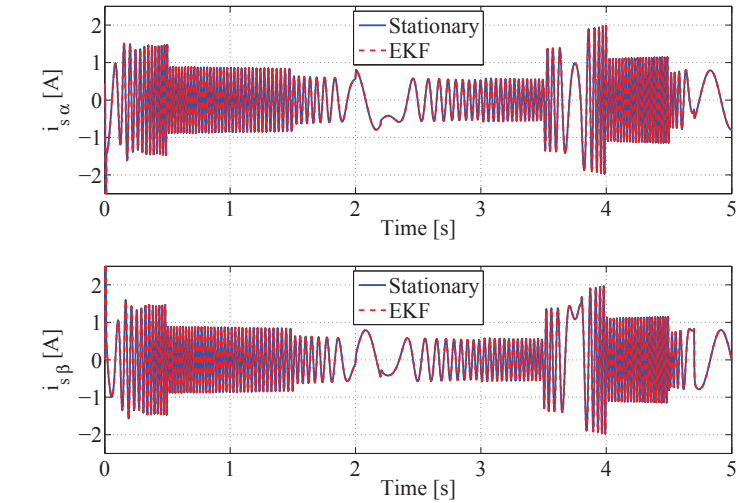
(a) Motor current profiles.
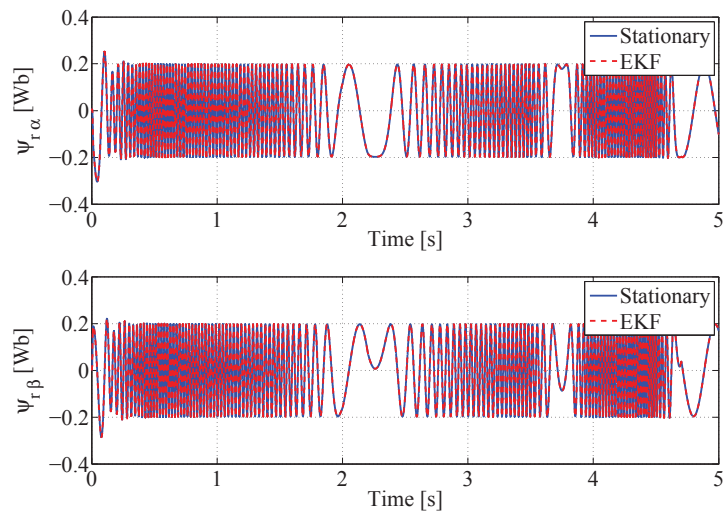
(b) Motor flux profiles.

(c) Motor speed and torque profiles.

Figure 8.2: Verification of the EKF-based estimation and control against stationary model results [274].

8.3.3 Validation

The next step to assess the performance of the proposed EKF is to validate the results by using noisy voltage and current signals acquired on the experimental setup. The EKF-based state estimation is simulated on a computer offline and obtained results are benchmarked with the experimental results produced by the test bench which uses the encoder speed feedback. In addition, the reference velocity signals and load torques reproduced by the development platform motors are the scaled-down profiles recorded during hoisting/lowering of tubulars by the gripper arm of VPR, as explained in Section 7.3. Both motor speed and electromagnetic torque estimated by the EKF closely resemble the original scaled-down signals, as illustrated in Fig. 8.3.
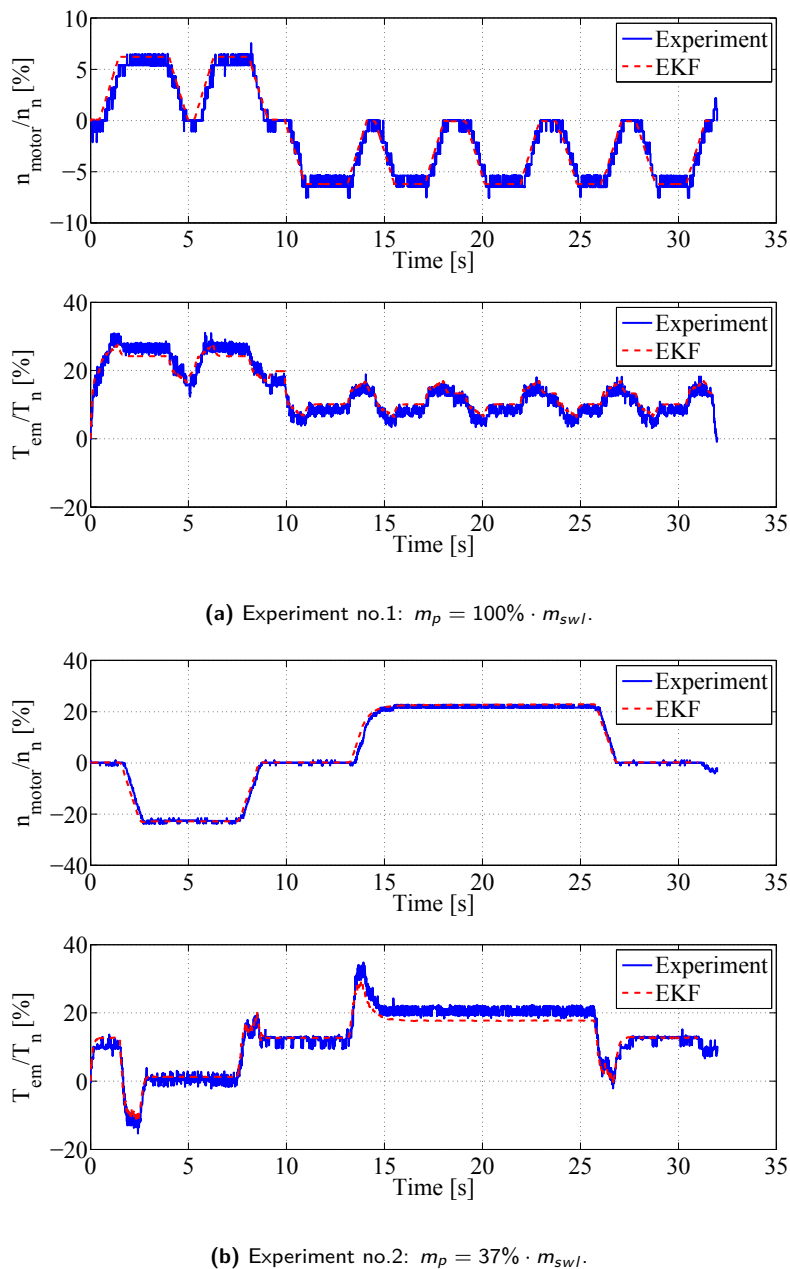

(a) Experiment no.1: $m_p = 100\% \cdot m_{swl}$.

(b) Experiment no.2: $m_p = 37\% \cdot m_{swl}$.

Figure 8.3: Validation of the EKF-based estimation and control against scaled-down experimental results [274].

The obtained results are normalized with respect to the rated parameters of the experimental motors. It is confirmed that a physical speed sensor could be removed from the hardware setup and replaced by the implemented EKF to provide for a successful speed sensorless control of an induction motor (as long as the continuous operation in the vicinity of zero speed is properly addressed – recall the comment from Section 4.6.3).

8.4 Conclusion

The EKF-based estimation and control method of an induction motor is verified and validated in this Chapter. The currents, fluxes, and speed estimation results are compared with the reference signals of the stationary frame model. The predicted and original states are identical. Also, the experimental setup is used to reproduce operation of a full-scale offshore drilling machine. The scaled-down speed profiles and the corresponding load torques are replicated by the test bench and the EKF algorithm is used to represent operation of the development platform motors. The results obtained in both steps show a high degree of accuracy and prove that the EKF-based sensorless control has a potential to reduce the number of data acquisition devices in actuation systems working in offshore drilling equipment. Although at the current stage of development the EKF is not yet running online (and cannot readily replace the encoder), a fault in the speed sensor can still be detected by executing the EKF algorithm at regular intervals.

There are three recommendations to boost the impact of this work in the future. One is to apply other signals estimated by the EKF (e.g. rotor fluxes) in IM control schemes (e.g. in DTC or DFOC) to benchmark their performance under offshore load conditions. The other is to realize the proposed EKF on experimental hardware and validate its real-time performance and control action. Finally, in order to implement this method in an industrial environment, its robustness has to be improved by solving the problem of operation near zero speed (for instance by using the techniques discussed in Section 4.6.3).

9 Mitigation of Fatigue Damage and Vibration Severity

The offshore drilling industry is among the most demanding markets for electrical equipment.[19] Heave motion, irregular cyclic loads, harsh weather conditions, and vibrations are causing accelerated deterioration of drilling equipment and contribute especially to mechanical failures, as explained in Section 2.3.3. One of the most common solutions to these problems is to design actuation systems of such machinery overly conservative to gain additional safety, which results in too high initial investment and maintenance costs. Contrary to that, to mitigate the fatigue damage and vibration severity of rotating elements of electric drivetrains operating offshore, this Chapter presents a comparative analysis of four popular input functions used in motion control of industrial systems. We evaluate them not only by using the well-known performance indicators, such as maximum load or velocity, but also by assessing their influence on fatigue life and vibration severity of electric drivetrains. The rainflow counting algorithm is used to assign amplitudes and mean values of distinguished cycles from random loading history. Then, the Palmgren–Miner rule together with S–N curves are applied to determine the total damage for cycles with varying amplitudes. In addition, we quantify the cumulative effect of vibrations and jerk on machine damage by using the metric based on the jerk energy. Importance of the current work is illustrated on the full-scale offshore pipe handling machine from Section A.4 by benchmarking simulation results with the field data. The outcomes demonstrate not only a serious decrease in damage caused by vibrations for smooth motion profiles, but also provide for a basis to formulate rules of thumb for selection of the most suitable motion profile for certain applications.

9.1 Review of Common Motion Profiles

When deciding about a motion control strategy, one of the aims is to minimize dynamic forces experienced by the machine, and thus minimize the magnitude of the acceleration and keep it continuous. Also, one should minimize stored kinetic energy, and, as a consequence, be concerned with the magnitude of the velocity as well. In addition, the goal should be to mitigate vibrations in the machine as well as to prevent fatigue damage. Hence, the selection of the appropriate motion control input signal becomes not a trivial task. Therefore, in this Chapter, we analyze and compare four motion profiles which are typically applied in industrial actuation systems. According to [255], the following functions, which either minimize peak acceleration/velocity or remove jerk discontinuities, are examined:

1. Constant acceleration.

2. Modified trapezoidal acceleration.

---

19. This Chapter is reproduced (with minor changes) from publication [271].

3. Modified sinusoidal acceleration.

4. Trigonometric jerk.

The goal is to judge which of them provides for the best performance of a selected machine given the above objectives. This Chapter considers the gripper arm and its drivetrain presented in Section A.4 as a case study for testing the influence of different motion profiles on the machine fatigue and vibration damage.

9.1.1 Constant Acceleration

A commonly used signal is a simple constant acceleration function expressed as

$$a_c(t) = \begin{cases} a_{max} & \text{if } \; t_0 \leq t \leq t_3 \\ -a_{max} & \text{if } \; t_3 < t \leq t_7. \end{cases} \tag{9.1}$$

It provides for a minimum peak value of acceleration, resulting in fast motions. However, an inherent problem related to the associated velocity signal is that when it reaches the maximum value, there is a jump in acceleration from a constant value to zero [246]. Similar jumps occur when velocity changes its orientation. These acceleration discontinuities lead to infinite jerks at such time instants. Hence, the constant acceleration (also called trapezoidal velocity) profiles typically lead to overshoots and induce vibrations which, among other drawbacks, can damage the mechanical system and make it difficult for the final position to be reached with a desired precision [272].

9.1.2 Modified Trapezoidal Acceleration

The discontinuities in the square acceleration wave are removed by smoothing its corners. The removed area is replaced by increasing the peak magnitude as compared to the constant acceleration profile to satisfy requirements on final position and duration. To avoid jerk discontinuities which are associated with a simple trapezoidal acceleration profile, an improvement is made where linear ramp portions of the signal are replaced by pieces of sine waves. The most common approach, according to [255], is to assume that the acceleration ramp time is equal to $t_1 = (1/8)\,T$ (this assumption is valid for the other examined profiles as well). The modified trapezoidal acceleration function is then described as

$$a_{mt}(t) = \begin{cases} \dfrac{8\pi}{2+\pi} \cdot \dfrac{h}{T^2} \sin\left(4\pi \dfrac{t}{T}\right) & \text{if } \; t_0 \leq t \leq t_1 \\[2mm] \dfrac{8\pi}{2+\pi} \cdot \dfrac{h}{T^2} & \text{if } \; t_1 < t \leq t_2 \\[2mm] \dfrac{8\pi}{2+\pi} \cdot \dfrac{h}{T^2} \sin\left(4\pi \dfrac{t}{T} - \pi\right) & \text{if } \; t_2 < t \leq t_5 \\[2mm] -\dfrac{8\pi}{2+\pi} \cdot \dfrac{h}{T^2} & \text{if } \; t_5 < t \leq t_6 \\[2mm] -\dfrac{8\pi}{2+\pi} \cdot \dfrac{h}{T^2} \sin\left(4\pi \dfrac{t}{T} - 3\pi\right) & \text{if } \; t_6 < t \leq t_7 \end{cases} \tag{9.2}$$

where h is the final position and T is the duration of the profile. This function has the advantage of relatively low theoretical peak acceleration and reasonably rapid, smooth transitions at the beginning and end of the interval [255].

9.1.3 Modified Sinusoidal Acceleration

Combination of two sinusoid curves of different frequencies allows to retain smooth characteristics of the cycloid and reduce peak acceleration, as compared to the case of a single frequency sine function. In addition, the peak velocity of this profile is lower than for the constant and modified trapezoidal accelerations. The equations for the modified sine curve are as follows

$$
a_{ms}(t) = \begin{cases} \dfrac{8\pi^2}{2(4+\pi)} \cdot \dfrac{h}{T^2} \sin\left(4\pi \dfrac{t}{T}\right) & \text{if } t_0 \leq t \leq t_1 \\[2ex] \dfrac{8\pi^2}{2(4+\pi)} \cdot \dfrac{h}{T^2} \cos\left(\dfrac{4\pi}{3}\dfrac{t}{T} - \dfrac{\pi}{6}\right) & \text{if } t_1 < t \leq t_6 \\[2ex] \dfrac{8\pi^2}{2(4+\pi)} \cdot \dfrac{h}{T^2} \sin\left(2\pi\left(2\dfrac{t}{T} - 1\right)\right) & \text{if } t_6 < t \leq t_7. \end{cases} \tag{9.3}
$$

9.1.4 Trigonometric Jerk

The trigonometric jerk model removes all jerk discontinuities at the cost of increased jerk peak value [272]

$$
j_t(t) = \begin{cases} \dfrac{J_{peak}}{2}\left(1 - \sin\left(\dfrac{2\pi}{t_j}t + \dfrac{\pi}{2}\right)\right) & \text{if } t_0 \leq t \leq t_1 \\[2ex] 0 & \text{if } t_1 < t \leq t_2 \\[2ex] -\dfrac{J_{peak}}{2}\left(1 - \sin\left(\dfrac{2\pi}{t_j}t + \dfrac{\pi}{2}\right)\right) & \text{if } t_2 < t \leq t_5 \\[2ex] 0 & \text{if } t_5 < t \leq t_6 \\[2ex] \dfrac{J_{peak}}{2}\left(1 - \sin\left(\dfrac{2\pi}{t_j}t + \dfrac{\pi}{2}\right)\right) & \text{if } t_6 < t \leq t_7. \end{cases} \tag{9.4}
$$

Equation (9.4) can be expressed as the following acceleration function of the trigonometric jerk profile (refer to [246] and [247])

$$
a_t(t) = \begin{cases} \dfrac{64}{3\pi} \cdot \dfrac{h}{T^3}\left(2\pi t - t_j \sin\left(\dfrac{2\pi}{t_j}t\right)\right) & \text{if } t_0 \leq t \leq t_1 \\[2ex] \dfrac{16}{3} \cdot \dfrac{h}{T^2} & \text{if } t_1 < t \leq t_2 \\[2ex] -\dfrac{64}{3\pi} \cdot \dfrac{h}{T^3}\left(2\pi t - t_j \sin\left(\dfrac{2\pi}{t_j}t\right)\right) & \text{if } t_2 < t \leq t_5 \\[2ex] -\dfrac{16}{3} \cdot \dfrac{h}{T^2} & \text{if } t_5 < t \leq t_6 \\[2ex] \dfrac{64}{3\pi} \cdot \dfrac{h}{T^3}\left(2\pi t - t_j \sin\left(\dfrac{2\pi}{t_j}t\right)\right) & \text{if } t_6 < t \leq t_7 \end{cases} \tag{9.5}
$$

where the jerk period is a parameter being equal to $t_j = (1/8)\, T$.

9.1.5 Summary

Fig. 9.1a shows the comparison of the normalized shapes and relative magnitudes of the four considered motion profiles. For (9.1)-(9.5) the period of signal T is divided into such portions

$$t_i = i\frac{1}{8}T \qquad \text{where } i = 0, 1, 4, 5 \tag{9.6}$$

$$t_i = i\frac{1}{8}T + \frac{1}{8}T \qquad \text{where } i = 2, 6, 7 \tag{9.7}$$

$$t_3 = t_4. \tag{9.8}$$

In addition, (9.1)-(9.5) can easily be adapted to include a period of constant velocity at t_3, as stated in [255]. For the sake of brevity, the detailed derivation is omitted here, however, such exemplary profiles are illustrated in Fig. 9.1b.
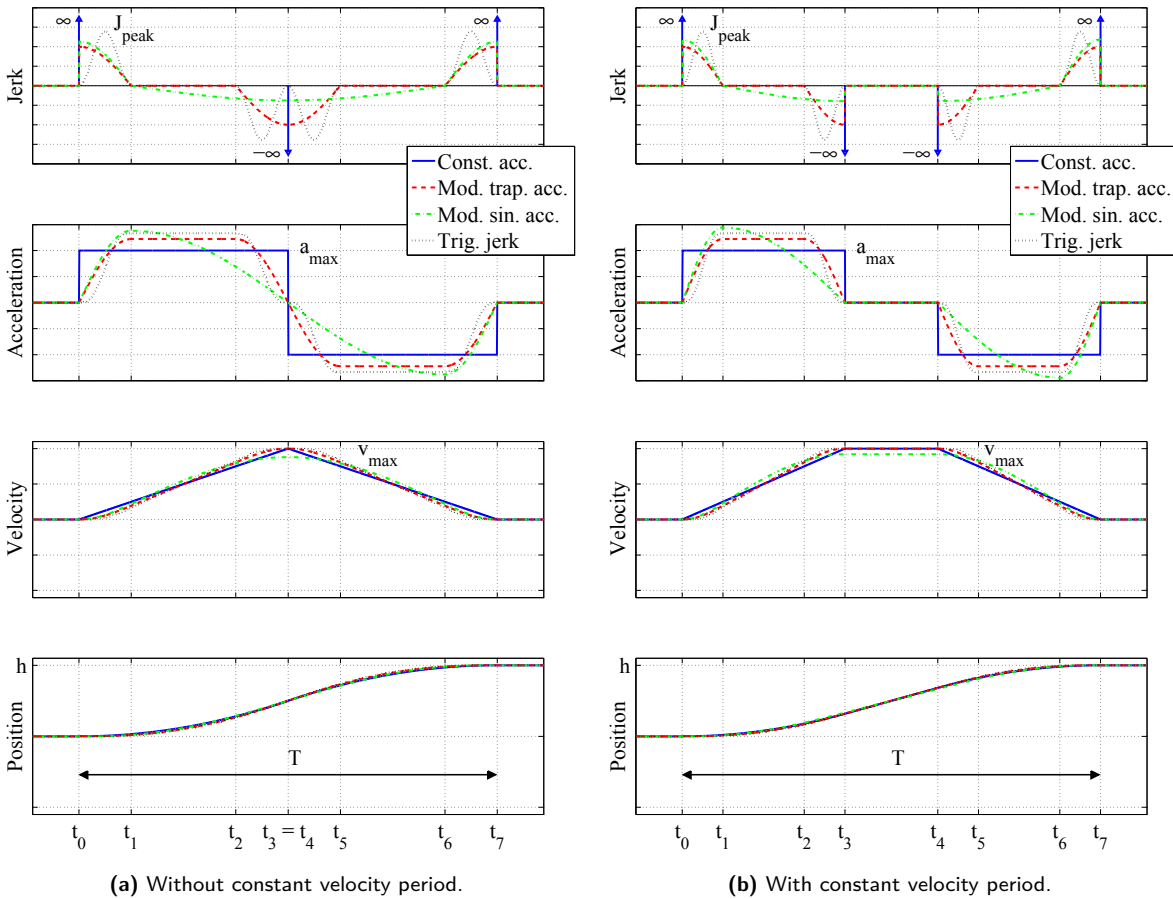

(a) Without constant velocity period.   **(b)** With constant velocity period.

Figure 9.1: Comparison of studied motion profiles [271].

According to [255], by expressing (9.1)-(9.5) in terms of the total displacement h and duration of motion T, it becomes straightforward to formulate their maximum values of velocity, acceleration, and jerk, which are summarized in Table 9.1. By doing so, it becomes clear that the jerk peak value of the trigonometric jerk profile has the largest finite value and that this profile yields smooth jerk during entire motion; the modified sinusoidal function has the highest peak acceleration and the lowest peak velocity; and the peak acceleration of the modified trapezoid is between that of the constant acceleration and trigonometric jerk.

Function	Max. Velocity	Max. Acceleration	Max. Jerk
Constant accel.	2.000 h/T	4.000 h/T^2	∞
Mod. trap. accel.	2.000 h/T	4.888 h/T^2	61 h/T^3
Mod. sin. accel.	1.760 h/T	5.528 h/T^2	69 h/T^3
Trig. jerk	2.000 h/T	5.333 h/T^2	85 h/T^3

Table 9.1: Factors for peak velocity, acceleration, and jerk of selected functions [255].

9.2 Vibration Severity Evaluation

It is recognized that the jerk (the slope or time derivative of acceleration) is mainly responsible for vibrations induced by the reference trajectory [37]. In general, the smoother the motion profile, the less residual vibrations in the machine. There are different techniques to quantify damage related to vibrations and jerk and to classify "smoothness" of motion profiles – see [20] and [112] and the references therein. In this Chapter, we are interested in finding the cumulative effect of jerk on machine damage, hence we use the metric which is based on the jerk energy [241]

$$JE(t) = \int_{t_0}^{t} (j(t))^2 \, dt \tag{9.9}$$

where $j(t)$ is the variable jerk value over time. This method is suitable for evaluating damage severity of rotating machine elements and, as compared to other vibration monitoring techniques, it offers an advantage of semi-linear behavior for all fault types and at different operating conditions, according to [161].

9.3 Fatigue Estimation Method

9.3.1 Fatigue Life Assessment

A popular approach for estimation of fatigue damage based on S–N curve assumes perfectly cyclic loads. In reality, typically we deal with varying amplitude loads which have to be converted first into the cyclic ones. For this purpose, according to [94] and [249], cycle counting methods are applied which identify fatigue cycles by combining and extrapolating information from extrema in a time series. Cumulative damage is then determined as a sum of particular damages caused by distinguished cycles. The so-called rainflow counting method is among the most popular ways of fatigue cycles identification [105]. Together with the Palmgren–Miner rule of linear damage accumulation, it is used to calculate the expected damage – see [236] and [262]. The proposed procedure for damage estimation is illustrated in Fig. 9.2.

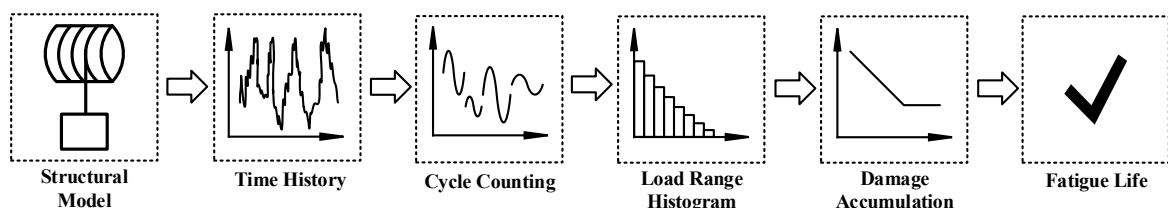

Structural Model   **Time History**   **Cycle Counting**   **Load Range Histogram**   **Damage Accumulation**   **Fatigue Life**

Figure 9.2: Fatigue damage estimation procedure based on rainflow counting [271] – adapted from [249].

9.3.2 Rainflow Counting

The rainflow algorithm allows us to assign amplitudes and mean values to cycles distinguished from random loading history [249]. Load signals are discretized to a certain number of intervals and for each identified cycle, a corresponding value of amplitude and mean load is found. It is a common assumption to neglect the time of the cycle occurrence and its period, as their effect does not contribute significantly to fatigue life. Hence, the considered signal is analyzed in terms of detected local extrema, instead of time. This enables to represent distinguished cycles as the rainflow matrix which contains information about the number of counted cycles with the given amplitude and mean value detected in the considered load history [24]. There are different rainflow algorithms proposed in the literature. In this thesis, we use the toolbox described in [250]. An exemplary signal subjected to the rainflow counting algorithm is shown in Fig. 9.3. According to [326], the so-called half-cycles, i.e. a series of unmatched peaks and
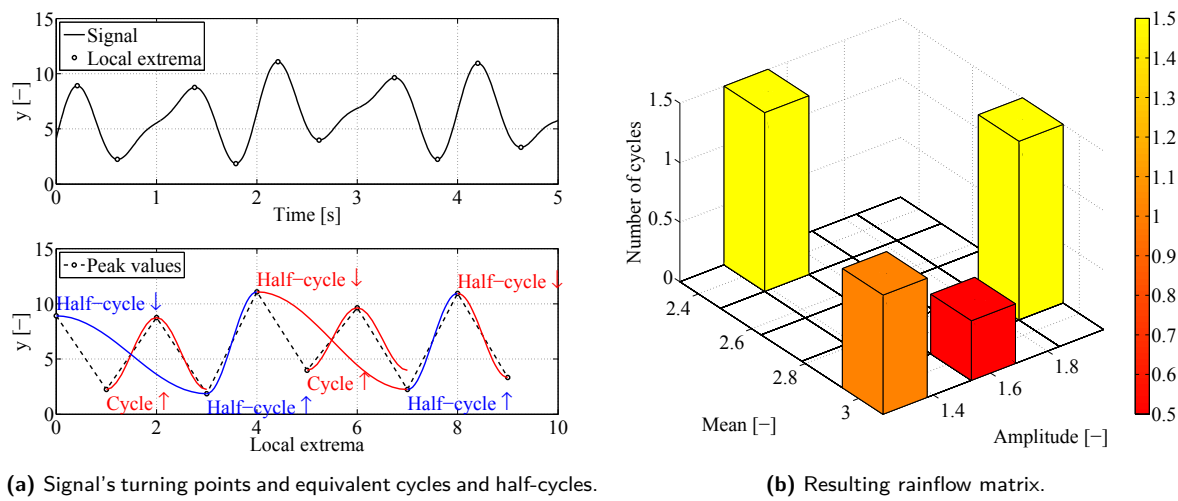

(a) Signal's turning points and equivalent cycles and half-cycles.

(b) Resulting rainflow matrix.

Figure 9.3: Exemplary signal subjected to the rainflow algorithm [271] – adapted from [250].

valleys, are also included in the cycle count, since they might carry information about the most damaging events (the largest cycles) which are not counted by the classical formulation of the rainflow algorithm. What is recommended in the IEC standard [152] is to treat all unclosed cycles as half-cycles, and this is the approach followed in this thesis.

9.3.3 Cumulative Damage

The well-known S–N (or Wöhler) curve defines the relation between the number of cycles to failure and cycle amplitude for a given material [94]. In log-log scale this curve is given as [230]

$$N_i = cS_i^{-b} \tag{9.10}$$

where N_i is the number of cycles with stress amplitude S_i needed to cause failure, c is the material specific parameter, and b is the fatigue exponent. Using the Palmgren–Miner linear accumulation damage law from [236] and [262], the total damage for cycles with different amplitudes is determined to be

$$D_S = \sum_i^m \frac{n_i}{N_i} = \frac{1}{c} \sum_i^m n_i S_i^b \tag{9.11}$$

where n_i is the number of cycles with stress amplitude S_i. According to [199] and [230], torque is roughly proportional to average stress by a constant r. This is an assumption, as in reality, stress may also depend on speed and/or present a non-proportional relation to the torque. Since proportionality does not affect the use of fatigue damage accumulation for comparative purposes, constants c and r can be set to unit values. Therefore, when the load is considered in the form of torque instead of stress, the following damage equation is arrived at [230]

$$D_T = \frac{r^b}{c} \sum_i^m n_i T_i^b = \sum_i^m n_i T_i^b. \tag{9.12}$$

S–N curves can be applied only for completely reversed loads. Therefore, when mean stress is present in loads, it has to be taken into account when finding an equivalent cyclic load. One of the most common approaches is to use the so-called Goodman relation, which has the following form

$$\sigma_{amp}^m = \frac{\sigma_{amp}}{\left(1 - \frac{\sigma_{mean}}{\sigma_u}\right)} \tag{9.13}$$

where σ_{amp}^m is the modified stress amplitude, σ_{amp} and σ_{mean} are amplitude and mean value of stress in a given cycle, respectively, and σ_u is the ultimate strength. According to [101], (9.13) is applicable to torque loads as well. Of course, loading cycles less than the endurance limit do not contribute to fatigue in stress-based fatigue analysis. Therefore, to determine the critical number of cycles that a component can withstand, it is essential to analyze only those stress levels that correspond to its S–N curve. However, knowledge of the S–N curve is not required if one's goal is to asses only the relative magnitude of cumulative damage that a given motion profile results in – which is the very goal of this Chapter.

9.4 Results and Discussion

The model of the full-scale electric drivetrain of the gripper arm illustrated in Fig. A.13 is implemented in the software SimulationX, as mentioned in Section A.4.2. Standard libraries and blocks from the domains of electro-mechanics and multibody systems are used to model the reference machine and its powertrain in order to benchmark the presented simulation results against the full-scale data logs. This modeling strategy is deliberately chosen in contrast to the techniques that require relatively deeper theoretical background and which are presented in Chapters 7 and 8. The reason is to illustrate that fatigue of drivetrain components can be conveniently assessed in initial phases of product development by relying exclusively on commercial multi-domain simulation software tools. What is particularly relevant in multidisciplinary industrial environment is that this modeling approach does not require expert knowledge of induction motor drives (or, in general, electrical engineering).

9.4.1 Vibration Severity

The reference data used for benchmarking simulation results for different motion profiles were acquired on the machine during hoisting and lowering a drill pipe for a simple constant acceleration input signal. The remaining three motion profiles are tested in a virtual simulation environment to reproduce operation of the full-scale machine in a pipe handling sequence. For each motion profile, we determine the corresponding jerk signal (using smooth differentiation

techniques from [144] and [212]) and the associated jerk energy, according to (9.9).[20]

The obtained results are illustrated in Fig. 9.4. They are normalized either with respect to the rated motor parameters, nominal vertical travel of the gripper arm, or to the associated nominal jerk values. Signal noise is neglected in the simulation, since it is justified for the purpose of comparative analysis. Acceleration ramp up/down periods are equal to 1/8 of the time provided to achieve a certain position (recall Section 9.1). The maximum allowable vertical acceleration of the gripper arm is selected to be $a_{max} = 5\ \% \cdot d_n/s^2$, according to specifications of the real machine for a constant acceleration function. The remaining three motion profiles are determined based on this requirement, as explained in Section 9.1 (they follow the relationships summarized in Table 9.1).

The resulting vertical travel of the machine is identical for each examined motion profile. The highest accumulated jerk energy is obtained for the constant acceleration profile (normalized value $JE = 23.5\%$). On the other hand, the profile which offers the lowest damage due to jerk discontinuities and vibrations is the modified trapezoidal one (normalized value $JE = 12.7\ \%$). The modified sinusoidal acceleration function gives lower value of the steady velocity at the cost of higher jerk energy. An interesting observation is made for the trigonometric jerk profile. Even though it is continuous, its jerk energy is relatively high, leading to potentially higher damage caused by vibrations. In the considered example, the increase in vibration severity for the examined motion profiles follows the relationships for the maximum jerk values presented in Table 9.1.

9.4.2 Fatigue Damage

For the period of machine operation shown in Fig. 9.4, we perform assessment of the fatigue damage caused by the examined motion profiles. We apply the rainflow algorithm to each torque signal in order to determine mean values and amplitudes of the corresponding cyclic loads, as explained in Section 9.3.2. The results are shown in Fig. 9.5. The equivalent cyclic amplitudes are found using the Goodman relation (9.13) and applied to determine the level of cumulative damage on drivetrain bearings. To improve clarity, an absolute damage (9.12) is expressed as the damage normalized with respect to the rated motor torque T_n

$$D_{TN} = \frac{\sum\limits_{i}^{m} n_i\, T_i^b}{\sum\limits_{i}^{m} n_i\, T_n^b}.$$

(9.14)

Since this study is focused on the relative damage rather than the absolute damage, material properties (fatigue exponent b and ultimate load S_u) of the considered drivetrain are selected according to [362] for a typical roller bearing. The normalized cumulative damage caused by each of the four examined motion profiles is summarized in Table 9.2. As expected, since the constant acceleration profile offers the lowest value of maximum acceleration (recall Table 9.1), it causes the lowest cumulative damage among the investigated functions. Although the maximum acceleration of the trigonometric jerk profile is just slightly lower than that of the

---

20. It is well-known that flexibility in a system (caused not only by its structural properties but also by controller action) smooths the actual velocity signal and mitigates the dynamic load on the machine, which is similar to using motion profiles derived from smooth acceleration functions. Therefore, to disregard the effect of the real-world controller on machine's vibration severity (and to provide for a fair comparison of the examined motion patterns), the jerk energy for the constant acceleration profile is computed based on the simulated jerk profile.
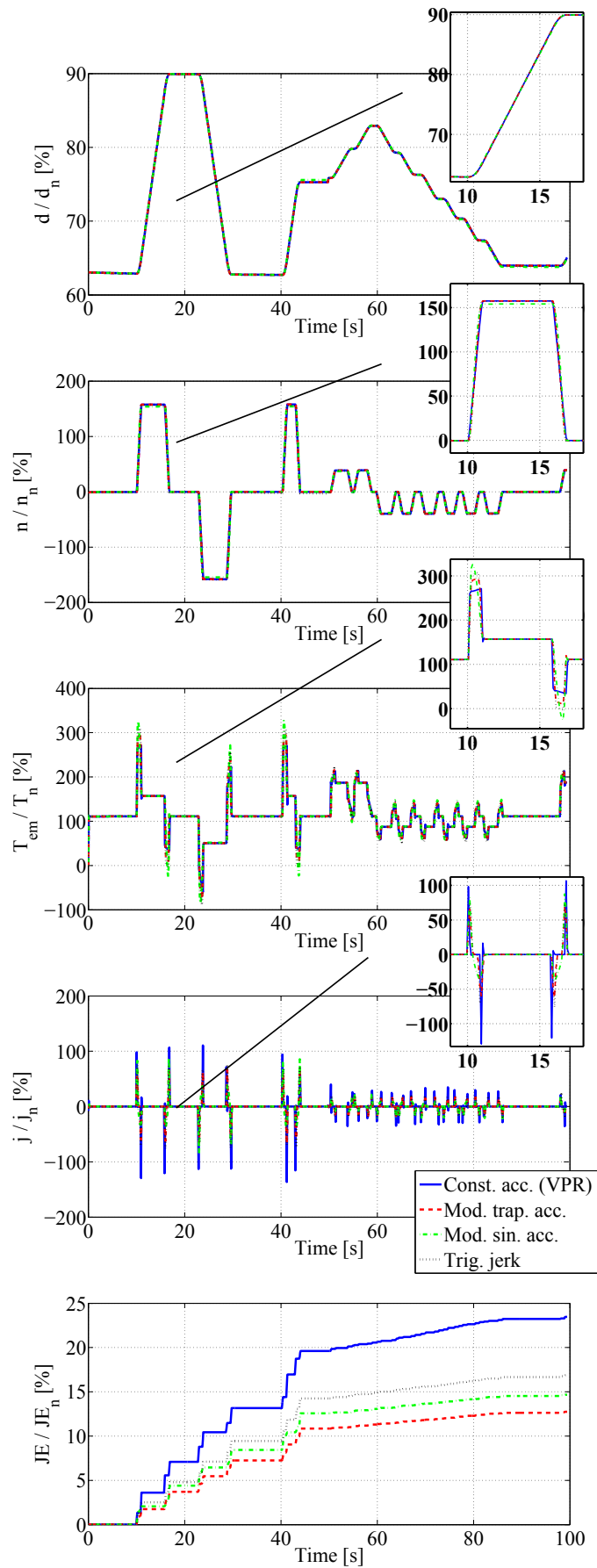
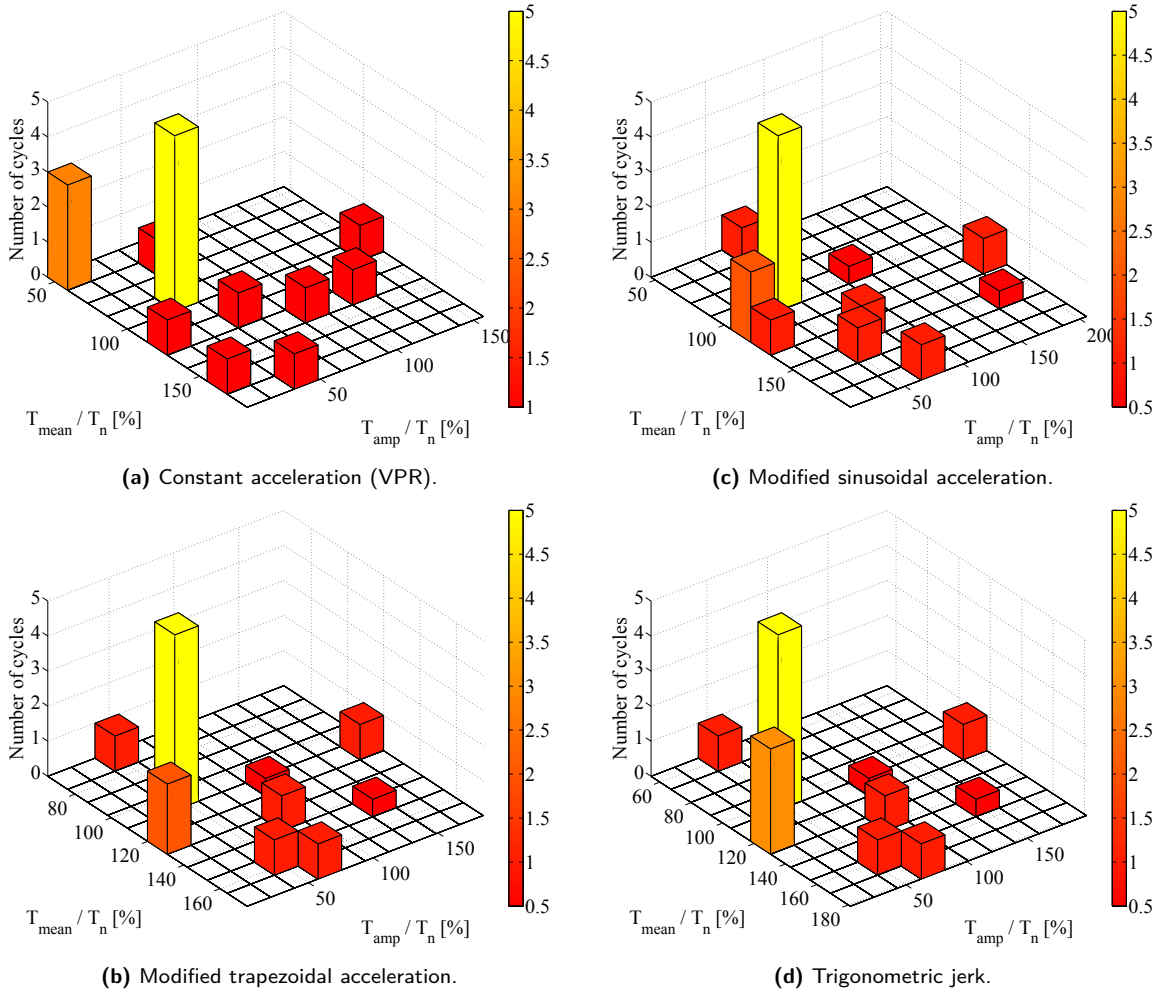**Figure 9.4:** Influence of motion profiles on drivetrain kinematics, torque, and jerk energy [271].

145

(a) Constant acceleration (VPR).

(c) Modified sinusoidal acceleration.

(b) Modified trapezoidal acceleration.

(d) Trigonometric jerk.

Figure 9.5: Rainflow counting for examined motion profiles [271].

Motion profile	Cumulative damage D_{TN}
Constant accel. (VPR)	0.2963
Mod. trapezoidal accel.	0.5682
Mod. sinusoidal accel.	0.8138
Trigonometric jerk	0.6707

Table 9.2: Cumulative damage benchmark for each motion profile

modified sinusoidal acceleration, the cumulative damage caused by the latter one is significantly higher. Therefore, even though the effect of torque on the cumulative damage is significant – power of b in (9.14) – it is still the number of identified cycles that plays an important role. Hence, in some cases, a profile that causes more oscillations of the machine but with lower amplitudes might be more severe to its life than a smooth steady profile characterized by higher loads.

Simulation results show that the popular constant acceleration profile gives the lowest cumulative damage at the cost of high jerk energy. Therefore, if there is enough flexibility in the machine (e.g. elasticity or dynamics affected by the control system) which could compensate for high jerk values, this profile is a justified choice. However, as soon as we deal with systems where the effect of vibrations cannot be disregarded, it becomes necessary to use profiles which provide for finite jerk shapes. The modified trapezoidal acceleration function gives both

the lowest cumulative damage and jerk energy which makes it a reasonable choice for such applications.

9.5 Conclusion

This study deals with comparative analysis of motion profiles used in actuation systems of offshore drilling equipment. Contrary to previous works, the proposed approach allows not only to benchmark which function gives the highest or lowest performance specifications (such as torque or speed) but also to explicitly assess levels of both fatigue and vibration severity of the system. In addition, it enables to estimate fatigue life of drivetrain components in the presence of changing loads. This could be applied to determine with a higher degree of confidence when a failure in rotating drivetrain elements might occur and schedule maintenance tasks well in advance to avoid machine downtime and high replacement costs. As a consequence, the current approach facilitates the drivetrain design process, since the information about the estimated fatigue life of a given component related to a certain motion pattern can now be made available to a design engineer early enough. This makes it possible not only to treat fatigue minimization as one of the design objectives, but also to incorporate the selection of the most appropriate motion profile into the drivetrain dimensioning procedure itself.

In the future, it is suggested to numerically evaluate the optimal selection of motion profiles and include this as an additional constraint in the optimization routine presented in Chapter 10, as it might lead to reduced conservatism when designing actuation systems. This should involve studying the absolute effect of full-scale stress profiles on machine components' life in order to validate/reject the assumption of torque-stress proportionality. In addition, high levels of torque experienced at low speeds are typically dangerous for induction motors due to the lack of proper cooling. It is obvious that from such a perspective, the constant acceleration profile is the worst, as it requires the full torque to be instantaneously available. Therefore, it is recommended to investigate the impact of various motion profiles on motor thermal behavior as well. Finally, analyzing their effects in combination with different controllers will give a better insight into the associated influence on fatigue and vibration severity and enable to quantify how much of e.g. jerk discontinuities can be additionally compensated by the controller action.

Part IV

Dimensioning of Induction Motor Drives

10 Optimal Selection of Drivetrain Components

This Chapter presents a method to optimally select components of a drivetrain for an electrically actuated machine.[21] A simple mathematical model of the machine is established and inequality constraints which determine the choice of drivetrain components are formulated, based on the background information given in Chapter 5. Elements to be picked (namely, a motor, a gearbox, and a drive) are taken from a discrete set of data provided in the catalogs of industrial motors and drives manufacturers. By solving an optimization problem, established by following the principles discussed in Chapter 6, a combination of components which both satisfies design requirements and minimizes total drivetrain cost is selected. The operation of the designed drivetrain is verified against the motor loadability curves. In addition, feasibility of other possible drivetrain configurations is checked and benchmarked with the optimal solution. Practical significance of the current work is demonstrated on a winch mechanism which is a popular part of many engineering applications, however, methods presented here could easily be adapted to other machines and industries. The results of the current work allow to reduce conservatism when designing actuation systems, while still satisfying the safety requirements specified by the designer. The system operating conditions are therefore effectively shifted to be closer to the constraints, which results in increasing the overall efficiency of the design and proving its cost-effectiveness.

10.1 Problem Statement

10.1.1 Drivetrain Design Optimization

A system being studied in the current work, as shown in Fig. 10.1, is a simplified representation of many industrial drivetrains. It consists of four parts, namely: a drive, an induction motor, a transmission, and a load. A common challenge for a design engineer is to pick from catalogs such a combination of the drive, motor, and gearbox that will both provide for handling the load according to specifications and be as cheap as possible. We present a method to optimally select these components by considering both the design requirements (expressed as inequality constraints) and the optimization objective (minimization of the drivetrain total cost).

10.1.2 Mathematical Formulation

As discussed in Section 6.4.2, if some decision variables x of a nonlinear optimization problem (6.2) are binary or integer (n_b), and belong to a real Euclidean space [53], as well as the objective and constraint functions are linear (recall Section 6.2.1), the problem is called a

---

21. This Chapter is reproduced (with minor changes) from publication [270].
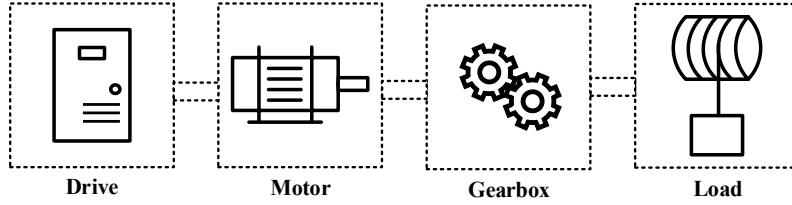
Figure 10.1: Schematic representation of a typical industrial drivetrain system [270].

mixed integer linear program (MILP). Such an optimization problem can be rewritten based on (6.76) as

$$
\begin{aligned}
\min_{x} \quad & c^T x \\
\text{s.t.} \quad & a_i^T x \leq b_i, \quad i = 1, \ldots, k \\
& x \in \{0, 1\}^{n_b} \cup \mathbb{R}^{n - n_b}
\end{aligned}
\tag{10.1}
$$

where the vectors $c, a_1, \ldots, a_k \in \mathbb{R}^n$ and scalars $b_1, \ldots, b_k \in \mathbb{R}$ are problem parameters that specify the objective and constraint functions.

10.2 Case Study

10.2.1 Mechanical System Modeling

As an example of a mechanical system actuated by an electric drivetrain, we pick a simple winch mechanism [7] – see Fig. 10.2. A common requirement for this type of a machine
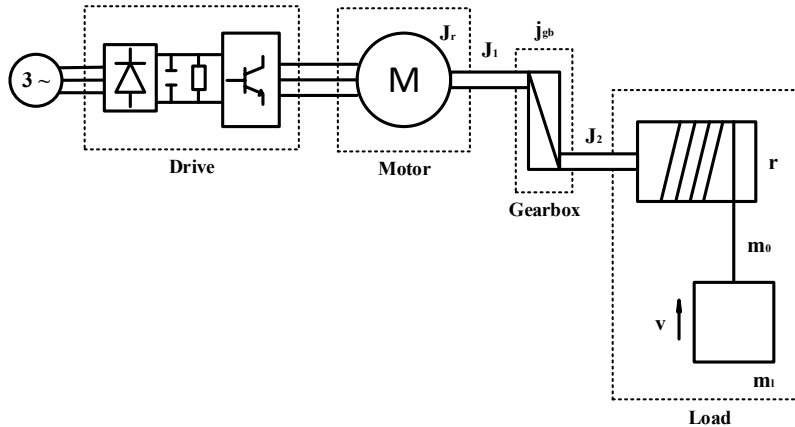

Figure 10.2: A hoist drive system used as a case study [270].

is to achieve certain vertical hoisting speeds of the payload within the given time intervals. Typically, three operating speeds are defined: minimum v_{min}, base v_{base}, and maximum v_{max} (all in $[m/s]$). The corresponding motor speed n $[rpm]$ for each range satisfies

$$
n = \omega \cdot \frac{60}{2\pi} = \frac{v}{r} \cdot j_{gb} \cdot \frac{60}{2\pi}
\tag{10.2}
$$

where ω $[rad/s]$ is the angular velocity, r $[m]$ is the drum radius and j_{gb} is the gearbox ratio. The effective mass moment of inertia J_{eff} $[kgm^2]$ seen by the motor is computed as (recall

Examples 5.2 and 5.3)

$$J_{eff} = J_r + J_1 + \frac{J_2 + \dfrac{1}{\eta_{mech}} \cdot (m_0 + m_l) \cdot r^2}{j_{gb}^2} \tag{10.3}$$

where J_r is the rotor inertia, J_1 is the inertia of the motor's side shaft, J_2 is the inertia of the drum's side (shaft, winch, and gearbox), m_0 is the mass of the wire, m_l is the payload mass, and η_{mech} is the total mechanical efficiency of the drivetrain. A constant torque/power application illustrated in Fig. 10.3 is considered here, contrary to constant torque application examined in Examples 5.3 and 5.4. It is a combination of the constant torque load type
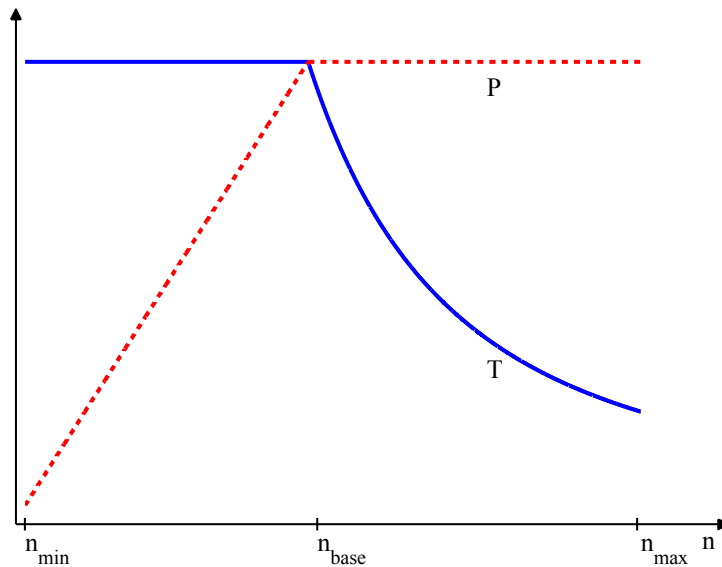

Figure 10.3: Torque and power curves in a conventional constant torque/power application [270].

(common for handling fixed volumes) and constant power load type (applicable where the power demand is independent of motor speed). In this load scenario, the required torque at n_{min} is the same as at n_{base}. The convention of notation assumes using the subscripts for speed ranges and superscripts for load properties. Hence, the required continuous hoisting torques are (in $[Nm]$)[22]

$$T_{min}^{cont} = T_{base}^{cont} = T_{base}^{ss} \cdot \text{RMS} = \frac{(m_0 + m_l) \cdot g \cdot v_{base}}{\omega_{base} \cdot \eta_{mech}} \cdot \text{RMS} \tag{10.4}$$

$$T_{max}^{cont} = \frac{P_{max}^{cont}}{\omega_{max}} \tag{10.5}$$

where g is the gravity constant. Similarly, the required hoisting powers become (in $[W]$)

$$P_{min}^{cont} = \frac{(m_0 + m_l) \cdot g \cdot v_{min}}{\eta_{mech}} \cdot \text{RMS} \tag{10.6}$$

$$P_{max}^{cont} = P_{base}^{cont} = \frac{(m_0 + m_l) \cdot g \cdot v_{base}}{\eta_{mech}} \cdot \text{RMS}. \tag{10.7}$$

---

22. Remember to increase the continuous torque and power demand by the RMS value of a desired duty cycle, as presented in Example 5.4.

By considering the required acceleration times for both speed ranges t_{base}^{acc} and t_{max}^{acc}, it is possible to determine relationships for the maximum (i.e. overload) values of motor torque, according to the specified constant torque/power load type [12]

$$T_{min}^{ovrl} = T_{base}^{ovrl} = T_{base}^{acc} + T_{base}^{ss} = \frac{\omega_{base}}{t_{base}^{acc}} \cdot J_{eff} + T_{base}^{ss} \qquad (10.8)$$

$$T_{max}^{ovrl} = \begin{cases} T_{max}^{ovrl,act} & \text{if } T_{max}^{ovrl,act} > T_{max}^{cont} \\ T_{max}^{cont} & \text{if } T_{max}^{ovrl,act} \leq T_{max}^{cont} \end{cases} \qquad (10.9)$$

where

$$T_{max}^{ovrl,act} = \frac{P_{base}^{cont}}{\omega_{max}} \cdot \frac{\text{OL}_{max}}{\text{RMS}} \qquad (10.10)$$

$$\text{OL}_{max} = \frac{T_{max}^{ovrl,theor}}{T_{base}^{ss}} \cdot 100\ \% \qquad (10.11)$$

$$T_{max}^{ovrl,theor} = T_{max}^{acc} + T_{base}^{ss} = \frac{\omega_{max}}{t_{max}^{acc}} \cdot J_{eff} + T_{base}^{ss}. \qquad (10.12)$$

The theoretical overload torque at maximum speed $T_{max}^{ovrl,theor}$ (computed in (10.12) analogously to (10.8)) has to be lowered due to constant power demand (if, of course, $n_{max} > n_n$), as visualized in Fig. 10.3. Therefore, the actual value of the overload torque $T_{max}^{ovrl,act}$ is computed in (10.10), according to [12]. There is no point in considering this torque as overload anymore if its value is less than or equal to the continuous torque demand at maximum speed T_{max}^{cont}, hence the if-condition in (10.9). Also, if T_{max}^{acc} is replaced in (10.12) by T_{base}^{acc}, the familiar overload relationship at base speed is obtained (recall Example 5.4)

$$\text{OL} = \frac{T_{base}^{ovrl}}{T_{base}^{ss}} \cdot 100\ \%. \qquad (10.13)$$

If the acceleration time and hoisting speed demands are identical, i.e.

$$\frac{v_{base}}{t_{base}^{acc}} = \frac{v_{max}}{t_{max}^{acc}} \qquad (10.14)$$

the overload ratios at base and maximum speeds become equal: $\text{OL} = \text{OL}_{max}$. Similarly, as there are no additional requirements on acceleration time at v_{min}, it is reasonable to assume $T_{min}^{ovrl} = T_{base}^{ovrl}$, as shown in (10.8).

10.2.2 Electrical System Modeling

According to [7], below the field weakening point, the direct and quadratic current components of the induction motor can be approximated as, respectively

$$I_{sd} = I_n \left(\sin \varphi_n + \cos \varphi_n \left(\sqrt{\left(\frac{T_b}{T_n}\right)^2 - 1} - \sqrt{\left(\frac{T_b}{T_n}\right)^2 - \left(\frac{T_{load}}{T_n}\right)^2} \right) \right) \qquad (10.15)$$

$$I_{sq} = I_n \left(\frac{T_{load}}{T_n} \right) \cos \varphi_n \qquad (10.16)$$

where T_b, T_n and I_n are the motor maximum and rated torques and current, respectively, and $\cos \varphi_n$ is the motor power factor. Hence, the total motor current is

$$I_m = \sqrt{I_{sd}^2 + I_{sq}^2}. \qquad (10.17)$$

According to [7] and as already mentioned in Example 5.6, the final approximation for the motor total current in the constant flux range is

$$I_{m,cf} = I_n \left(\frac{T_{load}}{T_n} \right) \quad \text{if} \ \ 0.8 \cdot T_n \leq T_{load} \leq 0.7 \cdot T_b. \tag{10.18}$$

Therefore, to compute the resulting motor current, two cases have to be studied: the continuous and maximum loads. This gives the values of motor currents in each scenario

$$I_{m,cf}^{cont} = I_n \left(\frac{T_{base}^{cont}}{T_n} \right) \tag{10.19}$$

$$I_{m,cf}^{ovrl} = I_n \left(\frac{T_{base}^{ovrl}}{T_n} \right). \tag{10.20}$$

In the field weakening region, the motor currents additionally depend on speed and can be approximated as

$$I_{sd} = I_n \left[\frac{n_n}{n} \left(\sin \varphi_n + \cos \varphi_n \sqrt{\left(\frac{T_b}{T_n} \right)^2 - 1} \right) - \cos \varphi_n \sqrt{\left(\frac{T_b}{T_n} \cdot \frac{n_n}{n} \right)^2 - \left(\frac{T_{load}}{T_n} \cdot \frac{n}{n_n} \right)^2} \right] \tag{10.21}$$

$$I_{sq} = I_n \left(\frac{T_{load}}{T_n} \cdot \frac{n}{n_n} \right) \cos \varphi_n. \tag{10.22}$$

Hence, the final approximation for the motor total current in the field weakening range is

$$I_{m,fw} = I_n \left(\frac{T_{load}}{T_n} \cdot \frac{n}{n_n} \right) \quad \text{if} \ \ 0.8 \cdot T_n \left(\frac{n_n}{n} \right) \leq T_{load} \leq 0.7 \cdot T_b \left(\frac{n_n}{n} \right)^2. \tag{10.23}$$

Therefore, we compute the resulting motor currents in the field weakening range in a similar manner as in the constant flux range

$$I_{m,fw}^{cont} = I_n \left(\frac{T_{base}^{cont}}{T_n} \cdot \frac{n}{n_n} \right) \tag{10.24}$$

$$I_{m,fw}^{ovrl} = I_n \left(\frac{T_{base}^{ovrl}}{T_n} \cdot \frac{n}{n_n} \right). \tag{10.25}$$

Finally, the maximum power required by the drive is equal to

$$P_m^{ovrl} = \frac{P_{base}^{ovrl}}{\eta_m} \tag{10.26}$$

where η_m is the motor efficiency and the maximum required motor power is

$$P_{base}^{ovrl} = P_{base}^{cont} \cdot \frac{T_{base}^{ovrl}}{T_{base}^{cont}}. \tag{10.27}$$

10.3 Method for Drivetrain Design

The electric drivetrain design procedure presented in Chapter 5 (illustrated in Examples 5.5 and 5.6) is benchmarked with the proposed modified design process. The former approach assumes that the gear ratio is known *a priori*, however, as shown in Section 10.5, we incorporate the selection of the transmission into the drivetrain dimensioning. Also, we introduce additional performance/safety constraints, such as constraints on the available torque, that allow to control how much additional safety is required for a given application. They are defined for each speed region n_{min}, n_{base}, and n_{max} as

$$\delta T_m^{cont} = \left(\frac{T_m^{cont}}{T^{cont}} - 1 \right) \cdot 100 \ \% \tag{10.28}$$

$$\delta P_m^{cont} = \left(\frac{P_m^{cont}}{P^{cont}} - 1 \right) \cdot 100 \ \% \tag{10.29}$$

$$\delta I_d = \left(\frac{I_d}{I_m} - 1 \right) \cdot 100 \ \% \tag{10.30}$$

$$\delta P_d = \left(\frac{P_d^{ovrl}}{P_m^{ovrl}} - 1 \right) \cdot 100 \ \%. \tag{10.31}$$

According to [7], the first step when designing an electric actuation system is to check the mains supply voltage level U_{sup} and frequency f_{sup}. Then, process requirements are investigated – starting torque, speed range, or load types. This information is a basis to select the motor. It needs to withstand process overloads and deliver a specified amount of torque. Finally, the frequency converter is selected according to the initial conditions and the selected motor. Its capability of producing the required current and power is evaluated. The resulting drive power is computed as (5.32) and rewritten here for convenience [12]

$$P_d^{ovrl} = \sqrt{3} \cdot U_{sup} \cdot I_{hd} \cdot (OL_{hd}/100) \cdot PF \tag{10.32}$$

where I_{hd} is the drive heavy duty current, OL_{hd} is the heavy duty overload allowing 150 % of overload for 1min / 5min at 40°C – see [10], and PF is the motor power factor. To check the conditions for motor allowable torque, we use the motor loadability curves available from the manufacturers catalogs, e.g. [13], as explained in Section 5.3. Loadability curves for a typical, self-ventilated induction motor are shown in Fig. 10.4. Based on them, we also find the actual motor power values at each point of interest, namely: $P_{m,min}^{cont}$, $P_{m,base}^{cont}$, and $P_{m,max}^{cont}$.

The inequality constraints summarized in (10.33) define the conditions that need to be satisfied by the selected drivetrain components, so that the machine performs according to the design specifications. In addition, it should be checked that the required overload torque stays below the maximum motor loadability curve $T^{ovrl} \leq T_m^{ovrl}$ (as illustrated in Example 5.5, for instance). This is omitted here to simplify the analysis, under the assumption that the motor duty cycle is formulated in a way which prevents the motor drive from overheating. As a consequence, no temperature rise of the motor drive is investigated, however, a solution to this problem is thoroughly elaborated on in Chapter 11.
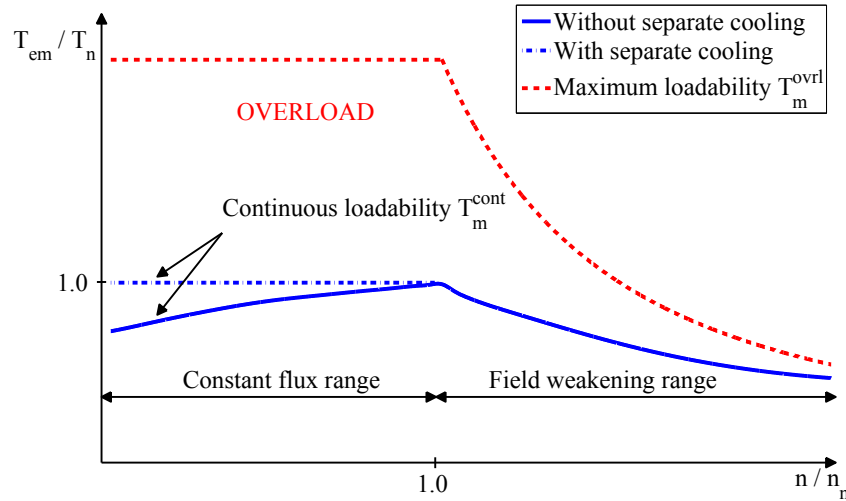
Figure 10.4: Typical loadability curves for inverter-fed induction motor [276].

Motor torque
$$\begin{cases} T_{m,min}^{cont} \geq T_{min}^{cont} \\ T_{m,base}^{cont} \geq T_{base}^{cont} \\ T_{m,max}^{cont} \geq T_{max}^{cont} \end{cases} \quad (10.33a)$$

Drive current
$$\begin{cases} I_d^{cont} \geq I_m^{cont} \\ I_d^{ovrl} \geq I_m^{ovrl} \end{cases} \quad (10.33b)$$

Drive power
$$\begin{cases} P_d^{ovrl} \geq P_m^{ovrl} \end{cases} \quad (10.33c)$$

Motor torque margins
$$\begin{cases} \delta T_{m,min}^{cont} \geq \delta_T \\ \delta T_{m,base}^{cont} \geq \delta_T \\ \delta T_{m,max}^{cont} \geq \delta_T \end{cases} \quad (10.33d)$$

Motor power margins
$$\begin{cases} \delta P_{m,min}^{cont} \geq \delta_P \\ \delta P_{m,base}^{cont} \geq \delta_P \\ \delta P_{m,max}^{cont} \geq \delta_P \end{cases} \quad (10.33e)$$

Drive current margins
$$\begin{cases} \delta I_d^{cont} \geq \delta_I \\ \delta I_d^{ovrl} \geq \delta_I \end{cases} \quad (10.33f)$$

Drive power margin
$$\begin{cases} \delta P_d^{ovrl} \geq \delta_{P,d}. \end{cases} \quad (10.33g)$$

10.4 Design Example

The selected parameters of the system shown in Fig. 10.2 and its design requirements are summarized in Table 10.1. The required duty cycle which defines the magnitude and duration of overloads both at n_{base} and n_{max} is illustrated in Fig. 10.5.

The lists of drives and motors available for selection, shown in Tables 10.2 and 10.4, are composed of products chosen from [10] and [13], respectively. The allowable gear ratios are listed in Table 10.3. The presented cost is not the real price of the components, rather it is an estimate based on the motor weight, drive frame size, and gearbox ratio. This assumption is
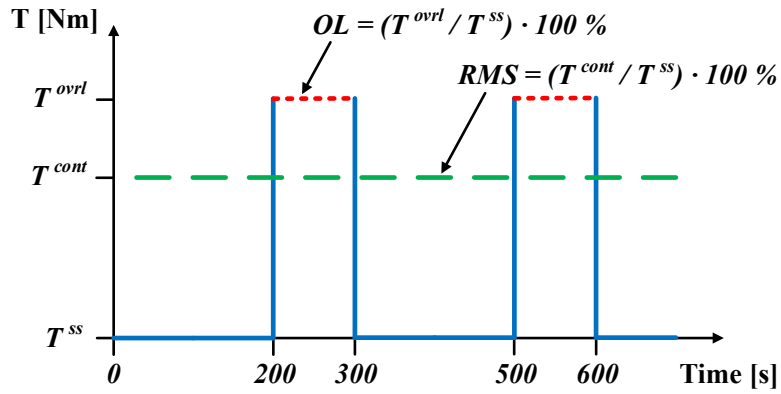
Figure 10.5: Duty cycle assumed for overloads at base and maximum speeds.

sufficient for testing the optimization algorithm. The task of a design engineer (here replaced by the optimization routine) is to select such a combination of drive, motor, and gearbox so that the design requirements from (10.33) and Table 10.1 are met and the total cost of all components is the lowest possible.

System data	Requirements	Safety margins
$m_0 = 1000 \; [kg]$	$v_{min} = 0.1 \; [m/s]$	Motor torque $\delta_T = 10 \; \%$
$m_l = 4000 \; [kg]$	$v_{base} = 0.5 \; [m/s]$	Motor power $\delta_P = 10 \; \%$
$\eta_{mech} = 0.855 \; [-]$	$v_{max} = 0.8 \; [m/s]$	Drive current $\delta_I = 10 \; \%$
$r = 1 \; [m]$	$t_{base}^{acc} = 1 \; [s]$	Drive power $\delta_{P,d} = 10 \; \%$
$J_1 = 0.1 \; [kgm^2]$	$t_{max}^{acc} = 6 \; [s]$	
$J_2 = 1 \; [kgm^2]$		

Table 10.1: Numerical data of mechanical system and powertrain design specifications [270].

No.	$I_d^{cont} \; [A]$	$I_d^{ovrl} \; [A]$	$I_{hd} \; [A]$	Cost [$]
#1	34	46	23	500
#2	44	62	32	800
#3	55	72	37	850
#4	72	86	49	1100
#5	86	112	60	1150
#6	103	138	69	1200
#7	145	170	100	1250
#8	166	202	115	1550

No.	$j_{gb} \; [-]$	Cost [$]
#1	200	145
#2	250	155
#3	300	195
#4	350	210
#5	400	230
#6	450	295
#7	500	310
#8	550	330
#9	600	395
#10	650	410
#11	700	430

Table 10.2: Frequency converters catalog data [270].   **Table 10.3:** Gearboxes catalog data [270].

No.	P_n [kW]	T_n [Nm]	n_n [rpm]	I_n [A]	J_r [kgm²]	$2p$ [−]	PF [−]	η_m [−]	Cost [$]
#1	7.5	49.3	1450	14.9	0.037	4	0.81	0.89	73
#2	15	194	737	32.4	0.450	8	0.74	0.90	290
#3	18.5	178	988	36.4	0.382	6	0.80	0.92	269
#4	18.5	239	739	40.1	0.669	8	0.73	0.91	350
#5	22	142	1475	40.9	0.195	4	0.84	0.92	222
#6	22	212	987	42.0	0.448	6	0.82	0.92	291
#7	22	284	738	46.8	0.722	8	0.74	0.92	363
#8	30	193	1480	55.3	0.309	4	0.84	0.93	291
#9	30	290	986	56.2	0.663	6	0.83	0.93	349
#10	37	119	2959	63.5	0.196	2	0.90	0.93	298
#11	37	238	1479	68.0	0.356	4	0.84	0.93	324
#12	45	290	1480	81.3	0.440	4	0.85	0.94	356
#13	55	354	1480	98.9	0.765	4	0.85	0.94	414

Table 10.4: Induction motors catalog data [270].

10.5 Solution Strategy

Due to the nonlinearity of the drivetrain design optimization problem – e.g. the torque delivered by the motor is multiplied by the gear ratio and both have to be optimized (i.e. (10.2) appears in (10.4)) – adapting a nonlinear problem of the form (6.87) to find the solution will not be efficient. Therefore, the optimization problem is reformulated according to (10.1) as a binary linear program (BLP) (6.71) and becomes (recall Example 6.7)[23]

$$
\begin{aligned}
\min_{x} \quad & \mathbf{J}^T\mathbf{x} \\
\text{s.t.} \quad & \mathbf{A}\mathbf{x} \le \mathbf{b} \\
& x_i \in \{0, 1\}, \quad i = 1, \dots, n
\end{aligned}
\tag{10.34}
$$

where $\mathbf{x} \in \{0,1\}^n$ is the decision variable, $\mathbf{J} \in \mathbb{R}^n$ is the cost function to be minimized, $\mathbf{A} \in \mathbb{R}^{m \times n}$ is the constraint matrix, and $\mathbf{b} \in \mathbb{R}^m$ is the constraint vector. Each x_i is one particular combination of a drive, a motor, and a gearbox. Hence, the length of the optimization variable vector, $n = 1144$, is equal to the product of the number of available drives, $n_d = 8$, motors, $n_m = 13$, and gearboxes, $n_{gb} = 11$, whereas the number of rows of the constraint matrix $\mathbf{A}$ corresponds to the number of inequality constraints introduced in (10.33), $m = 16$. The last constraint of $\mathbf{A}$ in (10.36) ensures that no more than only one combination of drivetrain components is selected, i.e.

$$
\sum_{i=1}^{n} x_i \le 1.
\tag{10.35}
$$

Therefore, each of the specification inequalities from (10.33) is now considered to be a row vector which elements are indexed according to a given combination of drivetrain components. The objective function is the total cost of the selected parts. The final optimization problem is formulated based on (10.33) and (10.34) as (10.36). This combinatorial problem is solved using MATLAB interfaced with YALMIP modeling language [209] and CPLEX solver [151]. The obtained solution $x^\star$ is a vector with all zeros and a single one, that corresponds to the most cost-effective selection of components that satisfies the design requirements.

---

23. For better clarity, boldface letters are used to denote vectors and matrices.

$$
\min_{x} \quad \underbrace{[\mathbf{J}_d + \mathbf{J}_m + \mathbf{J}_{gb}]}_{\mathbf{J}_{(1 \times n)}} \cdot \underbrace{\begin{bmatrix} x_1 \\ \dots \\ x_n \end{bmatrix}}_{\mathbf{x}_{(n \times 1)}}
$$

$$
\text{s.t.} \quad \underbrace{\begin{bmatrix} \mathbf{T}^{cont}_{min} - \mathbf{T}^{cont}_{m,min} \\ \mathbf{T}^{cont}_{base} - \mathbf{T}^{cont}_{m,base} \\ \mathbf{T}^{cont}_{max} - \mathbf{T}^{cont}_{m,max} \\ \mathbf{I}^{cont}_{m} - \mathbf{I}^{cont}_{d} \\ \mathbf{I}^{ovrl}_{m} - \mathbf{I}^{ovrl}_{d} \\ \mathbf{P}^{ovrl}_{m} - \mathbf{P}^{ovrl}_{d} \\ -\delta T^{cont}_{m,min} \\ -\delta T^{cont}_{m,base} \\ -\delta T^{cont}_{m,max} \\ -\delta P^{cont}_{m,min} \\ -\delta P^{cont}_{m,base} \\ -\delta P^{cont}_{m,max} \\ -\delta I^{cont}_{d} \\ -\delta I^{ovrl}_{d} \\ -\delta P^{ovrl}_{d} \\ 1 \end{bmatrix}}_{\mathbf{A}_{(m \times n)}} \cdot \underbrace{\begin{bmatrix} x_1 \\ \dots \\ x_n \end{bmatrix}}_{\mathbf{x}_{(n \times 1)}} \leq \underbrace{\begin{bmatrix} 0 \\ 0 \\ 0 \\ 0 \\ 0 \\ 0 \\ -\delta_T \\ -\delta_T \\ -\delta_T \\ -\delta_P \\ -\delta_P \\ -\delta_P \\ -\delta_I \\ -\delta_I \\ -\delta_{P,d} \\ 1 \end{bmatrix}}_{\mathbf{b}_{(m \times 1)}} \tag{10.36}
$$

$$
x_i \in \{0, 1\}, \quad i = 1, \dots, n
$$

10.6 Optimization Results

The combination of drivetrain components which is found to be the optimal solution of the problem (10.36) has the index value of $i_{opt} = 696$. Fig. 10.6a shows that this configuration gives the lowest cost out of all the feasible solutions. The resulting loadability of the designed drivetrain is benchmarked with the mechanical loads in Fig. 10.6b. The speeds of the motor that correspond to the requirements from Table 10.1 are determined to be $n_{min} = 286 \; rpm$, $n_{base} = 1432 \; rpm$, and $n_{max} = 2292 \; rpm$. The results show that the motor continuous loadability is above the continuous mechanical load in the whole speed range and that the maximum mechanical load stays almost entirely below the continuous motor loadability curve.[24] Table 10.5 summarizes the optimization results, including the final values of safety margins which are above the required limits specified in Table 10.1. In addition, this drivetrain optimization problem was solved in less than 1 s on a desktop PC.

---

24. This is, by the way, similar to the observation made in Example 5.5.
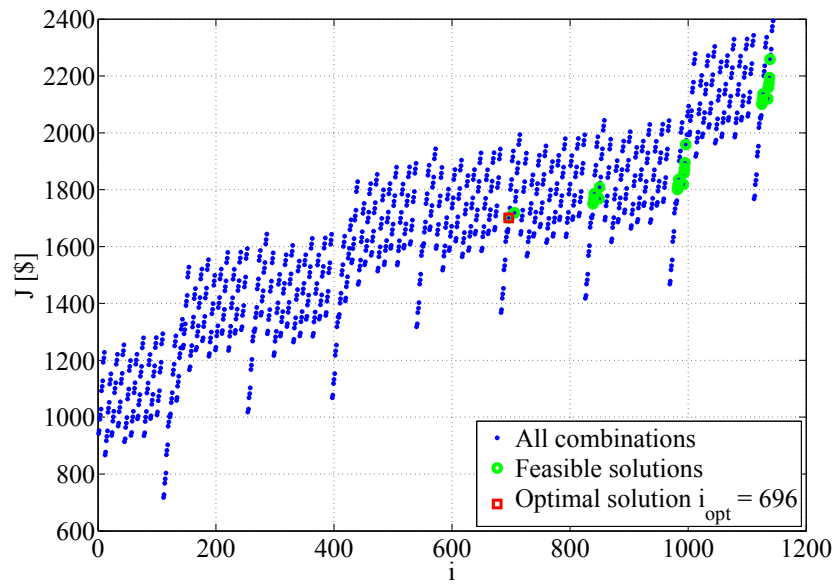
(a) Optimal configuration of drivetrain components [270].
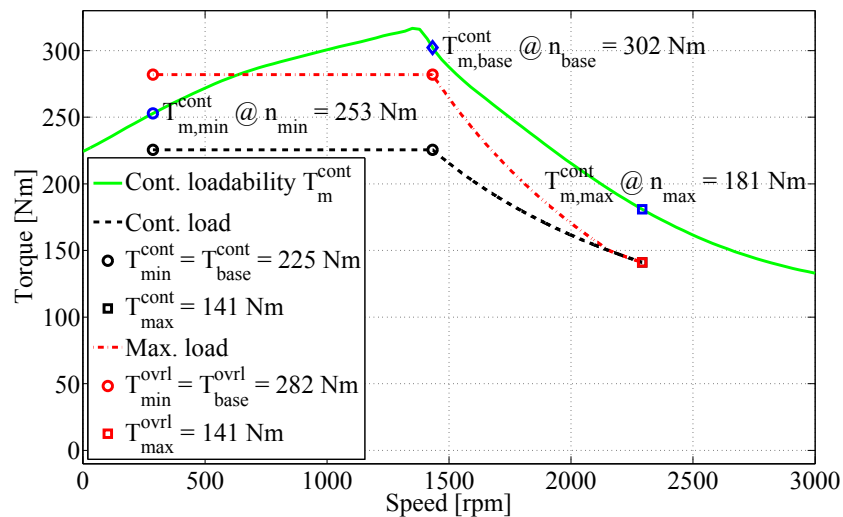
(b) Loadability of the selected motor #12.

Figure 10.6: Optimization results.

	Total	**Drive**	**Motor**	**Gearbox**
Solution index i_{opt}	#696	#5	#12	#3
Cost [$]	1701	1150	356	195

Resulting safety margins − motor					
$\delta T_{m,min}^{cont}$	$\delta T_{m,base}^{cont}$	$\delta T_{m,max}^{cont}$	$\delta P_{m,min}^{cont}$	$\delta P_{m,base}^{cont}$	$\delta P_{m,max}^{cont}$
12.1 %	34.0 %	28.3 %	12.1 %	34.0 %	28.3 %

Resulting safety margins − drive		
δI_d^{cont}	δI_d^{ovrl}	δP_d^{ovrl}
36.0 %	41.7 %	17.7 %

Table 10.5: Optimal drivetrain design [270].

10.7 Conclusion

In this Chapter, we develop a method to optimally select components of an electrical actuation system. The resulting combinatorial problem is formulated as a binary linear program and implemented in software composed of YALMIP as interface to MATLAB and CPLEX solver. Although such problems are known to be computationally demanding, this particular optimization problem appears to be tractable in practice, even for a large number of possible components. The results indicate a potential improvement in terms of effectiveness of drivetrain design optimization compared to other available solutions, with a certificate of global optimality being a significant advantage of the proposed method. In addition, the selection of the gearbox ratio becomes an integral part of the optimization process, in contrast to some toolboxes currently being used for drivetrains design, where the gearbox ratio has to be specified *a priori*. Finally, the solution time is negligible compared to the time that a design engineer would spend finding the right components manually in the catalogs.

In the future, it is recommended to include more constraints in the design process, e.g. maximum loadability curves, temperature limits for motor drives presented in Chapter 11, or selection of an optimal motion control pattern discussed in Chapter 9. Also, the approach introduced in Chapter 7 can be useful in order to determine the exact profile of the required electromagnetic torque for similar type of equipment. Finally, further verification and validation of an optimal drivetrain configuration will strengthen the impact of the proposed selection algorithm. This should involve both the evaluation of the designed actuation system in a virtual simulation environment and the experimental testing.

11 Temperature Rise Estimation of Electric Powertrains

Selection of components of electric drivetrains should not only be based on evaluating their ability to perform according to mechanical specifications, but – what is equally important – on assessing their thermal protection limits.[25] These are typically affected by electrical and thermal properties of motors and drives. Although rated parameters (such as power, torque, speed, current, etc.) are easily accessible in catalogs of equipment producers and drivetrain dimensioning based on using them is rather straightforward (as discussed in Chapters 5 and 10), more specific properties like mass/length of copper winding, heat dissipation factor, rotor/stator dimensions etc. are not available to customers. Therefore, the effective selection of drivetrain components is limited due to the lack of sufficient data and the need to consult critical design decisions with suppliers. To overcome this limitation, we propose a method to estimate temperature rise of motor drives based on popular loadability curves which are provided in catalogs. A simple first order thermal model is applied to represent heating/cooling phenomenon of inverter-fed induction motor. Parameters identification process is formulated as a nonlinear optimization problem and solved using commercial software products. Within the proposed approach it becomes possible to include the effect of reduced torque availability at low speeds in self-ventilated motors during design of electric actuation systems. Contrary to using a discrete set of permissible overload conditions that are provided in catalogs, the current methodology allows for evaluating a temperature rise of a motor drive for any overload magnitude, duty cycle, and ambient temperature. This has a potential to further improve the flexibility of the design process presented in Chapter 10 and facilitate communication in a supplier-customer dialog. The discussed method is verified against the overload recommendations suggested by the suppliers, yielding the same limits of temperature rise as given in the IEC standard [154].

11.1 Thermal Protection Theory

Degradation of stator insulation and rotor conductors are two main thermal risks for an overheated motor, according to [342]. It has been found ([63] and the references therein), that thermal aging of insulation could be represented as the Arrhenius chemical rate equation, which yields the following relationship for the life of insulation aged at elevated temperatures

$$L = D \exp\left(\frac{\varphi}{k\Theta}\right) \tag{11.1}$$

where L is the life in units of time, D is an experimentally determined constant, φ is the activation energy $[eV]$, Θ is the absolute temperature $[K]$, and $k = 0.8617 \cdot 10^{-4}$ $[eV/K]$

---

25. Some parts of this Chapter are reproduced (with minor changes) from publication [276].

is the Boltzmann constant. The IEC standard [154] defines the permissible operating temperatures and maximum allowable temperature rises above the ambient for induction motors. Table 11.1 and Fig. 11.1 show these safety margins for different thermal classes of motors. Typically, manufacturers use class F insulation with class B rise to gain additional 25 °C safety margin [228]. The recommended maximum temperature for class F is 155 °C, which consists of a maximum ambient temperature of 40 °C, permissible temperature rise of 105 °C, and a hot spot temperature margin of 10 °C. Obviously, lowering the value of ambient temperature allows for higher temperature rise, as long as the maximum limit of 155 °C is not violated.

Thermal level	Class A	Class B	Class F	Class H
Max ambient temp. [°C]	40	40	40	40
Permissible temp. rise [°C]	60	80	105	125
Hot spot temp. margin [°C]	105	130	155	180

Table 11.1: Composition of common insulation classes [276] − adapted from [154].
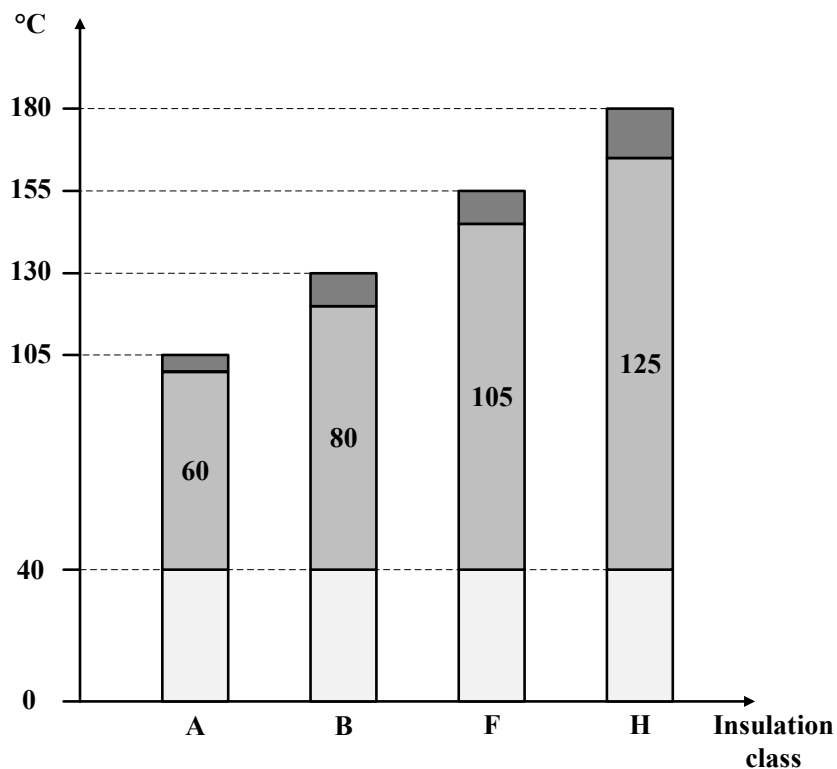

Figure 11.1: Temperature limits per thermal class − adapted from [154].

Exceeding the thermal limit causes gradual degradation of the expected lifetime of insulation. Fig. 11.2 illustrates the relationship (11.1) for different classes of insulation and based on the accepted rule that thermal life is halved for each increase of 10 °C above the maximum thermal limit, according to [63] and [342].

Therefore, apart from checking if a given motor will satisfy mechanical specifications (in short − if it provides sufficient torque at certain speeds), design engineers have to investigate if overloads do not violate thermal margins of the drivetrains they design. Motors and drives manufacturers provide guidelines and recommendations for maximum permissible thermal overload magnitudes and durations, but these suggestions are typically so general that they
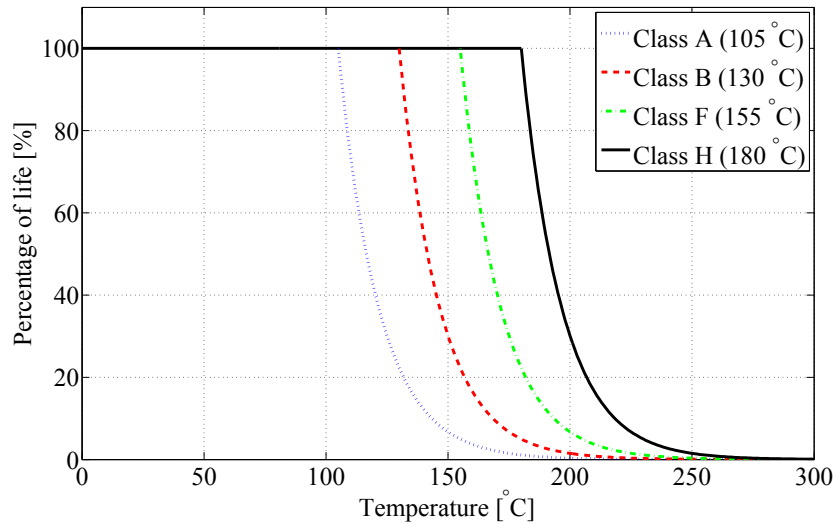
Figure 11.2: Influence of thermal aging on motor insulation life – reproduced from [342].

could only be applied in a few very specific scenarios [10, 13, 146, 297, 310, 315], as briefly commented on in Section 5.2.2. To address this issue, we introduce a more general framework to examine drivetrains thermal performance, which allows to estimate motor temperature in various operating conditions using the available limited catalog data.

11.2 Power Flow and Losses Modeling

The power flow diagram which represents the relationship between the input electric power and the output mechanical power of an induction motor is illustrated in Fig. 11.3. The three-
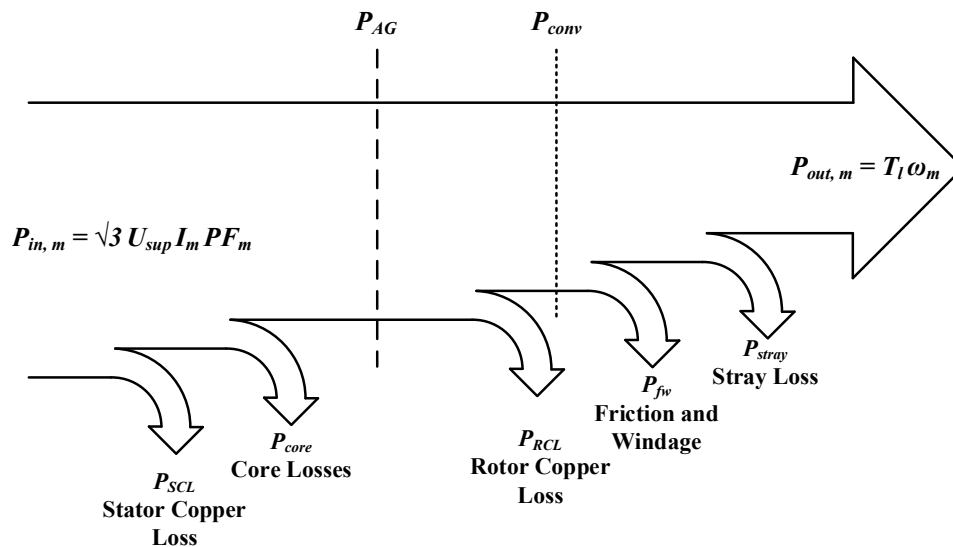

Figure 11.3: Power flow diagram of induction motor [75].

phase electric supply determines the input power $P_{in,m}$ to the motor. The stator winding losses $P_{SCL} = I^2 R_s$ (also referred to as stator copper losses) and the core losses due to eddy currents and hysteresis P_{core} are the first encountered losses before the remaining power is transferred to the rotor of the machine across the air gap [75]. The air gap power P_{AG} is then reduced due to the rotor copper losses $P_{RCL} = I^2 R_r$ and the remaining power is converted from electrical

to mechanical form P_{conv}. Friction and windage losses P_{fw} as well as stray losses P_{stray} are final factors that contribute to lowering the output motor power $P_{out,m}$. According to [75], friction, windage, and stray losses increase with higher speeds of IM, while core losses become lower (up to synchronous speed ω_s). These three types of losses are normally combined and called rotational losses. As a consequence, it is a common assumption to consider rotational losses to be constant regardless of motor speed, since their components change in opposite directions for variable frequencies [75].

A popular approach to model losses in induction motors is to represent each loss in Fig. 11.3 by the corresponding resistance element in the motor equivalent circuit [198]. In that case, the resistive losses are separated from the other losses (core, stray, and mechanical). When no field data are available, it is an accepted practice to assume their typical values in relation to the total losses $P_{loss,m} = P_{in,m} - P_{out,m}$, for instance: mechanical losses constitute approx. 14 % of total losses, whereas core losses account for approx. 12 %. In addition, the IEEE standard [157] defines guidelines for determining stray losses depending on motor size. Finally, the resistive losses of stator and rotor windings can be identified analytically, as presented in [198]. The overall efficiency of the drivetrain $\eta = P_{out}/P_{in}$ is affected by efficiency of both motor and VFD. Since both motor's and VFD's losses are of thermal character, they appear as extra induced heat [6]. Therefore, Fig. 11.3 can be generalized to consider the nature of losses of a generic electric powertrain, as presented in Fig. 11.4. The electrical input power
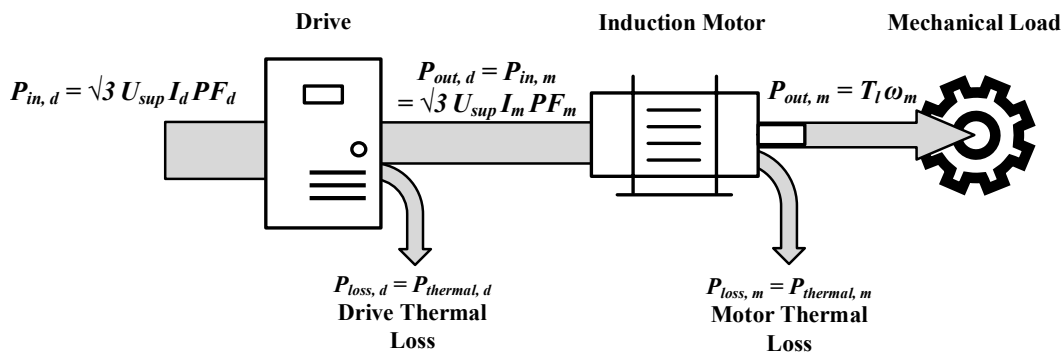

Figure 11.4: Simplified representation of thermal losses in electric drivetrain [6].

of a three-phase system P_{in} depends on the supplied voltage U_{sup}, current I and power factor PF (also denoted as $\cos\varphi_n$), and holds for both drive (subscript d) and motor (subscript m). The power factor describes the share of active power (production of mechanical power) and reactive power (production of motor magnetization) in the total electric power. The mechanical motor power is affected by the required load torque T_l and motor rotational speed ω_m. VFD manipulates the voltage fed to the motor to meet these load demands and hence, it controls its power consumption. Example 11.1 demonstrates a typical power flow in an induction motor drive.

> **Example 11.1 (Drivetrain Power Consumption)**
> Suppose there is a 45 kW/400 V induction motor drive system, characterized as (it is actually composed of motor #12 from Table 10.4) [13]:
>
> - motor mechanical power $P_n = P_{out,m} = 45\ kW$,
> - input voltage $U_{sup} = 400\ V$,
> - motor efficiency $\eta_m = 93.9$ %,
> - motor power factor $PF_m = 0.85$.

The motor electrical input power and current (i.e. drive output power and current) become, respectively

$$P_{in,m} = P_{out,d} = \frac{P_{out,m}}{\eta_m} = \frac{45\ kW}{0.939} = 47.9\ kW \tag{11.2}$$

$$I_m = \frac{1000 \cdot P_{in,m}}{\sqrt{3} \cdot U_{sup} \cdot PF_m} = \frac{1000 \cdot 47.9}{\sqrt{3} \cdot 400 \cdot 0.85} = 81.3\ A. \tag{11.3}$$

Therefore, assuming the drive efficiency $\eta_d = 99\ \%$ and power factor $PF_d = 0.97$, we obtain the drive input power and current, respectively

$$P_{in,d} = \frac{P_{out,d}}{\eta_d} = \frac{47.9\ kW}{0.99} = 48.4\ kW \tag{11.4}$$

$$I_d = \frac{1000 \cdot P_{in,d}}{\sqrt{3} \cdot U_{sup} \cdot PF_d} = \frac{1000 \cdot 48.4}{\sqrt{3} \cdot 400 \cdot 0.97} = 72.0\ A. \tag{11.5}$$

The drive input current I_d is approx. 11 % lower than the drive output current to the motor I_m. This difference shows how VFD can improve the power factor of the three-phase system [280]. The price to pay, however, is the drive input power $P_{in,d}$ being higher than the motor input power $P_{in,m}$ but this variation is only 1 % in the considered example. Even though the primary reason for using variable speed AC drives is not improvement of power factor but better process control, cost-effective operation, and reduced wear of machinery, the lowered drive input current is a positive side effect that this solution offers [280].

Finally, the knowledge of the input and output power of both motor and VFD allows to compute their total losses which contribute to increasing their temperature

$$P_{thermal,m} = P_{in,m} - P_{out,m} = 47.9 - 45 = 2.9\ kW \tag{11.6}$$

$$P_{thermal,d} = P_{in,d} - P_{out,d} = 48.4 - 47.9 = 0.5\ kW. \tag{11.7}$$

The total thermal losses, as the ones computed in Example 11.1, can be used to determine losses of particular elements of both motor and drive, provided that their physical properties are known. Although a model of the IM drive losses based on resistance elements and equivalent circuit is confirmed to have a good level of accuracy, the identification process is troublesome and requires both analysis of machine construction and knowledge/estimation of its specific parameters, which typically are not publicly available. This, in turn, makes it not suitable to efficiently assess the overall thermal performance of a large volume of motors, which is normally required when designing electric drivetrains [34]. Therefore, the thermal model of an induction motor drive proposed in this thesis is based on loadability curves which are one of the most important constraints when designing electric powertrains, as discussed in Chapters 5 and 10.

11.3 Thermal Performance Modeling

11.3.1 Loadability Curves

According to manufacturers' guidelines (for instance [2]), the continuous maximum load of a converter driven motor is mainly influenced by the modulation pattern and switching frequency of the converter and by the motor design.[26] The practical solution that suppliers use is to display these guidelines in the form of loadability curves. Loadability curves for a typical, self-ventilated induction motor are already shown in Fig. 10.4 but, for convenience, they are illustrated once more in Fig. 11.5. Loadability curves "present the maximum continuous load

---

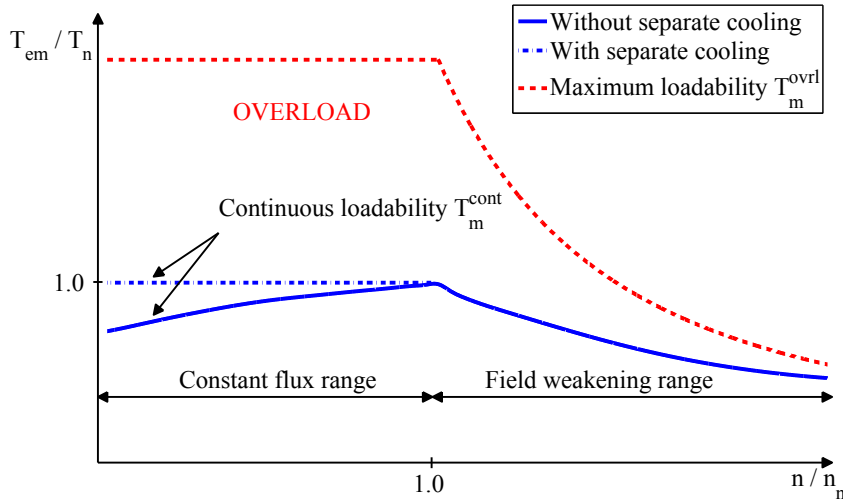26. This Section is partially based on publication [272].

Figure 11.5: Typical loadability curves for inverter-fed induction motor [276].

torque of a motor as a function of frequency (speed) to give the same temperature rise as with rated sinusoidal voltage supply at nominal frequency and full rated load" [2]. They do not specify thermal limits of a motor alone, but are applicable only to inverter-fed motors. Hence, they provide basic information about the thermal loadability of a VFD as well, which makes them a convenient tool to monitor the combined heating effect on both motor and drive.

Therefore, loadability curves might be perceived as an attempt to integrate the influence of different types of losses on thermal loadability of a VFD-controlled induction motor. Whether such an approach is accurate enough or not, is a matter of how detailed thermal model one seeks to obtain. The fact is, that loadability curves are not only recommended by producers but – most importantly – followed by customers when designing electric actuation systems and selecting their components (see for instance [7, 310, 315]). Taking advantage of loadability curves to arrive at a thermal model of motor drive does not require neglecting some of the losses to simplify the analysis (as done for instance in [190]), since the bottom line for constructing these curves is the overall temperature rise of the inverter-fed motor.

Due to self-ventilation, motor thermal loadability decreases in the range below the rated speed n_n, limiting the continuous available torque, as mentioned in Section 5.3. If separate cooling is used, however, motor loadability at low speeds is increased. For both separate and self-cooling, torque is equally limited in the field weakening range as well. Two main specification inequalities, taken from the more comprehensive list given in Section 10.3, that need to be satisfied by the motor drive are

$$T^{cont} \leq T_m^{cont} \tag{11.8}$$
$$T^{ovrl} \leq T_m^{ovrl} \tag{11.9}$$

where T^{cont} and T^{ovrl} are continuous and maximum loads experienced by the motor, respectively, T_m^{cont} specifies the maximum allowable continuous load, whereas T_m^{ovrl} determines the permissible motor overload. In principle, the mechanical load during overload T^{ovrl} should be between the dashed and solid lines in Fig. 11.5. Such short term overloads are allowed as long as they do not cause motor overheating.

However, the problem that loadability curves are associated with is that they do not give sufficient information regarding permissible overload duration [276]. Instead, catalogs provide only general guidelines regarding allowable overloads in the form of discretized set of operating

conditions – for instance "light overload" of a frequency converter is defined as an overload current of 110 % · I_n acting for 1 *min* every 5 *min* at an ambient temperature of 40 °C [10]. Therefore, in the case of arbitrary load profiles that differ from the tabulated catalog data, it becomes impossible to assess the overall thermal performance of the drivetrain without consulting the suppliers. This challenge is tackled in this thesis by proposing a thermal model of the motor drive based on both loadability curves and permissible temperature margins illustrated in Fig. 11.1.

Remark 11.1. *In fact, catalogs (e.g. [10]) specify the allowable overload durations in terms of drive currents to account for shorter temperature rises of frequency converters, i.e.:*

- *Light overload – 110 % · I_{lo} acting for 1 min every 5 min at an ambient temperature of 40 °C, where I_{lo} is the light overload drive current.*

- *Heavy-duty overload – 150 % · I_{hd} acting for 1 min every 5 min at an ambient temperature of 40 °C, where I_{hd} is the heavy-duty drive current.*

Therefore, in order to separately assess the drive thermal loadability, one should evaluate the temperature rise of the drive under light, heavy-duty, and arbitrary overloads, and benchmark the results not with the limits given by the motor insulation classes in Fig. 11.1, but with the maximum allowable temperature of the drive heat sinks [91]. These temperature limits vary depending on the supplier but usually lie within the range of 85–125 °C ([4] and [91]), depending on the size of the drive and its output rating. It means, that about the same temperature limits are obtained for an average drive as for the motor manufactured in the temperature insulation class B (hot spot temperature of 130 °C). Hence, in such cases, it is enough to evaluate temperature rise of the motor alone to assess the overall thermal performance of the electric drivetrain. In addition, since both I_{lo} and I_{hd} are lower than the continuous drive current I_d^{cont} (refer e.g. to [10]), and – as shown in Chapter 10 – they are also usually lower than the rated current I_n of the motor they drive, using the motor rated current in the overload formulas is more conservative than relying just on the drive currents. In that way, increasing the overload drive currents compensates for their shorter thermal time constants but, of course, further research is required to quantify this influence. Although this approach is sufficient for conventional induction motor drives, in the future it is recommended to extend the analysis to the evaluation of the drive heat sinks temperature as well.

11.3.2 Temperature Rise Model

The thermal model of IM is derived from the same principles as in [342]. The difference is, however, that the model presented there (or in [371], for instance) is applicable together with the so-called motor thermal limit curves (which are typically not provided by the manufacturers), whereas the one introduced here requires knowledge of loadability curves (which are easily accessible in catalogs) and thermal protection limits from the IEC standard [154]. It is assumed that heating and cooling of an induction motor (its stator winding, to be more precise) is represented by the simple first order thermal model illustrated in Fig. 11.6 and expressed as ([342] and [371])

$$C\frac{d\Delta\Theta(t)}{dt} = R\left(I_m(t)\right)^2 - H\Delta\Theta(t) \tag{11.10}$$

where $\Delta\Theta(t) = \Theta(t) - \Theta_{amb}$ is motor temperature rise above ambient [K], $I_m(t)$ is motor current [A], C is heat capacity [J/K], H is the running heat dissipation factor [W/K], and R is electrical resistance [Ω].

   Normally, detailed parameters of motors (such as copper winding length or mass) are not available to customers, which makes it burdensome to determine fundamental thermal model parameters (R, C, H). Therefore, we simplify model (11.10) so that it contains two unknown
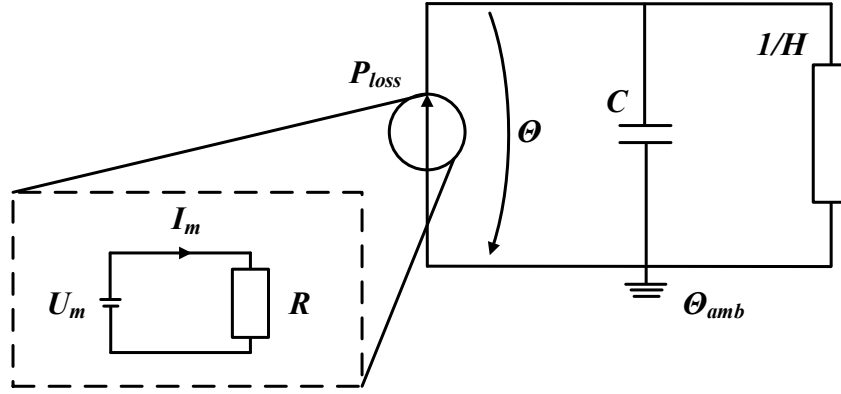
Figure 11.6: First order thermal model of IM [367].

parameters: factor $B = R/C$ $[K/(sA^2)]$ and thermal time constant $\tau = C/H$ $[s]$, according to [342] and [367]

$$\frac{d\Delta\Theta(t)}{dt} = \frac{R}{C}\left(I_m(t)\right)^2 - \frac{H}{C}\Delta\Theta(t) \tag{11.11}$$

$$\frac{d\Delta\Theta(t)}{dt} = B\left(I_m(t)\right)^2 - \frac{1}{\tau}\Delta\Theta(t). \tag{11.12}$$

Parameter B includes the combined effect of electrical and thermal resistances as well as the heat capacity of the motor. Such representation facilitates model identification, since what influences its response is not the individual values of parameters (R, C, H), but the ratio of electrical resistance and heat capacity R/C, and the thermal time constant τ. In addition, the only input variable in (11.12) is motor current I_m which accounts for torque variations only. In reality, however, speed variations also have significant impact on thermal performance of motor drives as they contribute to e.g. iron losses. This phenomenon is included in this study by making parameters of model (11.12) speed-dependent

$$\frac{d\Delta\Theta(t)}{dt} = B(n)\left(I_m(t)\right)^2 - \frac{1}{\tau(n)}\Delta\Theta(t). \tag{11.13}$$

In fact, since as shown further in the text, the reference time constant τ_{ref} is independent on speed, $\tau(n)$ is assumed to be close to a constant value as well.

Remark 11.2. *The temperature increase of stator winding is the most critical factor that affects thermal life of motor's insulation [330]. Therefore, in this thesis, the term "motor temperature" is used interchangeably with the more precise notion "stator winding average temperature".*

Motor current I_m could easily be obtained given motor torque and speed values, as shown in Section 10.2.2. Reference values of thermal time constants τ_{ref} are provided in [297] and reproduced in Table 11.2. They are treated as general guidelines when generating reference temperature rise profiles for model identification purpose. Although the single time constant model is not always adequate to represent detailed temperature changes in a motor [51] (e.g. in reality, there might be multiple time constants which describe temperature rise in the stator), it is still an effective method to quickly assess thermal protection levels of motor drives in industrial applications [342]. Even if using the approximated values of τ_{ref} is not an ideal approach and it requires further experimental validation, it is already by all means more

Rated power P_n [kW]	2 pole [min]	4 pole [min]	6 pole [min]	8 pole [min]
0.09 . . . 1.1	7 . . . 10	11 . . . 10	12	−
1.5 . . . 3.0	5 . . . 8	9 . . . 12	12	12 . . . 16
4.0	14	11	13	12
5.5 . . . 18.5	11 . . . 15	10 . . . 19	13 . . . 20	10 . . . 14
22 . . . 45	25 . . . 35	30 . . . 40	40 . . . 50	45 . . . 55
55 . . . 90	40	45 . . . 50	50 . . . 55	55 . . . 65
110 . . . 132	45 . . . 50	55	60	75

Table 11.2: Typical thermal time constants τ_{ref} for induction motors [276] − reproduced from [297].

practical (and equally accurate − which is shown in Section 11.5.3) than relying on a discrete set of allowable overload durations provided in catalogs.

There are the following limitations of the proposed method:

1. It is not applicable for checking the intermittent temperature rise caused by the motor starting current (i.e. a short term overload with approx. $6I_n$).

2. In general, parameters of the thermal model depend on both speed and load/current. In this study, however, the parameters $B(n)$ and $\tau(n)$ depend only on motor speed.

3. Actually (maybe even more importantly), these parameters also depend on temperature which should ideally make the coefficients of (11.13) become functions of the dependent variable $\Delta\Theta$ as well (this is listed as a future work in Section 11.7).

Temperature rise estimated by (11.13) is shown in Example 11.2 for an arbitrary IM.

Example 11.2 (Temperature Rise of Stator Winding)
Let us consider the 4 pole induction motor from Example 11.1 characterized by the additional parameters [13]:

- rated torque $T_n = 290\ Nm$,

- rated speed $n_n = 1480\ rpm$,

- rated current $I_n = 81.3\ A$.

Its temperature rise is simulated using (11.13) by assuming constant values of $B = 0.012\ K/(sA^2)$ and $\tau = 40\ min$. The thermal time constant is selected according to the general guidelines summarized in Table 11.2, whereas the value of factor B is identified for the rated speed operation of the motor, as presented in Section 11.5.2. The load profile is varied under this constant speed, according to a typical duty cycle specified in the standard [154]. The motion profile similar to the popular continuous-operation periodic duty (designated by $S6$ duty type in the standard) is chosen in this Example. It is characterized by identical duty cycles, where each period consists of two different levels of constant load [34]. Normally, under this type of operation, the thermal equilibrium is not obtained. Two cases are investigated: Fig. 11.7a shows a high pulse amplitude but shorter pulse duration, whereas Fig. 11.7b illustrates a small pulse amplitude and longer pulse duration.
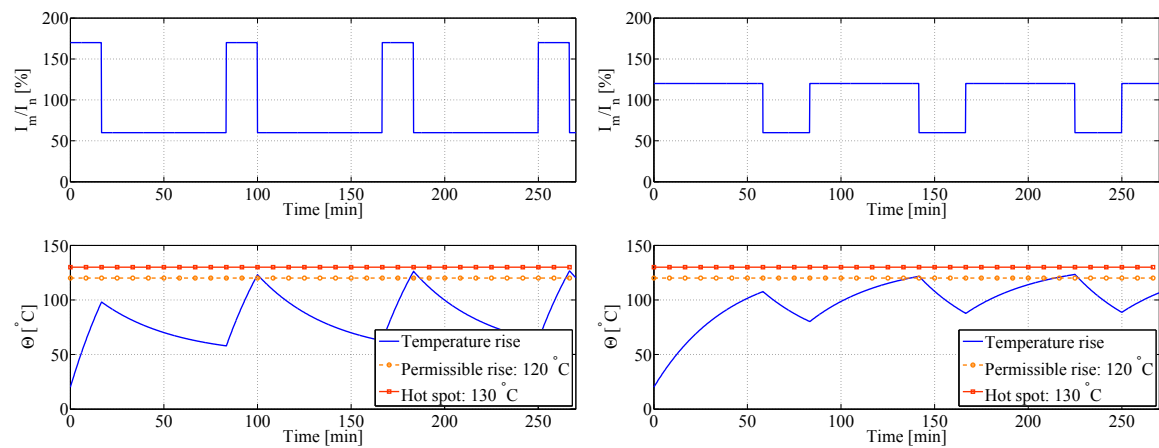
(a) Maximum overload: $170\ \% \cdot I_n$, base load: $60\ \% \cdot I_n$, cycle duration: $83\ min$, pulse duration: $17\ min$.

(b) Maximum overload: $120\ \% \cdot I_n$, base load: $60\ \% \cdot I_n$, cycle duration: $83\ min$, pulse duration: $58\ min$.

Figure 11.8: Estimated temperature rise of the stator winding in a 45 kW, insulation class B motor.

Considering that the motor is produced in the insulation class B, short term overloads of up to 130 $°C$ are allowed. One can observe that what affects the thermal loadability of the motor is the root-mean-square (RMS) value of the load profile, similarly to what is commented on in Example 5.4. Therefore, monitoring temperature of the stator winding can be a convenient way to check if mechanical loadability limits of the motor are not violated.

11.3.3 Further Comments

In general terms, P_{loss} in Fig. 11.6 represents heat losses in the stator winding which from the physical point of view are mainly the copper losses [367]. However, as shown in Fig. 11.3, there exist other types of losses that contribute to the increased waste heat emission of induction motors, e.g. core losses, friction and windage, or no-load Joule stator losses. Since the proposed thermal model is based on loadability curves that portray the overload capacity of inverter-fed IMs, it is assumed that even though (11.13) describes the average temperature rise of the stator winding, parameters of (11.13) are not those of the stator alone, but are rather

considered to represent the combined heating effects of both motor and drive which contribute to increasing the temperature of the stator winding. Under this assumption, the total power loss of the motor drive is consumed by the thermal heating $P_{loss} = P_{loss,m} + P_{loss,d}$.

Representing all kinds of losses in the electric powertrain exclusively as simple Joule losses is a somewhat drastic simplification. However, as long as the parameters of such a thermal model are not those of just the stator but they capture the complex drivetrain heating phenomenon with a similar level of accuracy to what manufacturers recommend nowadays (recall Remark 11.1), this assumption is reasonable. This, in turn, allows to claim (and this hypothesis is confirmed in Section 11.5) that comparable effectiveness in predicting thermal limits of induction motor drives can be achieved when following the general manufacturers' guidelines and when using the thermal model which parameters are deduced from the loadability curves. This conviction rests on the following presumptions:

1. The definition of the loadability curves, quoted in Section 11.3.1, clearly correlates mechanical performance of a motor drive with its thermal capacity.

2. The fact that the allowable motor operating temperatures and insulation classes (illustrated in Fig. 11.1) are defined in the standards (e.g. in [154]) means they must be applicable to majority of commercially available machines.

3. Categorization of allowable overloads into discrete set of conditions in manufacturers' catalogs (e.g. in [10]) indicates a rather simple and conservative approach to the evaluation of temperature rise of VFD-controlled IMs in typical industrial applications.

The remaining challenge is the selection of the parameters identification method which allows for sufficient model's accuracy and flexibility. This aspect is discussed in Section 6.7.2. Although applying a single thermal time constant might not always be adequate to model detailed heat transfer in IM [51], it is undoubtedly the most popular method to assess motor drive temperature in industrial applications (in both dimensioning and operation) – see for instance [3, 158, 190, 366] and the references therein.

Remark 11.3. *Thermal time constants of inverters are typically a few times shorter than those of induction motors, according to [7]. As a consequence, short term loadability of the drive is often more critical than that of the motor. Therefore, manufacturers define maximum durations of drive currents that can safely be supplied to the motor without causing damage not only to motor's insulation but also to drive's electronic components. These guidelines (discussed in Remark 11.1) are utilized in this thesis to calibrate the estimated drivetrain thermal models. Hence, even though the thermal time constant τ in (11.13) characterizes only the motor, rise times of frequency converters still play an essential role in model verification presented in Section 11.5.3.*

11.4 Parameters Identification as Optimization Problem

According to the information presented in Chapter 6 (especially Section 6.5.1 and Example 6.9), the following nonlinear optimization problem is used to identify parameters of thermal model (11.13) ([60] and [338])

$$\underbrace{\begin{bmatrix} x_{1,1} \\ x_{2,1} \end{bmatrix}}_{\mathbf{x}_{(2 \times 1)}} = \underbrace{\begin{bmatrix} x_{1,init} \\ x_{2,init} \end{bmatrix}}_{\mathbf{x}_{init\ (2 \times 1)}}$$

FOR $j := 1$ TO m

$$\min_{x} \quad \underbrace{\sum_{i=1}^{r} \left(\Delta \Theta_{i,j}^{ref} - \Delta \hat{\Theta}_{i,j} \right)^2}_{\mathbf{J}_{(r \times m)}} \qquad (11.14)$$

s.t. $\qquad \underbrace{\begin{bmatrix} b_{low}^{B} \\ b_{low}^{\tau} \end{bmatrix}}_{\mathbf{b}_{low\ (2 \times 1)}} \leq \underbrace{\begin{bmatrix} x_{1,j} \\ x_{2,j} \end{bmatrix}}_{\mathbf{x}_{(2 \times m)}} \leq \underbrace{\begin{bmatrix} b_{up}^{B} \\ b_{up}^{\tau} \end{bmatrix}}_{\mathbf{b}_{up\ (2 \times 1)}}$

END

where $\mathbf{x} \in \mathbb{R}^{n \times m}$ is the matrix of parameters ($x_{1,j} = B$ and $x_{2,j} = \tau$), $\mathbf{J} \in \mathbb{R}^{r \times m}$ is the cost function to be minimized, $(\mathbf{b}_{low}, \mathbf{b}_{up}) \in \mathbb{R}^n$ are the constraint vectors, and $\mathbf{x}_{init} \in \mathbb{R}^n$ is the vector of initial values of parameters. The estimated temperature $\Delta \hat{\Theta}_{i,j}$ is obtained by solving (11.13) at each evaluation point j and time instant i. The length of time vector r should be long enough for the motor temperature to settle at a steady state value, whereas the final number of evaluation points m depends on how frequently we update the model with a new set of parameters. The reference temperature rise $\Delta \Theta^{ref}(t)$ corresponds to an increase in motor temperature at each point of the continuous loadability curve illustrated in Fig. 11.5. It follows the first order model:

$$\Delta \Theta^{ref}(t) = \Delta \Theta_{max} \left(1 - \exp\left(\frac{-t}{\tau_{ref}} \right) \right) \qquad (11.15)$$

where the maximum operating temperature $\Delta \Theta_{max}$ is taken from Table 11.1 for a given motor insulation class, whereas the reference thermal time constant τ_{ref} reflects the size of the motor, as presented in Table 11.2.

11.5 Results

11.5.1 Parameters Estimation Procedure

The underlying assumption for constructing a loadability curve is that at each value of speed and the corresponding torque the temperature rise is the same – recall Section 11.3.1. Therefore, the loadability curve for a self-ventilated motor from Fig. 11.5 is discretized into m points, such that the identified parameters of the thermal model (11.13) depend on motor speed n. At each evaluation point, the thermal model is simulated and its parameters $(B(n), \tau(n))$ are adjusted until its response is as close to the reference temperature rise (11.15) as possible. Then, the optimization routine (11.14) saves those identified parameters which yield the minimum error signal and moves on to the next evaluation point. In this study, we use the `fmincon` function with the interior-point algorithm from MATLAB optimization toolbox [52]. Detailed information about this solver can be found in MATLAB documentation [224]. Since the solution is not guaranteed to be the global optimum, the algorithm can be strongly influenced by the initial point. Therefore, we determine the initial values of parameters $\mathbf{x}_{init}$ in the trial

and error method to achieve the best convergence of the model's response, so that the sum of squared errors (SSE) between the reference and estimated temperatures is negligible.

11.5.2 Outcomes of Identification

We investigate four commercially available, self-ventilated IMs which parameters are summarized in Table 11.3. As motor thermal time constants are rarely given by manufacturers, their typical values follow the general guidelines summarized in Table 11.2. Each motor uses class B

Parameter	Motor type			
	#1	#2	#3	#4
Rated power P_n [kW]	0.75	18.5	45	132
Rated torque T_n [Nm]	5	119	290	847
Max torque T_{max} [Nm]	$3.2T_n$	$2.9T_n$	$3.2T_n$	$2.7T_n$
Rated speed n_n [rpm]	1430	1477	1480	1487
Rated current I_n [A]	1.83	34.5	81.3	232
Power factor $\cos\varphi_n$ [$-$]	0.73	0.84	0.85	0.86
Time constant τ_{ref} [min]	10	19	40	55

Table 11.3: Parameters of selected 4-pole IMs [276] – reproduced from [13].

temperature rise with class F insulation, which gives a permissible temperature rise of 120 $°C$ at rated conditions and a maximum allowable temperature of 155 $°C$. According to [41], given the typical stator temperature of 100 $°C$ at rated conditions, we assume an ambient temperature of 20 $°C$, which results in the reference permissible temperature rise of $\Delta\Theta_{max} = 80\ °C$ (i.e. rise class B) at each point of the loadability curve. For every investigated motor we generate a set of reference temperature rise profiles, according to (11.15). The last step is to identify parameters of thermal models, as presented in Fig. 11.9.

For all four motors, the temperature rise estimated by the identified model $\Delta\hat{\Theta}(t)$ follows exactly the same reference profile $\Delta\Theta^{ref}(t)$. Similarly, the differences between the reference thermal time constant τ_{ref} and the estimated one $\hat{\tau}$ are negligible. Factor B clearly depends on motor speed, allowing to capture the phenomenon of reduced torque availability in the area of reduced cooling. It is also observed that its value becomes lower as the motor size increases.

11.5.3 Verification of Thermal Models

Two common definitions regarding the magnitude and duration of permissible motor drive overloads are light overload and heavy-duty operation, which allow the overload motor current of 110 % $\cdot I_n$ and 150 % $\cdot I_n$, respectively, both acting for 1 min every 5 min at ambient temperature of 40 $°C$, as discussed in Remark 11.1. We apply these two current patterns to verify if responses of the identified models do not violate the thermal limits discussed in Section 11.1. The simulation results illustrated in Fig. 11.10 confirm that our method, when used together with the general overload instructions presented in catalogs, yields almost the same thermal protection limits as these given in Table 11.1.

Under light overload conditions shown in Fig. 11.10a, the estimated motor drive's temperature converges to 125 $°C$ which is below the hot spot margin for insulation class B. Similarly, as illustrated in Fig. 11.10b, the responses of estimated thermal models at rated motor speeds under heavy-duty overload reach the same steady state temperature regardless of the size of the motor: 140 $°C$, which is close to the permissible temperature rise for insulation class F.
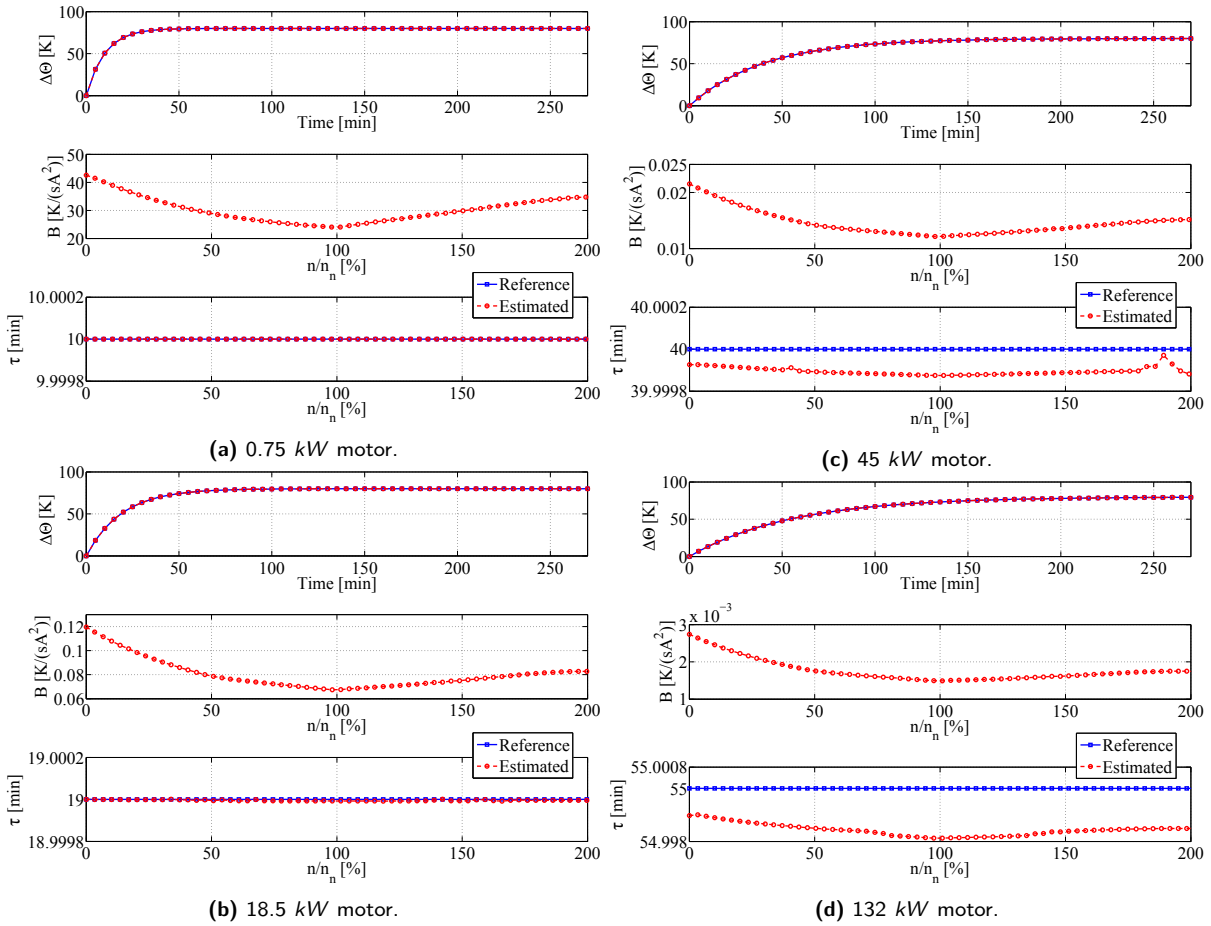
(a) 0.75 *kW* motor.

(b) 18.5 *kW* motor.

(c) 45 *kW* motor.

(d) 132 *kW* motor.

Figure 11.9: Results of thermal model's parameters identification [276].

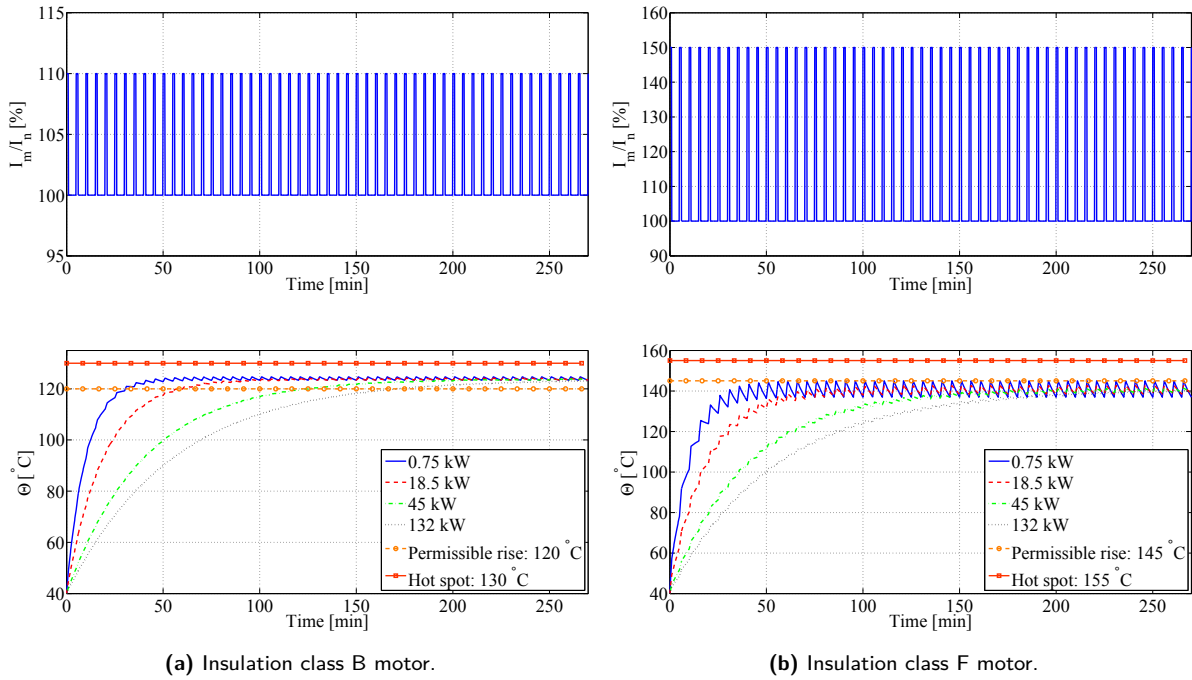**(a)** Insulation class B motor.

(b) Insulation class F motor.

Figure 11.10: Responses of identified thermal models benchmarked with general thermal protection guidelines from [10] and [154] – reproduced from [276].

In addition, as shown in Fig. 11.10a, even if the insulation class B is used, the light overload conditions are specified in catalogs in such a way, that they do not violate the hot spot thermal limit provided in the standard [154]. Of course, operating at ambient temperatures lower than 40 $^{\circ}C$ increases continuous loadability of the motor, as it is the absolute value of the permissible temperature rise which limits motor performance under continuous load.

The presented results confirm that about the same performance limits are obtained when using the identified thermal models and when following the catalogs' recommendations. In addition, it is concluded that the constraints of light overload and heavy-duty modes of operation of drives are satisfied when relying on the proposed thermal model based on motor loadability curves. In other words, for instance, the restriction of the light overload of drive $OL = 110 \% \cdot I_n$ for 1 min / 5 min at 40 $^{\circ}C$ ambient corresponds to the temperature rise of the motor almost reaching the hot spot of insulation class B at 40 $^{\circ}C$ ambient, i.e. approx. 130 $^{\circ}C$. Finally, within the discussed approach it becomes possible to evaluate thermal performance of motor drives operating at various overload conditions and ambient temperatures, contrary to relying on general guidelines allowing only certain overload magnitudes and duty cycles. To illustrate this, we show the temperature rise of each motor operating under arbitrary load and speed profiles and at an ambient temperature of 20 $^{\circ}C$. Two cases are presented: class B insulation is shown in Fig. 11.11a and class F insulation is illustrated in Fig. 11.11b. Based on these examples, we can conclude that e.g. the 18.5 kW motor's temperature goes above safety limits, as opposed to e.g. the 132 kW motor which temperature stays below the hot spot limit throughout the entire motion cycles. Such information is crucial when designing electric powertrains, as it allows to select such components which do not violate the thermal constraints when operating under the desired load conditions.

11.6 Discussion

Validation of the developed thermal modeling method (e.g on an experimental setup) would significantly strengthen its impact. This activity is listed in Section 11.7 as a future work. However, given the scope of this thesis, which is to improve the flexibility of the industrially accepted design procedure of electric drivetrains, to our understanding, benchmarking the estimation results with the full-scale experimental data is not critical at this stage. The following argumentation tries to defend this claim.

As mentioned in Section 5.6, the dimensioning procedure recommended by manufacturers is characterized by a number of disadvantages. The most important limitation which this Chapter aims to tackle are cryptic thermal performance indicators. In order for the improved selection method to become attractive to the industry, it cannot be completely revolutionary but it has to be based on what the industry is used to – at least in businesses where conservatism is highly valued, such as the oil and gas offshore drilling. Therefore, to verify that the proposed temperature rise prediction method is reliable, it has to be benchmarked with something that is already recommended by the producers and followed by the customers.

One of these universally adopted guidelines is a discrete set of allowable overload conditions, such as these discussed in Remark 11.1, suggested by manufacturers to do the final check of thermal overloads. Since the allowable motor operating temperatures and insulation classes are defined in the standards (e.g. [154]), it means they must be applicable to majority of machines on the market. Therefore, the categorization of allowable overloads into the discrete set of conditions must somehow be based on the thermal limits defined in these standards, as discussed in Section 11.3.3. Since the proposed thermal modeling method does not violate the limits listed in Table 11.1 when subjected to the overload profiles specified by suppliers, it can
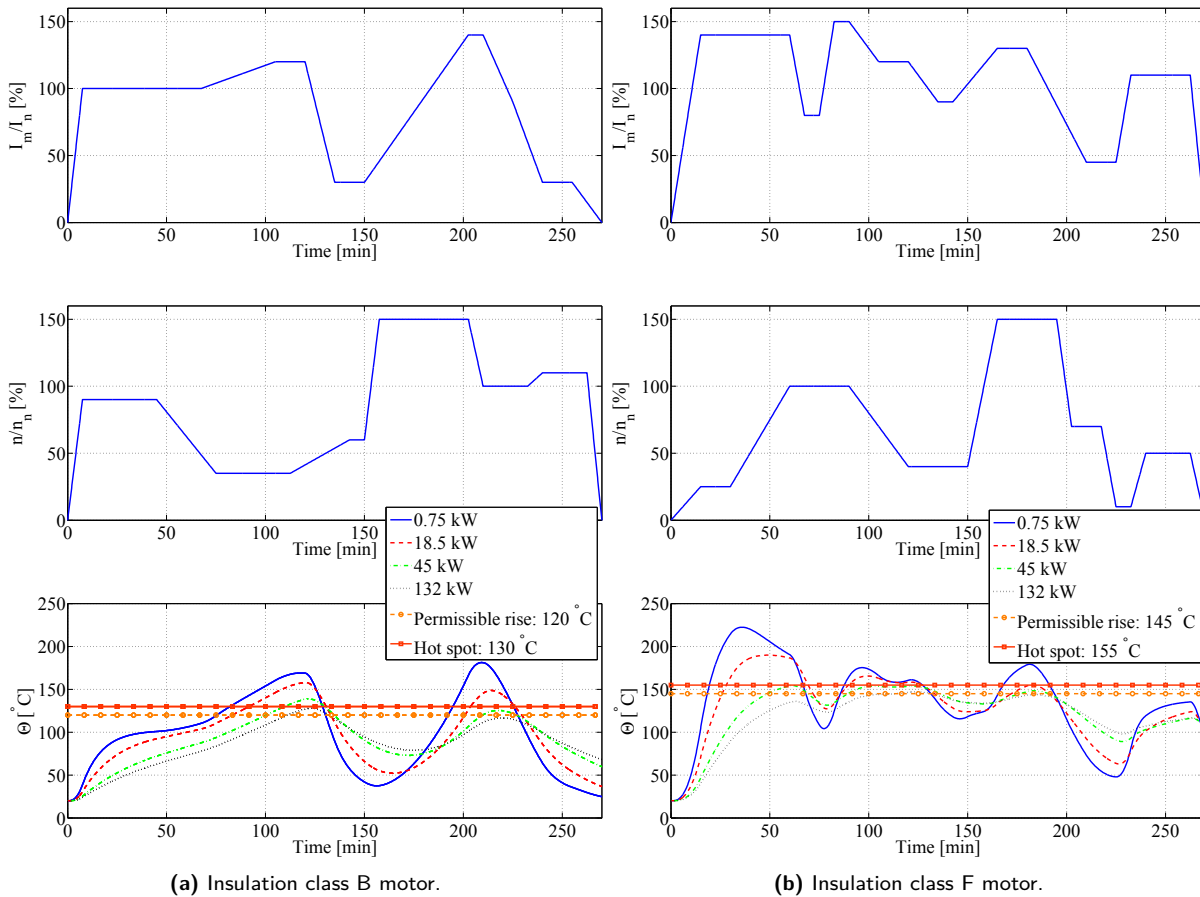
Figure 11.11: Responses of identified thermal models under arbitrary operating conditions [276].

be considered to offer the same degree of conservatism as their guidelines. This verification step is presented in Fig. 11.10a (by assuming that the light overload conditions are calibrated in catalogs to correspond to the thermal loadability of motors produced in class B) and in Fig. 11.10b (by assuming that the heavy-duty overload conditions are calibrated in catalogs to correspond to the thermal loadability of motors produced in class F). It turns out that these assumptions are reasonable, since the model closely matches the limiting temperatures from the IEC standard [154]. In addition, the proposed technique provides for improved flexibility, as it enables evaluation of effects of any arbitrary overload profile on drivetrain thermal performance – something that has not been possible so far without asking a supplier for an advice. These seems to be already strong arguments, since, all in all, what is in general valued in the industry is conforming to the standards. However, as mentioned above, in order to further enhance the developed method, experimental testing is required.

11.7 Conclusion

The relationship between the loadability curves and the first order thermal model of VFD-controlled IMs is established in this Chapter. The accuracy of the estimated model is verified against thermal protection principles provided in catalogs. Not only does the presented approach reproduce particular thermal limits specified by manufacturers, but it also allows to evaluate drivetrain thermal response in different operating conditions and ambient temperatures. Since the loadability curves contain information about permissible overload of both the motor and frequency converter, the current methodology makes it possible to assess thermal

protection levels of combined electric drivetrains, not induction motors alone. This plays an important role in enhancing the design process of electrically actuated systems, as it enables to replace fragmentary information and rules of thumb from the manufacturers' catalogs with a more reliable method which is based on both fundamental principles and accepted industrial practices. Ultimately, the proposed approach provides for more efficient product development, as it reduces the need to contact suppliers for checking thermal performance of a design under operating conditions which are not covered and explained in catalogs.

In addition, it is confirmed that it is not just the rated parameters of an electric powertrain that should be looked into when selecting its components, but it is rather its combined thermal behavior that should be used as one of the main design criteria. The permissible temperature rise decides about the capability of the drivetrain to operate continuously under a given load, whereas when the overload conditions are considered, a design engineer has to be concerned with the hot spot limit.

Experimental testing is required to further strengthen the significance of the presented concept and to assess the levels of accuracy of the established models under real load conditions. Such validated models should then be implemented in the optimal drivetrain design algorithm presented in Chapter 10, and the resulting solution be compared with the one obtained when strictly following the essential producers' guidelines summarized in Chapter 5. Also, the application of a more detailed thermal model (e.g. with two distinct time constants or with temperature-dependent parameters) has a potential to improve the fidelity of the method. Likewise, the proposed temperature rise estimation procedure will become more robust if the motor thermal time constant is determined separately for each investigated machine based on e.g its nameplate (or, in general, catalog) data, instead of using only rough approximations from Table 11.2. Finally, other methods (such as e.g metaheuristic techniques) can be used to identify parameters of thermal models to avoid the problem of the influence of initial values on estimation results.

12 Conclusion and Outlook

The objective of this thesis is the development of improved design and analysis methods for electric powertrains operating in offshore drilling equipment.[27] The benefits of using such actuation systems compared to hydraulic drivetrains (which are still more popular nowadays) are briefly identified and tools and techniques that improve the state-of-the-art dimensioning guidelines are proposed. The problem is solved by adopting the mechatronic design approach and by simultaneous consideration of constraints and objectives from a system perspective rather than separate analysis of domain-specific issues.

The foundation for combining the choice of motor control strategy with assessment of the expected lifetime of drivetrain elements is created by the application of cycle counting methods and cumulative damage theory. Since the results show that the relative fatigue levels and vibration severity can be estimated early in the design stage, the natural extension will be to validate the absolute damage of the considered rotating powertrain components and include this knowledge in the sizing process. Although we have shown that the selection of the motion control pattern not only can reduce maximum loads of the machine but also extend its lifecycle, an open question remains if, and how, the temperature rise of the electric drivetrain can be lowered by optimizing the desired duty cycles. Since loadability of self-ventilated induction motors is reduced in the low speed range, what seems to be an interesting idea is to incorporate in the dimensioning process the minimization of high torque occurrences in the area of reduced cooling. Extracting from a load history the relationship between the values of torque, speed, and number of detected cycles, and using this information to select such a motion control scheme that offers the least number (and/or the least magnitude) of torque peaks for slow operation has a potential to partially solve the problems related to overheating.

We also show that apart from small adjustments to the control software that can be beneficial to the overall machine performance, the modification of the control hardware might yield positive effects too. Certainly, reducing the amount of physical devices that may fail is desirable in industrial applications (especially in such harsh conditions as offshore environment). However, the EKF-based control method of the induction motor discussed in this thesis has an additional key feature – it allows for benchmarking of other sensorless control methods implemented in the commercially available VFDs. Typically, the drives that can be purchased do not give the possibility to access some signals that are measured on the motor and used in their internal control algorithms, which reduces flexibility of operation if such third-party devices have to be interfaced with the control system of a complete industrial product. Therefore, further investigation should be carried out to determine whether some of the functions of VFDs can be realized by the in-house proprietary control systems developed by producers of the final equipment (e.g. by manufacturers of offshore drilling machines).

To tackle the problem of the lack of optimality of electric actuation systems, we propose

---

27. However, as mentioned several times throughout this thesis, the presented techniques can also be applied to other industries.

a method for the selection of their components based on mixed integer programming, which results in a simple and easy to implement dimensioning algorithm. The optimization routine is formulated in a way that allows for developing it further and including more constraints and cost functions, e.g. these related to thermal performance or condition monitoring. Therefore, an obvious direction for future work is to implement multiobjective design functionality within the proposed approach to allow for an optimal trade-off between contradictory objectives typically encountered in engineering applications (e.g. cost vs. reliability). So far, the introduced design optimization algorithm has proven its effectiveness in dealing with a realistic but simplified dimensioning problem, therefore, the next step will be to apply it to sizing an actuation system of a full-scale machine and investigating its performance in practice (this can also include laboratory testing). An interesting question is if the exact knowledge of the required torque profile and its precise distribution over time and speed range can possibly give an advantage when dimensioning drivetrains. Specifically, future research should focus on utilizing the accurate load and speed profiles together with the statistical/probabilistic information about the expected overloads when deciding about the size of the equipment, instead of relying exclusively on a somewhat conservative approximation of the continuous loads by the RMS values of overloads.

Optimization techniques can equally well be applied to standardize the produced equipment. An example is evaluation of all feasible combinations of drives, motors, and gearboxes for each manufactured machine and limiting the number of applied drivetrains to only a few "off-the-shelf" solutions, contrary to designing a tailor-made actuation system for every product, which, in turn, is usually associated with greater engineering effort. Although some combinations might not be optimal and result in higher cost, the development process itself is optimized and this is where the cost savings are generated. In addition, a higher cost of the over-dimensioned powertrains may not necessarily increase linearly with the increase of their safety margins (e.g. it might happen that a lot more additional safety is achieved for only a slight growth of the drivetrain total cost). The knowledge of this kind is particularly relevant in optimizing the product portfolio.

The last part of this thesis focuses on improving the flexibility of the industrially accepted practices regarding dimensioning of induction motor drives. The proposed approach is based on the estimation of temperature rise of stator winding by synthesizing the information concerning loadability and thermal overloads available in catalogs and identification of a first order model that can be used for arbitrary duty cycles and at any ambient temperature. Given the fact that the loadability curves utilized to estimate the model's parameters actually characterize both the induction motor and the converter, the discussed temperature estimation technique can be essentially applied to complete electric powertrains, which makes it a powerful tool to be used when sizing their components. Since verification of the model against thermal protection limits given in the standards and manufacturers' guidelines yields promising results, it is recommended to further improve the robustness of the proposed approach by: a) formulating a method for determining the motor thermal time constant based on catalog data; b) creating separate thermal models of the frequency converter and motor; c) experimental validation of the simulation results. The introduced technique allows for evaluation of the temperature rise over time, however, what also appears to have practical relevance is specification of the allowable duration and frequency of the desired motion profiles to arrive at a quantitative measure of permissible overloads which can be used as a design constraint in the discussed powertrain optimization algorithm. Our understanding of the obtained results is that such flexible overload assessment methods can considerably speed up the drivetrain design process and make the extensive support from suppliers obsolete at this stage of product development.

References

[1] A.-K. Aadland and K. Petersen. Subsea all electric. In *Offshore Technology Conference*, pages 1–8, 2010.

[2] ABB. *The Motor Guide*, 2005. Available online at www.abb.com.

[3] ABB. *Three-phase asynchronous motors: Generalities and ABB proposals for the coordination of protective devices*, 2008. Available online at www.abb.com.

[4] ABB. *ACH550-UH HVAC drives: 1...550 HP – user's manual*, 2010. Available online at www.abb.com.

[5] ABB. *Technical guide no.1: Direct torque control – the world's most advanced AC drive technology*, 2011. Available online at www.abb.com.

[6] ABB. *Technical guide no.4: Guide to variable speed drives*, 2011. Available online at www.abb.com.

[7] ABB. *Technical guide no.7: Dimensioning of a drive system*, 2011. Available online at www.abb.com.

[8] ABB. *Technical guide no.8: Electrical braking*, 2011. Available online at www.abb.com.

[9] ABB. *DriveWindow 2 – user's manual*, 2012. Available online at www.abb.com.

[10] ABB. *Industrial drives ACS800: Single drives: 0.55 to 5600 kW catalog*, 2013. Available online at www.abb.com.

[11] ABB. *Low voltage: Motors for explosive atmospheres*, 2013. Available online at www.abb.com.

[12] ABB. *DriveSize 4.0 – user's manual*, 2014.

[13] ABB. *Low voltage: Process performance motors according to EU MEPS*, 2014. Available online at www.abb.com.

[14] D. Abicht. DC electric standalone choke. In *SPE Production and Operations Conference and Exhibition*, pages 1–7, 2010.

[15] ABS. *ABS guidance notes on control of harmonics in electrical power systems*. American Bureau of Shipping, 2006.

[16] A. K. Ådnanes. *Maritime Electrical Installations and Diesel Electric Propulsion*. ABB, 2003.

[17] A. Albert, O. M. Aamo, J. M. Godhavn, and A. Pavlov. Suppressing pressure oscillations in offshore drilling: Control design and experimental results. *IEEE Transactions on Control Systems Technology*, 23(2):813–819, 2015.

[18] H. G. Allen and P. Scott. Semi-automatic drilling rig. In *SPE Automation Symposium*, pages 65–70, 1966.

[19] F. Alonge, T. Cangemi, F. D'Ippolito, A. Fagiolini, and A. Sferlazza. Convergence analysis of extended Kalman filter for sensorless control of induction motor. *IEEE Transactions on Industrial Electronics*, 62(4):2341–2352, 2015.

[20] Y. An, B. F. Spencer, and J. Ou. Real-time fast damage detection of shear structures with random base excitation. *Measurement*, 74:92–102, 2015.

[21] M. Andersen, J. Dahl, and L. Vandenberghe. CVXOPT: Python software for convex optimization. http://cvxopt.org/index.html, 2016. Accessed: 2016-07-25.

[22] J. L. Andrus, R. L. Lewis, and H. B. Anderson. A new concept in offshore drilling rig power distribution. In *Symposium on Offshore Technology and Operations*, pages 1–15, 1966.

[23] J. L. Arendt, D. A. McAdams, and R. J. Malak. Uncertain technology evolution and decision making in design. *Journal of Mechanical Design*, 134(10):100904:1–11, 2012.

[24] ASTM. *ASTM E 1049-85 (Reapproved 1997), Standard practices for cycle counting in fatigue analysis.* Annual Book of ASTM Standards, Philadelphia, 1999. vol. 03.01, pp. 710-718.

[25] D. J. Atkinson, P. P. Acarnley, and J. W. Finch. Observers for induction motor state and parameter estimation. *IEEE Transactions on Industry Applications*, 27(6):1119–1127, 1991.

[26] F. Auger, M. Hilairet, J. M. Guerrero, E. Monmasson, T. Orłowska-Kowalska, and S. Katsura. Industrial applications of the Kalman filter: A review. *IEEE Transactions on Industrial Electronics*, 60(12):5458–5471, 2013.

[27] A. Austigard. Robotic Drilling Systems. `http://rds.no`, 2016. Accessed: 2016-03-14.

[28] M. Aziz and R. Mohd-Mokhtar. Performance measure of some subspace-based methods for closed-loop system identification. In *Computational Intelligence, Modelling and Simulation (CIMSiM), 2010 Second International Conference on*, pages 255–260, 2010.

[29] S. M. Baek and J. W. Park. Hessian matrix estimation in hybrid systems based on an embedded FFNN. *IEEE Transactions on Neural Networks*, 21(10):1533–1542, 2010.

[30] M. K. Bak. *Model Based Design of Electro-Hydraulic Motion Control Systems for Offshore Pipe Handling Equipment.* PhD thesis, Univeristy of Agder, 2014.

[31] M. K. Bak and M. R. Hansen. Analysis of offshore knuckle boom crane – part one: Modeling and parameter identification. *Modeling, Identification and Control*, 34(4):157–174, 2013.

[32] M. K. Bak and M. R. Hansen. Analysis of offshore knuckle boom crane – part two: Motion control. *Modeling, Identification and Control*, 34(4):175–181, 2013.

[33] M. K. Bak and M. R. Hansen. Model based design optimization of operational reliability in offshore boom cranes. *International Journal of Fluid Power*, 14(3):53–65, 2013.

[34] M. Barnes. *Practical Variable Speed Drives and Power Electronics*. Elsevier/Newnes, Jordan Hill, Oxford, 2009.

[35] M. Barut, R. Demir, E. Zerdali, and R. Inan. Real-time implementation of bi input-extended Kalman filter-based estimator for speed-sensorless control of induction motors. *IEEE Transactions on Industrial Electronics*, 59(11):4197–4206, 2012.

[36] M. S. Bazaraa, J. J. Jarvis, and H. D. Sherali. *Linear Programming and Network Flows*. John Wiley & Sons, New York, 2010.

[37] R. Béarée. New damped-jerk trajectory for vibration reduction. *Control Engineering Practice*, 28:112–120, 2014.

[38] R. Beguenane and M. Benbouzid. Induction motors thermal monitoring by means of rotor resistance identification. *IEEE Transactions on Energy Conversion*, 14(3):566–570, 1999.

[39] A. Bemporad and M. Morari. Control of systems integrating logic, dynamics, and constraints. *Automatica*, 35:407–427, 1999.

[40] F. A. Bender, M. Kaszynski, and O. Sawodny. Drive cycle prediction and energy management optimization for hybrid hydraulic vehicles. *IEEE Transactions on Vehicular Technology*, 62(8):3581–3592, 2013.

[41] M. Benhaddadi, R. Khaldi, and M. Benghanem. Experimental study of heating in induction motor fed by PWM inverter. In *Instrumentation and Measurement Technology Conference, 1997. IMTC/97. Proceedings. Sensing, Processing, Networking., IEEE*, volume 1, pages 335–338, 1997.

[42] J. R. Bibbins. Double-deck steam turbine power plants. *Proceedings of the American Institute of Electrical Engineers*, 27(7):1251–1269, 1908.

[43] K. J. Binns and D. W. Shimmin. Relationship between rated torque and size of permanent magnet machines. *IEE Proceedings – Electric Power Applications*, 143(6):417–422, 1996.

[44] L. Birk. Application of constrained multi-objective optimization to the design of offshore structure hulls. *ASME Journal of Offshore Mechanics and Arctic Engineering*, 131(1):011301:1–9, 2009.

[45] R. H. Bishop. *The Mechatronics Handbook*. CRC Press, Boca Raton, 2002.

[46] F. Blaschke. The principle of field orientation applied to the new transvector closed loop control system for rotating field machines. *Siemens Rev.*, 34:217–220, 1972.

[47] F. Blaschke. *Das Verfahren der Feldorientierung zur Regelung der Drehfeldmachine*. PhD thesis, Technische Universität Braunschweig, 1973.

[48] A. Boglietti, A. Cavagnino, A. Tenconi, S. Vaschetto, and P. di Torino. The safety critical electric machines and drives in the more electric aircraft: A survey. In *Industrial Electronics Society, IECON 2009 – 35th Annual Conference of the IEEE*, pages 2587–2594, 2009.

[49] I. Boldea and S. A. Nasar. *The Induction Machine Handbook*. CRC Press, Boca Raton, 2002.

[50] A. Bonnett. Root cause methodology for induction motors: A step-by-step guide to examining failure. *IEEE Industry Applications Magazine*, 18(6):50–62, 2012.

[51] D. Boothman, E. C. Elgar, R. Rehder, and R. Wooddall. Thermal tracking – a rational approach to motor protection. *IEEE Transactions on Power Apparatus and Systems*, PAS-93(5):1335–1344, 1974.

[52] A. Bornschlegell, J. Pelle, S. Harmand, A. Fasquelle, and J.-P. Corriou. Thermal optimization of a high-power salient-pole electrical machine. *IEEE Transactions on Industrial Electronics*, 60(5):1734–1746, 2013.

[53] F. Borrelli, A. Bemporad, and M. Morari. *Predictive Control for Linear and Hybrid Systems*. Cambridge University Press, Cambridge, 2011. In press, version updated: October 19, 2015.

[54] B. K. Bose. *Adjustable Speed AC Drive Systems*. IEEE Press, New York, 1981.

[55] B. K. Bose. Power electronics – an emerging technology. *IEEE Transactions on Industrial Electronics*, 36(3):403–412, 1989.

[56] B. K. Bose. Recent advances in power electronics. *IEEE Transactions on Power Electronics*, 7(1):2–16, 1992.

[57] B. K. Bose. Energy, environment, and advances in power electronics. In *Industrial Electronics, ISIE 2000. Proceedings of the 2000 IEEE International Symposium on*, volume 1, pages TU1–T14, 2000.

[58] B. K. Bose. *Modern Power Electronics and AC Drives*. Prentice Hall, Upper Saddle River, 2002.

[59] B. E. Boser, I. M. Guyon, and V. N. Vapnik. A training algorithm for optimal margin classifiers. In *Computational Learning Theory, Proceedings of the 5th Annual ACM Workshop on*, pages 144–152, 1992.

[60] S. Boyd and L. Vandenberghe. *Convex Optimization*. Cambridge University Press, Cambridge, 2009.

[61] BP. *Energy Outlook 2016*. 2016.

[62] E. L. Brancato. Insulation aging: A historical and critical review. *IEEE Transactions on Electrical Insulation*, EI-13(4):308–317, 1978.

[63] E. L. Brancato. Estimation of lifetime expectancies of motors. *IEEE Electrical Insulation Magazine*, 8(3):5–13, 1992.

[64] Ø. Breyholtz and M. Nikolaou. Drilling automation: Presenting a framework for automated operations. *SPE Drilling & Completion*, 27(1):118–126, 2012.

[65] T. R. Brinner, R. H. McCoy, and T. Kopecky. Induction versus permanent-magnet motors for electric submersible pump field and laboratory comparisons. *IEEE Transactions on Industry Applications*, 50(1):174–181, 2014.

[66] R. S. Burns. *Advanced Control Engineering*. Butterworth-Heinemann, Oxford, 2001.

[67] B. Camburn, B. Dunlap, T. Gurjar, C. Hamon, M. Green, D. Jensen, R. Crawford, K. Otto, and K. Wood. A systematic method for design prototyping. *Journal of Mechanical Design*, 137(8):081102:1–12, 2015.

[68] C. Canudas-de Wit, H. Olsson, K. J. Åström, and P. Lischinsky. A new model for control of systems with friction. *IEEE Transactions on Automatic Control*, 40(3):419–425, 1995.

[69] C. Canudas-de Wit, A. Youssef, J.-P. Barbot, P. Martin, and F. Malrait. Observability conditions of induction motors at low frequencies. In *Decision and Control, 2000. Proceedings of the 39th IEEE Conference on*, volume 3, pages 2044–2049, 2000.

[70] D. Casadei, F. Profumo, G. Serra, and A. Tani. FOC and DTC: two viable schemes for induction motors torque control. *IEEE Transactions on Power Electronics*, 17(5):779–787, 2002.

[71] Y. Censor. Pareto optimality in multiobjective problems. *Applied Mathematics and Optimization*, 4:41–59, 1977.

[72] T. Chakravarty, A. Chowdhury, A. Ghose, C. Bhaumik, and P. Balamuralidhar. Statistical analysis of road-vehicle-driver interaction as an enabler to designing behavioural models. *Journal of Physics: Conference Series*, 490(1):1–4, 2014.

[73] T.-F. Chan and K. Shi. *Applied Intelligent Control of Induction Motor Drives*. John Wiley & Sons, Singapore, 2011.

[74] S. W. Changchien and L. Lin. Concurrent design of machined products: A multivariate decision approach. *IEEE Transactions on Systems, Man, and Cybernetics, Part C (Applications and Reviews)*, 30(2):252–264, 2000.

[75] S. J. Chapman. *Electric Machinery Fundamentals*. McGraw-Hill, New York, 2012.

[76] A. Charnes, S. Duffuaa, and M. Ryan. The more-for-less paradox in linear programming. *European Journal of Operational Research*, 31(2):194–197, 1987.

[77] A. K. Chattopadhyay. Advances in vector control of ac motor drives – a review. *Sadhana*, 22(6):797–820, 1997.

[78] D. Z. Chen and L. W. Tsai. The generalized principle of inertia match for geared robotic mechanisms. In *Robotics and Automation, 1991 IEEE International Conference on*, pages 1282–1287, 1991.

[79] F. Chen and M. Dunnigan. Comparative study of a sliding-mode observer and Kalman filters for full state estimation in an induction machine. *IEE Proceedings – Electric Power Applications*, 149(1):53–64, 2002.

[80] H. Chen, T. Moan, and H. Verhoeven. Safety of dynamic positioning operations on mobile offshore drilling units. *Reliability Engineering & System Safety*, 93(7):1072–1090, 2008.

[81] S. M. Chhaya and B. K. Bose. Expert system based automated simulation and design optimization of a voltage-fed inverter for induction motor drive. In *Industrial Electronics, Control, and Instrumentation, 1993. Proceedings of the IECON '93., International Conference on*, pages 1065–1070 vol.2, 1993.

[82] M. Choux. *Nonlinear, Adaptive and Fault-Tolerant Control for Electro Hydraulic Servo Systems*. PhD thesis, Technical University of Denmark, 2011.

[83] M. L. Christensen and D. L. Zimmerman. Optimization of offshore electrical power systems. *IEEE Transactions on Industry Applications*, IA-22(1):148–160, 1986.

[84] G. A. Christopoulos, A. N. Safacas, and A. Zafiris. Energy savings and operation improvement of rotating cement kiln by the implementation of a unique new drive system. *IET Electric Power Applications*, 10(2):101–109, 2016.

[85] M. Ciechanowska. Hydrocarbonic potential of the Arctic. *Nafta i Gaz*, 68(12):1176–1182, 2011.

[86] J. Conti. *The International Energy Outlook 2013*. U.S. Energy Information Administration, Washington, 2013.

[87] P. Correa, M. Pacas, and J. Rodríguez. Predictive torque control for inverter-fed induction machines. *IEEE Transactions on Industrial Electronics*, 54(2):1073–1079, 2007.

[88] J. R. Couper, W. R. Penney, J. R. Fair, and S. M. Walas. *Chemical Process Equipment – Selection and Design*. Elsevier, Waltham, 2012.

[89] C. Craig and M. Islam. Integrated power system design for offshore energy vessels and deepwater drilling rigs. *IEEE Transactions on Industry Applications*, 48(4):1251–1257, 2012.

[90] S. M. A. Cruz and A. J. M. Cardoso. Diagnosis of rotor faults in direct and indirect FOC induction motor drives. In *Power Electronics and Applications, 2007 European Conference on*, pages 1–10, 2007.

[91] Danfoss. *VLT HVAC drive*, 2011. Available online at www.danfoss.com.

[92] G. B. Dantzig. Programming in a linear structure. *Econometria*, 27:73–74, 1949.

[93] J. G. de Jalón and E. Bayo. *Kinematic and Dynamic Simulation of Multibody Systems*. Springer, New York, 1994.

[94] J. de Jesus Barradas-Berglind, R. Wisniewski, and M. Soltani. Fatigue damage estimation and data-based control for wind turbines. *IET Control Theory & Applications*, 9(7):1042–1050, 2015.

[95] C. W. de Silva. *Mechatronic Systems: Devices, Design, Control, Operation and Monitoring*. CRC Press, Boca Raton, 2008.

[96] J. P. de Wardt, M. Behounek, C. Chapman, and D. Putra. Drilling systems automation – preparing for the big jump forward. In *SPE/IADC Drilling Conference and Exhibition*, pages 1–16, 2013.

[97] M. Depenbrock. Direkte Selbstregelung (DSR) für hochdynamische Drehfeldantriebe mit Stromrichter-speisung. *ETZ Archive*, 7:211–218, 1985.

[98] M. Depenbrock. Direct self-control (DSC) of inverter-fed induction machine. *IEEE Transactions on Power Electronics*, 3(4):420–429, 1988.

[99] W.-H. Ding, H. Deng, Q.-M. Li, and Y.-M. Xia. Control-orientated dynamic modeling of forging manipulators with multi-closed kinematic chains. *Robotics and Computer-Integrated Manufacturing*, 30(5):421–431, 2014.

[100] DNV. Electrical Installations. *Offshore Standard DNV-OS-D201*, 2011.

[101] DNV. Type approval of composite drive shafts and flexible couplings. *Standard for Certification, no. 2.9 Approval Programmes*, 2014.

[102] A. Domahidi. *Methods and Tools for Embedded Optimization and Control*. PhD thesis, ETH Zürich, 2013.

[103] A. Domahidi and J. Jerez. FORCES Professional. embotech GmbH. `http://embotech.com/FORCES-Pro`, 2016. Accessed: 2016-07-25.

[104] G. Downton. Systems modeling and design of automated-directional-drilling systems. *SPE Drilling & Completion*, 27(1):212–232, 2015.

[105] T. Endo, K. Mitsunaga, and H. Nakagawa. Fatigue of metals subjected to varying stress prediction of fatigue lives. In *Preliminary Proceedings of the Chugoku-Shikoku District Meeting*, pages 41–44, 1967.

[106] European Commission. Directive 2014/34/EU of the European Parliament and of the Council. *Official Journal of the European Union L96*, 2014.

[107] Y. Fang, P. Wang, N. Sun, and Y. Zhang. Dynamics analysis and nonlinear control of an offshore boom crane. *IEEE Transactions on Industrial Electronics*, 61(1):414–427, 2014.

[108] F. J. T. E. Ferreira, J. A. C. Fong, and A. T. de Almeida. Ecoanalysis of variable-speed drives for flow regulation in pumping systems. *IEEE Transactions on Industrial Electronics*, 58(6):2117–2125, 2011.

[109] P. Flores and J. Ambrósio. Revolute joints with clearance in multibody systems. *Computers & Structures*, 82(17-19):1359–1369, 2004.

[110] C. A. Floudas. *Nonlinear and Mixed-Integer Optimization*. Oxford University Press, Oxford, 1995.

[111] G. Fouad. *AC Electric Motors Control – Advanced Design Techniques and Applications*. John Wiley & Sons, Chichester, 2013.

[112] S. Foulard, S. Rinderknecht, M. Ichchou, and J. Perret-Liaudet. Automotive drivetrain model for transmission damage prediction. *Mechatronics*, 30:27–54, 2015.

[113] R. Fourer, D. M. Gay, and B. W. Kernighan. A modeling language for mathematical programming. *Management Science*, 36:519–554, 1990.

[114] G. D. Friedlander. Railroad electrification: Past, present, and future history of systems in the United States. *IEEE Spectrum*, 5(7):50–65, 1968.

[115] M. Friedman. *There's No Such Thing as a Free Lunch*. Open Court Publishing Company, LaSalle, 1975.

[116] T. A. Gallant and K. M. Andrews. Large cage induction motors for offshore machinery drive applications. In *Petroleum and Chemical Industry (PCIC), 2006 IEEE Industry Applications Society Technical Conference on*, pages 1155–1159, 2006.

[117] GAMBICA/REMA. *Application of the ATEX directives to power drive systems*, 2004. Available online at www.gambica.org.uk.

[118] C. E. García, D. M. Prett, and M. Morari. Model predictive control: Theory and practice – a survey. *Automatica*, 25(3):335–348, 1989.

[119] W. Gautschi. *Numerical Analysis*. Springer/Birkhäuser, New York, 2012.

[120] T. Geyer, G. Papafotiou, and M. Morari. Model predictive direct torque control – part I: Concept, algorithm, and analysis. *IEEE Transactions on Industrial Electronics*, 56(6):1894–1905, 2009.

[121] J. F. Gieras. *Advancements in Electric Machines*. Springer, Berlin, 2008.

[122] P. J. Goulart. *Affine Feedback Policies for Robust Control with Constraints*. PhD thesis, University of Cambridge, 2007.

[123] R. Graham, E. Lawler, J. Lenstra, and A. Kan. Optimization and approximation in deterministic sequencing and scheduling: A survey. In *Annals of Discrete Mathematics*, volume 5, pages 287–326. 1979.

[124] M. Grant and S. Boyd. Graph implementations for nonsmooth convex programs. In V. Blondel, S. Boyd, and H. Kimura, editors, *Recent Advances in Learning and Control*, Lecture Notes in Control and Information Sciences, pages 95–110. Springer-Verlag Limited, 2008. `http://stanford.edu/~boyd/graph_dcp.html`.

[125] M. Grant and S. Boyd. CVX: Matlab software for disciplined convex programming, version 2.1. `http://cvxr.com/cvx`, 2015. Accessed: 2016-07-25.

[126] R. L. Grossmann, A. Nerode, A. P. Ravn, and H. Rischel. *Hybrid Systems*. Springer, New York, 1993. Lecture Notes in Computer Science (vol. 736).

[127] E. I. Grøtli and T. A. Johansen. Motion- and communication-planning of unmanned aerial vehicles in delay tolerant network using mixed-integer linear programming. *Modeling, Identification and Control*, 37(2):77–97, 2016.

[128] J. M. Gutierrez-Villalobos, J. Rodriguez-Resendiz, E. A. Rivas-Araiza, and V. H. Mucino. A review of parameter estimators and controllers for induction motors based on artificial neural networks. *Neurocomputing*, 118:87–100, 2013.

[129] T. G. Habetler, F. Profumo, M. Pastorelli, and L. M. Tolbert. Direct torque control of induction machines using space vector modulation. *IEEE Transactions on Industry Applications*, 28(5):1045–1053, 1992.

[130] M. T. Hagan, H. B. Demuth, and M. Beale. *Neural Network Design*. PWS Publishing Company, USA, 1996.

[131] D. K. Han and J. H. Chang. Design of electromagnetic linear actuator using the equivalent magnetic circuit method. *IEEE Transactions on Magnetics*, 52(3):1–4, 2016.

[132] L. Harnefors. *Control of Variable-Speed Drives*. Mälardalen University, Västerås, 2003.

[133] Ø. Harsem, A. Eide, and K. Heen. Factors influencing future oil and gas prospects in the Arctic. *Energy Policy*, 39(12):8037–8045, 2011.

[134] K. Hasse. *Zur Dynamik drehzahlgeregelter Antriebe mit stromrichtergespeisten Asynchron-Kurzschlussläufermaschinen*. PhD thesis, Technische Hochschule Darmstadt, 1969.

[135] T. Hazel, H. H. Baerd, J. J. Legeay, and J. J. Bremnes. Taking power distribution under the sea: Design, manufacture, and assembly of a subsea electrical distribution system. *IEEE Industry Applications Magazine*, 19(5):58–67, 2013.

[136] S. S. Heragu and A. Kusiak. Analysis of expert systems in manufacturing design. *IEEE Transactions on Systems, Man, and Cybernetics*, 17(6):898–912, 1987.

[137] M. Hilairet, F. Auger, and E. Berthelot. Speed and rotor flux estimation of induction machines using a two-stage extended Kalman filter. *Automatica*, 45(8):1819–1827, 2009.

[138] M. Hinkkanen, A.-K. Repo, M. Ranta, and J. Luomi. Small-signal modeling of mutual saturation in induction machines. *IEEE Transactions on Industry Applications*, 46(3):965–973, 2010.

[139] S. L. Ho, S. Yang, G. Ni, and H. C. Wong. A particle swarm optimization method with enhanced global search ability for design optimizations of electromagnetic devices. *IEEE Transactions on Magnetics*, 42(4):1107–1110, 2006.

[140] A. H. Hoevenaars, I. C. Evans, and B. Desai. Preventing AC drive failures due to commutation notches on a drilling rig. *IEEE Transactions on Industry Applications*, 49(3):1215–1220, 2013.

[141] A. H. Hoevenaars, M. McGraw, and K. Rittammer. Preventing centrifuge failures due to voltage distortion on a drilling rig. *IEEE Transactions on Industry Applications*, 52(1):633–640, 2016.

[142] T. Hoevenaars, I. C. Evans, and A. Lawson. New marine harmonic standards. *IEEE Industry Applications Magazine*, 16(1):16–25, 2010.

[143] R. K. Holm, N. I. Berg, M. Walkusch, P. O. Rasmussen, and R. H. Hansen. Design of a magnetic lead screw for wave energy conversion. *IEEE Transactions on Industry Applications*, 49(6):2699–2708, 2013.

[144] P. Holoborodko. Smooth noise robust differentiators. `http://www.holoborodko.com/pavel/numerical-methods/numerical-derivative/smooth-low-noise-differentiators/`, 2008. Accessed: 2015-11-11.

[145] J. Holtz. Sensorless control of induction machines – with or without signal injection? *IEEE Transactions on Industrial Electronics*, 53(1):7–30, 2005.

[146] Honeywell. *Variable frequency drive (VFD): Application guide*, 2014. Available online at www.customer.honeywell.com.

[147] M. Höök and K. Aleklett. A decline rate study of Norwegian oil production. *Energy Policy*, 36(11):4262–4271, 2008.

[148] B. Houska, H. J. Ferreau, and M. Diehl. ACADO toolkit – an open-source framework for automatic control and dynamic optimization. *Optimal Control Applications and Methods*, 32(3):298–312, 2011.

[149] A. Hughes and B. Drury. *Electric Motors and Drives: Fundamentals, Types, and Applications*. Elsevier/Newnes, Kidlington, Oxford, 2013.

[150] IBM. *IBM ILOG CPLEX Optimization Studio: CPLEX user's manual*, 2014.

[151] IBM. IBM ILOG CPLEX Optimization Studio. `http://www-01.ibm.com/software/commerce/optimization/cplex-optimizer`, 2016. Accessed: 2016-07-25.

[152] IEC. Wind turbine generator systems – part 13: Measurement of mechanical loads. *IEC 61400-13*, 1998.

[153] IEC. Rotating electrical machines – part 12: Starting performance of single-speed three-phase cage induction motors. *IEC 60034-12*, 2002.

[154] IEC. Rotating electrical machines – part 1: Rating and performance. *IEC 60034-1*, 2010.

[155] IEC. Explosive atmospheres – part 1: Equipment protection by flameproof enclosures "d". *IEC 60079-1*, 2014.

[156] IEC. Explosive atmospheres – part 7: Equipment protection by increased safety "e". *IEC 60079-7*, 2015.

[157] IEEE. IEEE standard test procedure for polyphase induction motors and generators. *IEEE Standard 112*, 2004.

[158] N. F. Ilinski. A new approach to AC motor selection and checking. In *Electrical Machines and Drives, 1995. 7th International Conference on (Conf. Publ. No. 412)*, pages 32–36, 1995.

[159] R. Isermann, R. Schwarz, and S. Stolzl. Fault-tolerant drive-by-wire systems. *IEEE Control Systems*, 22(5):64–81, 2002.

[160] A. Isidori. *Nonlinear Control Systems: Part II*. Springer, London, 1999.

[161] M. A. Ismail, N. Sawalhi, and T.-H. Pham. Quantifying bearing fault severity using time synchronous averaging jerk energy. In *Sound and Vibration, 22nd International Congress on*, pages 1–8, 2015.

[162] ITI GmbH. *SimulationX 3.6: user's manual*, 2013.

[163] S. Jafarzadeh, C. Lascu, and M. S. Fadali. State estimation of induction motor drives using the unscented Kalman filter. *IEEE Transactions on Industrial Electronics*, 59(11):4207–4216, 2012.

[164] M. I. Jahmeerbacus. Flow rate regulation of a variable speed driven pumping system using fuzzy logic. In *Electric Power and Energy Conversion Systems (EPECS), 2015 4th International Conference on*, pages 1–6, 2015.

[165] T. A. Jankowski, F. C. Prenger, D. D. Hill, S. R. O'Bryan, K. K. Sheth, E. B. Brookbank, D. F. A. Hunt, and Y. A. Orrego. Development and validation of a thermal model for electric induction motors. *IEEE Transactions on Industrial Electronics*, 57(12):4043–4054, 2010.

[166] H. Janocha. *Actuators: Basics and Applications*. Springer, Berlin, 2004.

[167] J. D. Jansen, L. van den Steen, and E. Zachariasen. Active damping of torsional drillstring vibrations with a hydraulic top drive. *SPE Drilling & Completion*, 10(4):250–254, 1995.

[168] P. L. Jansen, R. D. Lorenz, and D. W. Novotny. Observer-based direct field orientation: Analysis and comparison of alternative methods. *IEEE Transactions on Industry Applications*, 30(4):945–953, 1994.

[169] T. Jernstrøm, S. Sangesland, and A. Hägglin. An all-electric system for subsea well control. In *Offshore Technology Conference*, pages 705–711, 1993.

[170] T. A. Johansen and T. I. Fossen. Control allocation: A survey. *Automatica*, 49(5):1087–1103, 2013.

[171] R. Jönsson. Method and apparatus for controlling an AC induction motor, 1984. US Patent 4458193.

[172] A. Josifovic, J. Corney, and B. Davies. Modeling a variable speed drive for positive displacement pump. In *Advanced Intelligent Mechatronics (AIM), 2014 IEEE/ASME International Conference on*, pages 1218–1223, 2014.

[173] J. Kallrath. Mixed integer optimization in the chemical process industry: Experience, potential and future perspectives. *Chemical Engineering Research and Design*, 78(6):809–822, 2000.

[174] R. E. Kalman. A new approach to linear filtering and prediction problems. *ASME Transactions (Journal of Basic Engineering)*, 82 D:33–45, 1960.

[175] S. T. Kandukuri, A. Klausen, H. R. Karimi, and K. G. Robbersmyr. A review of diagnostics and prognostics of low-speed machinery towards wind turbine farm-level health management. *Renewable and Sustainable Energy Reviews*, 53:697–708, 2016.

[176] G. A. Kaufman and M. J. Kocher. Fail-safe dynamic brake for three-phase induction machines. *IEEE Transactions on Industry Applications*, IA-20(5):1229–1237, 1984.

[177] A. Kaufmann and A. Henry-Labordère. *Integer and Mixed Programming: Theory and Applications*. Academic Press, New York, 1977.

[178] M. P. Kaźmierkowski, R. Krishnan, and F. Blaabjerg. *Control in Power Electronics*. Academic Press, San Diego/London, 2002.

[179] M. P. Kaźmierkowski and L. Malesani. Current control techniques for three-phase voltage-source PWM converters: A survey. *IEEE Transactions on Industrial Electronics*, 45(5):691–703, 1998.

[180] H. Khalil. *Nonlinear Systems*. Prentice Hall, Upper Saddle River, 2003.

[181] J.-H. Kim and J.-H. Chang. A new electromagnetic linear actuator for quick latching. *IEEE Transactions on Magnetics*, 43(4):1849–1852, 2007.

[182] J.-H. Kim, J.-H. Chang, S.-M. Park, K.-I. Hwang, and J.-Y. Lee. A novel electromagnetic latching device for variable valve timing in automotive engine. In *Electromagnetic Field Computation (CEFC), 2010 14th Biennial IEEE Conference on*, pages 1–1, 2010.

[183] S. Kim and S. K. Sul. High performance position sensorless control using rotating voltage signal injection in IPMSM. In *Power Electronics and Applications (EPE 2011), Proceedings of the 2011-14th European Conference on*, pages 1–10, 2011.

[184] Y.-R. Kim, S.-K. Sul, and M.-H. Park. Speed sensorless vector control of induction motor using extended Kalman filter. *IEEE Transactions on Industry Applications*, 30(5):1225–1233, 1994.

[185] J. L. Kirtley, A. Banerjee, and S. Englebretson. Motors for ship propulsion. *Proceedings of the IEEE*, 103(12):2320–2332, 2015.

[186] J. Ko, S. Ko, H. Son, B. Yoo, J. Cheon, and H. Kim. Development of brake system and regenerative braking cooperative control algorithm for automatic-transmission-based hybrid electric vehicles. *IEEE Transactions on Vehicular Technology*, 64(2):431–440, 2015.

[187] A. Kodali, Y. Zhang, C. Sankavaram, K. Pattipati, and M. Salman. Fault diagnosis in the automotive electric power generation and storage system (EPGS). *IEEE/ASME Transactions on Mechatronics*, 18(6):1809–1818, 2013.

[188] K. P. Kovács and I. Rácz. *Transiente Vorgänge in Wechselstrommaschinen*. Verlag der Ungarischen Akademie der Wissenschaften, Budapest, 1959.

[189] M. Kozlowski. Wound rotor to induction motor and VFD conversion case study. *IEEE Transactions on Industry Applications*, 49(3):1221–1227, 2013.

[190] C. Kral, T. G. Habetler, R. G. Harley, F. Pirker, G. Pascoli, H. Oberguggenberger, and C. J. M. Fenz. Rotor temperature estimation of squirrel cage induction motors by means of a combined scheme of parameter estimation and a thermal equivalent model. In *Electric Machines and Drives Conference, 2003. IEEE International*, volume 2, pages 931–937, 2003.

[191] P. C. Krause and C. H. Thomas. Simulation of symmetrical induction machinery. *IEEE Transactions on Power Apparatus and Systems*, 84(11):1038–1053, 1965.

[192] N. A. H. Kremers, E. Detournay, and N. van de Wouw. Model-based robust control of directional drilling systems. *IEEE Transactions on Control Systems Technology*, 24(1):226–239, 2016.

[193] E. J. Kreuzer. Mathematical modeling of complex mechanical systems. *Mathematical Modelling*, 8:37–42, 1987.

[194] Z. Krzemiński. Nonlinear control of the induction motor. In *10th IFAC World Congress*, pages 349–354, 1987.

[195] W. Kuo and R. Wan. Recent advances in optimal reliability allocation. *IEEE Transactions on Systems, Man, and Cybernetics – Part A: Systems and Humans*, 37(2):143–156, 2007.

[196] C. S. G. Lee and M. Ziegler. Geometric approach in solving inverse kinematics of PUMA robots. *IEEE Transactions on Aerospace and Electronic Systems*, AES-20(6):695–706, 1984.

[197] J. Lee and S. Leyffer. *Mixed Integer Nonlinear Programming*. Springer, New York, 2012.

[198] K. Lee, S. Frank, P. K. Sen, L. G. Polese, M. Alahmad, and C. Waters. Estimation of induction motor equivalent circuit parameters from nameplate data. In *North American Power Symposium (NAPS), 2012*, pages 1–6, 2012.

[199] S.-H. Lee, J.-H. Lee, S.-H. Goo, Y.-C. Cho, and H.-Y. Cho. An evaluation of relative damage to the powertrain system in tracked vehicles. *Sensors*, 9(3):1845–1859, 2009.

[200] B. J. Leira, Q. Chen, A. J. Sørensen, and C. M. Larsen. Modeling of riser response for DP control. *ASME Journal of Offshore Mechanics and Arctic Engineering*, 124(4):219–225, 2002.

[201] A. Leite, R. Araujo, and D. Freitas. Full and reduced order extended Kalman filter for speed estimation in induction motor drives: A comparative study. In *Power Electronics Specialists Conference, 2004 IEEE 35th Annual*, volume 3, pages 2293–2299, 2004.

[202] F. Lewis. *Applied Optimal Control and Estimation – Digital Design and Implementation*. Prentice Hall, New York, 1992.

[203] B. Li, E. Zhou, B. Huang, J. Duan, Y. Wang, N. Xu, J. Zhang, and H. Yang. Large scale recurrent neural network on GPU. In *Neural Networks (IJCNN), 2014 International Joint Conference on*, pages 4062–4069, 2014.

[204] L. Li, Y. Tang, and D. Pan. Design optimization of air-cored PMLSM with overlapping windings by multiple population genetic algorithm. *IEEE Transactions on Magnetics*, 50(11):1–5, 2014.

[205] K.-Y. Lian, C.-Y. Hung, C.-S. Chiu, and P. Liu. Induction motor control with friction compensation: An approach of virtual-desired-variable synthesis. *IEEE Transactions on Power Electronics*, 20(5):1066–1074, 2005.

[206] T. A. Lipo. *Analysis of Synchronous Machines*. CRC Press, Boca Raton, 2012.

[207] L. Ljung. *System Identification: Theory for the User*. Prentice Hall, Eaglewood Cliffs, 1987.

[208] L. Ljung and T. Glad. *Modeling of Dynamic Systems*. Prentice Hall, Eaglewood Cliffs, 1994.

[209] J. Löfberg. YALMIP : A toolbox for modeling and optimization in MATLAB. In *Proceedings of the CACSD Conference*, Taipei, Taiwan, 2004.

[210] S. M. Lord, R. A. Layton, and M. W. Ohland. Trajectories of electrical engineering and computer engineering students by race and gender. *IEEE Transactions on Education*, 54(4):610–618, 2011.

[211] Z. Lujun. Study on an electric drilling rig with hydraulic energy storage. In *Computing, Control and Industrial Engineering (CCIE), 2010 International Conference on*, volume 2, pages 315–318, 2010.

[212] J. Luo, J. Bai, P. He, and K. Ying. Axial strain calculation using a low-pass digital differentiator in ultrasound elastography. *IEEE Transactions on Ultrasonics, Ferroelectrics, and Frequency Control*, 51(9):1119–1127, 2004.

[213] J. D. Macpherson, J. P. de Wardt, F. Florence, C. Chapman, M. Zamora, M. Laing, and F. Iversen. Drilling-systems automation: Current state, initiatives, and potential impact. *SPE Drilling & Completion*, 28(4):296–308, 2013.

[214] Ø. Magnussen, G. Hovland, and M. Ottestad. Multicopter UAV design optimization. In *Mechatronic and Embedded Systems and Applications (MESA), 2014 IEEE/ASME 10th International Conference on*, pages 1–6, 2014.

[215] Ø. Magnussen, M. Ottestad, and G. Hovland. Multicopter design optimization and validation. *Modeling, Identification and Control*, 36(2):67–79, 2015.

[216] S. Mahdavi, M. E. Shiri, and S. Rahnamayan. Metaheuristics in large-scale global continuous optimization: A survey. *Information Sciences*, 295:407–428, 2015.

[217] M. Malinowski, A. Milczarek, R. Kot, Z. Goryca, and J. Szuster. Optimized energy-conversion systems for small wind turbines: Renewable energy sources in modern distributed power generation systems. *IEEE Power Electronics Magazine*, 2(3):16–30, 2015.

[218] R. Marino, S. Peresada, and P. Valigi. Adaptive input-output linearizing control of induction motors. *IEEE Transactions on Automatic Control*, 38(2):208–221, 1993.

[219] R. Marino, P. Tomei, and C. M. Verrelli. *Induction Motor Control Design*. Springer, London, 2010.

[220] M. R. Martins and D. F. S. Burgos. Multi-objective optimization design of tanker ships via a genetic algorithm. *ASME Journal of Offshore Mechanics and Arctic Engineering*, 133(4):041303:1–12, 2011.

[221] J. I. Marvik, E. V. Øyslebø, and M. Korpås. Electrification of offshore petroleum installations with offshore wind integration. *Renewable Energy*, 50:558–564, 2013.

[222] P. Matic, M. Gecic, D. Lekic, and D. Marcetic. Thermal protection of vector-controlled IM drive based on DC current injection. *IEEE Transactions on Industrial Electronics*, 62(4):2082–2089, 2015.

[223] MATLAB. *Neural Network Toolbox: Users' Guide*, 2002. Available online at www.mathworks.com.

[224] MATLAB. *Optimization Toolbox: Users' Guide*, 2015. Available online at www.mathworks.com.

[225] J. Mattingley and S. Boyd. CVXGEN: A code generator for embedded convex optimization. *Optimization and Engineering*, 13(1):1–27, 2012.

[226] J. Mattingley, Y. Wang, and S. Boyd. Code generation for receding horizon control. In *Computer-Aided Control System Design, 2010 IEEE International Symposium on*, pages 985–992, 2010.

[227] B. S. Mattu and R. Shankar. Test driven design methodology for component-based system. In *Systems Conference, 2007 1st Annual IEEE*, pages 1–7, 2007.

[228] R. McElveen, J. Korkeakoski, and J. Malinowski. Electrical and mechanical differences between NEMA/IEEE and IEC AC low voltage random wound induction motors. In *Petroleum and Chemical Industry (PCIC), 2012 IEEE Industry Applications Society Technical Conference on*, pages 1–10, 2012.

[229] W. McMurray and D. P. Shattuck. A silicon-controlled rectifier inverter with improved commutation. *Transactions of the American Institute of Electrical Engineers, Part I: Communication and Electronics*, 80(5):531–542, 1961.

[230] S. I. McNeill. Implementing the fatigue damage spectrum and fatigue damage equivalent vibration testing. In *Shock and Vibration, 79th Symposium*, pages 1–20, 2008.

[231] P. Meckl. Optimized s-curve motion profiles for minimum residual vibration. In *American Control Conference, 1998. Proceedings of the*, volume 5, pages 2627–2631, 1998.

[232] S. Mehrotra. On the implementation of a primal-dual interior point method. *SIAM Journal on Optimization*, 2:575–601, 1992.

[233] J. L. Meriam and L. G. Kraige. *Engineering Mechanics: Dynamics*. John Wiley & Sons, New York, 2012.

[234] H. E. Meritt. *Hydraulic Control Systems*. John Wiley & Sons, New York, 1967.

[235] J. Mindykowski, T. Tarasiuk, M. Szweda, and I. C. Evans. *Electric power quality measurements on an all electric ship with active front end propulsion drives*. Polish Register of Shipping, Gdynia Maritime University, 2007.

[236] M. Miner. Cumulative damage in fatigue. *Journal of Applied Mechanics*, 12(3):159–164, 1945.

[237] V. Mini and S. Ushakumari. Incipient fault detection and diagnosis of induction motor using fuzzy logic. In *Recent Advances in Intelligent Computational Systems (RAICS), 2011 IEEE*, pages 675–681, 2011.

[238] Motor Reliability Working Group. Report of large motor reliability survey of industrial and commercial installations, part I. *IEEE Transactions on Industry Applications*, IA-21(4):853–864, 1985.

[239] M. Musio, M. Porru, A. Serpi, I. Marongiu, and A. Damiano. Optimal electric vehicle charging strategy for energy management in microgrids. In *Electric Vehicle Conference (IEVC), 2014 IEEE International*, pages 1–8, 2014.

[240] A. Myklebust and L. Eriksson. Modeling, observability, and estimation of thermal effects and aging on transmitted torque in a heavy duty truck with a dry clutch. *IEEE/ASME Transactions on Mechatronics*, 20(1):61–72, 2015.

[241] R. Nataraj, C. Pasluosta, and Z.-M. Li. Online kinematic regulation by visual feedback for grasp versus transport during reach-to-pinch. *Human Movement Science*, 36:134–153, 2014.

[242] J. A. Nelder and R. Mead. A simplex method for function minimization. *The Computer Journal*, 7(4):308–313, 1965.

[243] K. Neleman. Motor controls for Ex motors in hazardous areas: An application guide! In *2009 Conference Record PCIC Europe*, pages 132–145, 2009.

[244] G. Nelson, R. Rajamani, A. Gastineau, S. Wojtkiewicz, and A. Schultz. Bridge life extension using semiactive vibration control. *IEEE/ASME Transactions on Mechatronics*, 20(1):207–216, 2015.

[245] M. Neufeld, O. Ramirez, and A. Ustinovich. A comparative study of fixed speed vs. variable speed control of a series configured pipeline pumping application. In *Petroleum and Chemical Industry (PCIC), 2014 IEEE Industry Applications Society Technical Conference on*, pages 491–500, 2014.

[246] K. D. Nguyen, I.-M. Chen, and T.-C. Ng. Planning algorithms for s-curve trajectories. In *Advanced Intelligent Mechatronics, 2007 IEEE/ASME International Conference on*, pages 1–6, 2007.

[247] K. D. Nguyen, I.-M. Chen, and T.-C. Ng. On algorithms for planning s-curve motion profiles. *International Journal of Advanced Robotic Systems*, 5(1):99–106, 2008.

[248] S. Ni, W. Qiu, A. Zhang, and D. Prior. Hydrodynamic simulation and optimization of an oil skimmer. *ASME Journal of Offshore Mechanics and Arctic Engineering*, 137(2):021301:1–10, 2015.

[249] A. Niesłony. Determination of fragments of multiaxial service loading strongly influencing the fatigue of machine components. *Mechanical Systems and Signal Processing*, 23(8):2712–2721, 2009.

[250] A. Niesłony and C. Sonsino. Calculating the fatigue crack initiation in machine parts under random multiaxial loading. In *COMSOL Multiphysics Konferenz 2006 – Neue Wege der Multiphysik Simulation*, pages 106–111, 2006.

[251] P. E. Nikravesh. *Computer-Aided Analysis of Mechanical Systems*. Prentice Hall, Eaglewood Cliffs, 1988.

[252] P. E. Nikravesh. *Planar Multibody Dynamics: Formulation, Programming, and Applications.* CRC Press, Boca Raton, 2007.

[253] J. Nocedal and S. J. Wright. *Numerical Optimization.* Springer, New York, 2006.

[254] P. A. Nordhammer, M. K. Bak, and M. R. Hansen. Controlling the slewing motion of hydraulically actuated cranes using sequential activation of counterbalance valves. In *Control, Automation and Systems (ICCAS), 2012 12th International Conference on*, pages 773–778, 2012.

[255] R. L. Norton. *Design of Machinery: An Introduction to the Synthesis and Analysis of Mechanisms and Machines.* McGraw-Hill, Worcester, 1999.

[256] I. Novak. *Relaxation and Decomposition Methods for Mixed Integer Nonlinear Programming.* Birkhäuser, Basel, 2005.

[257] H. I. Okumus and M. Aktas. Direct torque control of induction machine drives using adaptive hysteresis band for constant switching frequency. In *2007 IEEE International Electric Machines Drives Conference*, volume 2, pages 1762–1767, 2007.

[258] F. Oldewurtel. *Stochastic Model Predictive Control for Buidling Climate Control.* PhD thesis, ETH Zürich, 2011.

[259] T. Orłowska-Kowalska. Application of extended Luenberger observer for flux and rotor time-constant estimation in induction motor drives. *IEE Proceedings D – Control Theory and Applications*, 136(6):324–330, 1989.

[260] R. Ortega, P. J. Nicklasson, and H. Sira-Ramirez. *Passivity-Based Control of Euler-Lagrange Systems.* Springer, Berlin, 1998.

[261] M. Ottestad, N. Nilsen, and M. R. Hansen. Reducing the static friction in hydraulic cylinders by maintaining relative velocity between piston and cylinder. In *Control, Automation and Systems (ICCAS), 2012 12th International Conference on*, pages 764–769, 2012.

[262] A. Palmgren. Die Lebensdauer von Kugellagern. *Zeitschrift des Vereins Deutscher Ingenieure*, 68(14):339–341, 1924.

[263] G. Papafotiou, J. Kley, K. Papadopoulos, P. Bohren, and M. Morari. Model predictive direct torque control – part II: Implementation and experimental evaluation. *IEEE Transactions on Industrial Electronics*, 56(6):1906–1915, 2009.

[264] E. J. Park and J. K. Mills. Static shape and vibration control of flexible payloads with applications to robotic assembly. *IEEE/ASME Transactions on Mechatronics*, 10(6):675–687, 2005.

[265] W. Pawlus, M. Choux, and M. R. Hansen. Hydraulic vs. electric: A review of actuation systems in offshore drilling equipment. *Modeling, Identification and Control*, 37(1):1–17, 2016.

[266] W. Pawlus, M. Choux, M. R. Hansen, and G. Hovland. Load torque estimation method to design electric drivetrains for offshore pipe handling equipment. *ASME Journal of Offshore Mechanics and Arctic Engineering*, 138(4):041301:1–9, 2016.

[267] W. Pawlus, M. Choux, G. Hovland, and H. V. Khang. Parameters identification of induction motor dynamic model for offshore applications. In *Mechatronic and Embedded Systems and Applications (MESA), 2014 IEEE/ASME 10th International Conference on*, pages 1–6, 2014.

[268] W. Pawlus, M. Choux, G. Hovland, S. Øydna, and M. R. Hansen. Modeling and simulation of an offshore pipe handling machine. In *Simulation and Modeling, 2014 SIMS 55th Conference on*, pages 277–284, 2014.

[269] W. Pawlus, M. K. Ebbesen, M. R. Hansen, M. Choux, and G. Hovland. Comparative analysis of numerical models of pipe handling equipment used in offshore drilling applications. In *Numerical Analysis and Applied Mathematics, 13th International Conference of*, pages 370013:1–4, 2016.

[270] W. Pawlus, D. Frick, M. Morari, G. Hovland, and M. Choux. Drivetrain design optimization for electrically actuated systems via Mixed Integer Programing. In *Industrial Electronics Society, IECON 2015 – 41st Annual Conference of the IEEE*, pages 1465–1470, 2015.

[271] W. Pawlus, M. R. Hansen, M. Choux, and G. Hovland. Mitigation of fatigue damage and vibration severity of electric drivetrains by systematic selection of motion profiles. *IEEE/ASME Transactions on Mechatronics*, 2016. In press, `http://dx.doi.org/10.1109/TMECH.2016.2573587`.

[272] W. Pawlus, M. R. Hansen, G. Hovland, and M. Choux. Torque peak reduction and overload monitoring of induction motors in offshore drilling operations. In *ACEMP-OPTIM-ELECTROMOTION, 2015 IEEE Joint Conference*, pages 393–398, 2015.

[273] W. Pawlus, I. C. Inouva, S. Øydna, T. K. Wroldsen, and G. Hovland. Next generation hardware-in-the-loop simulation enables advanced testing of offshore hydraulic systems. In *IADC Advanced Rig Technology Conference and Exhibition*, pages 1–7, 2015.

[274] W. Pawlus, S. T. Kandukuri, G. Hovland, M. Choux, and M. R. Hansen. EKF-based estimation and control of electric drivetrain in offshore pipe racking machine. In *Industrial Technology (ICIT), 2016 IEEE International Conference on*, pages 153–158, 2016.

[275] W. Pawlus, H. R. Karimi, and K. G. Robbersmyr. Data-based modeling of vehicle collisions by nonlinear autoregressive model and feedforward neural network. *Information Sciences*, 235:65–79, 2013.

[276] W. Pawlus, H. V. Khang, and M. R. Hansen. Identification of induction motor thermal model for improved drivetrain design. In *Electrical Machines (ICEM), 2016 International Conference on*, 2016. In press.

[277] W. Pawlus, F. Liland, N. Nilsen, S. Øydna, G. Hovland, and T. K. Wroldsen. Optimization of a high fidelity virtual model of a hydraulic hoisting system for real-time simulations. In *8th International Petroleum Technology Conference*, pages 1–11, 2014.

[278] H. C. Pedersen, P. Johansen, C. Yigen, T. O. Andersen, and D. B. Rømer. Analysis of temperature's influence on a digital displacement pump's volumetric efficiency. *Applied Mechanics and Materials*, 233:24–27, 2012.

[279] T. Pedersen and Ø. Smogeli. Experience from hardware-in-the-loop testing of drilling control systems. *SPE Drilling & Completion*, 28(4):309–315, 2013.

[280] M. Peltola. *Power factor improved by variable speed AC drives*, 2003. Press Release. Available online at www.abb.com.

[281] S. Perumaal and N. Jawahar. Synchronized trigonometric s-curve trajectory for jerk-bounded time-optimal pick and place operation. *International Journal of Robotics and Automation*, 27(4):385–395, 2012.

[282] T. Pettersen. Second well in production at Prirazlomnoye. `http://bit.ly/22R4BYn`, 2015. Accessed: 2016-03-31.

[283] M. Pettersson and J. Ölvander. Drive train optimization for industrial robots. *IEEE Transactions on Robotics*, 25(6):1419–1424, 2009.

[284] R. D. Phillips and R. N. Laberge. A smart relief valve. *IEEE Transactions on Industry Applications*, IA-20(2):413–417, 1984.

[285] T. Pipe. Subsea hydraulic power generation and distribution for subsea control systems. In *European Petroleum Conference*, pages 829–835, 1982.

[286] M. Rahimi, M. Rausand, and S. Wu. Reliability prediction of offshore oil and gas equipment for use in an Arctic environment. In *International Conference on Quality, Reliability, Risk, Maintenance, and Safety Engineering*, pages 81–86, 2011.

[287] A. M. Rahman and R. Abdullah. Noise survey in offshore operations. In *SPE Health, Safety and Environment in Oil and Gas Exploration and Production Conference*, pages 131–144, 1991.

[288] K. Rajashekara. History of electric vehicles in General Motors. *IEEE Transactions on Industry Applications*, 30(4):897–904, 1994.

[289] R. Raman and I. Grossmann. Relation between MILP modelling and logical inference for chemical process synthesis. *Computers & Chemical Engineering*, 15(2):73–84, 1991.

[290] D. Ransom and R. Hamilton. Extending motor life with updated thermal model overload protection. *IEEE Transactions on Industry Applications*, 49(6):2471–2477, 2013.

[291] S. Rassenfoss. Drilling automation: A catalyst for change. *Journal of Petroleum Technology*, 63(9):28–34, 2011.

[292] S. Rezazadeh and J. W. Hurst. On the optimal selection of motors and transmissions for electromechanical and robotic systems. In *Intelligent Robots and Systems (IROS 2014), 2014 IEEE/RSJ International Conference on*, pages 4605–4611, 2014.

[293] T. R. Rhea. Modern diesel-electric drilling rig equipment. *Transactions of the American Institute of Electrical Engineers*, 65(7):447–453, 1946.

[294] M. Rivenbark, S. Khater, W. Dietz, and S. Barnes. An innovative all electric well production system. In *SPE Production and Operations Symposium*, pages 1–9, 2007.

[295] M. L. Rizzone. Electric drilling rig developments. *IEEE Transactions on Industry and General Applications*, IGA-3(2):194–197, 1967.

[296] R. Robinson, C. Kothera, R. Sanner, and N. Wereley. Nonlinear control of robotic manipulators driven by pneumatic artificial muscles. *IEEE/ASME Transactions on Mechatronics*, 21(1):55–68, 2015.

[297] Rockwell Automation. *Application basics of operation of three-phase induction motors*, 1996. Available online at www.rockwellautomation.com.

[298] J. A. Rodriguez, H. Nasr, M. Scott, A. K. Al-Jasmi, G. Velasquez, H. K. Goel, G. A. Carvajal, A. S. Cullick, C. E. Bravo, and A. Al-Abbasi. New generation of petroleum workflow automation: Philosophy and practice. In *SPE/IADC Drilling Conference and Exhibition*, pages 1–13, 2013.

[299] D. B. Roemer, M. M. Bech, P. Johansen, and H. C. Pedersen. Optimum design of a moving coil actuator for fast-switching valves in digital hydraulic pumps and motors. *IEEE/ASME Transactions on Mechatronics*, 20(6):2761–2770, 2015.

[300] F. Roos, H. Johansson, and J. Wikander. Optimal selection of motor and gearhead in mechatronic applications. *Mechatronics*, 16(1):63–72, 2006.

[301] E. Rouse, L. Hargrove, E. Perreault, and T. Kuiken. Estimation of human ankle impedance during walking using the perturberator robot. In *Biomedical Robotics and Biomechatronics (BioRob), 2012 4th IEEE RAS EMBS International Conference on*, pages 373–378, 2012.

[302] D. E. Rumelhart, G. E. Hinton, and R. J. Williams. Learning representations by back-propagating errors. *Nature*, 323:533–536, 1986.

[303] J. G. Rye. Offshore drilling trends. In *SPE California Regional Meeting*, pages 1–5, 1972.

[304] A. G. Sadlier and M. L. Laing. Interoperability: An enabler for drilling automation and a driver for innovation. In *SPE/IADC Drilling Conference and Exhibition*, pages 1–12, 2011.

[305] J. Sakuraba, F. Hata, C. C. Kung, K. Sotooka, H. Mori, and N. Takarada. Development of superconducting electric ship propulsion system. In *The Second International Offshore and Polar Engineering Conference*, pages 1–7, 1992.

[306] S. Sastry. *Nonlinear Systems: Analysis, Stability, and Control*. Springer, New York, 1999.

[307] L. Schmidt. *Robust Control of Industrial Hydraulic Cylinder Drives – with Special Reference to Sliding Mode- & Finite-Time Control*. PhD thesis, Aalborg University, 2015.

[308] R. Schupbach and J. Balda. A versatile laboratory test bench for developing powertrains of electric vehicles. In *2002 IEEE 56th Vehicular Technology Conference*, volume 3, pages 1666–1670, 2002.

[309] G. Seggewiss, J. Dai, and M. Fanslow. Synchronous motors on grinding mills: the different excitation types and resulting performance characteristics with VFD control for new or retrofit installations. *IEEE Industry Applications Magazine*, 21(6):60–67, 2015.

[310] SEW Eurodrive. *AC motors: Inverter assignments and characteristic curves*, 2009. Available online at www.sew-eurodrive.com.

[311] H. L. Shatto. Diesel electric drilling. In *3rd World Petroleum Congress*, pages 127–143, 1951.

[312] K. Shi, T. F. Chan, Y. K. Wong, and S. L. Ho. Speed estimation of an induction motor drive using an optimized extended Kalman filter. *IEEE Transactions on Industrial Electronics*, 49(1):124–133, 2002.

[313] L. Shuguang, C. Yunheng, J. Chenhui, and T. Yamin. Design of electric and control system of offshore drilling rig and its key technologies. In *Control and Decision Conference (CCDC), 2015 27th Chinese*, pages 4288–4293, 2015.

[314] A. Siddiqi, G. Bounova, O. L. de Weck, R. Keller, and B. Robinson. A posteriori design change analysis for complex engineering projects. *Journal of Mechanical Design*, 133(10):101005:1–11, 2011.

[315] Siemens. *SIMOTICS GP/SD VSD10 line standard motors for converter operation*, 2015. Available online at www.industry.siemens.com.

[316] G. Sierksma and Y. Zwols. *Linear and Integer Optimization: Theory and Practice*. CRC Press, Boca Raton, 2015.

[317] S. Sood. Use of real-time operations growing upstream. *Journal of Petroleum Technology*, 59(07):44–45, 2007.

[318] F. B. Springett, A. D. Shelton, J. A. Swain, H. F. Valdez, C. A. Goetz, N. Wong, K. A. Womer, and M. Killalea. Advanced rig technology – future technology subcommittee report of activities and industry survey results. In *IADC/SPE Drilling Conference and Exhibition*, pages 1–10, 2010.

[319] M. Srinivas and L. M. Patnaik. Genetic algorithms: A survey. *Computer*, 27(6):17–26, 1994.

[320] H. C. Stanley. An analysis of the induction machine. *Transactions of the American Institute of Electrical Engineers*, 57(12):751–757, 1938.

[321] G. T. Stigler. The cost of subsistence. *Journal of Farm Economics*, 27(2):303–314, 1945.

[322] F. M. Stone, D. N. Bishop, J. D. Cospolich, G. J. Mahl, D. R. Stewart, and H. R. Stewart. Update: Offshore electrical installation practices. *IEEE Industry Applications Magazine*, 7(1):56–63, 2001.

[323] J. D. Strickler. Electrified offshore drilling and production facilities on Island Esther. *IEEE Transactions on Industry and General Applications*, IGA-3(1):43–51, 1967.

[324] S. D. Sudhoff, B. T. Kuhn, D. C. Aliprantis, and P. L. Chapman. An advanced induction machine model for predicting inverter-machine interaction. In *Power Electronics Specialists Conference, PESC 2001 – IEEE 32nd Annual*, volume 4, pages 2043–2052, 2001.

[325] Z. Sun and T. W. Kuo. Transient control of electro-hydraulic fully flexible engine valve actuation system. *IEEE Transactions on Control Systems Technology*, 18(3):613–621, 2010.

[326] H. J. Sutherland. *On the Fatigue Analysis of Wind Turbines*. Sandia National Laboratories, Albuquerque, 1999.

[327] M. M. Swamy, J.-K. Kang, and K. Shirabe. Power loss, system efficiency, and leakage current comparison between Si IGBT VFD and SiC FET VFD with various filtering options. *IEEE Transactions on Industry Applications*, 51(5):3858–3866, 2015.

[328] I. Takahashi and T. Noguchi. A new quick-response and high-efficiency control strategy of an induction motor. *IEEE Transactions on Industry Applications*, IA-22(5):820–827, 1986.

[329] M. Takeda, Y. Hosoyamada, N. Motoi, and A. Kawamura. Development of the experiment platform for electric vehicles by using motor test bench with the same environment as the actual vehicle. In *Advanced Motion Control (AMC), 2014 IEEE 13th International Workshop on*, pages 356–361, 2014.

[330] R. M. Tallam, S. B. Lee, G. C. Stone, G. B. Kliman, J. Yoo, T. G. Habetler, and R. G. Harley. A survey of methods for detection of stator-related faults in induction machines. *IEEE Transactions on Industry Applications*, 43(4):920–933, 2007.

[331] R. L. Tanaka and C. de Arruda Martins. Parallel dynamic optimization of steel risers. *ASME Journal of Offshore Mechanics and Arctic Engineering*, 133(1):011302:1–9, 2011.

[332] M. Tawarmalani and N. V. Sahinidis. *Convexification and Global Optimization in Continuous and Mixed-Integer Nonlinear Programming*. Springer Science + Business Media, Dordrecht, 2002.

[333] Technosoft. *DMCode-MS(IM) MATLAB library for MCK28335*, 2011.

[334] F. E. Terman. A brief history of electrical engineering education. *Proceedings of the IEEE*, 86(8):1792–1800, 1998.

[335] O. Thorsen and M. Dalva. A survey of faults on induction motors in offshore oil industry, petrochemical industry, gas terminals, and oil refineries. *IEEE Transactions on Industry Applications*, 31(5):1186–1196, 1995.

[336] P. Tiitinen and M. Surandra. The next generation motor control method, DTC direct torque control. In *Power Electronics, Drives and Energy Systems for Industrial Growth, Proceedings of the 1996 International Conference on*, pages 37–43, 1996.

[337] F. Torrisi, A. Bemporad, G. Bertini, P. Hertach, D. Jost, and D. Mignone. HYSDEL – User Manual. `http://control.ee.ethz.ch/~cohysys/hysdel/index.php`, 2002. Accessed: 2016-07-25.

[338] G. Torrisi, S. Mariéthoz, and R. Smith. Identification of magnetic characteristics of induction motors based on the Jiles-Atherton model. In *Power Electronics and Applications (EPE'14-ECCE Europe), 2014 16th European Conference on*, pages 1–10, 2014.

[339] R. B. Ummaneni, R. Nilssen, and J. E. Brennvall. Force analysis in design of high power linear permanent magnet actuator with gas springs in drilling applications. In *2007 IEEE International Electric Machines Drives Conference*, pages 285–288, 2007.

[340] M. A. Valenzuela and P. Reyes. Simple and reliable model for the thermal protection of variable-speed self-ventilated induction motor drives. *IEEE Transactions on Industry Applications*, 46(2):770–778, 2010.

[341] P. Vas. *Sensorless Vector and Direct Torque Control*. Oxford University Press, Oxford, 1998.

[342] B. Venkataraman, B. Godsey, W. Premerlani, E. Shulman, M. Thakur, and R. Midence. Fundamentals of a motor thermal model and its applications in motor protection. In *Protective Relay Engineers, 2005 58th Annual Conference for*, pages 127–144, 2005.

[343] G. C. Verghese and S. R. Sanders. Observers for flux estimation in induction machines. *IEEE Transactions on Industrial Electronics*, 35(1):85–94, 1988.

[344] M. Vidyasagar. *Nonlinear Systems Analysis*. Society for Industrial and Applied Mathematics, Philadelphia, 2002.

[345] F. Volle, S. V. Garimella, and M. A. Juds. Thermal management of a soft starter: Transient thermal impedance model and performance enhancements using phase change materials. *IEEE Transactions on Power Electronics*, 25(6):1395–1405, 2010.

[346] D. A. Voltz, S. C. Beaver, and C. L. McDonald. The right mix of drivers and power generation. *IEEE Industry Applications Magazine*, 10(6):43–52, 2004.

[347] F. Wang and K. A. Stelson. An efficient fan drive system based on a novel hydraulic transmission. *IEEE/ASME Transactions on Mechatronics*, 20(5):2234–2241, 2015.

[348] C. N. Weygandt and S. Charp. Electromechanical transient performance of induction motors. *Electrical Engineering*, 65(12):1000–1009, 1946.

[349] B. M. Wilamowski and J. D. Irwin. *The Industrial Electronics Handbook: Power Electronics and Motor Drives*. CRC Press, Boca Raton, 2011.

[350] H. P. Williams. *Model Building in Mathematical Programming*. John Wiley & Sons, Chichester, 2013.

[351] M. Williams. Top-drive drilling systems: Electric vs. hydraulic – a technical overview and comparison. In *SPE/IADC Drilling Conference*, pages 539–548, 1991.

[352] M. Wråke. *Energy Technology Perspectives 2012*. International Energy Agency, Paris, 2012.

[353] S. Wright and T. Marwala. Artificial intelligence techniques for steam generator modelling, 2006. arXiv:0811.1711.

[354] S. J. Wright. *Primal-Dual Interior-Point Methods*. Society for Industrial and Applied Mathematics, Philadelphia, 1997.

[355] P. Yadav, R. Kumar, S. K. Panda, and C. S. Chang. Optimal thrust allocation for semisubmersible oil rig platforms using improved harmony search algorithm. *IEEE Journal of Oceanic Engineering*, 39(3):526–539, 2014.

[356] G. Y. Yang, G. Hovland, R. Majumder, and Z. Y. Dong. TCSC allocation based on line flow based equations via mixed-integer programming. *IEEE Transactions on Power Systems*, 22(4):2262–2269, 2007.

[357] J. Yang and G. G. Zhu. Adaptive recursive prediction of the desired torque of a hybrid powertrain. *IEEE Transactions on Vehicular Technology*, 64(8):3402–3413, 2015.

[358] J. I. Yoon, A. K. Kwan, and D. Q. Truong. A study on an energy saving electro-hydraulic excavator. In *ICCAS-SICE, 2009*, pages 3825–3830, 2009.

[359] Zacks Equity Research. Eni announces first oil yield from Goliat field off Norway. `http://bit.ly/1ZMFZug`, 2016. Accessed: 2016-03-31.

[360] L. A. Zadeh. Optimality and non-scalar-valued performance criteria. *IEEE Transactions on Automatic Control*, 8(1):59–60, 1963.

[361] L. A. Zadeh. Outline of a new approach to the analysis of complex systems and decision processes. *IEEE Transactions on Systems, Man, and Cybernetics*, SMC-3(1):28–44, 1973.

[362] E. V. Zaretsky, D. G. Lewicki, M. Savage, and B. L. Vlcek. Determination of turboprop reduction gearbox system fatigue life and reliability. *Tribology Transactions*, 50(4):507–516, 2007.

[363] M. N. Zeilinger. *Real-time Model Predictive Control*. PhD thesis, ETH Zürich, 2011.

[364] D. Zhang, C. DeVore, and E. Johnson. Response modification to improve the parameter identification of shear structures: An experimental verification. *IEEE/ASME Transactions on Mechatronics*, 18(6):1683–1690, 2013.

[365] G. Q. Zhang, X. Li, R. Boca, J. Newkirk, B. Zhang, T. A. Fuhlbrigge, H. K. Feng, and N. J. Hunt. Use of industrial robots in additive manufacturing – a survey and feasibility study. In *ISR/Robotik 2014, 41st International Symposium on Robotics, Proceedings of*, pages 1–6, 2014.

[366] P. Zhang. *Active Thermal Protection for Induction Motors fed by Motor Control Devices*. PhD thesis, Georgia Institute of Technology, 2010.

[367] P. Zhang, B. Lu, and T. Habetler. Active stator winding thermal protection for AC motors. In *Pulp and Paper Industry Technical Conference, Conference Record of 2009 Annual*, pages 11–19, 2009.

[368] L. Zhao, W. Pawlus, H. R. Karimi, and K. G. Robbersmyr. Data-based modeling of vehicle crash using adaptive neural-fuzzy inference system. *IEEE/ASME Transactions on Mechatronics*, 19(2):684–696, 2014.

[369] S. Ziaeinejad, Y. Sangsefidi, H. Nabi, and A. Shoulaie. Direct torque control of two-phase induction and synchronous motors. *IEEE Transactions on Power Electronics*, 28(8):4041–4050, 2013.

[370] S. E. Zocholl. Optimizing motor thermal models. In *Petroleum and Chemical Industry (PCIC), 2006 IEEE Industry Applications Society Technical Conference on*, pages 1–9, 2006.

[371] S. E. Zocholl and G. Benmouyal. Using thermal limit curves to define thermal models of induction motors. *SEL Journal of Reliable Power*, 3(1):65–70, 2012.

[372] A. Zolotukhin and V. Gawrilov. Russian Arctic petroleum resources. *Oil and Gas Science and Technology*, 66(6):899–910, 2011.

Part V

Supplementary Material

A Experimental Hardware

Some methods proposed in this thesis and the associated findings require experimental validation (refer especially to Chapters 3, 7, 8, and 9). This Chapter presents the laboratory setups and the full-scale offshore drilling machines that are used to test the developed techniques in real-world conditions to prove their feasibility, accuracy, suitability, etc.

A.1 Development Platform

The first experimental setup is developed by Technosoft company [333] and consists of two induction motors, 3-phase IGBT power bridges, and digital signal controller (DSC) boards connected to a computer and supplied by a 5 V energy source as shown in Fig. A.1. The setup is also equipped with brake resistors allowing for motor braking. Its schematics is illustrated in Fig. A.2. The same connection scheme applies to the second induction motor
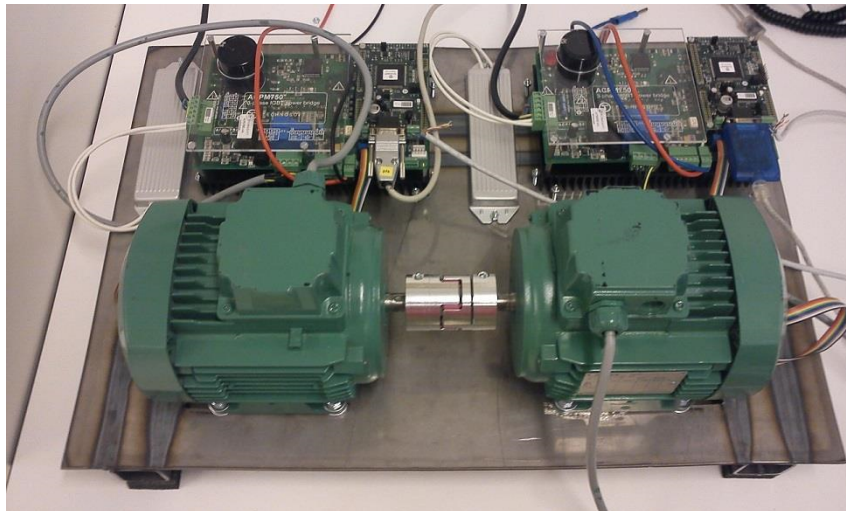
Figure A.1: Test bench for running the scaled-down experiments.

marked as "Load". Parameters of motors are defined for a T-equivalent circuit illustrated in Fig. 4.3, however, they can easily be converted to the parameters of the inverse-Γ-equivalent circuit shown in Fig. 4.4 if needed, according to (4.34)-(4.36). The numerical values of setup's parameters are provided in Table A.1. The test bench allows for evaluation of control algorithms and overall motor performance in the presence of external loads. One motor typically runs in a speed control mode to follow the desired trajectory, whereas the other motor runs in a torque control mode to reproduce a given load profile.

In this thesis, these load characteristics resemble conditions experienced by a reference real-world machine. The motor labeled "Induction motor" is assumed to imitate the winch motor that drives the gripper arm of the vertical pipe racker presented in Section A.4. The
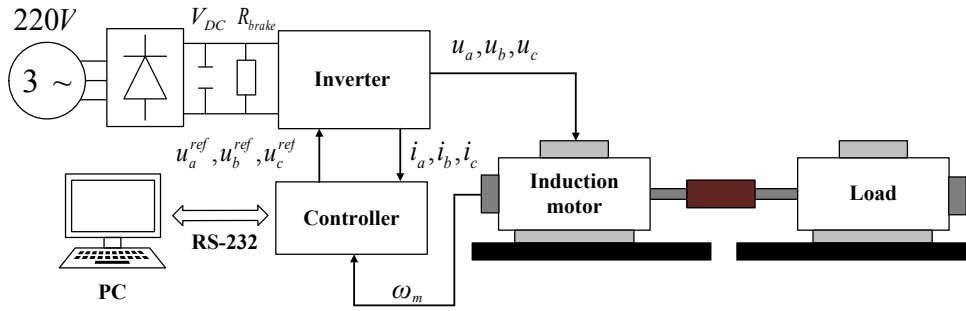
Figure A.2: Control system and interface diagram of the small-scale test setup.

Parameter	Value
Stator resistance R_s	8.20 Ω
Rotor resistance R_r	5.37 Ω
Magnetizing inductance L_m	0.49 H
Stator inductance L_s	0.49 H
Rotor inductance L_r	0.49 H
Rated power P_n	0.37 kW
Rated speed n_n	2780 rpm
Rated current I_n	0.95 A
Rated line voltage U_{sup}	400 V
Frequency f_{sup}	50 Hz
Pole pairs p	1
Power factor $\cos\varphi_n$	0.8
Motor inertia J_r	$1.4e^{-4}\ kgm^2$

Table A.1: Parameters of the experimental induction motor.

motor labeled "Load" mimics all kinds of external loads acting on the full-scale drivetrain. These include both static and dynamic load as well as the combined friction present in both the mechanical system and in the motor itself. By using the appropriate scaling techniques, discussed in Chapter 7, it becomes possible to scale down the load torque acting on the reference drivetrain, emulate it on the "Load" motor, record the speed and torque profiles measured on the "Induction motor", and scale them up again. This helps to assess the level of loads that a considered real-world powertrain is expected to withstand during regular machine operation.

Also, the accuracy of the Kalman filter-based estimation and control method is verified by using this lab setup, as discussed in Chapter 8.

A.2 Full-size Test Bench

The full-size test bench is supplied by ABB and, in principle, it offers similar functionality to the development platform setup described in Section A.1. As illustrated in Fig. A.3, it is composed of two industrial drives (from [10]) connected to two induction motors (from [13]). VFDs are controlled by means of DTC. They are equipped with extension modules allowing for communication with programmable logic controllers (PLCs) through Profibus protocol. The current generated in the braking motor is converted into heat and dissipated on brake resistors. Schematic representation of the test bench is shown in Fig. A.4 The two M3BP 132 SMB 6 motors are depicted in Fig. A.5 and their parameters are summarized in Table A.2. There is a Dodge® Para-Flex® coupling installed on both motors' shafts to provide the torque transfer.
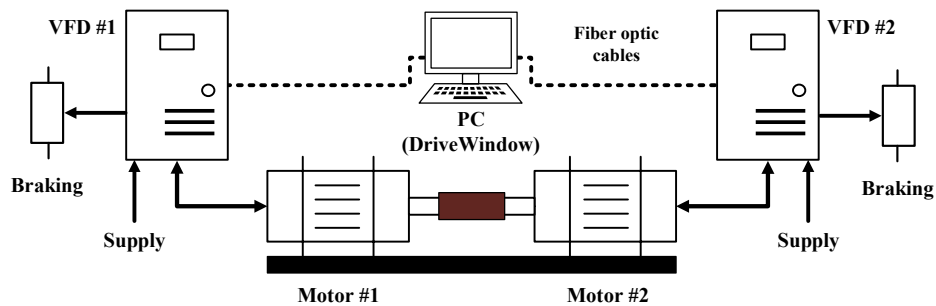
Figure A.3: Full-size experimental test bench.

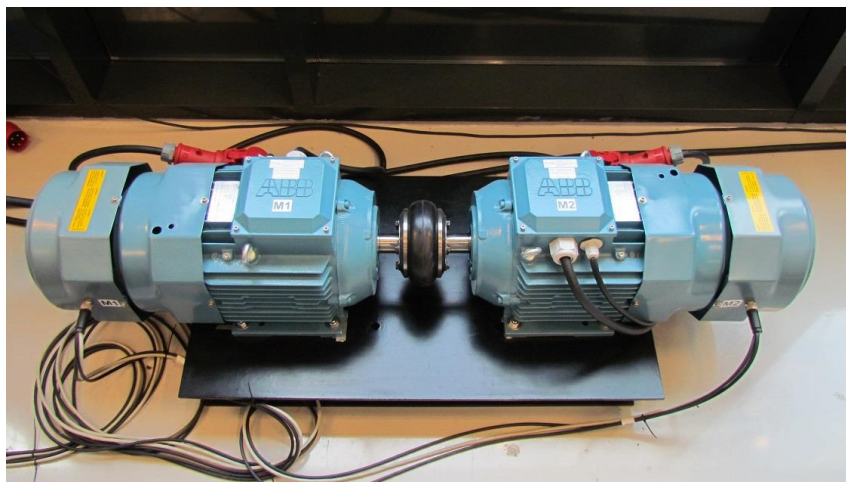**Figure A.4:** Configuration of the full-size laboratory setup.

Figure A.5: Two M3BP 132 SMB 6 motors connected through the coupling.

The motors are controlled by two ACS800-01-0016-3 VFDs. They communicate with the PC via fiber optic cables. The ABB software for commissioning and maintaining the drives, DriveWindow [9], is applied to monitor and remotely control the motors. Fig. A.6 illustrates the frequency converters installed inside a control cabinet. Exemplary testing results are depicted in Fig. A.7. The first motor follows a velocity trajectory, whereas the second motor produces an arbitrary torque profile to imitate the mechanical load coming from a machine.

Parameter	Value
Stator resistance R_s	1.21 Ω
Rotor resistance R_r	1.22 Ω
Magnetizing inductance L_m	0.13 H
Stator inductance L_s	0.14 H
Rotor inductance L_r	0.14 H
Rated power P_n	4.0 kW
Rated speed n_n	960 rpm
Rated current I_n	10.0 A
Rated line voltage U_{sup}	400 V
Frequency f_{sup}	50 Hz
Pole pairs p	3
Power factor $\cos \varphi_n$	0.68
Motor inertia J_r	0.03 $kg\,m^2$

Table A.2: Parameters of the M3BP 132 SMB 6 motor.
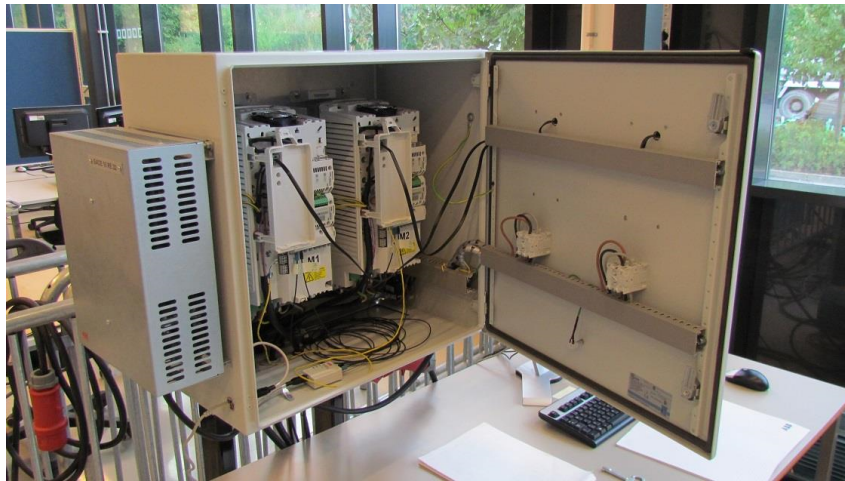
Figure A.6: Two ACS800-01-0016-3 frequency converters.

(a) Motors' speed.
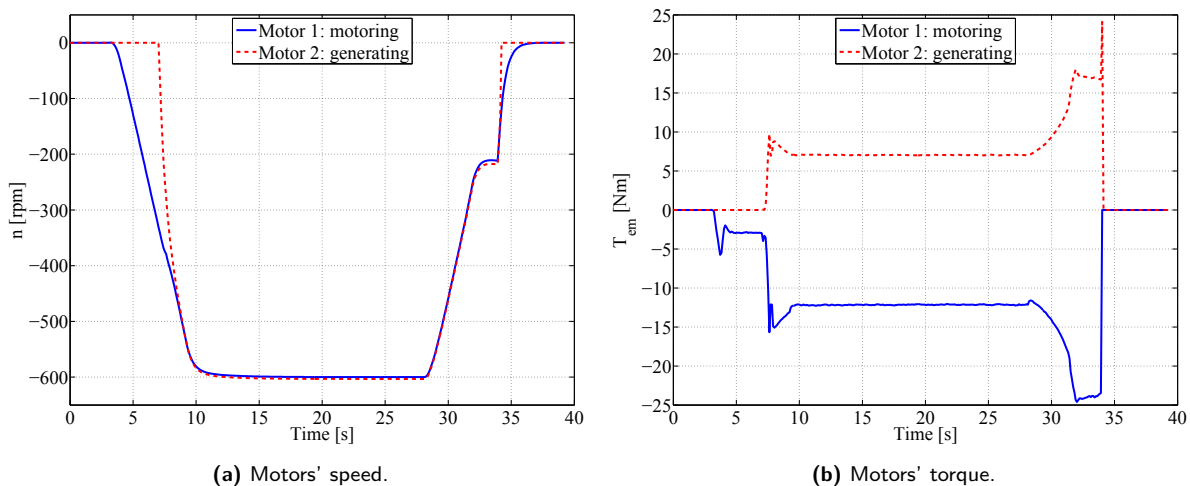
(b) Motors' torque.

Figure A.7: Exemplary results of running the full-size motors in torque-speed control modes.

Although the experimental results obtained on this setup are not explicitly included in the body of this thesis, there are at least five areas where using it was identified as beneficial to further strengthen the proposed techniques and approaches:

1. Reproduction of the operation of a real-world machine (Chapter 7).

2. Implementation of the EKF to estimate and control IM (Chapter 8).

3. Investigation of the influence of motion profiles on motor thermal behavior (Chapter 9).

4. Validation of the proposed drivetrain design optimization algorithm (Chapter 10).

5. Evaluation of the developed method for temperature rise estimation (Chapter 11).

A.3   Gantry Crane

The gantry crane illustrated in Fig. A.8 is designed for handling drill pipes from pipe deck to tubular shuttle and vice versa.[28] The crane is equipped with a parallel yoke for single and dual pipe handling. The lifting yoke is attached to the horizontal lifting telescope. The trolley on which the lifting yoke is located is fitted with two winches: one for hoisting/lowering the parallel yoke and the other (manually controlled) for utility operation. Main specifications of the machine are summarized in Table A.3.
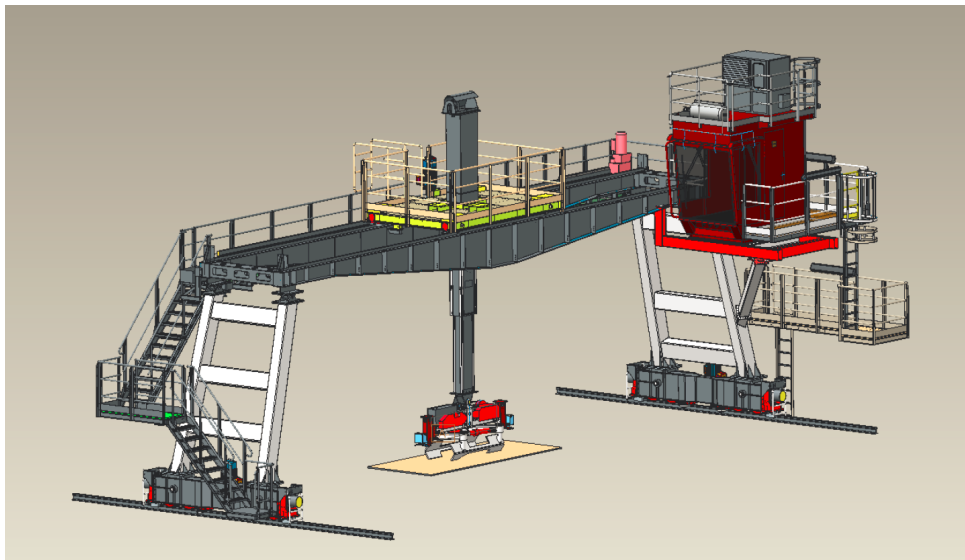
Figure A.8: The gantry crane – courtesy of MHWirth AS.

Property	Value
Safe working load (SWL)	3.5 *t*
Gantry travel	50.0 *m*
Gantry rail span	18.5 *m*
Trolley travel	12.0 *m*
Trolley rail span	2.3 *m*
Telescope stroke	3.7 *m*
Total weight	37.8 *t*

Table A.3: Characteristic features of the gantry crane.

---

28. This Section is reproduced from publication [265].

A.3.1 Electric Motion Control

The gantry crane is available as both hydraulically and electrically actuated system. The gripper on the parallel yoke is the only part of the machine that is driven by a hydraulic drivetrain in the electric version. Apart from it, there are 3 axes which are electrically actuated by VFD-controlled IMs:

1. Crane travel using rack and pinion system.

2. Trolley travel using rack and pinion system.

3. Hoisting/lowering of parallel yoke using winch mechanism.

There is one induction motor on each of the two gantry crane carriages – see Figure A.9. Each of the two motors has a hydraulic fail-safe brake activated when loss of electric power is detected. The trolley travels horizontally on top of the main beam. Similarly to crane
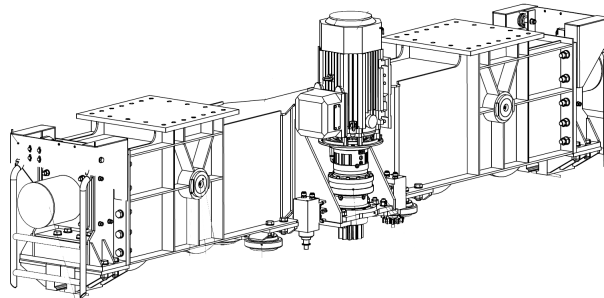
Figure A.9: The carriage assembly – courtesy of MHWirth AS.

carriages, travel function of trolleys is achieved by using rack and pinion system and electric powertrains with the same mechanism for emergency braking. The telescopic arm consists of two rectangular hollow sections. The outer box is fixed to the trolley frame, whereas the inner box moves up and down. The trolley telescope is actuated by means of an electrically driven winch and wire sheave system. The wire runs from the winch to a sheave located on top of the outer box and then down to the inner telescopic box. The winch is fitted with the fail-safe brake as well, thus ensuring safe handling of loads in case of power loss. The complete subsystem is shown in Figure A.10.

A.3.2 Benefits

Table A.4 summarizes some of the most important differences between the hydraulically and electrically actuated gantry cranes. Although this list is not exhaustive (e.g. it does not contain detailed information regarding scheduling and cost of maintenance tasks) and presents only the most essential features, it clearly shows an advantage of using VFDs over traditional hydraulic drivetrains. Not only offers the electrically actuated machine a significant reduction of power consumption (no big-size HPU) but also provides for improved control performance and weight reduction of the total system. The last feature is especially relevant for offshore applications, since according to [83], the platform deck area is valued at approximately 6 500–65 000 $/$m^2$ and every saved kilogram of weight yields a saving of 2–10 $ on structural material (recall Section 3.4.2). Of course, the electrically actuated system demands additional equipment and functions (e.g. fail-safe brakes) which are not required in the case of hydraulic drivetrains, however, these drawbacks are of marginal relevance given the above advantages. In addition,
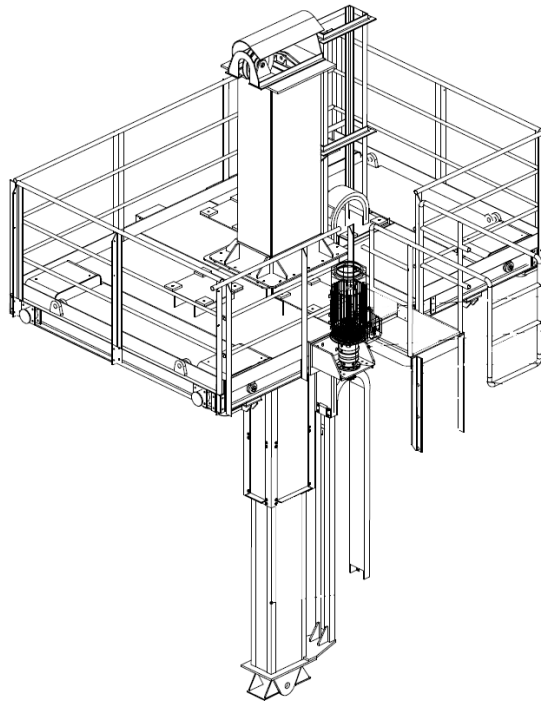
Figure A.10: The trolley arrangement with the telescopic arm – courtesy of MHWirth AS.

Mass	✓ Total weight reduced by 10 %.
Energy	✓ Total power consumption reduced by 70 %.
	✓ Power optimization (higher speed at zero hook load).
Environment	✓ Noise level reduced by 20 %.
	✓ Removal of high pressure hoses.
	✓ Hydraulic leakage and oil contamination reduced to minimum.
	✓ No need to warm up oil for operation in cold weather.
Control	✓ Better dynamic control during load handling.
	✓ One VFD to control two winch motors.
	✓ No need for valve overlap correction/tuning due to wear of hydraulic system.
Maintenance	✓ Lower volume of oil.
	✓ Conservation tasks of pipes, pumps, valves, etc. reduced to minimum.

Table A.4: Advantages of the electrically actuated gantry crane compared to its hydraulically driven counterpart – courtesy of MHWirth AS.

although the initial investment is comparable for both electric and hydraulic systems, the former offers, in general, significantly lower maintenance costs and reduced service tasks. Therefore, the electrically actuated gantry crane grants all the benefits that are identified in the literature survey presented in Chapter 3 (recall the summary in Section 3.2.3).

A.4 Vertical Pipe Handling Machine

The vertical pipe racker (VPR) shown in Fig. A.11 is a machine which assembles and delivers stands or pipes to the well center as the drilling process continues. It is a column supported at the top and bottom by tracks and a rack and pinion system [268]. The lower track is mounted directly on the drill floor, whereas the upper track is connected to the derrick structure. At both ends of the column there are located trolleys which allow for horizontal movement of the

machine along the tracks. In total, the column includes three arms which role is to assemble, handle, and deliver pipes. The upper and lower arms only guide tubulars, whereas the middle arm (the so-called gripper arm) is responsible for holding them in a secure grip. It is possible to hoist or lower this arm by using a winch located on top of the column. All three arms are equipped with hydraulic cylinders which allow for their extension/retraction in order to position pipes in the finger boards or well center. The machine can rotate about its vertical axis thanks to slew motors mounted on the lower trolley. Key features of the machine are listed in Table A.5. In this thesis, the gripper arm together with the winch hoisting system are selected as a case study.
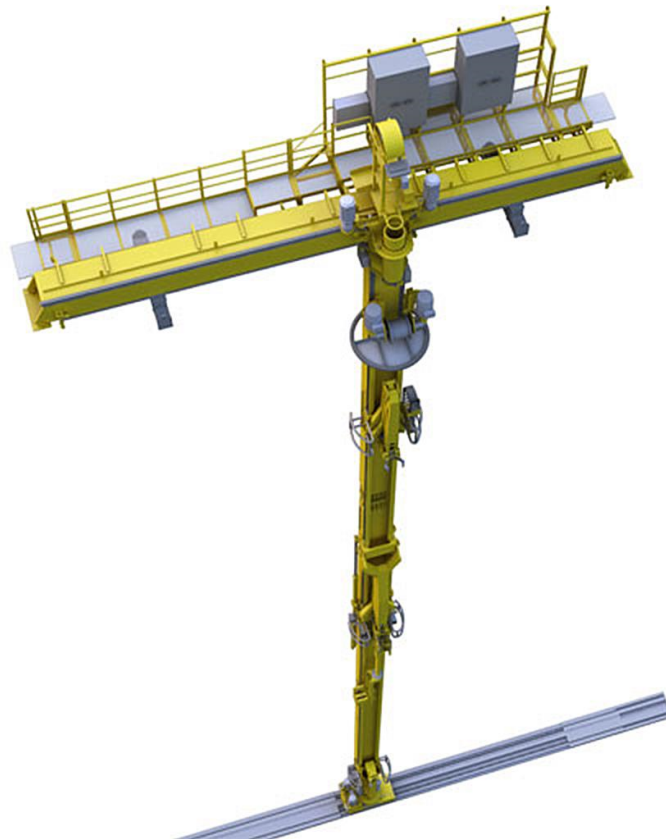
Figure A.11: Vertical pipe handling machine (VPR) – courtesy of MHWirth AS.

Property	Value
Lifting capacity (SWL)	15.0 t
Gripper arm vertical travel	17.5 m
Maximum horizontal reach	4.7 m
Trolley travel (upper and lower)	11.0 m
Total height	50.0 m
Total weight	40.0 t

Table A.5: Characteristic features of the VPR.

A.4.1 Gripper Arm

The gripper arm illustrated in Fig. A.12 is connected to the column through two dollies that are equipped with trolleys. Trolleys roll up and down on the column within the guide rails,

allowing, together with the winch mechanism, for vertical motion of the gripper arm. The geometry of the arms ensures that the head moves in a straight horizontal line from the column during extension/retraction cycles. The winch drive consists of two motors, a hydraulic brake, a planetary gearbox, and a winch drum directly connected to the hoisting wire. The hoisting wire is connected to the dead anchor at the top of the column via the sheave, located on the lower dolly. In addition, there are two hydraulic cylinders installed between the lower and upper dollies that allow for horizontal extension/retraction of the arm by changing their stroke.

Figure A.12: The gripper arm of VPR – courtesy of MHWirth AS.

A.4.2 Modeling Simplifications

In this thesis, it is often assumed (refer especially to Chapter 9) that the only degree of freedom in the machine is the relative motion of the lower dolly (with the upper dolly, gripper arm, etc.) with respect to the winch. Therefore, in order to formulate a computationally efficient model of the system, the simplified structure of the gripper arm is considered, as shown in Fig. A.13. In addition, the following modeling assumptions are introduced:

1. Drum radius is constant. Normally, there are two layers of wire in use but, for the sake of simplicity, it is assumed that there is no layer shift.

2. Wire mass is ignored, since it constitutes only a small portion of the system total mass.

3. Interactions between the winch and the combined mass m_{tot} are modeled as kinematic constraints, without considering wires elasticity.

4. Gearbox and drum inertia are neglected, as they do not contribute significantly to the effective inertia of the modeled system.
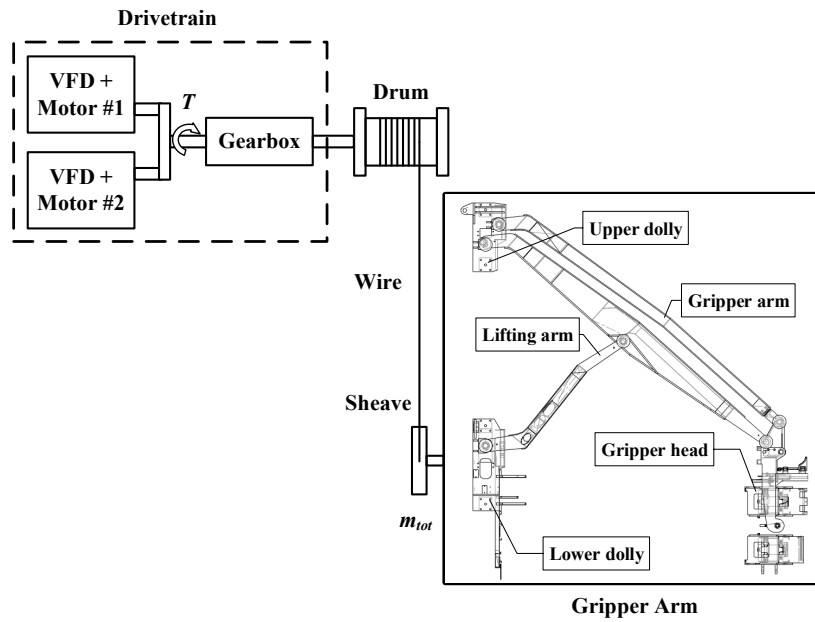
Figure A.13: Simplified representation of the gripper arm connected to the winch drivetrain [268].

The model of the gripper arm and its powertrain illustrated in Fig. A.13 is implemented in the multi-domain modeling software SimulationX, according to [162]. This model is used e.g. in Chapter 9 to evaluate the expected fatigue and vibration damage of the drivetrain. Details on model validation (essentially – tuning parameters of the friction model) are explained in [268] and omitted here.[29]

Also, an analytical model of the gripper arm is established, as discussed in Chapter B, in order to verify the accuracy of the simulation results produced by the commercial software.

---

29. The complete multi-domain model is proprietary and cannot be disclosed. Conceptually, however, it is identical to the system shown in Fig. A.13.

B Modeling of Dynamic Mechanical Systems

The fundamentals of kinematic and dynamic analysis of a mechanical system can be best understood when illustrated on an example. Therefore, this Chapter considers as a case study the gripper arm of the vertical pipe handling machine presented in Section A.4.[30]

There are two typical approaches to simulate motion of mechanical systems [251]: analytical modeling and commercial software-based modeling. The comparative analysis of modeling and simulation of an offshore drilling machine using these two methods is conceptually represented in Fig. B.1.
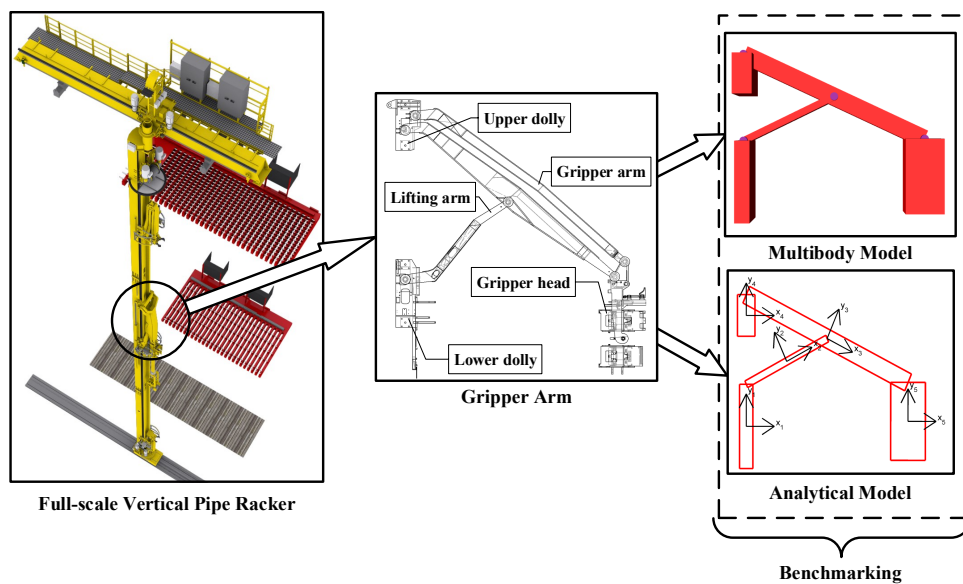
Figure B.1: Workflow for modeling and simulation of the vertical pipe handling machine [269].

The role of the numerical examples presented throughout this Chapter is to investigate two simulation scenarios of this machine: forward kinematics – to verify that geometry of both models is matching, and forward dynamics – to verify if both models handle external loads in the same way.

B.1 Multibody Modeling

Although analytical modeling normally also involves using third-party software to solve equations of motion (EOMs) and determine the resulting motion numerically, the geometric, kine-

---

30. The analysis, examples, and results discussed in this Chapter are partially reproduced from publications [268] and [269].

matic, and dynamic constraints have to be individually formulated beforehand. This step, however, is omitted when using the commercial multibody products, as it is the software itself that establishes equations which describe behavior of the modeled machine. Usually, the role of the user is to determine parent-child relationships between the bodies, assign parameters of the system, and define inputs to the model. The choice of the modeling and simulation strategy usually depends on the desired level of complexity of the model, accuracy of the simulation, modeling effort, and available time and resources. Example B.1 presents the case study machine that is used in the following part of the text to benchmark the results of modeling aided by commercial multibody software products and analytical methods.

Example B.1 (Gripper Arm of VPR)
The schematic representation of the gripper arm of the vertical pipe handling machine presented in Section A.4 is illustrated in Fig. B.2. Details on modeling this machine using SimulationX are presented in [268] and for the sake of brevity are omitted in this thesis, as explained in Section A.4.2.
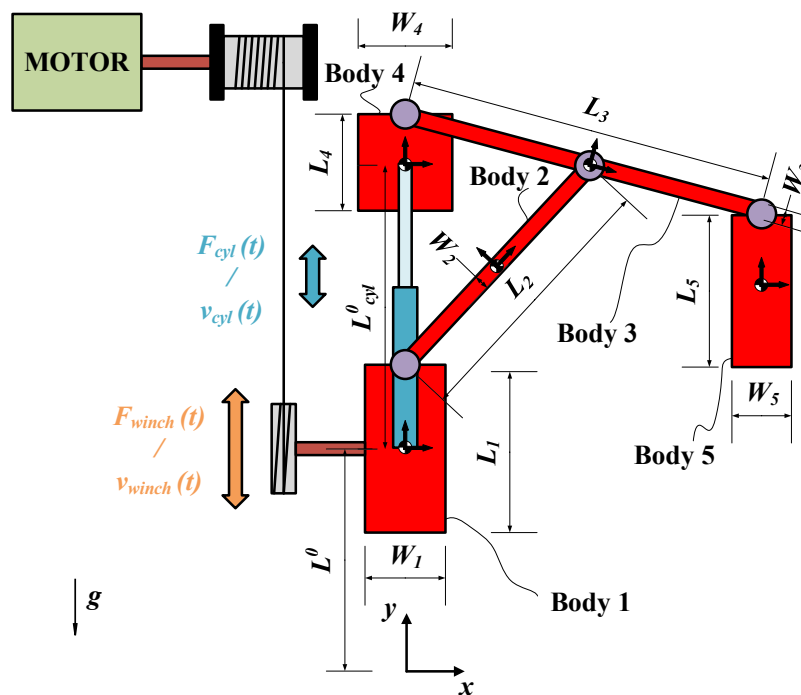

Figure B.2: Schematic representation of the gripper arm of the vertical pipe handling machine [269].

The software SimulationX consists of a number of libraries from various physical domains (e.g. rigid body mechanics or hydraulic actuation systems) which elements can be conveniently connected to form complex models of full-scale machines [162]. Therefore, design, analysis, and integration of subsystems which typically a mechatronic system is composed of, become straightforward when following this modeling strategy, which, in turn, contributes to its popularity in industrial environment. However, the accessibility of such computer packages and relatively low level of expertise required to create moderately complex physical models might be a potential source of errors and misinterpretations of simulation results [269]. Hence, in some cases, it is advisable to verify if simulation results produced using different modeling approaches are comparable to be able to assess their accuracy and reliability. This is exactly the goal of the numerical examples presented throughout this Chapter.

Remark B.1. *If all bodies of a mechanical system undergo motion in one plane or in parallel planes, the system is said to be experiencing planar motion [251]. This Chapter deals exclusively with planar mechanisms to simplify the analysis and reduce the computational burden. Similarly, it introduces only the fundamental principles of mechanical systems analysis, which are followed by numerical examples to illustrate the modeling workflow. Detailed derivation of mathematical formulas and discussion on accompanying assumptions and limitations is comprehensively presented in [251].*

B.2 Planar Kinematics of Rigid Body

A planar mechanical system can be described by an appropriate coordinate system which specifies the configuration and state of each body, according to [251]. Fig. B.3 illustrates a body i with the attached local frame $(\xi_i \eta_i)$ moving in a global reference frame (xy). Its motion is fully described by the global coordinates of its fixed frame $\mathbf{r}_i = [x_i, y_i]^T$ and by its angle of rotation ϕ_i relative to the global frame (the superscript T stands for vector transpose).
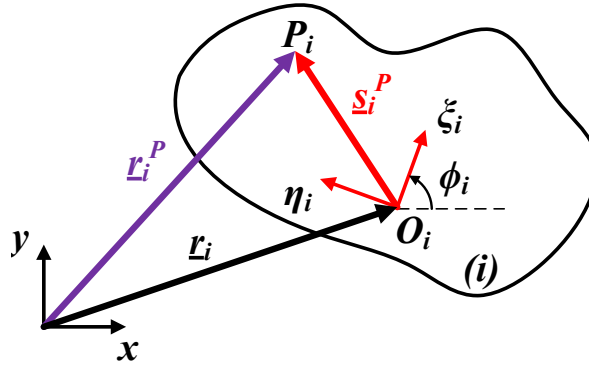

Figure B.3: Location of point P_i relative to the frame fixed to the body (i) and to the global frame (xy) [251].

Remark B.2. *A vector denoted as e.g. $\underline{a}$ is understood to have geometric sense: it stretches from the point of origin A to the end point B. Its coordinates, on the other hand, are included in a so-called column matrix denoted by a boldface lower-case letter, e.g. $\mathbf{a}$. Hence, the vector $\underline{a}$ is uniquely defined by its Cartesian components and is written in matrix notation as [251]*

$$\mathbf{a} = \begin{bmatrix} a_{(x)} \\ a_{(y)} \\ a_{(z)} \end{bmatrix} = \begin{bmatrix} a_{(x)}, a_{(y)}, a_{(z)} \end{bmatrix}^T \tag{B.1}$$

which, for planar coordinates, is simplified and becomes

$$\mathbf{a} = \begin{bmatrix} a_{(x)} \\ a_{(y)} \end{bmatrix} = \begin{bmatrix} a_{(x)}, a_{(y)} \end{bmatrix}^T . \tag{B.2}$$

B.2.1 Cartesian Coordinates

The vector $\underline{s}_i^P$ describes the position of point P_i on body i relative to its local coordinate system $(\xi_i \eta_i)$. The local position of point P_i is described by the components of the vector $\underline{s}_i^P$ as $\mathbf{s}_i'^P = [\xi_i^P, \eta_i^P]^T$ (a vector with a superscript prime denotes local components). $\mathbf{s}_i'^P$ is a constant vector, since P_i is fixed to body i. On the other hand, the global components (no superscript prime) of vector $\underline{s}_i^P$ are denoted as $\mathbf{s}_i^P$ and vary when body i is in motion. Then, the varying components of vector $\underline{r}_i^P$ which describe the global position of point P_i are denoted

as $\mathbf{r}_i^P = [x_i^P, y_i^P]^T$. The discussed position vectors $\mathbf{r}_i^P$, $\mathbf{s}_i^P$, $\mathbf{s}_i^{'P}$, $\mathbf{r}_i$ are 3×1 vectors, however, in the planar case, since their z-component remains constant, they become 2×1 vectors [251]. Hence, the location of point P_i in the global frame can be derived from its location in the local frame [251]

$$\mathbf{r}_i^P = \mathbf{r}_i + \underbrace{\mathbf{A}_i \mathbf{s}_i^{'P}}_{\mathbf{s}_i^P} \tag{B.3}$$

where

$$\mathbf{A}_i = \begin{bmatrix} \cos(\phi_i) & -\sin(\phi_i) \\ \sin(\phi_i) & \cos(\phi_i) \end{bmatrix} \tag{B.4}$$

is the rotational transformation matrix for ith body. It is derived from the following 3×3 matrix applicable to spatial systems

$$\mathbf{A}_i = \begin{bmatrix} \cos(\phi_i) & -\sin(\phi_i) & 0 \\ \sin(\phi_i) & \cos(\phi_i) & 0 \\ 0 & 0 & 1 \end{bmatrix}. \tag{B.5}$$

Therefore, (B.3) can be rewritten in its expanded form as [251]

$$\begin{bmatrix} x_i^P \\ y_i^P \end{bmatrix} = \begin{bmatrix} x_i \\ y_i \end{bmatrix} + \begin{bmatrix} \cos(\phi_i) & -\sin(\phi_i) \\ \sin(\phi_i) & \cos(\phi_i) \end{bmatrix} \begin{bmatrix} \xi_i^P \\ \eta_i^P \end{bmatrix}. \tag{B.6}$$

To fully describe kinematics of the body presented in Fig. B.3 one needs to determine its velocity and acceleration as well. Their derivation is based on time derivatives of position equation (B.3). By assuming that the local position of the point P_i attached to the body i and the global coordinates of the body are known, the velocity of the point P_i in the global reference frame (xy) is found by taking the time derivative of (B.3)

$$\dot{\mathbf{r}}_i^P = \dot{\mathbf{r}}_i + \dot{\mathbf{A}}_i \mathbf{s}_i^{'P} \tag{B.7}$$
$$= \dot{\mathbf{r}}_i + \mathbf{B}_i \mathbf{s}_i^{'P} \dot{\phi}_i$$

where

$$\mathbf{B}_i = \begin{bmatrix} -\sin(\phi_i) & -\cos(\phi_i) \\ \cos(\phi_i) & -\sin(\phi_i) \end{bmatrix}. \tag{B.8}$$

Likewise, the time derivative of (B.7) yields the acceleration of point P_i

$$\ddot{\mathbf{r}}_i^P = \ddot{\mathbf{r}}_i + \ddot{\mathbf{A}}_i \mathbf{s}_i^{'P} \tag{B.9}$$
$$= \ddot{\mathbf{r}}_i + \mathbf{B}_i \mathbf{s}_i^{'P} \ddot{\phi}_i - \mathbf{A}_i \mathbf{s}_i^{'P} \dot{\phi}_i^2.$$

B.2.2 Vector of Coordinates

A useful approach is to combine coordinates of all bodies present in the mechanical system in one vector $\mathbf{q}$, the so-called vector of coordinates [251]. Such representation (together with the corresponding vectors of velocities $\dot{\mathbf{q}}$ and accelerations $\ddot{\mathbf{q}}$) facilitates analysis of the system, as it helps e.g. to conveniently solve the equations of motion. The global position of a rigid body's i reference frame is hence denoted in Cartesian coordinates as [109]

$$\mathbf{q}_i = \begin{bmatrix} \mathbf{r}_i^T, \phi_i \end{bmatrix}^T \tag{B.10}$$
$$= [x_i, y_i, \phi_i]^T.$$

Similarly, if the mechanical system consists of *b* bodies, its vector of coordinates becomes $3 \times b$ vector [251]

$$\mathbf{q} = \left[\mathbf{q}_1^T, \mathbf{q}_2^T, \ldots, \mathbf{q}_b^T\right]^T \tag{B.11}$$
$$= \left[x_1, y_1, \phi_1, x_2, y_2, \phi_2, \ldots, x_b, y_b, \phi_b\right]^T.$$

Finally, the velocities and accelerations of body *i* are derived from (B.11) as the corresponding time derivatives

$$\dot{\mathbf{q}}_i = \left[\dot{\mathbf{r}}_i^T, \dot{\phi}_i\right]^T \tag{B.12}$$

$$\ddot{\mathbf{q}}_i = \left[\ddot{\mathbf{r}}_i^T, \ddot{\phi}_i\right]^T \tag{B.13}$$

which for a system of *b* bodies become, respectively

$$\dot{\mathbf{q}} = \left[\dot{\mathbf{q}}_1^T, \dot{\mathbf{q}}_2^T, \ldots, \dot{\mathbf{q}}_b^T\right]^T \tag{B.14}$$
$$= \left[\dot{x}_1, \dot{y}_1, \dot{\phi}_1, \dot{x}_2, \dot{y}_2, \dot{\phi}_2, \ldots, \dot{x}_b, \dot{y}_b, \dot{\phi}_b\right]^T$$

$$\ddot{\mathbf{q}} = \left[\ddot{\mathbf{q}}_1^T, \ddot{\mathbf{q}}_2^T, \ldots, \ddot{\mathbf{q}}_b^T\right]^T \tag{B.15}$$
$$= \left[\ddot{x}_1, \ddot{y}_1, \ddot{\phi}_1, \ddot{x}_2, \ddot{y}_2, \ddot{\phi}_2, \ldots, \ddot{x}_b, \ddot{y}_b, \ddot{\phi}_b\right]^T.$$

B.3 Kinematic Constraints

Kinematic joints typically connect bodies in a mechanical system [251]. In the case of planar motion, each body is described by three coordinates – two translations and one rotation. In such systems, the kinematic joints are formulated as algebraic constraint equations denoted by $\mathbf{\Phi}$. To indicate a particular joint, $\mathbf{\Phi}$ is accompanied by a superscript which indicates the constraint type and the number of algebraic equations of that expression. There are two common categories of joints [251]: lower-pair and higher-pair. The former group does not require any information about the shape of the connected bodies, whereas for the latter one it is essential to know the entire/partial shape of connected bodies (e.g. cam-follower pair). Lower-pair category joints are usually simpler in construction and, hence, more common in applications [251]. Therefore, the two lower-pair joints that are the most popular are further discussed: revolute and translational joints.

B.3.1 Revolute Joint

A revolute joint is schematically represented in Fig. B.4. Center of the joint is located in point *P* which is considered to be two coincident points: P_i on body *i* and P_j on body *j* [251]. Location of point *P* is described by two vectors $\underline{s}_i^P$ and $\underline{s}_j^P$, respectively. By solving the vector loop equation, we obtain

$$\mathbf{r}_i + \mathbf{s}_i^P - \mathbf{r}_j - \mathbf{s}_j^P = \mathbf{0} \tag{B.16}$$

which is equivalent to

$$\mathbf{\Phi}^{r,2} = \mathbf{r}_i + \mathbf{A}_i \mathbf{s}_i^{\prime P} - \mathbf{r}_j - \mathbf{A}_j \mathbf{s}_j^{\prime P} = \mathbf{0}. \tag{B.17}$$

Similarly to (B.7) and (B.9), by taking the time derivative of (B.17) it becomes possible to formulate the corresponding velocity and acceleration constraints which are associated with
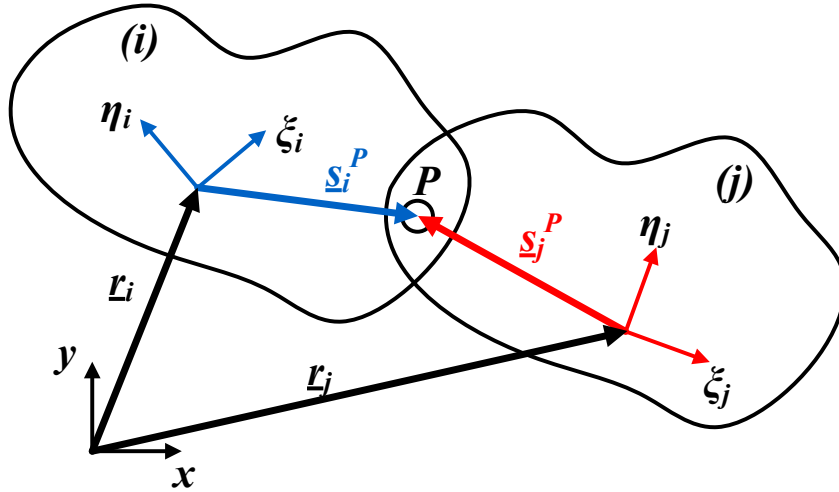
Figure B.4: Revolute joint P connecting bodies i and j [251].

the revolute joint

$$\dot{\boldsymbol{\Phi}}^{r,2} = \dot{\mathbf{r}}_i + \dot{\mathbf{A}}_i \mathbf{s}_i^{'P} - \dot{\mathbf{r}}_j - \dot{\mathbf{A}}_j \mathbf{s}_j^{'P} = \mathbf{0} \tag{B.18}$$
$$= \dot{\mathbf{r}}_i + \mathbf{B}_i \mathbf{s}_i^{'P} \dot{\phi}_i - \dot{\mathbf{r}}_j - \mathbf{B}_j \mathbf{s}_j^{'P} \dot{\phi}_j = \mathbf{0}$$
$$\ddot{\boldsymbol{\Phi}}^{r,2} = \ddot{\mathbf{r}}_i + \ddot{\mathbf{A}}_i \mathbf{s}_i^{'P} - \ddot{\mathbf{r}}_j - \ddot{\mathbf{A}}_j \mathbf{s}_j^{'P} = \mathbf{0} \tag{B.19}$$
$$= \ddot{\mathbf{r}}_i + \mathbf{B}_i \mathbf{s}_i^{'P} \ddot{\phi}_i - \mathbf{A}_i \mathbf{s}_i^{'P} \dot{\phi}_i^2 - \ddot{\mathbf{r}}_j - \mathbf{B}_j \mathbf{s}_j^{'P} \ddot{\phi}_j + \mathbf{A}_j \mathbf{s}_j^{'P} \dot{\phi}_j^2 = \mathbf{0}.$$

The two constraints of (B.17) allow only rotational motion of a system and reduce its degree of freedom (DOF) by two, according to [251].

B.3.2 Translational Joint

A translational joint depicted in Fig. B.5 enables relative motion of two bodies along an axis known as line of translation [251]. Therefore, the relative rotation between the bodies as well
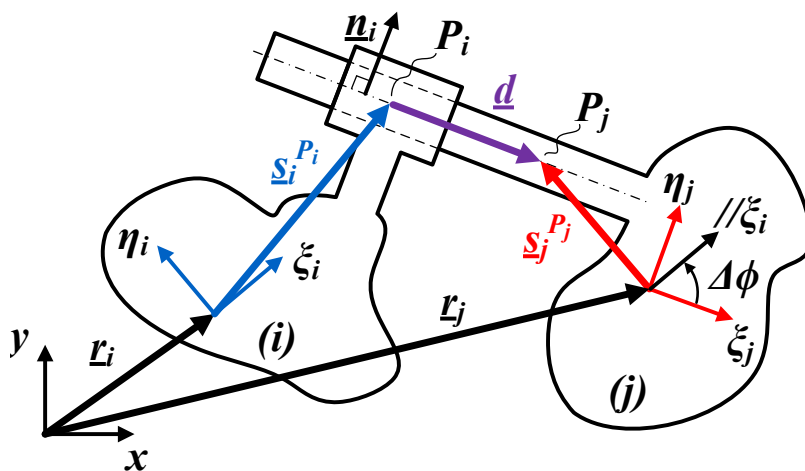

Figure B.5: Translational joint between bodies i and j [251].

as their relative motion in a direction perpendicular to the line of translation are eliminated. To satisfy the former condition, it is sufficient to ensure that at all times both local coordinate

systems $(\xi_i \eta_i)$ and $(\xi_j \eta_j)$ have the same orientation. To exclude the latter one, however, the auxiliary vector $\underline{n}_i$ perpendicular to the line of translation must also be perpendicular to the vector $\underline{d}$ which connects two points of reference on the selected line of translation: P_i on body i and P_j on body j. These two conditions are satisfied when [251]

$$\mathbf{\Phi}^{t,2} = \begin{cases} \phi_i - \phi_j - \Delta\phi = 0 & \text{(prohibits relative rotation)} \\ \mathbf{n}_i^T \mathbf{d} = 0 & \text{(constrains relative translation)} \end{cases} \tag{B.20}$$

$$\mathbf{n}_i = \mathbf{A}_i \mathbf{n}_i'$$

$$\mathbf{d} = \mathbf{r}_j + \mathbf{A}_j \mathbf{s}_j'^{P_j} - \mathbf{r}_i - \mathbf{A}_i \mathbf{s}_i'^{P_i}$$

where $\Delta\phi$ is the difference between the initial orientation of the local frames and $\mathbf{n}_i'$ is a constant vector (which is normal to the line of translation) in the ith body reference frame. Analogously to (B.18) and (B.19), the velocity and acceleration constraints of the translational joint become [251]

$$\dot{\mathbf{\Phi}}^{t,2} = \begin{cases} \dot{\phi}_i - \dot{\phi}_j = 0 \\ \dot{\mathbf{n}}_i^T \mathbf{d} + \mathbf{n}_i^T \dot{\mathbf{d}} = 0 \end{cases} \tag{B.21}$$

$$\dot{\mathbf{n}}_i = \mathbf{B}_i \mathbf{n}_i' \dot{\phi}_i$$

$$\dot{\mathbf{d}} = \dot{\mathbf{r}}_j + \mathbf{B}_j \mathbf{s}_j'^{P_j} \dot{\phi}_j - \dot{\mathbf{r}}_i - \mathbf{B}_i \mathbf{s}_i'^{P_i} \dot{\phi}_i$$

$$\ddot{\mathbf{\Phi}}^{t,2} = \begin{cases} \ddot{\phi}_i - \ddot{\phi}_j = 0 \\ \ddot{\mathbf{n}}_i^T \mathbf{d} + \mathbf{n}_i^T \ddot{\mathbf{d}} + 2\dot{\mathbf{n}}_i^T \dot{\mathbf{d}} = 0 \end{cases} \tag{B.22}$$

$$\ddot{\mathbf{n}}_i = \mathbf{B}_i \mathbf{n}_i' \ddot{\phi}_i - \mathbf{A}_i \mathbf{n}_i' \dot{\phi}_i^2$$

$$\ddot{\mathbf{d}} = \ddot{\mathbf{r}}_j + \mathbf{B}_j \mathbf{s}_j'^{P_j} \ddot{\phi}_j - \mathbf{A}_j \mathbf{s}_j'^{P_j} \dot{\phi}_j^2 - \ddot{\mathbf{r}}_i - \mathbf{B}_i \mathbf{s}_i'^{P_i} \ddot{\phi}_i + \mathbf{A}_i \mathbf{s}_i'^{P_i} \dot{\phi}_i^2.$$

The translational joint also reduces the number of DOFs of a system by two. The position constraints of the gripper arm machine illustrated in Example B.1 are derived in Example B.2.

Example B.2 (Position Constraints)
Let us examine the vertical motion of the gripper arm with the effect of extension/retraction of the hydraulic cylinder which is installed between the lower and upper dollies, as depicted in Fig. B.2. The system is simplified by considering only the most important overall dimensions and masses which, together with locations and types of joints, are kept the same as in the original equipment. In addition, only the planar motion is analyzed and friction is neglected in the model [269].
The mechanical system depicted in Fig. B.2 is composed of 4 rotational and 2 translational joints. In addition, there are 2 linear actuators driven by either velocity (v_{cyl} and v_{winch}) or force (F_{cyl} and F_{winch}), and 1 immobilized rotational joint between bodies 3 and 5. The position constraints vector $\mathbf{\Phi}_{12\times1}$ is therefore written as (without considering the actuators)

$$\mathbf{\Phi}(\mathbf{q}) = \begin{bmatrix} \mathbf{r}_1 + \mathbf{A}_1 \begin{bmatrix} 0 \\ 0.5 \cdot L_1 \end{bmatrix} - \mathbf{A}_2 \begin{bmatrix} 0.5 \cdot L_2 \\ 0 \end{bmatrix} - \mathbf{r}_2 \\ \mathbf{r}_2 + \mathbf{A}_2 \begin{bmatrix} 0.5 \cdot L_2 \\ 0 \end{bmatrix} - \mathbf{r}_3 \\ \mathbf{r}_4 + \mathbf{A}_4 \begin{bmatrix} 0 \\ 0.5 \cdot L_4 \end{bmatrix} - \mathbf{A}_3 \begin{bmatrix} -0.5 \cdot L_3 \\ 0 \end{bmatrix} - \mathbf{r}_3 \\ \mathbf{r}_3 + \mathbf{A}_3 \begin{bmatrix} 0.5 \cdot L_3 \\ 0 \end{bmatrix} - \mathbf{A}_5 \begin{bmatrix} 0 \\ 0.5 \cdot L_5 \end{bmatrix} - \mathbf{r}_5 \\ \phi_1 \\ x_1 \\ \phi_4 \\ x_4 \end{bmatrix} = 0. \tag{B.23}$$

B.4 Kinematic Analysis

As already discussed in Section 2.4, kinematics deals with positions, velocities, and accelerations of mechanisms. In kinematic analysis, forces and torques causing the motion are kept outside the scope. Hence, to describe kinematics of a system, it is sufficient to consider only its constraint equations. In constrained systems (which this thesis studies) the number of defined coordinates is greater than the number of system's DOFs. For a mechanism with n_c independent constraint equations and n_v coordinates, the number of DOFs is [251]

$$n_d = n_v - n_c. \tag{B.24}$$

The position, velocity, and acceleration constraints represented by $n_c = n_v - n_d$ equations become, respectively [252]

$$\mathbf{\Phi}(\mathbf{q}) = \mathbf{0} \tag{B.25}$$

$$\dot{\mathbf{\Phi}}(\mathbf{q}) = \mathbf{\Phi}_q \dot{\mathbf{q}} = \mathbf{0} \tag{B.26}$$

$$\ddot{\mathbf{\Phi}}(\mathbf{q}) = \mathbf{\Phi}_q \ddot{\mathbf{q}} + \dot{\mathbf{\Phi}}_q \dot{\mathbf{q}} = \mathbf{0} \tag{B.27}$$

where the right-hand side of the acceleration equation is denoted as $\boldsymbol{\gamma} = -\dot{\mathbf{\Phi}}_q \dot{\mathbf{q}}$ [252] and the Jacobian matrix $\mathbf{\Phi}_q$ which contains partial derivatives of the constraint equations with respect to the coordinates is defined as [251]

$$\mathbf{\Phi}_q = \frac{\partial \mathbf{\Phi}}{\partial \mathbf{q}}. \tag{B.28}$$

The goal of the kinematic analysis is to solve (B.25)-(B.27) if n_d is known. This necessitates formulation of the so-called driver constraints that provide values for n_d number of coordinates as a function of time. The two most popular drivers are rotational and translational actuators illustrated in Figs. B.6a and B.6b, respectively. Their role is to define motion of one or more
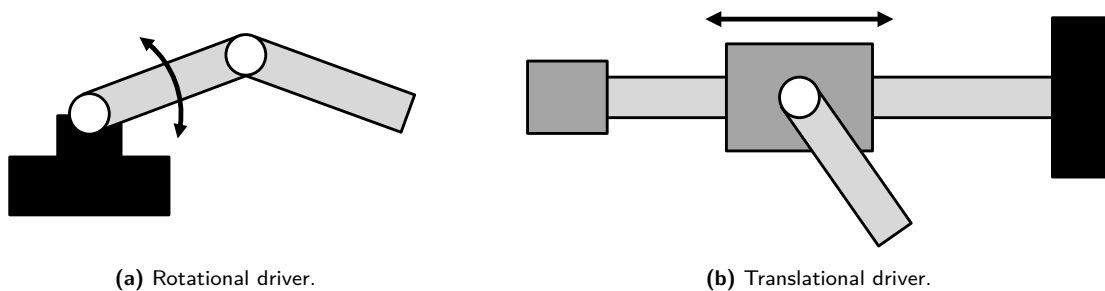

(a) Rotational driver.   **(b)** Translational driver.

Figure B.6: Examples of popular drivers used in mechanical systems.

links using driver constraints. As discussed, the number of driver constraints must be equal to the number of DOFs of the system. Typically, driver constraints are functions of time and

for the driving links presented in Fig. B.6 they take the following form [252]

$$\Phi^{d-r,1} = \phi_i - h(t) = 0 \qquad \text{(rotational driver – Fig. B.6a)} \qquad (B.29)$$
$$h(t) = \phi_i^0 + \omega t \qquad \text{(constant velocity } \omega \text{ preset)}$$
$$h(t) = \phi_i^0 + \dot{\phi}_i^0 t + \frac{1}{2}\alpha t^2 \qquad \text{(constant acceleration } \alpha \text{ preset)}$$

$$\Phi^{d-t,1} = x_i - h(t) = 0 \qquad \text{(translational driver – Fig. B.6b)} \qquad (B.30)$$
$$h(t) = x_i^0 + vt \qquad \text{(constant velocity } v \text{ preset)}$$
$$h(t) = x_i^0 + \dot{x}_i^0 t + \frac{1}{2}at^2 \qquad \text{(constant acceleration } a \text{ preset).}$$

Equations (B.29) and (B.30) contain some exemplary functions $h(t)$ which either fix constant velocity or acceleration of the driver, however, in principle, any arbitrary function can be substituted as $h(t)$ to preset any kinematic feature of the driving link. Also, the initial values of positions/velocities should be assigned at $t = 0$. Therefore, for the system characterized by n_d degrees of freedom, the driver constraints are formulated as [252]

$$\Phi^d = \Phi^d(\mathbf{q}) - \mathbf{h}(t) = \mathbf{0} \qquad (B.31)$$
$$\dot{\Phi}^d = \Phi_q^d \dot{\mathbf{q}} - \dot{\mathbf{h}}(t) = \mathbf{0} \qquad (B.32)$$
$$\ddot{\Phi}^d = \Phi_q^d \ddot{\mathbf{q}} + \dot{\Phi}_q^d \dot{\mathbf{q}} - \ddot{\mathbf{h}}(t) = \mathbf{0} \qquad (B.33)$$

where Φ_q^d is the Jacobian of the driver constraints. Performing the kinematic analysis relies on finding at each time instant t_i positions, velocities, and accelerations of bodies in the mechanical system based on their kinematic and driver constraints. A popular approach to arrive at this solution is to use the so-called appended constraint method where the n_d driver expressions are appended to the n_c kinematic constraints to constitute n_v constraints in total. The complete analysis is formulated by combining (B.25)-(B.27) with (B.31)-(B.33) [252]

$$\Phi(\mathbf{q}, t) = \begin{bmatrix} \Phi(\mathbf{q}) \\ \Phi^d(\mathbf{q}) - \mathbf{h}(t) \end{bmatrix} = \begin{bmatrix} \mathbf{0} \\ \mathbf{0} \end{bmatrix} \qquad (B.34)$$

$$\dot{\Phi}(\mathbf{q}, t) = \begin{bmatrix} \Phi_q \dot{\mathbf{q}} \\ \Phi_q^d \dot{\mathbf{q}} - \dot{\mathbf{h}}(t) \end{bmatrix} = \begin{bmatrix} \mathbf{0} \\ \mathbf{0} \end{bmatrix} \qquad (B.35)$$

$$\ddot{\Phi}(\mathbf{q}, t) = \begin{bmatrix} \Phi_q \ddot{\mathbf{q}} + \dot{\Phi}_q \dot{\mathbf{q}} \\ \Phi_q^d \ddot{\mathbf{q}} + \dot{\Phi}_q^d \dot{\mathbf{q}} - \ddot{\mathbf{h}}(t) \end{bmatrix} = \begin{bmatrix} \mathbf{0} \\ \mathbf{0} \end{bmatrix}. \qquad (B.36)$$

It is common to further simplify the notation in order to avoid dealing with separate expressions for kinematic constraints and drivers [252]. Then, (B.34)-(B.36) simply become

$$\Phi(\mathbf{q}, t) = \mathbf{0} \qquad (B.37)$$

$$\dot{\Phi}(\mathbf{q}, t) = \Phi_q^v \dot{\mathbf{q}} = \begin{bmatrix} \mathbf{0} \\ \dot{\mathbf{h}}(t) \end{bmatrix} \qquad (B.38)$$

$$\ddot{\Phi}(\mathbf{q}, t) = \Phi_q^v \ddot{\mathbf{q}} = \begin{bmatrix} \boldsymbol{\gamma} \\ \ddot{\mathbf{h}}(t) \end{bmatrix} \qquad (B.39)$$

where $\Phi_q^v = [\Phi_q, \Phi_q^d]^T$.

Kinematic analysis of the case study machine is presented in Example B.3.

Example B.3 (Forward Kinematics)

According to (B.31), the following driver constraints are appended to the kinematic constraints (B.23) of the considered gripper arm machine shown in Fig. B.2

$$\mathbf{\Phi}^d_{3\times 1} = \mathbf{\Phi}^d(\mathbf{q}) - \mathbf{h}(t) = \mathbf{0}$$

$$= \begin{bmatrix} y_1 - s_{winch}(t) \\ y_4 - y_1 - \left(v_{cyl} \cdot t + L^0_{cyl} \right) \\ \phi_3 - \phi_5 + \phi^0_{3-5} + \omega_{3-5} \cdot t \end{bmatrix} = 0. \qquad (\text{B.40})$$

Therefore, the dimension of the vector of constraints $\mathbf{\Phi}_{15\times 1}(\mathbf{q}, t)$ is increased by 3, and the vector itself becomes time-dependent. The cylinder velocity and winch position presets are arbitrarily defined as, respectively

$$v_{cyl} = 0.2 \ [m/s], \qquad s_{winch}(t) = 0.7 \cdot \sin\left(\frac{2\pi}{3}t\right) + 2 \ [m]. \qquad (\text{B.41})$$

In addition, ω_{3-5} is set to zero, and the initial angle between bodies 3 and 5 is assigned a constant value of ω^0_{3-5}, similarly to the initial distance between the lower and upper dollies of L^0_{cyl}. This set of input data allows to perform the forward kinematic analysis. The simulated Cartesian coordinates of each body of the system in Fig. B.2 are illustrated in Fig. B.7.
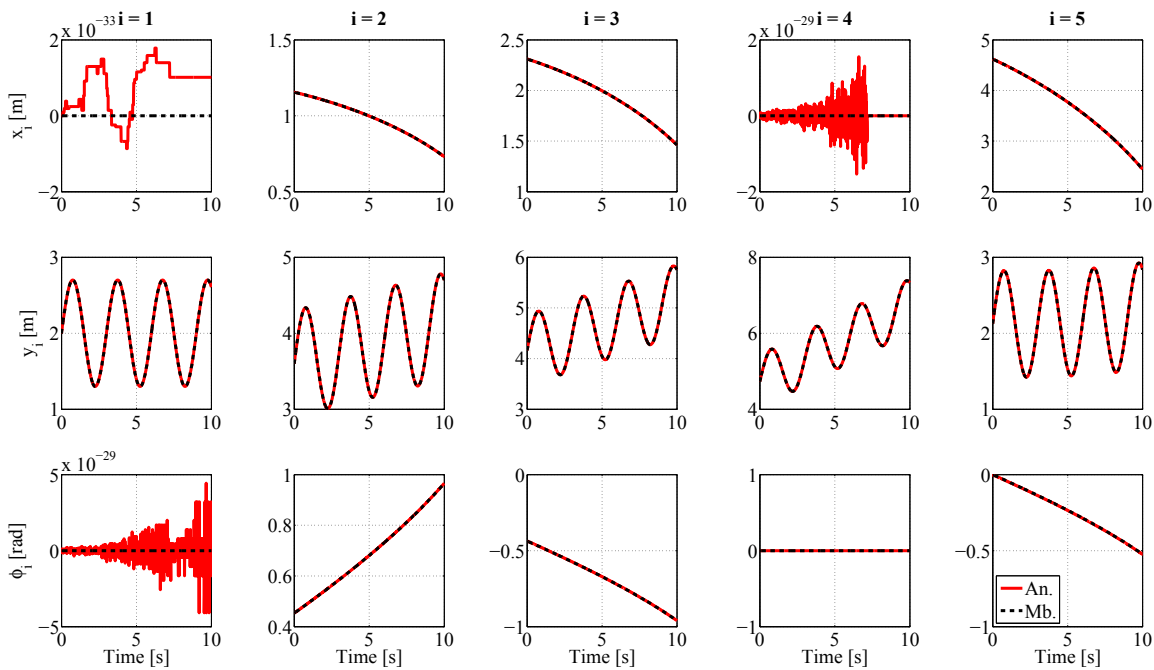

Figure B.7: Comparison of simulated positions of analytical (An.) and multibody (Mb.) models [269].

The results of the analytical modeling are identical to the simulation data generated by the commercial modeling software. The shown positions verify that the models geometry, the constraints vector $\mathbf{\Phi}(\mathbf{q}, t)$, and the Jacobian matrix $\mathbf{\Phi}^v_q$ are the same in both approaches. For further analysis of the investigated example and discussion, please refer to publication [269].

B.5 Dynamics of System of Rigid Bodies

Individual bodies of a mechanical system can be regarded as constrained (if they are connected by kinematic constraints) or unconstrained (if there are no kinematic joints in the system) [251].

In addition to kinematic constraints, a typical constrained mechanical system is also composed of force elements, such as springs and dampers, as illustrated in Fig. B.8.
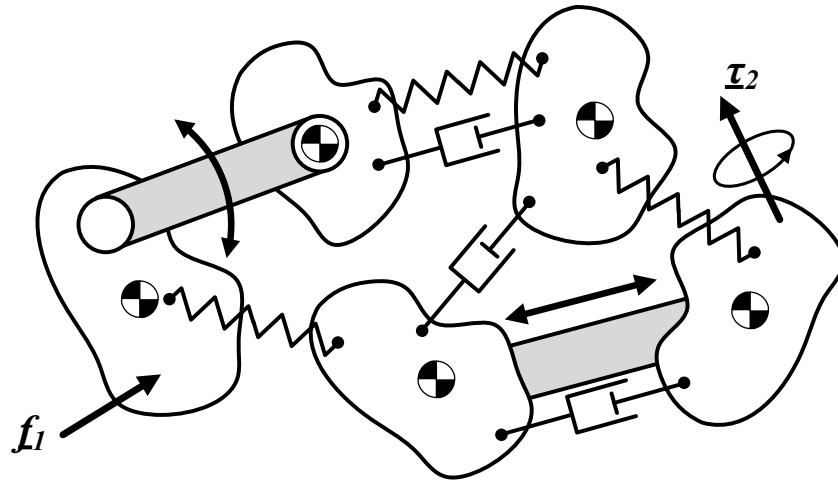

Figure B.8: A system of constrained bodies [251].

B.5.1 Center of Mass

A basis for describing dynamic behavior of a rigid body is to extend the governing laws of dynamics of its individual particles [252]. In an exemplary system of particles illustrated in Fig. B.9 each particle is characterized by its own mass m_i, position $\mathbf{r}_i$, and a set of forces $\mathbf{f}_i$
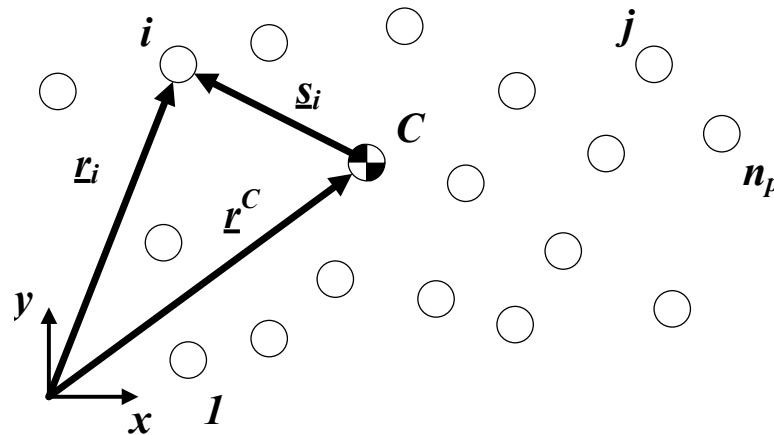

Figure B.9: Center of mass for a system of particles [252].

acting on it. The center of mass (centroid) is defined as [252]

$$\mathbf{r}^C = \frac{1}{m} \sum_{i=1}^{n_p} m^i \mathbf{r}^i.$$ (B.42)

and its motion is described by the Newton's second law as

$$m\ddot{\mathbf{r}}^C = \mathbf{f}$$ (B.43)

where $m = \sum_{i=1}^{n_p} m^i$ is the total mass and $\mathbf{f} = \sum_{i=1}^{n_p} \mathbf{f}^i$ is the sum of external forces acting on the system. This reasoning allows to state that the resultant of all external forces that a system of masses is subjected to is equal to the total mass of the system multiplied by the acceleration of its centroid [251]. It means that the centroid moves as if it were a particle of mass m under the action of the force $\mathbf{f}$. This greatly simplifies the dynamic analysis of rigid bodies, as shown further in the text.

B.5.2 Equations of Motion of Unconstrained System of Bodies

As long as planar motion is concerned, an unconstrained body can be described by the basic three equations of motion

$$m_i \ddot{x}_i = f_{(x)i} \tag{B.44}$$
$$m_i \ddot{y}_i = f_{(y)i} \tag{B.45}$$
$$J_i \ddot{\phi}_i = \tau_i \tag{B.46}$$

or in vector form

$$
\begin{bmatrix} m_i & & \\ & m_i & \\ & & J_i \end{bmatrix}
\begin{bmatrix} \ddot{x}_i \\ \ddot{y}_i \\ \ddot{\phi}_i \end{bmatrix}
=
\begin{bmatrix} f_{(x)i} \\ f_{(y)i} \\ \tau_i \end{bmatrix}
\tag{B.47}
$$

where $\mathbf{f}_i = \left[f_{(x)}, f_{(y)} \right]^T$ is the sum of forces acting on the centroid of the body in the xy plane, τ_i denotes the moment (torque) acting in the direction perpendicular to the xy plane, m_i is mass of the considered body, and J_i is its polar moment of inertia. Equation (B.47) can be rewritten in more compact form as [251]

$$\mathbf{M}_i \ddot{\mathbf{q}}_i = \mathbf{g}_i \tag{B.48}$$

where

$$\mathbf{M}_i = \text{diag} \left[m_i, m_i, J_i \right] \tag{B.49}$$
$$\mathbf{q}_i = \left[x_i, y_i, \phi_i \right]^T \tag{B.50}$$
$$\mathbf{g}_i = \left[f_{(x)i}, f_{(y)i}, \tau_i \right]^T \tag{B.51}$$

which yields the following formulation of EOM for a system of b unconstrained bodies

$$\mathbf{M} \ddot{\mathbf{q}} = \mathbf{g} \tag{B.52}$$

where

$$\mathbf{M} = \text{diag} \left[\mathbf{M}_1, \mathbf{M}_2, \dots, \mathbf{M}_b \right] \tag{B.53}$$
$$\mathbf{q} = \left[\mathbf{q}_1^T, \mathbf{q}_2^T, \dots, \mathbf{q}_b^T \right]^T \tag{B.54}$$
$$\mathbf{g} = \left[\mathbf{g}_1^T, \mathbf{g}_2^T, \dots, \mathbf{g}_b^T \right]^T. \tag{B.55}$$

The mass matrix of the system $\mathbf{M}$ is a $3b \times 3b$ constant diagonal matrix, and vectors $\mathbf{q}$, $\dot{\mathbf{q}}$, $\ddot{\mathbf{q}}$, and $\mathbf{g}$ are $3b$-vectors [251].

B.5.3 Equations of Motion of Constrained System of Bodies

The system of b constrained bodies is described by reformulating (B.52) as

$$\mathbf{M}\ddot{\mathbf{q}} = \mathbf{g} + \mathbf{g}^{(c)} \tag{B.56}$$

where $\mathbf{g}^{(c)}$ is the vector of reaction forces in constraints. It can be found (refer to [251] for detailed derivation) that reaction forces can be computed as

$$\mathbf{g}^{(c)} = \mathbf{\Phi}_q^T \boldsymbol{\lambda} \tag{B.57}$$

where $\boldsymbol{\lambda}$ is the vector of Lagrange multipliers. Hence, the final set of equations of motion of a system of constrained bodies is expressed as

$$\mathbf{M}\ddot{\mathbf{q}} - \mathbf{\Phi}_q^T \boldsymbol{\lambda} = \mathbf{g} \tag{B.58}$$

$$\mathbf{\Phi} = \mathbf{0}. \tag{B.59}$$

As already mentioned in Section B.4, this thesis presents modeling and simulation results of constrained mechanical systems, as they are more common in industrial applications.

B.6 Force Elements

To describe the dynamic behavior of a mechanical system, it is not sufficient to consider only the kinematic joints which connect its bodies, but one needs to take into account also the internal and external forces acting on it. As already discussed in Section B.5, the vector of forces $\mathbf{g}$ in (B.58)

$$\mathbf{g} = \left[\mathbf{g}_1^T, \mathbf{g}_2^T, \ldots, \mathbf{g}_b^T \right]^T \tag{B.60}$$

is constructed by determining all forces and torques acting on each body of the system

$$\mathbf{g}_i = \left[f_{(x)i}, f_{(y)i}, \tau_i \right]^T. \tag{B.61}$$

The most popular force elements which appear in mechanical systems are: gravity, actuation, springs, and dampers [251]. Therefore, this thesis gives a brief overview on their role and effect they have in translational motion. Similar relationships can also be formulated for rotating components (e.g. rotational springs) and are comprehensively presented in [251].

B.6.1 Gravity

A body subjected to the action of the gravitational field is illustrated in Fig. B.10. The negative y direction is chosen as the direction of gravity, which is a typical convention in planar motion [251]. The gravity force acting on body i is denoted as w_i and is basically equal to the mass of the body multiplied by the gravity constant. Its contribution to the vector of forces which the ith body is subjected to is

$$\mathbf{g}_i^{(g)} = [0, -w_i, 0]^T. \tag{B.62}$$

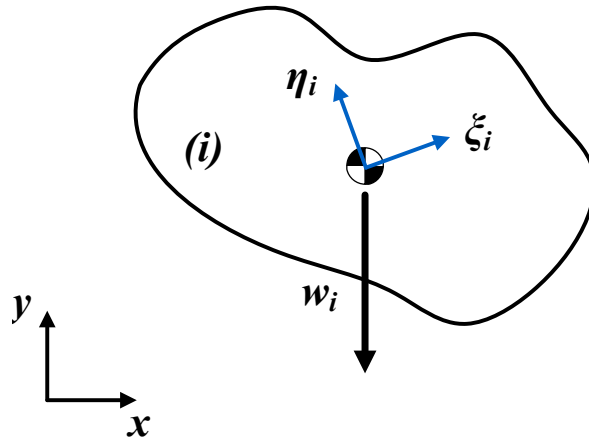**Figure B.10:** Gravitational field acting on a body [251].

B.6.2 Single Force or Torque

The single force acting at point P_i on body i, as shown in Fig. B.11a, has two components: $f_{(x)i}$ and $f_{(y)i}$. For the known local coordinates of P_i denoted as $\mathbf{s}_i'^{P_i} = \left[\xi_i^{P_i}, \eta_i^{P_i}\right]^T$, the torque of $\underline{f}_i$ acting on the body about its origin is (recall that $\mathbf{s}_i^{P_i} = \mathbf{A}_i \mathbf{s}_i'^{P_i}$)

$$\tau_i = s_{(y)i}^{P_i} f_{(x)i} + s_{(x)i}^{P_i} f_{(y)i} \tag{B.63}$$

$$= -\left(\xi_i^{P_i} \sin\left(\phi_i\right) + \eta_i^{P_i} \cos\left(\phi_i\right)\right) f_{(x)i} + \left(\xi_i^{P_i} \cos\left(\phi_i\right) - \eta_i^{P_i} \sin\left(\phi_i\right)\right) f_{(y)i}. \tag{B.64}$$
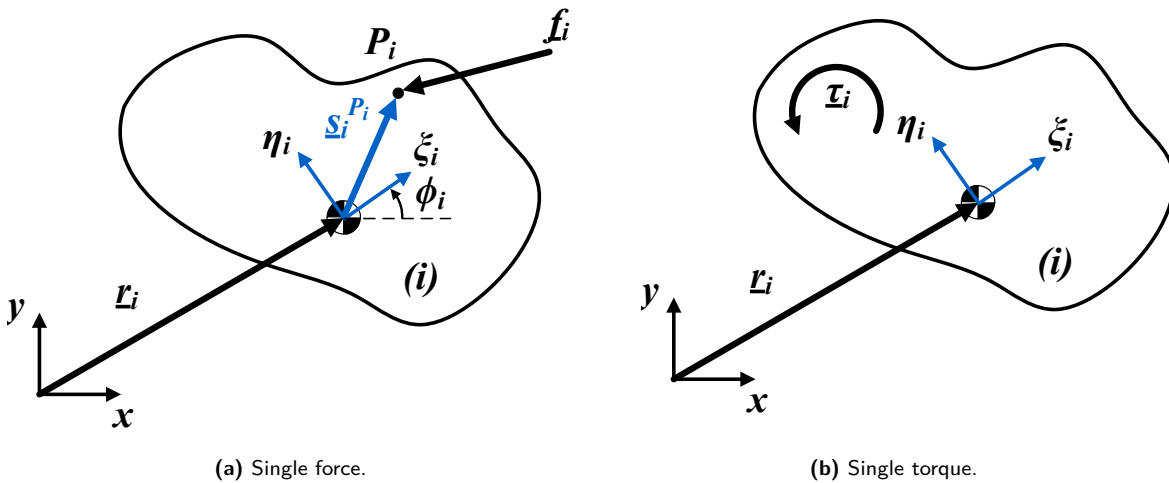
The single force contribution to the vector of forces acting on the body i is

$$\mathbf{g}_i^{(s,f)} = \left[f_{(x)i}, f_{(y)i}, \tau_i\right]^T. \tag{B.65}$$

Similarly, the effect of the single torque acting on the ith body shown in Fig. B.11b is

$$\mathbf{g}_i^{(s,\tau)} = [0, 0, \tau_i]^T. \tag{B.66}$$

Both (B.65) and (B.66) are applicable to either constant or time-varying forces or torques [251].

(a) Single force. (b) Single torque.

Figure B.11: Body subjected to the action of single force/torque [251].

B.6.3 Actuator Force

Linear actuators produce constant or time-dependent pair of forces acting on two bodies without a need to constrain them kinematically [251]. These forces act along the same line but have opposite directions. As presented in Fig. B.12, the actuator exerts the force in point P_i on body i and in point P_j on body j. The force is assumed to be positive ($f^{(a)} > 0$) when
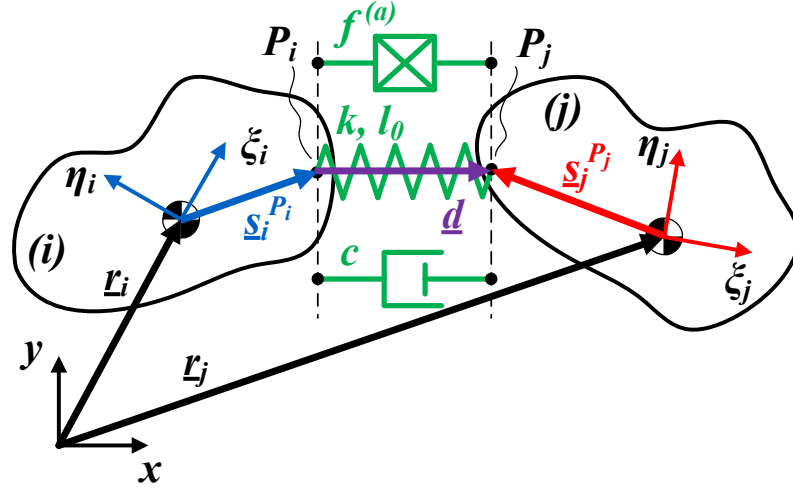

Figure B.12: Translational force elements acting between two bodies (actuator, spring, and damper) [251].

pulling the body and negative ($f^{(a)} < 0$) when pushing the body. To find numerical values of forces $f_i^{(a)}$ and $f_j^{(a)}$ acting on each body, a unit vector $\underline{u}$ is defined on the line of action of the actuator [251]. A vector $\underline{d}$ which connects points P_i and P_j is rewritten (recall (B.20))

$$\mathbf{d} = \mathbf{r}_j + \mathbf{A}_j \mathbf{s}_j^{'P_j} - \mathbf{r}_i - \mathbf{A}_i \mathbf{s}_i^{'P_i} \tag{B.67}$$

and its magnitude is found to be [251]

$$|\mathbf{d}| = l_{P_i P_j} = \sqrt{\mathbf{d}^T \mathbf{d}}. \tag{B.68}$$

The unit vector is then formulated as

$$\mathbf{u} = \frac{\mathbf{d}}{l_{P_i P_j}} \tag{B.69}$$

and it has the same direction as $\underline{f}_i^{(a)}$ in the case of pulling and $\underline{f}_j^{(a)}$ in the case of pushing

$$\mathbf{f}_i^{(a)} = f^{(a)} \mathbf{u} \tag{B.70}$$

$$\mathbf{f}_j^{(a)} = -f^{(a)} \mathbf{u}. \tag{B.71}$$

The contribution of the actuator force $\mathbf{f}_i^{(a)}$ (or $\mathbf{f}_j^{(a)}$) to the vector of forces $\mathbf{g}_i$ (or $\mathbf{g}_j$) is described by (B.65).

B.6.4 Spring Force

By replacing the actuator force in Fig. B.12 with the spring attached between the points P_i on body i and P_j on body j, it is possible to consider the effects of compressibility in the system.

It is self-explanatory that (B.67)-(B.69) also hold in this case. The force that the spring exerts on bodies i and j is expressed as, respectively [251]

$$\mathbf{f}_i^{(s)} = \left(l_{P_i P_j} - l_0\right) k\mathbf{u} \tag{B.72}$$

$$\mathbf{f}_j^{(s)} = -\left(l_{P_i P_j} - l_0\right) k\mathbf{u} \tag{B.73}$$

where l_0 is the undeformed length of the spring, $l_{P_i P_j}$ is the deformed length found from (B.68), k is the spring stiffness, and $\mathbf{u}$ is the unit vector defined in (B.69). The sign convention for the spring force is identical to that of the actuator force, i.e. the spring force is positive in tension/pull ($l_{P_i P_j} > l_0$) and negative in compression/push ($l_{P_i P_j} < l_0$) [252]. The contribution of the spring force $\mathbf{f}_i^{(s)}$ (or $\mathbf{f}_j^{(s)}$) to the vector of forces $\mathbf{g}_i$ (or $\mathbf{g}_j$) is also found from (B.65). In the considered case, a linear spring characterized by a single value of stiffness k is assumed. However, (B.72) and (B.73) may equally well involve nonlinear force-deformation relationships [251].

B.6.5 Damper Force

By putting the dissipative element in the place of the force element in Fig. B.12, a point-to-point damper is obtained. The damping force depends on the time rate of change of the distance between the points P_i and P_j and is expressed as

$$\mathbf{f}_i^{(d)} = \dot{l}_{P_i P_j} c\mathbf{u} \tag{B.74}$$

$$\mathbf{f}_j^{(d)} = -\dot{l}_{P_i P_j} c\mathbf{u} \tag{B.75}$$

where c is the damping coefficient and $\dot{l}_{P_i P_j}$ is the rate of change of the damper length which is computed by taking the time derivative of (B.68) [251]

$$\dot{l}_{P_i P_j} = \frac{\mathbf{d}^T \dot{\mathbf{d}}}{l_{P_i P_j}} \tag{B.76}$$

where $\dot{\mathbf{d}}$ is the time derivative of (B.67)

$$\dot{\mathbf{d}} = \dot{\mathbf{r}}_j + \mathbf{B}_j \mathbf{s}_j'^{P_j} \dot{\phi}_j - \dot{\mathbf{r}}_i - \mathbf{B}_i \mathbf{s}_i'^{P_i} \dot{\phi}_i. \tag{B.77}$$

Naturally, (B.67)-(B.69) are valid for the damper element as well. Analogously to the case of the spring force, the damper force is assumed to be positive for $\dot{l}_{P_i P_j} > 0$ and negative for $\dot{l}_{P_i P_j} < 0$. Positive damper force between the bodies i and j indicates that they move away from each other (pull), whereas the negative damper force means that they move towards each other (push) [251]. Finally, it is also possible to use a nonlinear damper characteristic to describe the relationship between force and deformation rate in (B.74) and (B.75).

B.7 Dynamic Analysis

In kinematic analysis, the sum of kinematic constraint equations n_c and driver equations n_d is equal to the number of coordinates n_v. This means that n_v unknowns are found by solving n_v equations and, as a result, a unique solution is obtained. In dynamic analysis, however, the driver constraints are usually not specified. Since $n_v > n_c$, the unique solution to the constraint equations (B.59) is found only when they are solved simultaneously with the differential EOMs

and proper initial conditions [251]. The procedure for solving a constrained dynamic system with n_c independent constraints is summarized in the following steps. First, the position, velocity, and acceleration constraints have to be recalled

$$\boldsymbol{\Phi} = \mathbf{0} \tag{B.78}$$

$$\dot{\boldsymbol{\Phi}} = \boldsymbol{\Phi}_q \dot{\mathbf{q}} = \mathbf{0} \tag{B.79}$$

$$\ddot{\boldsymbol{\Phi}} = \boldsymbol{\Phi}_q \ddot{\mathbf{q}} - \boldsymbol{\gamma} = \mathbf{0}. \tag{B.80}$$

Then, by appending (B.80) to (B.58), it is possible to include the constraints (algebraic equations – AEs) when solving equations of motion (ordinary differential equations – ODEs)

$$\begin{bmatrix} \mathbf{M} & -\boldsymbol{\Phi}_q^T \\ \boldsymbol{\Phi}_q & \mathbf{0} \end{bmatrix} \begin{bmatrix} \ddot{\mathbf{q}} \\ \boldsymbol{\lambda} \end{bmatrix} = \begin{bmatrix} \mathbf{g} \\ \boldsymbol{\gamma} \end{bmatrix}. \tag{B.81}$$

The solution of (B.81) becomes

$$\begin{bmatrix} \ddot{\mathbf{q}} \\ \boldsymbol{\lambda} \end{bmatrix} = \begin{bmatrix} \mathbf{M} & -\boldsymbol{\Phi}_q^T \\ \boldsymbol{\Phi}_q & \mathbf{0} \end{bmatrix}^{-1} \begin{bmatrix} \mathbf{g} \\ \boldsymbol{\gamma} \end{bmatrix} \tag{B.82}$$

which, under the assumption of constant, non-zero mass and inertia of each system's body (which makes calculation of the inverse mass matrix $\mathbf{M}^{-1}$ easy), is further decomposed into [251]

$$\ddot{\mathbf{q}} = \mathbf{M}^{-1} \left(\boldsymbol{\Phi}_q^T \boldsymbol{\lambda} + \mathbf{g} \right) \tag{B.83}$$

where the Lagrange multipliers vector is computed as

$$\boldsymbol{\lambda} = \left(\boldsymbol{\Phi}_q \mathbf{M}^{-1} \boldsymbol{\Phi}_q^T \right)^{-1} \left(\boldsymbol{\gamma} - \boldsymbol{\Phi}_q \mathbf{M}^{-1} \mathbf{g} \right). \tag{B.84}$$

The resulting velocities and positions of bodies are computed by taking the integral of the accelerations (B.83) – a variety of software products can perform that task numerically [251]. The Jacobian matrix $\boldsymbol{\Phi}_q$ is a function of $\mathbf{q}$, whereas vectors $\mathbf{g}$ and $\boldsymbol{\gamma}$ are functions of $\mathbf{q}$, $\dot{\mathbf{q}}$, and time t. Therefore, when $\mathbf{q}$ and $\dot{\mathbf{q}}$ are known at any time instant, (B.81) can be solved for $\ddot{\mathbf{q}}$ and $\boldsymbol{\lambda}$, as presented in (B.83) and (B.84), respectively. Finally, to solve mixed algebraic-differential equations for constrained mechanical systems, (B.58) and (B.78)-(B.80) must be considered simultaneously. There exist various methods for solving such equations of motion numerically, however, the most frequently used technique is known as the Newton–Raphson algorithm [251].

An illustration of dynamic analysis of the full-scale offshore pipe handling machine is demonstrated in Example B.4.

Remark B.3. *The solution of EOM (B.58) with known accelerations $\ddot{\mathbf{q}}$ in the kinematic analysis*

$$\mathbf{M}\ddot{\mathbf{q}} = \mathbf{g} + \boldsymbol{\Phi}_q^T \boldsymbol{\lambda} \tag{B.90}$$

gives the simplified expression of vector of Lagrange multipliers

$$\boldsymbol{\lambda} = \left(\boldsymbol{\Phi}_q^T \right)^{-1} \left(\mathbf{M}\ddot{\mathbf{q}} - \mathbf{g} \right) \tag{B.91}$$

which is applicable to finding reaction forces in joints of a mechanism also when performing the kinematic analysis, as shown in (B.57).

Example B.4 (Forward Dynamics)

For the considered gripper arm machine shown in Fig. B.2, only the kinematic constraints (B.23) are dealt with when performing the dynamic analysis. Behavior of the mechanism is governed by the action of the gravity, actuation, spring, and damper forces, as described by (B.60)

$$\mathbf{g} = [0, -m_1 g + F_{winch}^{(a)}(t) - F_{cyl}^{(a)}(t), 0, 0, -m_2 g, 0,$$
$$0, -m_3 g, -T^{(sd)}, 0, -m_4 g + F_{cyl}^{(a)}(t), 0, 0, -m_5 g, T^{(sd)}]^T \tag{B.85}$$

where g is the gravity constant and $m = \sum_{i=1}^{5} m_i$ is the total mass of the system. The actuation forces are defined as

$$F_{cyl}^{(a)}(t) = 22000 + 15000 \cdot \sin(\pi t) \ [N], \qquad F_{winch}^{(a)}(t) = mg + 10000 \cdot \cos\left(\frac{2\pi}{3}t\right) \ [N] \tag{B.86}$$

and the rotational spring and damper between bodies 3 and 5 is characterized by the following torques

$$T^{(s)} = \left(|\phi_3 - \phi_5| - \phi_{3-5}^0\right) \cdot k_{rot} \cdot \frac{\phi_3 - \phi_5}{|\phi_3 - \phi_5|} \tag{B.87}$$

$$T^{(d)} = \left(\dot{\phi}_3 - \dot{\phi}_5\right) \cdot c_{rot} \cdot \frac{\phi_3 - \phi_5}{|\phi_3 - \phi_5|} \tag{B.88}$$

$$T^{(sd)} = T^{(s)} + T^{(d)}. \tag{B.89}$$

The forward dynamic analysis is then performed for the machine shown in Fig. B.2 and characterized by the above force constraints. The simulated accelerations of each body of the system are shown in Fig. B.13. The accelerations found by solving (B.83) and these computed by the commercial multibody software are identical. To fully describe dynamic behavior of the machine, the resulting velocities and positions can easily be obtained by numerically integrating the acceleration signals.
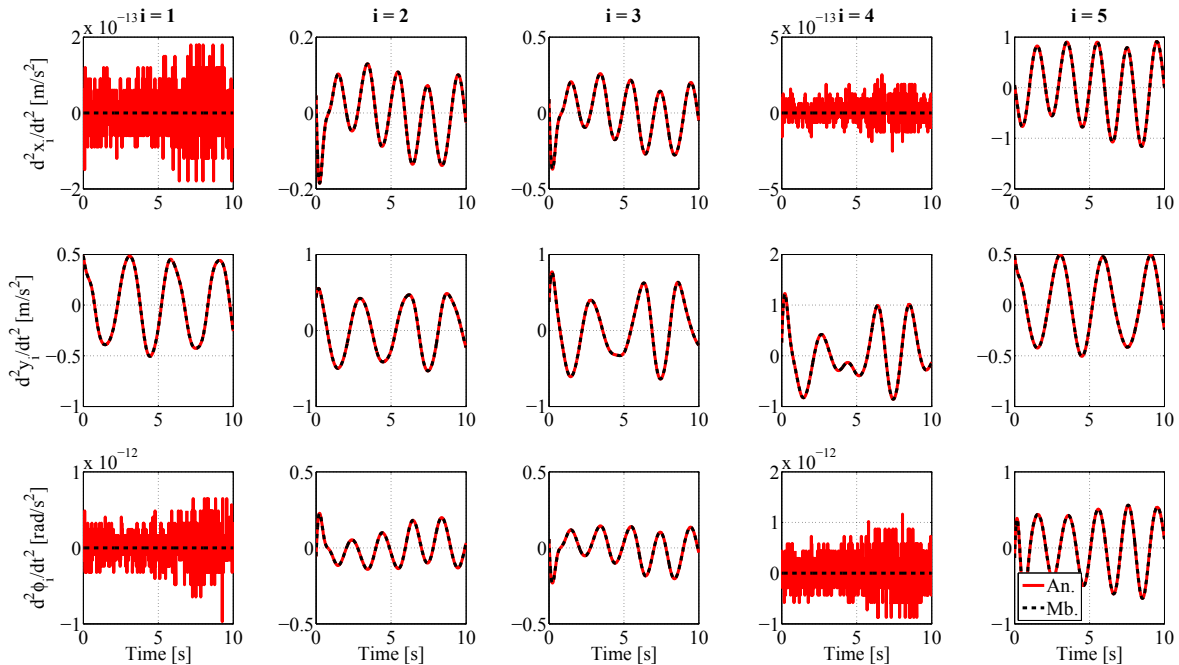

Figure B.13: Comparison of simulated accelerations of analytical (An.) and multibody (Mb.) models [269].

B.8 Newton–Raphson Method

A common problem in numerical analysis is to find the roots of one or a set of nonlinear algebraic equations of the form [251]

$$\mathbf{\Phi}(\mathbf{x}) = \mathbf{0}. \tag{B.92}$$

Solving this type of equations is also needed in kinematic (and − implicitly − also dynamic) analysis of mechanical systems. One approach to solve (B.92) is to use a popular iterative technique called the Newton–Raphson method. For a set of n equations, the solution vector $\mathbf{x}$ of (B.92) is found as a result of the following repetitive process [251]

$$\mathbf{x}^{j+1} = \mathbf{x}^j - \mathbf{\Phi}_x^{-1}\left(\mathbf{x}^j\right) \mathbf{\Phi}\left(\mathbf{x}^j\right) \tag{B.93}$$

where superscripts j and $j+1$ are the iteration numbers and $\mathbf{\Phi}_x^{-1}\left(\mathbf{x}^j\right)$ is the inverse Jacobian matrix computed at $\mathbf{x} = \mathbf{x}^j$. This method is illustrated graphically in Fig. B.14. The term
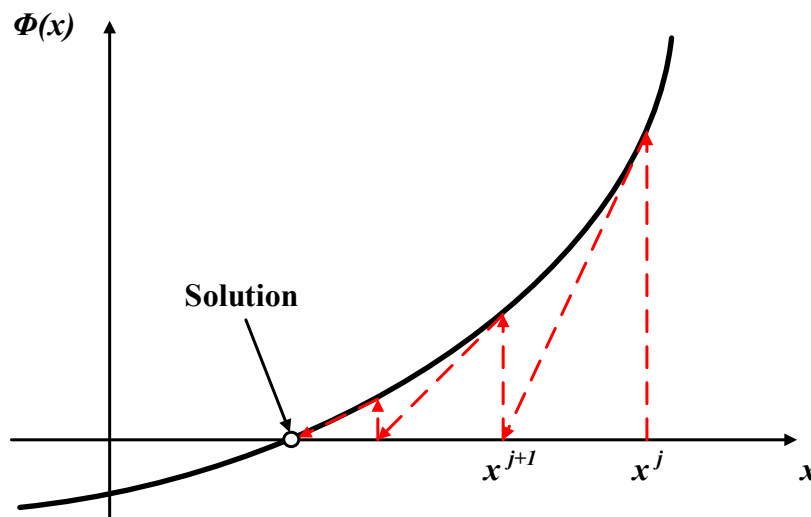

Figure B.14: Graphical representation of Newton–Raphson method [251].

$\mathbf{\Phi}\left(\mathbf{x}^j\right)$ is referred to as the vector of residuals which helps to monitor violation of the equations. The algorithm (B.93) can be split into a two-step operation

$$\mathbf{\Phi}_x\left(\mathbf{x}^j\right) \Delta\mathbf{x}^j = -\mathbf{\Phi}\left(\mathbf{x}^j\right) \tag{B.94}$$
$$\mathbf{x}^{j+1} = \mathbf{x}^j + \Delta\mathbf{x}^j \tag{B.95}$$

where (B.94) is solved for $\Delta\mathbf{x}^j$, which in turn is used in (B.95) to find $\mathbf{x}^{j+1}$. The expression $\Delta\mathbf{x}^j = \mathbf{x}^{j+1} - \mathbf{x}^j$ indicates by how much the approximated solution is corrected in jth iteration.

Remark B.4. *The presented Newton–Raphson algorithm is known to experience problems with robustness [251]. Not only are there multiple techniques to improve its convergence, but also totally different methods can be used to solve problems of the form presented in (B.92), e.g. the bisection method (characterized by improved robustness at the cost of longer computation time). However, the other approaches are not discussed in this thesis, as they are explained in textbooks on numerical analysis, for instance in [119].*

B.9 Final Remarks

In this Chapter, a case study of modeling and simulation of an offshore pipe handling machine using the commercial multibody software and analytical methods is presented. Both forward kinematics and forward dynamics scenarios are examined and the simulation results produced by these two different approaches are confirmed to be identical. The technique aided by the commercial modeling package seems to be more practical from the industrial perspective, since it allows rapid prototyping of new designs, saves both time and engineering effort, and does not require expert knowledge to use it successfully.

However, more thorough analysis makes it possible to check if the modeling process based on using market products is executed correctly and to avoid (or at least identify) mistakes by benchmarking the simulation outcomes of both modeling methods. The trade-off in this case is a rather complex and time-consuming analytical model derivation. Such additional study should be performed not only if simulation results do not appear to be realistic but also to double-check if the design choices made based on using the commercial software would be the same if another modeling strategy is employed.

In the future, it is advisable to investigate how specific multibody software products handle dynamics of complex, closed-loop mechanisms, as arriving at their computationally efficient models can be difficult [99]. One approach to troubleshoot potential problems associated with these models would be to examine the reaction forces in their joints by performing a similar comparative analysis to the one presented in this Chapter [93].